ACCSCIENCE
PUBLISHING

Advances in

Radiotherapy & Nuclear Medicine

Editor-in-Chief: Junjie Wang

ISSN: 3060-8554 (Print)
ISSN: 2972-4392 (Online)
Volume 3 · Issue 2
June 2025

ACCSCIENCE
PUBLISHING

Advances in Radiotherapy & Nuclear Medicine

Print ISSN: 3060-8554
Online ISSN: 2972-4392

Advances in Radiotherapy & Nuclear Medicine is a peer-reviewed and open-access journal that aims to publish and disseminate novel research in the breadth of radiation oncology, physics, and biology.

The journal aims to advance our understanding in the radiotherapy and provide a platform to oncologists and physicians to showcase their findings in original fundamental and clinical research as well as to present new ideas that highlight the changes in the radiation oncological clinical practice.

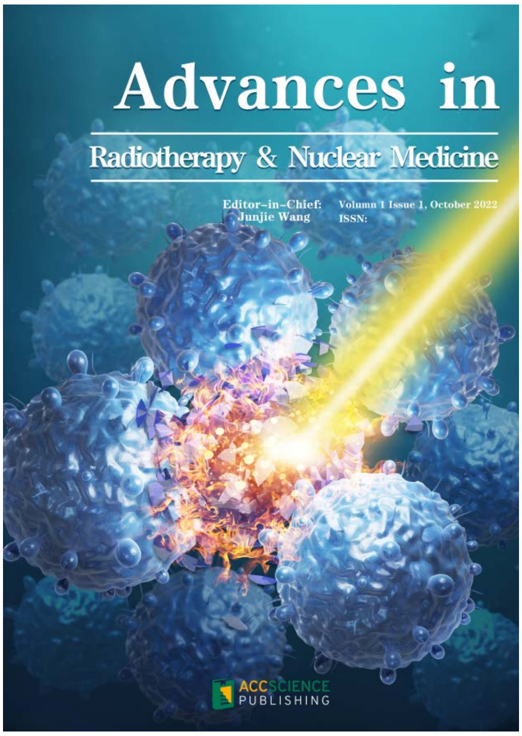

About the Publisher

AccScience Publishing is a publishing company based in Singapore. We publish a range of high-quality, open-access, peer-reviewed journals and books from a broad spectrum of disciplines.

Contact Us

Managing Editor
arnm.office@accscience.sg

AccScience Publishing
9 Raffles Place, Republic Plaza 1 #06-00 Singapore 048619.

Volume 3 • Issue 2 • June 2025
ISSN 3060-8554 (print)   ISSN 2972-4392 (online)

Advances in Radiotherapy & Nuclear Medicine

ACCSCIENCE PUBLISHING
Access Science Without Barriers

Full issue copyright © 2025 AccScience Publishing
All rights reserved. Without permission in writing from the publisher, this full issue publication in its entirety may not be reproduced or transmitted for commercial purposes in any form or by any means, electronic or mechanical, including photocopying, recording, or any information storage and retrieval system. Permissions may be sought from arnm.office@accscience.sg.

Article copyright © Respective Author(s)
See articles for copyright year. All articles in this full issue publication are open-access. There are no restrictions in the distribution and reproduction of individual articles, provided the original work is properly cited. However, permission to reuse copyrighted materials of an article for commercial purposes is applicable if the article is licensed under Creative Commons Attribution-NonCommercial License. Check the specific license before reusing.

ADVANCES IN RADIOTHERAPY & NUCLEAR MEDICINE

ISSN: 3060-8554 (print)
ISSN: 2972-4392 (online)

Editorial and Production Credits

Publisher: AccScience Publishing
Managing Editor: Freda Wang
Production Editor: Sharmila Velapasamy
Article Layout and Typeset: Sinjore Technologies (India)

For all advertising queries, contact arnm.office@accscience.sg.

Supplementary file

Supplementary files of articles can be obtained at https://accscience.com/journal/ARNM/3/2.

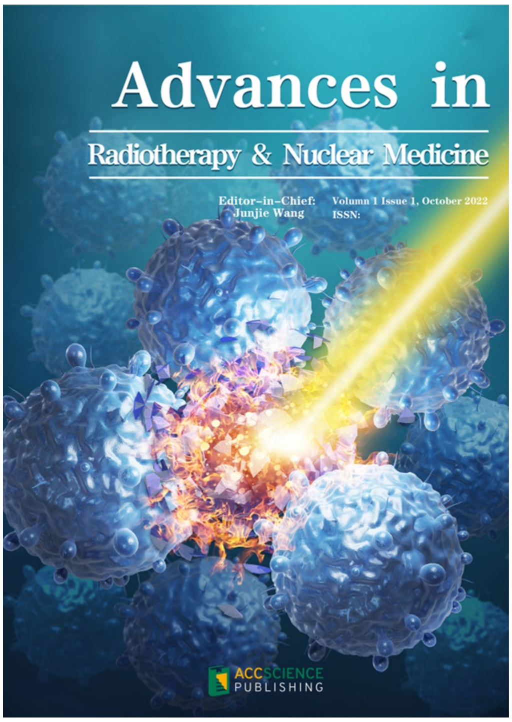

Disclaimer

AccScience Publishing is not liable to the statements, perspectives, and opinions contained in the publications. The appearance of advertisements in the journal shall not be construed as a warranty, endorsement, or approval of the products or services advertised and/or the safety thereof. AccScience Publishing disclaims responsibility for any injury to persons or property resulting from any ideas or products referred to in the publications or advertisements. AccScience Publishing remains neutral with regard to jurisdictional claims in published maps and institutional affiliations.

Advances in Radiotherapy & Nuclear Medicine

Editorial Board

Honorary Editors-in-Chief

Yazid Belkacemi, *France*
Gang Huang, *China*
Jinming Yu, *China*

Editors-in-Chief

Junjie Wang, *China*
Hongcheng Shi, *China*

Associate Editors

Hossein Arabi, *Switzerland*
Xinchen Sun, *China*
Robert Timmerman, *USA*
Ruoyu Wang, *China*
Jing Wang, *China*
Zhi Yang, *China*

*Editorial Board Members**

Dante Amelio, *Italy*
Abass Alavi, *USA*
Saverio Altieri, *Italy*
Richard A. Amos, *UK*
Matteo Bauckneht, *Italy*
Nan Bi, *China*
Mario Bignardi, *Italy*
Ramesh Bilimagga, *India*
David Brasse, *France*
Alessio Bruni, *Italy*
Jing Cai, *China*
Xinping Cao, *China*
Giuseppe Lucio Cascini, *Italy*
Francesco Cellini, *Italy*
Piergiorgio Cerello, *Italy*
Rubel Chakravarty, *India*
Wei Chen, *USA*
Kai Chen, *USA*
Yue Chen, *China*
Guanglie Chen, *China*
Haojun Chen, *China*
Aiping Cheng, *China*
Guanghui Cheng, *China*
Huijun Cheng, *China*
Wan Hang Keith Chiu, *UK*
Supriya Sastri Chopra, *India*
Francesco Cuccia, *Italy*
Rolando Maria D'Angelillo, *Italy*
Sergio A.L.D. Souza, *Brazil*
Alexander De Vries, *Austria*
Thorsten Ecke, *Austria*
Laura Evangelista, *Italy*
Mohammad Faheem, *Pakistan*
Zhaoyang Fan, *USA*
Yan Fan, *China*
Ruitai Fan, *China*
Golam M. Faruque, *Bangladesh*
Alfio Ferlito, *Italy*
Liping Fu, *China*
Xianshu Gao, *China*
Mihai Georgescu, *Romania*
Moshi Geso, *Australia*
Angela Giselvania, *Indonesia*
Soehartati Gondhowiardjo, *Indonesia*
Robert J. Griffin, *USA*
Flavia Groppi, *Italy*
Fada Guan, *USA*
Giuseppe Guglielmi, *Italy*
Cesare Guida, *Italy*
Arif Gulzar, *Australia*
Jean-Michel Hannoun-Levi, *France*
Xiaokun Hu, China
Yujie Huang, *China*
Bin Huo, *China*
Qazi M. Hussain, *Bangladesh*
Zhe Ji, *China*
Ping Jiang, *China*
Hongjun Jin, *China*
Julianna K. Bronk, *USA*
Gabriel Kacso, *Romania*
Kalevi Kairemo, *USA*
Min Kang, *China*,
Minglei Kang, *USA*
Lei Kang, *China*
Shinji Kawabata, *Japan*
Eric C. Ko, *USA*
Gyoergy Kovacs, *Italy*
Deepak Kumar, *India*
Christian La Fougère, *Germany*
Andrea Lancia, *Italy*
Riccardo Laudicella, *Italy*
Wing Mui Anne Lee, *China*
Tsair-Fwu Lee, *Taiwan (China)*
Percy Lee, *USA*
Xiang Li, *Austria*
Shuren Li, *Austria*
Nan Li, *China*
Wenhui Li, *China*
Yongheng Li, *China*
Chunxiao Li, *China*
Minglun Li, *Germany*
Zuping Lian, *China*
Qin Lin, *China*
Chi Lin, *USA*
Zhibo Liu, *China*
Jianjun Liu, *China*
Zhaofei Liu, *China*
Zi Liu, *China*
Xiaodong Liu, *China*
Yi-Hwa Liu, *USA*
Cen Lou, *China*
Xia Lu, *China*
François Lucia, *France*
Alberto Luini, *Italy*
Jiahua Lv, *China*
Charlie Ma, *USA*
Nicolas Magné, *France*
Noeen Malik, *USA*
Gaurav Malviya, *UK*
Juliana Marchi, *Brazil*
Yasushi Nagata, *Japan*
Eiji Nakatani, *Japan*
Tianye Niu, *China*
Mattia Falchetto Osti, *Italy*
Haitao Pan, *USA*
Hua Pang, *China*
Dalong Pang, *USA*
Yiannis Parpottas, *Cyprus*
Tiara B.M. Permata, *Indonesia*
Pham Cam Phuong, *Vietnam*
Maria Picchio, *Italy*
Antonio Pontoriero, *Italy*
X. Sharon Qi, *USA*
Qiao Qiao, *China*
Xiaoguang Qiu, *China*
Baolin Qu, *South Korea*
Natale Quartuccio, *Italy*
David R. Grosshans, *USA*
Keith R. Unger, *USA*
Mayra Ramos-Suzarte, *Cuba*
Shiro Saito, *Japan*
Marco Salvatore, *Italy*
Ralph Santos-Oliveira, *Brazil*
Giuseppe Schettino, *UK*
Liangfang Shen, *China*
Shyam Shrivastava, *India*
Frank-André Siebert, *Germany*
Shaoli Song, *China*
Shiyu Song, *USA*
Chang Song, *USA*
Daniel Yeong-Jin Song, *USA*
Corrado Spatola, *Italy*
Alessandro Stefano, *Italy*
Arnold M. Strashun, *USA*
A. Sulieman, *Saudi Arabia*
Shubhankar Suman, *USA*
Xiaoge Sun, *China*
Baozhou Sun, *USA*
Luca Tagliaferri, *Italy*
Junko Takahashi, *Japan*
Linglong Tang, *China*

Ganghua Tang, *China*
Enrico Tangco, *Philippines*
Kyriaki Theodorou, *Greece*
M. Thiagarajan, *Malaysia*
Rong Tian, *China*
Paolo Tini, *Italy*
Uranchimeg Tsegmed, *Mongolia*
Ioannis Valais, *Greece*
Irina Velikyan, *Sweden*
Zhe Wang, *China*
Kezheng Wang, *China*
Xuejuan Wang, *China*
Feng Wang, *China*
Dian Wang, *USA*
Qifeng Wang, *China*
Ruozheng Wang, *China*
Jihong Wang, *USA*
Horng-Dar Wang, *Taiwan (China)*
Shang-Jui Wang, *USA*
Yoichi Watanabe, *USA*
Lichun Wei, *China*
Qichun Wei, *China*
Rebecca Wong, *Canada*
JiaMing Wu, *China*
HongGyun Wu, *Korea*
Jingbo Wu, *China*
Qiuwen Wu, *USA*
Congying Xie, *China*
Lei Xing, *USA*
Liming Xu, *China*
Huiqin Xu, *China*
Qin Xu, *China*
Benhua Xu, *China*
Jinbin Xu, *USA*
Zhiyuan Xu, *USA*
Xiaoying Xue, *China*
Sean X. Yan, *USA*
Jack Yang, *USA*
Kunyu Yang, *China*
Xing Yang, *China*
Minfu Yang, *China*
Yuchuan Yang, *China*
Jigang Yang, *China*
Chang-Tong Yang, *Singapore*
Yancheng Ye, *China*
Yasuo Yoshioka, *Japan*
Behrooz H. Yousefi, *Germany*
Tarek Yousry, *UK*
Jinbo Yue, *China*
Hesham Zakaly, *Russia*
Paul Zarogoulidis, *Greece*
Zhaochong Zeng, *China*
MingRong Zhang, *Japan*
Zhouen Zhang, *Japan*
Zhen Zhang, *China*
Liyuan Zhang, *China*
Yibao Zhang, *China*
Huojun Zhang, *China*
Tian Zhang, *China*
Hongtao Zhang, *China*
Kaixian Zhang, *China*
Fuquan Zhang, *China*
Shijun Zhang, *USA*
Jingjing Zhang, *Singapore*
Lina Zhao, *China*
Peng Zhen, *China*
Rong Zheng, *China*
Fugen Zhou, *China*
Hua Zhu, *China*
Xiaohua Zhu, *China*
Lijuan Zou, *China*

Youth Editorial Board Members

Kwangzoo Chung, *Korea*
Priscilla Guglielmo, *Italy*
Gaurav Malhotra, *India*
Tamer Soror, *Germany*
Hong Qi Tan, *Singapore*
Yufei Wang, *USA*

*Editorial Board Members as of June 26, 2025

ACCSCIENCE PUBLISHING

Volume 3 | Issue 2 | June 2025 | Page 1 – 101 |

Advances in Radiotherapy & Nuclear Medicine

https://accscience.com/journal/ARNM

CONTENTS

REVIEW ARTICLES

ORIGINAL RESEARCH ARTICLES

SHORT COMMUNICATIONS

LETTERS TO EDITOR

ACCSCIENCE PUBLISHING

Advances in Radiotherapy & Nuclear Medicine

REVIEW ARTICLE

Exploring tumor heterogeneity: The role of PET/CT with various radiopharmaceuticals in diagnosis and treatment guidance

Anjali Jain*, Subhash Kheruka, Sharjeel Usmani, Khulood Al Riyami, Asiya Al Busaidi, Sumit Bichpuria, and Rashid Al Sukaiti

Department of Radiology and Nuclear Medicine, Sultan Qaboos Comprehensive Cancer Care and Research Center, University Medical City, Muscat, Oman

(This article belongs to the *Special Issue: Recent Developments in Radiopharmaceuticals*)

Abstract

Cancer development is a multi-step process that undergoes multiple alterations over time. The tumor microenvironment (TME) contains tumor cells and stroma, including blood cells, fibroblasts, and immune cells, which undergo spatial and temporal changes. These changes contribute to tumor heterogeneity, leading to treatment failure and poor prognosis. As we move toward personalized medicine with the approval of targeted and other therapies, identifying tumor heterogeneity is becoming crucial to management. Positron emission tomography/computed tomography (PET/CT) with various radiopharmaceuticals plays an important role in diagnosing and highlighting heterogeneity non-invasively, guiding treatment decisions, and assessing treatment response. Variability in tracer distribution of ^{18}F-fluorodeoxyglucose (FDG) and various radiopharmaceuticals when coupled together can target various tumor characteristics and, therefore, play an important role in diagnosing heterogeneity. Some of the commonly paired radiopharmaceuticals include ^{18}F-FDG with ^{68}Gallium DOTA (1,4,7,10-tetraazacyclododecane-tetraacetic acid) peptide for neuroendocrine tumors, ^{18}F-FDG with ^{68}Ga-prostate specific membrane antigen for prostate cancers, ^{18}F-metafluorobenzylguanidine with ^{18}F-FDG and ^{68}Ga-DOTA peptide for neural crest tumors, and ^{18}F-fluoroestradiol with ^{18}F-FDG for breast cancers. Many other tracers, including ^{68}Ga-fibroblast activation protein inhibitor and labeled integrins, attach to various components on tumor cells and TME and have displayed significantly positive effects in certain tumors. However, their potential role as a biomarker to evaluate tumor heterogeneity and its clinical relevance remains largely uninvestigated.

Keywords: Cancer; Heterogeneity; ^{18}F- FDG; PET/CT

***Corresponding author:**
Anjali Jain
(a.jain@cccrc.gov.om)

Citation: Jain A, Kheruka S, Usmani S, *et al.*, Exploring tumor heterogeneity: The role of PET/CT with various radiopharmaceuticals in diagnosis and treatment guidance. *Adv Radiother Nucl Med.* 2025;3(2):1-15.
doi: 10.36922/ARNM025040005

Received: January 21, 2025

Revised: February 19, 2025

Accepted: March 5, 2025

1. Introduction

Cancer development is a multi-step process that undergoes multiple alterations spatially and temporally. During its evolution process, heterogeneity develops between various cancer cells, displaying distinct characteristics, either within the primary tumor or among its metastases.[1,2] Tumor heterogeneity plays a crucial role in cancer management as it directly impacts treatment outcomes and patient prognosis. As we move from traditional treatment methods (e.g., chemotherapy and radiotherapy) to more personalized (precise) medicine – incorporating targeted drugs and individualized treatments based on each patient's unique genes, environment, and lifestyle – assessing tumor heterogeneity becomes increasingly important. In recent years, several anticancer drugs have been approved and specifically developed to target the unique morphological, molecular, and genetic characteristics of cancer cells. Accurate diagnosis and quantification of tumor heterogeneity is crucial to predict disease progression, as heterogeneity can be highly variable even within a single individual.[3] Diagnosing tumor heterogeneity is quite challenging, and the role of pathology, radiological imaging, radiomics, and artificial intelligence (AI) has been described in various literature.[4] Radiological images, including ultrasound, computed tomography (CT), and magnetic resonance imaging (MRI), can identify heterogeneity to a certain extent by texture analysis and the shape and volume of lesions.[5] However, radiological imaging requires special software and expertise and cannot provide comprehensive information on total body lesions in a single scan, as positron emission tomography/CT (PET/CT) can. This review delves into various aspects of PET/CT in describing heterogeneity and its impact on clinical management. Radiomics and AI techniques are further enhancing our understanding of tumor complexity. This short review also describes the role of different PET radiopharmaceuticals (tracers) in imaging various characteristics of tumor tissue that contribute to heterogeneity in various cancers.

2. Tumor heterogeneity: Concepts and mechanisms

Cancer and its metastases arise from a process of uncontrolled and unchecked cell proliferation, which invades healthy tissues and spreads throughout the body. Tumor clonality represents a key characteristic of malignancy and is defined as the expansion of transformed cells derived from a founding cell that initially acquired deregulated growth capability. In contrast, cancer development is a multi-step process in which cells undergo several genetic or environmental alterations, transforming into cell types different from their original progenitor cells and contributing to heterogeneity.[1]

Solid cancer lesions consist of tumor cells and the tumor microenvironment (TME). The TME is made of cells and extracellular components (blood and lymphatic vessels, cytokines, mediators, etc.). The cellular components included in this complex are tumor cells, immune cells, and stromal cells (fibroblasts, mesenchymal stem cells, adipocytes, endothelial cells, and pericytes). Within the TME, stromal components secrete growth factors and angiogenic factors (e.g., transforming growth factor β1, vascular endothelial growth factor, interleukin 6, and tumor necrosis alpha [TNF-α]). This dynamic environment provides nutritional and mechanical support that enhances cancer metabolism, promoting tumor growth through local invasion and resistance to cell death signals. The characteristics of the TME vary greatly between tumor types – it can be fibrotic, rich in blood vessels, or even necrotic. Tumor cells also exhibit various phenotypic characteristics, such as cell surface receptors, rate of antigenicity, metabolic activity, hormone receptor status, and indicators of tumor aggressiveness or metastatic potential. These characteristics provide crucial insights into the behavior and biology of tumors, aiding in diagnosis, prognosis, and the development of targeted therapies. In addition, various factors, such as genetic mutations, cellular heterogeneity, and microenvironment interactions, also play significant roles in determining tumor behavior and treatment response. As tumors transition from primary to invasive disease, the tumor and its microenvironment evolve, resulting in the spatial and temporal emergence of tumor heterogeneity.[2,3]

Spatial heterogeneity refers to the variation in tumor characteristics, such as cell morphology and genetic makeup, within the primary tumor or between its metastases at a single time point. Conversely, temporal heterogeneity describes changes in these tumor characteristics that develop over time as the disease progresses. Both forms of heterogeneity play a critical role in understanding tumor behavior, treatment resistance, and disease evolution.[4] Detection and quantification of spatial and temporal tumor heterogeneity can provide critical insights for cancer treatment. Jonsson *et al.*[5] studied spatial heterogeneity on PET/CT scans in three types of cancers using an image registration-based framework. Their findings demonstrated that spatial tumor heterogeneity can be effectively detected and quantified based on lesion frequency, volume, and metabolic activity. This approach highlights the potential of advanced imaging techniques to better understand tumor behavior and guide personalized treatment strategies.[5] Hughes *et al.*,[6] in their study on lung cancer using PET/CT scans, demonstrated that quantification of spatial fluorodeoxyglucose (FDG) uptake heterogeneity provides prognostic value beyond standardized uptake value (SUV) and the clinical stage of cancer. Various studies have demonstrated that tumors and their metastases consist of different clones of cells, each with distinct genetic, epigenetic, proteomic, and transcriptomic profiles, yet descending from a common ancestor. These diverse clones may exhibit varying responses to treatment, with some clones resisting therapy and continuing to proliferate, ultimately leading to treatment failure. This dynamic process contributes to the development of visible heterogeneity over time, which is referred to as temporal heterogeneity.[7] In a study on neuroblastoma, the authors noted that PET/CT-based diagnosis of intratumor heterogeneity in high-risk patients served as a strong prognostic indicator. This highlights the importance of serial advanced imaging techniques in understanding temporal tumor evolution and predicting clinical outcomes.[8]

Heterogeneity can manifest between different cells within a single tumor (intra-tumor) or across different patients harboring the same tumor type and can even be observed when comparing primary tumors to their metastases (inter-lesion). The diverse nature of tumor heterogeneity presents a significant challenge in cancer management, highlighting the need for more sophisticated diagnostic and therapeutic approaches.[9]

3. Challenges in diagnosing tumor heterogeneity

Diagnosing and precisely characterizing tumor heterogeneity can be highly challenging. Cancers and their molecular subtypes are typically identified using small biopsy samples taken from the primary site or a metastatic site. However, these biopsy samples are often limited in size and may not fully represent the entire tumor's heterogeneity. In addition, performing biopsies on all metastatic sites involved in cancer is impractical. In a study by one of the authors on medulloblastoma, high-grade glioma, and renal cell carcinoma, it was demonstrated that, in terms of spatial heterogeneity, at least five biopsies are required to detect 80% of somatic variants.[10]

Similarly, other authors, like Savas *et al.*,[11] have demonstrated the presence of spatial heterogeneity between primary tumors and their metastases in biopsy samples from breast cancer patients.

As biopsy samples are small and may not fully capture tumor type and heterogeneity, this approach may result in inadequate treatment. This can lead to the administration of one or more therapies that are not beneficial for a given patient's cancer, with potential harm/morbidity through lack of an effective drug regime. Heterogeneity also appears to be the primary cause of drug resistance. While patients may initially react to a given therapy, new and resistant cancer cell clones regularly emerge within the tumor, leading to disease progression or relapse. This innate variability within tumors makes developing a one-size-fits-all treatment approach exceedingly difficult.[12]

Medical imaging techniques possess the ability to capture tumor characteristics at the cellular and molecular levels. Advanced radiological imaging modalities (e.g., CT and MRI) have demonstrated some capability in visualizing tumor heterogeneity; however, these techniques require the integration of advanced software radionics and AI.[13] The transformative development of PET/CT imaging has opened new avenues for investigating cancer characteristics and biology at the cellular and molecular levels. To date, ^{18}F-FDG has been the most widely used radiotracer for staging, restaging, and monitoring therapy response in different tumors. ^{18}F-FDG has also been used for prognostic assessments. Its role in diagnosing tumor heterogeneity appears promising. In addition, the broad range of radiopharmaceuticals (tracers) utilized for PET/CT, coupled with whole-body imaging, has made PET a potential option for non-invasively revealing tumor heterogeneity.

4. Tumor heterogeneity highlighted by various PET radiopharmaceuticals

In recent years, advances in PET/CT technology have transformed the field of oncology. With a deeper understanding of the intricate TME, scientists have developed an array of innovative PET tracers focusing on improving cancer staging, restaging, and management. PET radiopharmaceuticals target a variety of mediators that localize in tumor cells and the cancer microenvironment through various mechanisms, providing different information on cell biology and growth. The application of these specialized PET tracers has allowed physicians and researchers to gain a more nuanced view of tumor heterogeneity.

There are two potential methods for assessing tumor heterogeneity using PET scans: (i) assessing heterogeneity in tracer distribution and quantifying metabolic parameters in ^{18}F-FDG PET scans, and (ii) by utilizing multiple radiopharmaceuticals that target different characteristics of tumor cells and microenvironment.

5. ^{18}F-FDG PET/CT: The workhorse of oncological imaging

^{18}F-FDG PET/CT remains the most widely used radiopharmaceutical for staging and response assessment of various malignancies. Increased glucose metabolism and uptake are observed in various cancer cells due to the upregulation of GLUT transporters and hexokinase expression. ^{18}F-FDG enters the cells through glucose transporters and is phosphorylated by hexokinase to produce ^{18}F-FDG-6-phosphate, which remains trapped in the cell and can be detected by PET scan. FDG uptake in tumor cells depends on tumor histopathology, differentiation, aggressiveness, proliferative activity, and other biological processes.[14] ^{18}F-FDG PET scans can quantify voxel-based glucose metabolism within tumors; FDG uptake and distribution in a tumor are associated with the expression of glucose transporters and hexokinase within a given lesion, as well as between different sites of that single tumor.

^{18}F-FDG PET/CT scans can quantify variations in tracer uptake by assessing metabolic parameters, such as SUV (SUV_{max}; SUV_{mean}), metabolic tumor volume (MTV), and total lesion glycolysis (TLG). These metrics can be combined with other advanced texture features (e.g., entropy and uniformity) to capture tumor variability and heterogeneity.[14]

The potential of ^{18}F-FDG PET/CT scans in evaluating the heterogeneity at the tumor level has been explored by several authors.[15] It has been described that tumor heterogeneity may lead to heterogeneous or sparse ^{18}F-FDG distribution. High SUV regions on ^{18}F-FDG PET scans are indicative of aggressive clones. Cancers of lung, head and neck, and oligodendroglioma have revealed a clear relationship between the variability in FDG distribution with pathological variability. Increased heterogeneity of FDG uptake is associated with reduced survival, highlighting the prognostic importance of PET imaging.[16-18] Similarly, in sarcoma and cervical cancers, ^{18}F-FDG PET uptake and its heterogeneous distribution are also known to correlate with prognosis and patient outcomes. Variations in FDG uptake within these tumors can provide valuable insights into aggressiveness and potential behavior with higher variation in SUV uptake, indicating more aggressive tumor biology and poorer prognosis. Therefore, the future focus of ^{18}F-FDG PET scanning is to utilize this information on tumor heterogeneity to enhance precise treatment planning and diagnosis.[19-21]

Furthermore, this heterogeneity information is instrumental in radiotherapy planning. By identifying regions within the tumor that exhibit higher metabolic activity, clinicians can tailor radiotherapy treatments to target these areas more effectively, potentially improving treatment efficacy and minimizing damage to surrounding healthy tissue. This tailored approach aims to enhance treatment effectiveness and reduce harm to neighboring healthy tissue, ultimately contributing to better patient outcomes.[22,23]

6. Beyond ^{18}F-FDG: Commonly used paired specialized PET tracers in different cancers

In addition to ^{18}F-FDG, various PET tracers have been developed over time to target different tumor components. The distribution and uptake of these tracers provide a comprehensive, non-invasive map of both inter- and intratumoral heterogeneity. For example, endocrine-related cancers, such as thyroid and neuroendocrine tumors (NETs), exhibit a wide range of clinical behaviors. Well-differentiated tumors tend to be indolent and retain their endocrine function, while poorly differentiated tumors are more aggressive. ^{18}F-FDG PET is particularly effective in identifying this aggressive phenotype. Similarly, different molecular subtypes of breast cancer can be targeted with specific tracers, offering a complete picture of the tumor and its heterogeneity. Prostate cancers tend to be differentiated or poorly differentiated, with diagnosis performed using ^{68}Ga-PSMA and ^{18}F-FDG PET scans. In addition, some may even exhibit neuroendocrine differentiation, which can be identified with ^{68}Ga-DOTA peptide PET scans.[24] This approach captures complementary biological features of the tumor and its microenvironment, enabling a more comprehensive assessment of heterogeneity. Combining these methods can improve the characterization of tumor behavior, predict treatment resistance, and guide personalized therapy by mapping both metabolic and molecular heterogeneity.

Various PET radiopharmaceuticals used clinically and in research are shown in Table 1.[24,25] Herein, we describe some of these tracers, their known combinations, and their potential applications in various tumors.

6.1. ^{68}Ga-DOTA peptides PET/CT for NET

Tumor heterogeneity is seen commonly in NET. NET overexpresses somatostatin receptors (SSTRs); PET/CT with ^{68}Ga-DOTA peptide (DOTATATE/DOTANOC/DOTATOC) reflects somatostatin receptor expression in the tumor and identifies cell differentiation and grade of the tumor. High ^{68}Ga-labeled peptide binding is correlated with well-differentiated, low-grade lesions, while reduced binding implies poorly differentiated tumors or higher-grade tumors. ^{18}F-FDG PET is sometimes coupled with ^{68}Ga-labeled peptide scans, as FDG accumulation is related to the metabolic activity of the tumor, displaying higher sensitivity for poorly differentiated, aggressive tumors with poor outcomes.[26] The phenomenon observed between the two tracers reveals substantial metabolic and receptor heterogeneity. These methodologies enable doctors to evaluate inter-lesion variability, with differences in uptake between primary and metastatic locations, directly influencing therapy eligibility, such as patient selection for somatostatin receptor therapy (SSRT).[27] Peptide receptor radionuclide therapy (PRRT) is radionuclide therapy for NET, which is positive in ^{68}Ga- DOTA peptide PET/CT scans and displays minimal or no uptake in ^{18}F-FDG PET/CT scans. Therefore, combining DOTA peptide PET/CT scans with other tracers, most commonly FDG PET scans, can diagnose heterogeneous clones of tumors

Table 1. Mechanism of action and indications of various positron emission tomography (PET) radiopharmaceuticals[24,25]

PET radiopharmaceutical	Mechanism of localization	Oncological indication
^{18}F-fluorodeoxyglucose (FDG)	Enters the cell through GLUT 1 and 3 transporter, phosphorylated and trapped inside the cell	Staging, restaging, and response assessment of a wide range of tumors, including breast, lung, GI tumors, melanoma, etc.
^{68}Ga-DOTA -peptides	Binds to somatostatin receptors on tumor cells	Staging and restaging of neuroendocrine tumors
^{18}F-fluoro-L DOPA (^{18}F-DOPA)	Transported into the cell by large neutral amino acid transporters L-type (LAT) and stored in secretory vesicles	Diagnosis, staging, and follow-up of neural crest tumors, for example, neuroblastoma, paraganglioma, brain tumors, and congenital hyperinsulinemia
^{18}F-metafluorobenzylguanidine (mFBG)	Norepinephrine analog transported by norepinephrine transporters overexpressed on tumor cells	Detection and staging of neural crest tumors
^{68}Ga/^{18}F/^{64}Cu-prostate-specific membrane antigen (PSMA)	Binds to PSMA (type II transmembrane protein) on prostate cancer cells	Staging and detection of recurrence in prostate cancer
^{68}Ga-fibroblast activation protein inhibitor (FAPI)	Binds to FAP in the stroma of tumor microenvironment	Diagnosis and staging of various tumors, for example, pancreas, cholangiocarcinoma, breast, etc.
^{18}F-fluoroestradiol (FES)	Binds to estrogen receptors in the nucleus of ER-expressing cells	Diagnosis and follow-up of hormone-positive breast cancer
Various ^{89}Zirconium labeled tracers		
^{89}Zr-trastuzumab	Labeled antibodies (immune-PET); monoclonal antibody that binds to HER2; targets EGFR; binds to VEGFA; antibodies act against PD-L1; targets CD38 antigen expressed on myeloma cells	Diagnosis and staging of HER2-positive breast cancers
^{89}Zr-cituximab		Diagnosis of cancers with overexpression of EGFR
^{89}Zr-bevacizumab		Diagnosis of cancers with overexpression of VEGF
^{89}Zr-atezolizumab		Detection of PD-L1-positive tumors
^{89}Zr-DFO-daratumumab		Diagnosis of multiple myeloma
^{68}Ga-RGD/trivehexin	Binds with integrins expressed on tumor cells or angiogenic blood vessels	Diagnosis of cancers, for example, pancreas, head and neck, etc.
^{18}F-fluoroethyl-l-tyrosine (^{18}F-FET); ^{11}C-methyl-l-methionine (^{11}C-MET)	Amino acid analogs transported in cells by overexpressed transmembrane LAT on tumor cells	Diagnosis and grading of brain tumors
^{18}F-fluciclovine	Amino acid analog enters the cell by neutral amino acid transporter	Diagnosis of biochemically recurrent prostate cancer and other tumors
^{11}C-acetate/palmitate	Converted to acetyl CoA in cells for cholesterol and fatty acid synthesis, which are integrated into the cell membrane or oxidized in mitochondria	Diagnosis of prostate, renal, brain, and HCC cancers
^{18}F/^{11}C-choline	Phosphorylated to phosphorylcholine within cells and integrated into phospholipids in the cell membrane	Diagnosis of the brain, prostate, lung, bladder cancers, etc.
^{18}F-FLT (thymidine)	Enters cell by facilitated diffusion through nucleoside transporters and is trapped in the cell	Diagnosis and response assessment of cancers, for example, lung, breast, colon, lymphoma
^{18} F-misonidazole	Nitroimidazole compound that enters the cell through blood flow and gets trapped in hypoxic cells	Detects hypoxia in tumors, for example, lung, head and neck, and brain tumors

(Cont'd...)

Table 1. ***(Continued)***

PET radiopharmaceutical	Mechanism of localization	Oncological indication
^{18} F-ICMT-11	Binds in caspase 3-specific cells undergoing apoptosis	Identification of treatment-induced apoptosis and response to treatment in malignant tumors
^{124}I -annexin V	Binds to phosphatidyl serine on the surface of apoptotic cells	
^{18}F-sodium fluoride (NaF)	Deposits in bone through chemisorption, converting hydroxyapatite to fluorapatite	Detection of bony metastases
^{68}Ga-pentaxifor	Targets cells exhibiting CXCR 4 expression	Diagnosis of multiple myeloma and other tumors
^{68}Ga-DOTA exendin-4	Amino acid peptides, like GLP 1, bind to GLP receptors on pancreatic beta cells	Diagnosis of insulinoma
^{18}F-fludarabine	Purine analog that inhibits DNA synthesis	Diagnosis of hematological malignancies
^{68}Ga-glypican 3	Oncofetal acetyl heparan sulfate glycoprotein expressed on HCC	Diagnosis of HCC

Abbreviations: CXCR4: Chemokine receptor type 4; DNA; Deoxyribonucleic acid; DOPA: 1,4,7,10-Tetraazacyclododecane-tetraacetic acid; DOTA: 1,4,7,10-Tetraazacyclododecane-tetraacetic acid; 18 F-ICMT -11: (18F-(S)-1-((1-(2-fluoroethyl)-1H-[1,2,3]-triazol-4-yl) methyl)-5-(2 (2,4-difluorophenoxymethyl)-pyrrolidine-1-sulfonyl) isatin); ER: Estrogen receptors; EGFR: Epidermal growth factor receptor; FAP: Fibroblast activation protein; GLP-1: Glucagon-like peptide 1; GLUT: Facilitated diffusion Glucose Transporters; HCC: Hepatocellular carcinoma; HER2: Human epidermal growth factor receptor 2; PD-L1: Programmed cell death ligand-1; PSMA: Prostate specific membrane antigen; RGD: Peptide Arg-Gly-Asp; VEGFA; Vascular endothelial growth factor A.

and guide treatment strategies.[26] Kaewput *et al.*[28] have demonstrated that ^{68}Ga-DOTA peptide and ^{18}F-FDG PET scans serve complementary roles in patients with gastroenteropancreatic (GEP) NET, simultaneously enhancing diagnostic accuracy due to the heterogeneity of lesions. Similarly, many authors, including Zhou *et al.*,[29] have revealed that dual tracer PET with ^{68}Ga-DOTA peptide and ^{18}F-FDG PET should be performed in all patients with an initial diagnosis of NET due to the heterogeneous nature of these tumors. Nogareda Seoane *et al.*[30] demonstrated that ^{68}Ga-DOTA peptide and ^{18}F-FDG PET scans collectively reveal the molecular heterogeneity of metastatic lesions in G2 and G3 NET, facilitating the appropriate selection of patients for radionuclide therapy (PRRT). Dual tracer PET imaging with ^{18}F-FDG and ^{68}Ga-DOTA peptide demonstrating tumor heterogeneity is displayed in Figure 1.

6.2. PET/CT in neural crest tumors

PET/CT with various radiopharmaceuticals is remarkably effective for imaging a group of tumors arising from the neural crest, including medullary thyroid cancers, neuroblastoma, paraganglioma, pheochromocytoma, and ganglioneuroma. These tumors express different amines and peptides that can be targeted by various PET tracers, such as ^{18}F-dihydroxyphenylalanine (^{18}F-DOPA), ^{68}Ga-DOTA peptides, ^{18}F-FDG, and other tracers (norepinephrine analog ^{18}F- metafluorobenzylguanidine [MFBG], resembling single photon emission computed tomography [SPECT] tracer ^{123}Iodine-Meta-Iodobenzylguanidine [1231-MIBG]). These tracers exhibit variable uptake capacities in tumors, aiding in diagnosis and therapeutic management. These tumors accumulate amino acids and amine precursors. ^{18}F-DOPA is a radiolabeled amino acid that enters the tumor cell through the L-amino acid transporter (LAT1 and LAT2). In the cells, ^{18}F-DOPA is decarboxylated to dopamine and transported and stored inside secretory vesicles. Cancer cells have increased synthesis and storage of amines, like dopamine; therefore, PET imaging with DOPA enables the diagnosis of these tumor cells. This renders PET imaging with ^{18}F-DOPA remarkably helpful for diagnosing neuroblastoma and other neural crest tumors, as well as congenital hyperinsulinemia. Neural crest tumors frequently overexpress norepinephrine transporters, that is, proteins that facilitate the uptake of norepinephrine, epinephrine, and dopamine across cell membranes. ^{18}F-MFBG is a norepinephrine analog that can be targeted to diagnose neural crest tumors. These PET tracers have varied uptake capacities in tumor sites depending on their biological characteristics, demonstrating heterogeneity that helps refine oncology diagnosis and treatment strategies.[13,31]In a study, involving the evaluation of recurrent and metastatic paraganglioma with different PET tracers, authors found that ^{68}Ga-DOTA-1-Nal3-octreotide (DOTANOC) PET/CT displayed more bone lesions, while ^{18}F-3,4- dihydroxy-6-[^{18}F]fluoro (FDOPA) PET was superior in detecting liver lesions, demonstrating the heterogeneous nature of tumor lesions being detected variably by different PET tracers.[32] Similarly, in a study on

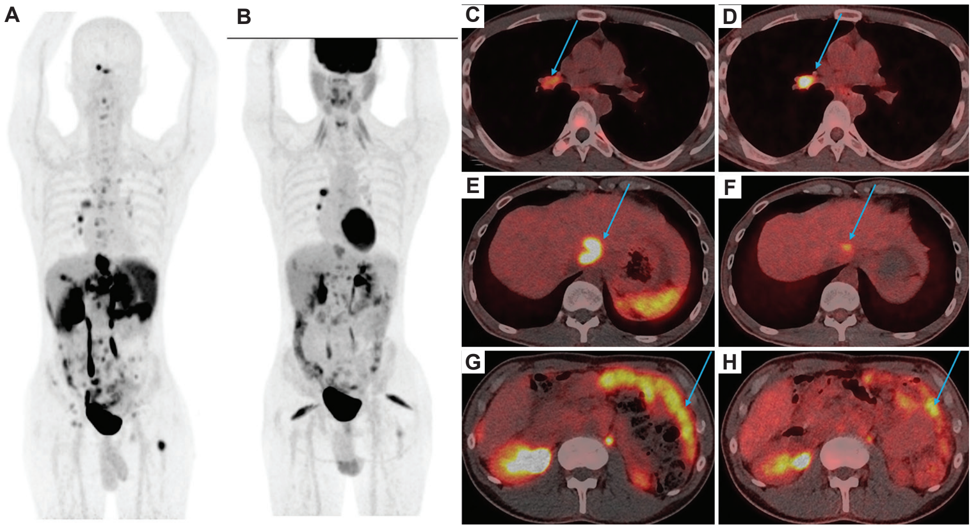

Figure 1. Positron emission tomography/computed tomography (PET/CT) imaging of a 33-year-old male with metastatic pancreatic cancer demonstrates heterogeneous lesions on the PET/CT scan. (A and B) maximum intensity projection (MIP) images of ^{68}Ga-DOTATOC-PET (A) and ^{18}F-FDG-PET (B) display multiple lung, liver, bone, lymph node, and peritoneal metastases. (C and D) Fused PET/CT of ^{68}Ga-DOTATOC (C) and ^{18}F-FDG PET (D) display higher uptake of ^{18}F-FDG in the right hilar node. (E–H) Fused ^{68}Ga-DOTATOC images of the abdomen (E and G) display higher uptake in liver and peritoneal metastases compared to the ^{18}F-FDG images (F and H). Blue arrows indicate metastatic lesions in the right hilar node, liver and peritoneum.

Abbreviations: DOTATOC: Gallium-68 (DOTA0-Phe1-Tyr3) octreotide; FDG: ^{18}F-fluorodeoxyglucose.

paraganglioma and pheochromocytoma, 68Ga-DOTA-DPhe1, Tyr3-octreotate (DOTATATE) is recommended for initial imaging, and depending on the findings, FDG and MIBG may be added in select cases for complete staging and guide treatment decisions.[33]

6.3. ^{68}Ga-PSMA PET/CT for prostate cancer

Prostate-specific membrane antigen (PSMA) is a type II transmembrane protein that is overexpressed on the surface of prostate cancer cells. ^{68}Ga-PSMA PET/CT is outstanding in its ability to bind prostate cancer cells and their metastases, making it highly effective for staging and biochemical recurrence in patients with prostate cancer, with high diagnostic accuracy. Despite PSMA PET being highly sensitive to well-differentiated tumor cells and having a significant diagnostic impact, some lesions may not be observed due to poor differentiation. Wang *et al.*[34] have demonstrated that the addition of FDG PET to PSMA PET scans increased lesion detection rates in high-risk prostate cancer compared to reliance on a single agent alone. In their study, a total of 114 lesions were diagnosed in 37 patients. Out of a total 114 lesions, 81 lesions were PSMA+FDG+/-, while 33 were PSMA-FDG+. Similarly, neuroendocrine differentiation of prostate cancer could be detected using ^{18}F- or ^{68}Ga-labeled DOTA peptides, therefore demonstrating tumor heterogeneity.[35]

Dual tracer PET/CT with ^{18}F-FDG and ^{68}Ga-PSMA also determines the eligibility and outcome of ^{177}lutetium (Lu)-PSMA therapy in metastatic castration-resistant prostate cancers. This radionuclide therapy leads to increased progression-free survival and overall survival.[36] Pabst *et al.*,[36] in their study on castration-resistant prostate carcinoma, identified significant tumor heterogeneity using PET/CT with three tracers, including ^{18}F-FDG, ^{68}Ga-fibroblast activation protein inhibitor (FAPI), and ^{68}Ga/^{18}F-PSMA. Patients selected for ^{177}Lu-PSMA with a PSMA-dominant phenotype experienced improved overall survival.[36]

6.4. Other novel radiopharmaceuticals

6.4.1. ^{68}Ga-FAPI PET/CT for imaging fibroblasts in the stroma of the TME

Fibroblast activation protein (FAP) is a cell surface type II serine protease overexpressed in the stromal tissues of certain tumors to which ^{68}Ga-FAPI can bind. ^{68}Ga-FAPI is a tracer capable of imaging highly fibrosis-rich tumors, such as pancreatic, cholangiocarcinoma, and breast cancers. FAPI PET scans have displayed higher sensitivity for certain low-grade or well-differentiated tumors, which have low uptake in ^{18}F-FDG PET scans.[37] Liu *et al.*,[38] in their review on diagnosing primary and metastatic lesions in various abdominal and pelvic malignancies, indicated that ^{18}F-FDG together with ^{68}Ga-FAPI have higher overall diagnostic performance, denoting the utility of two different tracers in detecting various malignant lesions. Similarly, Yue *et al.*,[39] in their study on recurrent colorectal cancers, demonstrated that ^{68}Ga-FAPI PET/CT had higher sensitivity in detecting lymph node and peritoneal metastases, while ^{18}F-FDG PET/CT had higher sensitivity in detecting bone metastases; therefore, they proposed a combination of two tracers for PET/CT imaging for better patient management. Patients with tumor lesions positive on ^{68}Ga-FAPI PET/CT scans can be considered for ^{177}Lu-FAPI therapy; however, clear indications and benefits are still under research.[37]

6.4.2. ^{18}F- FES PET/CT for breast cancer

^{18}F-FDG PET/CT scans are routinely conducted for staging and restaging of all types of breast cancer, including its various molecular subtypes. A large number of patients are hormone-positive, that is, estrogen receptor (ER)-positive and progesterone receptor (PR)-positive. Hormone-positive patients can be treated with targeted therapies. The diagnosis of hormone receptor status is performed using immunohistochemical straining of biopsy samples, but this approach has certain challenges and does not fully reflect hormone status and heterogeneity of the entire tumor burden. PET radiopharmaceutical ^{18}F-fluoroestradiol (FES) provides a noninvasive alternative by measuring ER expression in tumors. FES is a lipophilic molecule that is similar to estradiol and binds to ERs in the nucleus of ER-expressing cells. ^{18}F-FES PET scans can detect more lesions with mild or no uptake on FDG PET scans in receptor-positive breast cancer. Studies have demonstrated the superiority of FES PET over other modalities, such as bone scans or ^{18}F-FDG PET scans, in the staging and restaging of hormone-positive breast cancer.[40,41] Matushita *et al.*[40] demonstrated that FES PET has a pooled sensitivity of 82% and a pooled specificity of 94%, highlighting good diagnostic accuracy, with a pooled area under the curve (AUC) of 0.8899 for ER-positive lesions in breast cancer patients. Another study by Liu *et al.*[41] studied a total of 238 lesions in newly diagnosed ER-positive breast cancer. They reported a higher number of lesions detected with FES compared to FDG, with a higher sensitivity of 90.8% for ^{18}F-FES compared to 82.8% for ^{18}F-FDG PET.[41] Recent advancements in PET imaging have also enabled the use of ^{89}Zr-labeled trastuzumab, a monoclonal antibody that binds to human epidermal growth factor receptor 2 (HER2), to visualize HER2-positive breast cancer sites *in vivo*. These developments underscore the growing role of PET radiopharmaceuticals in personalizing breast cancer treatment.[42,43]

Tumor cells and their metastases may contain subclones of cells with variations in molecular subtypes; therefore, single tracers targeting a particular hormone subtype may be inadequate to identify all the tumor lesions. Combining ^{18}F-FES with ^{18}F-FDG and other PET tracers allows clinicians to better differentiate between tumors with varying receptor expressions, providing a clearer picture of tumor heterogeneity and enabling more effective patient management strategies. Several studies have suggested that combining two PET tracers (including metabolic tracer and HER2-targeting agent) provides a clear benefit in evaluating heterogeneity in breast cancer patients and planning treatment strategies.[44,45]

6.5. Various evolving tracers

6.5.1. ^{68}Ga-RGD PET/CT

Tumor cells and angiogenic blood vessels express integrins on their surface. These integrins, along with vascular endothelial growth factor receptors (VEGFRs), regulate the process of angiogenesis. As the peptide Arg-Gly-Asp (RGD) binds with $\alpha v\beta 3$ integrins, RGD labeled with ^{68}Ga or ^{18}F has been used for the diagnosis and staging of a wide range of cancers, including breast cancer, glioma, lung cancer, head-and-neck cancer, melanoma, renal cell cancer, etc. The sensitivity of ^{18}F-galacto-RGD or ^{18}F-fluciclatide was found to be 88–94% for all lesions, with a lower sensitivity of 71–88% for metastatic lymph nodes and distant metastases.[46] In addition, other integrins (e.g., $\alpha v\beta 6$), which are expressed in epithelial cells, have been targeted using ^{68}Ga-trivehexin PET. This imaging modality is particularly useful for diagnosing pancreatic cancer and head-and-neck squamous cell carcinoma.[47]

6.5.2. Other evolving tracers

Other PET tracers, such as ^{18}F-fluorothymidine (FLT), target cell proliferation, ^{11}C-methionine, and ^{18}F-fluoroethyltyrosine (FET), are amino acid analogs that exhibit uptake in enhanced protein synthesis. Tumor hypoxia can be imaged using ^{18}F-fluoromesonidazole (FMISO) and PET with ^{11}C-acetate as the marker for cell membrane lipid synthesis. These tracers have limited global availability and are used in only a few centers, primarily for research purposes. New tracers, such as ^{68}Ga-pentixafor for multiple myeloma and labeled antibodies, have demonstrated promising results and are currently undergoing various research and clinical trials. Chemokine receptor CXCR4 is overexpressed in certain tumors, especially lymphoproliferative diseases (e.g., lymphoma and multiple myeloma), and various agents, including ^{68}Ga-pentixafor, are used to target them.[48] Exendin-4 is similar to glucagon-like peptide-1 (GLP-1), which binds to pancreatic β-cells, and ^{68}Ga-DOTA-exendin-4 PET is utilized for imaging insulinoma.[49] Glypican 3 (GPC3) is a glycoprotein labeled with ^{68}Ga, displaying a high uptake in hepatocellular carcinoma on PET scans, with very low expression in normal tissue and hepatitis.[50] These tracers have proven to be beneficial in various tumors as described above; however, they are still under investigation, and their role in tumor heterogeneity remains undefined.

7. Clinical applications of PET/CT in tumor heterogeneity

7.1. Diagnosis and initial staging and treatment planning

Diagnosing and staging cancer can be complex and challenging due to the considerable biological, cellular, and tissue variation within tumors. This diversity occurs not only between cancer cells in an individual patient but also between tumors in different patients. Such heterogeneity complicates choosing appropriate treatment plans, as certain therapies may not be effective against different clones of cancer cells. The use of multiple PET radiotracers offers a solution by enabling visualization of the various parts of tumor cells and their microenvironments. In addition, PET scans provide full-body, non-invasive imaging in a solitary session, which is highly beneficial for detecting tumor heterogeneity. ^{18}F-FDG PET scans can diagnose heterogeneity by analyzing non-homogenous tracer distribution in the tumor sites with areas of high and low uptake. Similarly, applying multiple PET tracers can help identify tumor diversity, as different lesions may absorb various tracers differently, depending on the underlying biology of the tumor cells.

Various quantitative parameters (e.g., SUV, TLG, and MTV) further assist in diagnosing heterogeneity and assessing disease prognosis. Tracer uptake patterns may reveal the presence of different cancer cell clones, each with varying levels of aggressiveness, which can influence the overall prognosis of the patient. In addition, due to significant heterogeneity, the same treatment regime may not be equally effective on different clones of cancer cells and can lead to treatment failure or resistance. It has been reported that low-grade tumors exhibit lower SUV values on ^{18}F-FDG PET scans, while higher-grade tumors have high SUV values.[51] In addition, some lesions with low FDG uptake may exhibit high uptake when imaged with different tracers. Research conducted by Marusyk *et al.*[9] and Zhou *et al.*[52] has demonstrated that the integration of several tracers, including ^{18}F-FDG and ^{68}Ga-FAPI, enhances the visualization of tumor heterogeneity, uncovering metabolic and stromal variations that influence diagnostic and staging precision.[9,13,51,52] Therefore, combining multiple tracers in PET scans provides a more comprehensive view of all lesions and enhances the detection of tumor heterogeneity.

7.2. Monitoring treatment response

Heterogeneity in cancer leads to significant challenges in treatment response and its assessment and influences outcomes. Heterogeneity can be spatial (as described above) or temporal, which develops over time. Since the development of heterogeneity is a dynamic process and may develop temporally, serial PET/CT scans during the treatment process may provide diagnostic insights. As the disease progresses, the treatment-resistant clones of cancer cells continue growing, leading to disease progression; consequently necessitating a change in therapy regime. For example, breast cancer patients display significant intratumoral and interpatient heterogeneity due to the presence of various molecular subtypes. The tumor cells and their metastases express dynamic changes in their molecular subtypes over time, which affects treatment response to neoadjuvant therapy. These variations can be identified on PET/CT scans, thereby providing critical insights into patient management.[53]

Spatiotemporal heterogeneity is often seen in gastrointestinal tumors, as cells change their characteristics during metastases to different anatomical sites over time. The RECIST and PERCIST guidelines designed to assess response on radiological and PET imaging are not suitable for assessing response with targeted drugs, as the response is lesion- or organ-specific. Zhou *et al.*,[52] in their study on colorectal tumors, reported a better response in hepatic metastases compared to lungs and lymph nodes when treated with targeted therapies. In another study by Schmid *et al.*[53] on lung cancer patients treated with immunotherapy, an organ-specific response was observed, with better response in lymph nodes compared to liver, bone, and adrenal glands. Heterogeneity is associated with prognosis, overall progression-free survival, and overall survival, thus it is related to drug efficacy. Therefore, better strategies for diagnosis and response assessment to address heterogeneity are needed for cancer management.

7.3. Tumor heterogeneity as a cause of mixed response in patients on systemic therapies

Tumor heterogeneity frequently leads to difficulties in treatment and poor outcomes. In numerous cases, follow-up PET/CT scans after systemic therapy reveal a mixed response, where both responding and progressing cells (i.e., resistant to treatment) coexist inside the patient. This combined response reflects the heterogeneous characteristics of different tumor lesions. This heterogeneity is either present from the beginning or develops temporally during treatment, where some cancer cells become resistant to treatment. During therapy, the treatment-sensitive subclones of heterogenous tumors respond, while the resistant subclones continue growing and form tumors, leading to the detection of a mixed response on PET/CT scans. In a study on lung cancer, Zhong *et al.*[54] highlighted the high incidence of mixed response in lung cancer treated with targeted therapies. They concluded that mixed response is a poor prognostic factor and occurs due to inter-/intratumor heterogeneity.[54] Other studies have also demonstrated heterogeneity as a reason for poor prognosis and treatment failure.[3,55,56] ^{18}F-FDG PET/CT is also becoming a reliable tool for evaluating the response of tumors to immunotherapy. Takao *et al.*[57] evaluated lesion characteristics in patients with mixed response to immunotherapy and found a significant difference between clonality and tumor-infiltrating lymphocytes between primary lesions and lymph node metastases. This heterogeneity leads to mixed response and progression in lymph nodes with an overall poor prognosis.[57,58] A mixed response demonstrating the dynamic nature of tumor heterogeneity is presented in Figure 2.

8. Advanced techniques and future directions

8.1. Radiomics and texture analysis

Radiomics has recently become an area of substantial focus in medicine due to its potential to extract vast amounts of quantitative data from medical images that are difficult to reveal or quantify with the naked human eye. Radiomics features, such as texture, shape, and intensity, are strongly correlated with tissue heterogeneity and cancer aggressiveness, making it a powerful tool for diagnosing and characterizing tumors. In the domain of nuclear medicine, radiomics has been extensively applied to PET and SPECT scans, providing crucial insights into a patient's prognosis, treatment response, and tumor biology.[14,59,60]

Radiomics analysis of PET/CT images focuses on several key parameters, including:

(i) SUV: Reflects the metabolic activity of tumors and is widely used to assess tumor aggressiveness.
(ii) Total lesion glycolysis (TLG): Combines metabolic activity and tumor volume, providing a more comprehensive measure of tumor burden.
(iii) Metabolically active tumor volume (MTV): Quantifies the volume of tumor tissue with active glucose metabolism, which is useful for assessing tumor heterogeneity and treatment response.[14,59]

Texture analysis is a critical component of radiomics, enabling the quantification of spatial variations in tracer uptake within tumors. By analyzing various features, such as shape, size, volume, compactness, and sphericity, radiomics can extract information at the cellular level. These features can reveal subtle patterns indicative of tumor aggressiveness, treatment resistance, or response to therapy. For example, heterogeneous texture patterns on PET/CT scans have been associated with poorer prognosis and higher tumor aggressiveness in various cancers, including lung, breast, and head and neck cancers.[59]

8.2. Radiomics workflow

The radiomics workflow begins with the computerized extraction of features from the region of interest

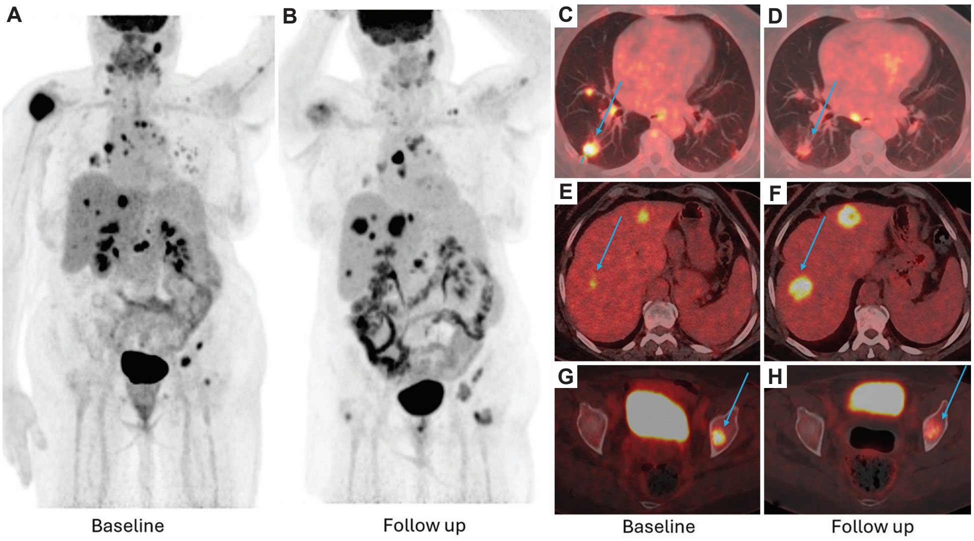

Figure 2. Positron emission tomography/computed tomography (PET/CT) imaging of a 60-year-old woman with lung cancer with multiple metastases. (A and B) Maximum Intensity Projection (MIP) images of ^{18}F-FDG-PET/CT at baseline (A) and ^{18}F-FDG-PET/CT at follow-up after three cycles of chemotherapy (B) display mixed responses in multiple metastases. (C–H) Fused PET/CT images at baseline (C, E, and G) and after chemotherapy (D, F, and H) display responses in lung and bone metastases and progression in liver metastases. Blue arrows indicate metastatic lesions in the lung, liver, and bone.
Abbreviation: FDG: ^{18}F-fluorodeoxyglucose.

(ROI) in medical images. Ensuring the robustness and reproducibility of these features is paramount, as variations in imaging protocols or segmentation methods can affect the results. After feature extraction, optimal features are selected, and AI-based models are incorporated to analyze the data. These models can predict clinical outcomes, such as treatment response or survival, based on the extracted radiomic features. For instance, AI-driven radiomics models have demonstrated promise in predicting responses to immunotherapy and chemotherapy in patients with non-small cell lung cancer (NSCLC) and breast cancer.[60]

8.3. Applications in tumor heterogeneity

Radiomics plays a significant role in characterizing tumor heterogeneity, which is a major challenge in cancer management. By analyzing spatial and temporal variations in tracer uptake, radiomics can identify subregions within tumors that exhibit different biological behaviors. This information is crucial for personalized treatment planning, as it allows clinicians to target aggressive tumor regions more effectively. For example, studies have demonstrated that radiomic features derived from ^{18}F-FDG PET/CT scans can predict intratumoral heterogeneity and guide radiotherapy planning by identifying regions with high metabolic activity.[14,59]

8.4. Future directions of radiomics

The integration of radiomics with AI and machine learning is expected to further enhance the diagnostic and predictive capabilities of PET/CT imaging. Advanced algorithms, such as convolutional neural networks (CNNs), can automatically segment tumors and classify them based on molecular subtypes with high accuracy. In addition, radiomics combined with multi-tracer PET imaging (e.g., ^{18}F-FDG and ^{68}Ga-PSMA) can provide a more comprehensive understanding of tumor heterogeneity, enabling more precise and personalized cancer management.[59]

9. AI and machine learning applications

The field of PET/CT imaging is rapidly evolving, with radiomics and AI emerging as powerful tools for enhancing tumor characterization and treatment planning. Incorporating radiomics with AI can develop models that will lead to detailed analysis of medical images. Radiomics offers a means to capture tumor heterogeneity beyond what is visually apparent by the high-throughput extraction of quantitative features from medical images. Texture analysis, a key component of radiomics, can quantify spatial variations in tracer uptake, potentially revealing subtle patterns indicative of tumor aggressiveness or treatment resistance.

Machine learning algorithms and AI, when applied to these radiomic features, can identify complex patterns and associations that may predict treatment outcomes or guide personalized therapy decisions. For example, CNNs have demonstrated the ability to automatically segment tumors and classify them based on molecular subtypes with high accuracy. In addition, AI-driven evaluation of PET/CT scans combined with clinical information can generate predictive analytics forecasting treatment outcomes and patient prognosis.

These advanced techniques are paving the way for more precise and personalized cancer management, potentially allowing for early identification of treatment resistance and enabling adaptive treatment strategies. However, it is important to note that while these methods are promising, they still require extensive validation in large, multi-center studies before widespread clinical implementation. The integration of AI and deep learning with conventional PET/CT analysis represents a major step toward unlocking the full diagnostic and predictive power of molecular imaging in oncology.[61-63]

10. Challenges and limitations of PET/CT

Future developments in PET/CT technology and the expanding knowledge of tumor heterogeneity will undoubtedly improve the diagnosis, restaging, and response prediction of new radiopharmaceuticals. However, the application of PET/CT with new radiopharmaceuticals in everyday clinical practice is also constrained by many challenges:

(i) Cost and accessibility: PET/CT scans are expensive, and the cost can be prohibitive for many patients, especially in low-resource settings. The high cost of radiopharmaceuticals, coupled with the need for specialized equipment and facilities, limits the widespread availability of this technology. Addressing disparities in access to advanced PET imaging technologies is crucial to ensure equitable healthcare delivery.[13,15]

(ii) Time and workflow: PET/CT scans require significant preparation, imaging, and interpretation time. The synthesis of radiopharmaceuticals, patient preparation, and the scanning process itself can be time-consuming, which may delay treatment decisions. In addition, the need for multiple scans to assess tumor heterogeneity further complicates the workflow.[13,17]

(iii) Radiation exposure: PET/CT scans involve exposure to ionizing radiation, which raises concerns, especially for patients requiring frequent follow-up scans. While the radiation dose is generally considered safe, cumulative exposure over time can increase the risk of secondary malignancies, particularly in younger patients.[13,15]

(iv) Availability of radiopharmaceuticals and trained personnel: The production and distribution of radiopharmaceuticals are complex and require specialized facilities. Many regions lack the infrastructure to produce these tracers, thereby limiting availability. In addition, the interpretation of PET/CT scans requires highly trained personnel, including nuclear medicine physicians and radiologists, which may not be available in all healthcare settings.[13,15]

(v) False positives and specificity: PET tracers can display false positivity in inflammatory and benign conditions, leading to potential misinterpretation and overdiagnosis. For example, ^{18}F-FDG, the most commonly used tracer, can accumulate in areas of infection or inflammation, mimicking malignant lesions. This lack of specificity can complicate treatment decisions and lead to unnecessary interventions.[13,17]

(vi) Ethical considerations and over-reliance on imaging: There is a growing concern about the over-reliance on imaging in cancer management, which may lead to overtreatment or unnecessary interventions. Ethical considerations, such as the balance between the benefits of early detection and the risks of overdiagnosis, need to be carefully weighed. In addition, the psychological impact of frequent imaging and the potential for false positives should be considered in patient management.[13,17]

(vii) PET/CT images have limited spatial resolution, and other factors, including scatter and attenuation artifacts, may lead to noisy images that adversely affect image analysis, even with AI. PET tracer uptake variability, due to various factors, including breathing artifacts, misregistrations, and truncation artifacts, may also be added to the challenges.[13]

11. Future directions

To overcome these limitations, ongoing research is focused on developing more cost-effective and widely available radiopharmaceuticals, reducing radiation exposure, and improving the specificity of PET tracers. Advances in AI and radiomics may also help streamline the interpretation process, reducing the reliance on highly specialized personnel. Furthermore, efforts to standardize protocols and improve access to PET/CT technology in underserved regions are essential to ensure equitable cancer care.[62]

12. Conclusion

Tumor heterogeneity is a complex and dynamic phenomenon that poses significant challenges for cancer diagnosis and treatment. PET/CT imaging, with its ability to provide metabolic and molecular insights, plays a crucial role in assessing tumor heterogeneity and guiding personalized treatment strategies. However, multiple PET/CT scans are coupled with multiple challenges which must be carefully considered. Despite these challenges, PET/CT remains a powerful tool in diagnosing heterogeneity and cancer management. Future developments in radiomics, AI, and novel tracers hold great promise for overcoming these challenges and improving patient outcomes.

Acknowledgments

None.

Funding

None.

Conflict of interest

The authors declare that they have no competing interests.

Author contributions

Conceptualization: Anjali Jain
Writing – original draft: Anjali Jain, Subhash Kheruka
Writing – review & editing: Sharjeel Usmani, Khulood Al Riyami, Asiya Al Busaidi, Sumit Bichpuria, Rashid Al Sukaiti

Ethics approval and consent to participate

Not applicable.

Consent for publication

Not applicable.

Availability of data

Not applicable.

References

1. Cooper GM. *The Cell: A Molecular Approach. The Development and Causes of Cancer*. 2nd ed. Sunderland, MA: Sinauer Associates; 2000. Available from: https://www.ncbi.nlm.nih.gov/books/NBK9963 [Last accessed on 2024 Dec 24].
2. Anderson NM, Simon MC. The tumor microenvironment. *Curr Biol*. 2020;30:921-925.

   doi: 10.1016/j.cub.2020.06.081
3. Zhang A, Miao K, Sun H, Deng CX. Tumor heterogeneity reshapes the tumor microenvironment to influence drug resistance. *Int J Biol Sci*. 2022;18:3019-3033.

   doi: 10.7150/ijbs.72534
4. Zhu L, Jiang M, Wang H, *et al*. A narrative review of tumor heterogeneity and challenges to tumor drug therapy. *Ann*

Transl Med. 2021;9:16.

doi: 10.21037/atm-21-1948

5. Jönsson H, Ahlström H, Kullberg, J. Spatial mapping of tumor heterogeneity in whole-body PET-CT: A feasibility study. *Biomed Eng Online*. 2023;22:110.

   doi: 10.1186/s12938-023-01173-0

6. Hughes NM, Mou T, O'Regan KN, *et al*. Tumor heterogeneity measurement using [18F] FDG PET/CT shows prognostic value in patients with non-small cell lung cancer. *Eur J Hybrid Imaging*. 2018;2:25.

   doi: 10.1186/s41824-018-0043-1

7. McQuerry JA, Chang JT, Bowtell DDL, Cohen A, Bild AH. Mechanisms and clinical implications of tumor heterogeneity and convergence on recurrent phenotypes. *J Mol Med (Berl)*. 2017;95:1167-1178.

   doi: 10.1007/s00109-017-1587-4

8. Li C, Wang S, Li C, Yin Y, *et al*. Improved risk stratification by PET-based intratumor heterogeneity in children with high-risk neuroblastoma. *Front Oncol*. 2022;12:896593.

   doi: 10.3389/fonc.2022.896593

9. Marusyk A, Polyak K. Tumor heterogeneity: Causes and consequences. *Biochim Biophys Acta*. 2010;1805:105-117.

   doi: 10.1016/j.bbcan.2009.11.002

10. Morrissy AS, Cavalli FMG, Remke M, *et al*. Spatial heterogeneity in medulloblastoma. *Nat Genet*. 2017;49: 780-788.

    doi: 10.1038/ng.3838

11. Savas P, Teo ZL, Lefevre C, *et al*. The subclonal architecture of metastatic breast cancer: Results from a prospective community-based rapid autopsy program "CASCADE". *PLoS Med*. 2016;13:e1002204.

    doi: 10.1371/journal.pmed.1002204. Erratum in: *PLoS Med*. 2017;14(4):e1002302.

    doi: 10.1371/journal.pmed.1002302

12. Dagogo-Jack I, Shaw AT. Tumour heterogeneity and resistance to cancer therapies. *Nat Rev Clin Oncol*. 2018;15:81-94.

    doi: 10.1038/nrclinonc.2017.166

13. Bailly C, Bodet-Milin C, Bourgeois M, *et al*. Exploring tumor heterogeneity using PET imaging: The big picture. *Cancers (Basel)*. 2019;11:1282.

    doi: 10.3390/cancers11091282

14. Anan N, Zainon R, Tamal M. A review on advances in ^{18}F-FDG PET/CT radiomics standardization and application in lung disease management. *Insights Imaging*. 2022;13:22.

    doi: 10.1186/s13244-021-01153-9. Erratum in: *Insights Imaging*. 2022;13(1):32.

    doi: 10.1186/s13244-022-01186-8

15. Zhao S, Kuge Y, Mochizuki T, *et al*. Biologic correlates of intratumoral heterogeneity in 18 F-FDG distribution with regional expression of glucose transporters and hexokinase-II in the experimental tumor. *J Nucl Med*. 2005;46:675-682.

16. Derlon JM, Chapon F, Noel MH, *et al*. Non-invasive grading of oligodendrogliomas: Correlation between *in vivo* metabolic pattern and histopathology. *Eur J Nucl Med*. 2000;27:778-787.

    doi: 10.1007/s002590000260

17. Henriksson E, Kjellen E, Wahlberg P, *et al*. 2-Deoxy-2-[18 F] fluoro-D-glucose uptake and correlation to intratumoral heterogeneity. *Anticancer Res*. 2007;27:2155-2159.

18. Van Baardwijk A, Bosmans G, Van Suylen RJ, *et al*. Correlation of intra-tumour heterogeneity on 18 F-FDG PET with pathologic features in nonsmall cell lung cancer: A feasibility study. *Radiother Oncol*. 2008;87:55-58.

    doi: 10.1016/j.radonc.2008.02.002

19. Eary JF, O'Sullivan F, O'Sullivan J, Conrad EU. Spatial heterogeneity in sarcoma 18F-FDG uptake as a predictor of patient outcome. *J Nucl Med*. 2008;49:1973-1979.

    doi: 10.2967/jnumed.108.053397

20. Kidd EA, Grigsby PW. Intratumoral metabolic heterogeneity of cervical cancer. *Clin Cancer Res*. 2008;14:5236-5241.

    doi: 10.1158/1078-0432.CCR-07-5252

21. Tixier F, Le Rest CC, Hatt M, *et al*. Intratumor heterogeneity characterized by textural features on baseline 18F-FDG PET images predicts response to concomitant radiochemotherapy in esophageal cancer. *J Nucl Med*. 2011;52:369-378.

    doi: 10.2967/jnumed.110.082404

22. Schinagl DA, Kaanders JH, Oyen WJ. From anatomical to biological target volumes: The role of PET in radiation treatment planning. *Cancer Imaging*. 2006;6:107-116.

    doi: 10.1102/1470-7330.2006.9017

23. Newbold KL, Partridge M, Cook G, *et al*. Evaluation of the role of 18FDG-PET/CT in radiotherapy target definition in patients with head and neck cancer. *Acta Oncol*. 2008;47:1229-1236.

    doi: 10.1080/02841860802256483.

24. Lopci E, Nanni C, Castellucci P, *et al*. Imaging with non-FDG PET tracers: Outlook for current clinical applications. *Insights Imaging*. 2010;1:373-385.

    doi: 10.1007/s13244-010-0040-9

25. Jadvar H, Delgado-Bolton R, Nadel H, *et al*. Appropriate use criteria for ^{18}F-FDG PET/CT in restaging and treatment response assessment of malignant disease. *J Nucl Med*. 2017;58:2026-3724.

doi: 10.2967/jnumed.117.197988

26. Binderup T, Knigge U, Loft A, *et al*. 18F-fluorodeoxyglucose positron emission tomography predicts survival of patients with neuroendocrine tumors. *Clin Cancer Res*. 2010; 16:978-985.

    doi: 10.1158/1078-0432.CCR-09-1759

27. Sanli Y, Garg I, Kandathil A, *et al*. Neuroendocrine tumor diagnosis and management: ^{68}Ga-DOTATATE PET/CT. *AJR Am J Roentgenol*. 2018;211:267-277.

    doi: 10.2214/AJR.18.19881

28. Kaewput C, Vinjamuri S. Role of combined ^{68}Ga DOTA-peptides and 18F FDG PET/CT in the evaluation of gastroenteropancreatic neuroendocrine neoplasms. *Diagnostics*. 2022;12:280.

    doi: 10.3390/diagnostics12020280

29. Zhou Y, Li L, Wang H, *et al*. Heterogeneous uptake of ^{68}Ga-DOTATATE and 18 F-FDG in initial diagnosed neuroendocrine tumors patients: Which patients are suitable for dual-tracer PET Imaging? *Clin Nucl Med*. 2024;49:516-520.

    doi: 10.1097/RLU.0000000000005231

30. Nogareda Seoane Z, Mallón Araújo MC, Calatayud Cubes A, *et al*. Functional imaging in neuroendocrine tumors: Assessment of molecular heterogeneity using [^{68}Ga]Ga-DOTA-TOC and [^{18}F]FDG PET/CT. *Rev Esp Med Nucl Imagen Mol (Engl Ed)*. 2024;43:500011.

    doi: 10.1016/j.remnie.2024.500011

31. Zhang H, Huang R, Cheung NK, *et al*. Imaging the norepinephrine transporter in neuroblastoma: A comparison of [18F]-MFBG and 123I-MIBG. *Clin Cancer Res*. 2014;20:2182-2191.

    doi: 10.1158/1078-0432.CCR-13-1153

32. Bian L, Xu J, Li P, Bai L, Song S. Comparison of ^{68}Ga-DOTANOC and ^{18}F-FDOPA PET/CT for detection of recurrent or metastatic paragangliomas. *Radiol Imaging Cancer*. 2024;7(1):e240059.

    doi: 10.1148/rycan.240059

33. Chang CA, Pattison DA, Tothill RW, *et al*. (68) Ga-DOTATATE and (18)F-FDG PET/CT in paraganglioma and pheochromocytoma: Utility, patterns and heterogeneity. *Cancer Imaging*. 2016;16:22.

    doi: 10.1186/s40644-016-0084-2

34. Wang B, Liu C, Wei Y, *et al*. A prospective trial of ^{68}Ga-PSMA and ^{18}F-FDG PET/CT in nonmetastatic prostate cancer patients with an early PSA progression during castration. *Clin Cancer Res*. 2020;26:4551-4558.

    doi: 10.1158/1078-0432.CCR-20-0587

35. Gofrit ON, Frank S, Meirovitz A, Nechushtan H, Orevi M. PET/CT With 68Ga-DOTA-TATE for diagnosis of neuroendocrine: Differentiation in patients with castrate-resistant prostate cancer. *Clin Nucl Med*. 2017;42:1-6.

    doi: 10.1097/rlu.0000000000001424

36. Pabst KM, Mei R, Lückerath K, *et al*. Detection of tumour heterogeneity in patients with advanced, metastatic castration-resistant prostate cancer on [^{68}Ga]Ga-/[^{18}F]F-PSMA-11/-1007, [^{68}Ga]Ga-FAPI-46 and 2-[^{18}F]FDG PET/CT: A pilot study. *Eur J Nucl Med Mol Imaging*. 2024;52:342-353.

    doi: 10.1007/s00259-024-06891-8

37. Mori Y, Dendl K, Cardinale J, Kratochwil C, Giesel FL, Haberkorn U. FAPI PET: Fibroblast activation protein inhibitor use in oncologic and nononcologic disease. *Radiology*. 2023;306:e220749.

    doi: 10.1148/radiol.220749

38. Liu X, Liu H, Gao C, Zeng W. Comparison of ^{68}Ga-FAPI and ^{18}F-FDG PET/CT for the diagnosis of primary and metastatic lesions in abdominal and pelvic malignancies: A systematic review and meta-analysis. *Front Oncol*. 2023;13:1093861.

    doi: 10.3389/fonc.2023.1093861

39. Xi Y, Sun Y, Gu B, Bian L, Song S. Evaluation of 68Ga-FAPI PET/CT and 18F-FDG PET/CT for the diagnosis of recurrent colorectal cancers. *Clin Transl Radiat Oncol*. 2024;49:100848.

    doi: 10.1016/j.ctro.2024.100848

40. Matushita CS, Coelho FARFB, Stasiak CES, *et al*. 18F-fluoroestradiol positron emission tomography in patients with breast cancer: A systematic review and meta-analysis. *Rev Assoc Med Bras (1992)*. 2023;69:e2023S116.

    doi: 10.1590/1806-9282.2023S116

41. Liu C, Gong C, Liu S, *et al*. 18F-FES PET/CT influences the staging and management of patients with newly diagnosed estrogen receptor-positive breast cancer: A retrospective comparative study with 18F-FDG PET/CT. *Oncologist*. 2019;24:e1277-e12785.

    doi: 10.1634/theoncologist.2019-0096

42. Kurland BF, Peterson LM, Lee JH, *et al*. Estrogen receptor binding (FES PET) and glycolytic activity (FDG PET) predict progression-free survival on endocrine therapy in patients with ER^{+} breast cancer. *Clin Cancer Res*. 2017;23:407-415.

    doi: 10.1158/1078-0432.CCR-16-0362

43. Mortimer JE, Dehdashti F, Siegel BA, Katzenellenbogen JA, Fracasso P, Welch MJ. Positron emission tomography with 2-[18F] Fluoro-2-deoxy-D-glucose and 16alpha-[18F] fluoro-17 beta-estradiol in breast cancer: Correlation with estrogen receptor status and response to systemic therapy. *Clin Cancer Res*. 1996;2:933-9.

44. Gebhart G, Lamberts LE, Wimana Z, *et al*. Molecular imaging as a tool to investigate heterogeneity of advanced HER2-positive breast cancer and to predict patient outcome

under trastuzumab emtansine (T-DM1): The ZEPHIR trial. *Ann Oncol*. 2016;27:619-624.

doi: 10.1093/annonc/mdv577

45. Clark AS, DeMichele A, Mankoff D. HER2 imaging in the ZEPHIR study. *Ann Oncol*. 2016;27:555-557.

doi: 10.1093/annonc/mdw033

46. Chen H, Niu G, Wu H, Chen X. Clinical application of radiolabeled RGD peptides for PET imaging of integrin $\alpha v\beta 3$. *Theranostics.* 2016;6:78-92.

doi: 10.7150/thno.13242

47. Das SS, Ahlawat S, Thakral P, *et al*. Potential efficacy of 68 Ga-trivehexin PET/CT and immunohistochemical validation of $\alpha v\beta 6$ integrin expression in patients with head and neck squamous cell carcinoma and pancreatic ductal adenocarcinoma. *Clin Nucl Med*. 2024;49:733-740.

doi: 10.1097/RLU.0000000000005278

48. Poschenrieder A, Osl T, Schottelius M, *et al*. First 18F-labeled pentixafor-based imaging agent for PET imaging of CXCR4 expression *in vivo*. *Tomography*. 2016;2:85-93.

doi: 10.18383/j.tom.2016.00130

49. Hicks RJ. Beyond FDG: Novel PET tracers for cancer imaging. *Cancer Imaging*. 2003;4:22-24.

doi: 10.1102/1470-7330.2003.0032

50. Li Z, Mo C, Li C, Wang Q, *et al*. Gallium-68 labeled positron emission computed tomography tracer targeting glypican-3 with high contrast for hepatocellular carcinoma imaging. *ACS Pharmacol Transl Sci*. 2024;7:4021-4031.

doi: 10.1021/acsptsci.4c00504

51. Kinahan PE, Fletcher JW. Positron emission tomography-computed tomography standardized uptake values in clinical practice and assessing response to therapy. *Semin Ultrasound CT MR*. 2010;31(6):496-505.

doi: 10.1053/j.sult.2010.10.001

52. Zhou J, Li Q, Cao Y. Spatiotemporal heterogeneity across metastases and organ-specific response informs drug efficacy and patient survival in colorectal cancer. *Cancer Res*. 2021;81:2522-2533.

doi: 10.1158/0008-5472.CAN-20-3665

53. Schmid S, Diem S, Li Q, *et al*. Organ-specific response to nivolumab in patients with non-small cell lung cancer (NSCLC). *Cancer Immunol Immunother*. 2018;67:1825-1832.

doi: 10.1007/s00262-018-2239-4

54. Dong ZY, Zhai HR, Hou QY, *et al*. Mixed responses to systemic therapy revealed potential genetic heterogeneity and poor survival in patients with non-small cell lung cancer. *Oncologist*. 2017;22:61-69.

doi: 10.1634/theoncologist.2016-0150

55. Janku F. Tumor heterogeneity in the clinic: Is it a real problem? *Ther Adv Med Oncol*. 2014;6:43-51.

doi: 10.1177/1758834013517414

56. Safri F, Nguyen R, Zerehpooshnesfchi S, George J, Qiao L. Heterogeneity of hepatocellular carcinoma: From mechanisms to clinical implications. *Cancer Gene Ther*. 2024;31:1105-1112.

doi: 10.1038/s41417-024-00764-w

57. Morinaga T, Inozume T, Kawazu M, *et al*. Mixed response to cancer immunotherapy is driven by intratumor heterogeneity and differential interlesion immune infiltration. *Cancer Res Commun*. 2022;2:739-753.

doi: 10.1158/2767-9764.CRC-22-0050

58. Sanli Y, Leake J, Odu A, Xi Y, Subramaniam RM. Tumor heterogeneity on FDG PET/CT and immunotherapy: An imaging biomarker for predicting treatment response in patients with metastatic melanoma. *AJR Am J Roentgenol*. 2019;212:1318-1326.

doi: 10.2214/AJR.18.19796

59. Mayerhoefer ME, Materka A, Langs G, *et al*. Introduction to radiomics. *J Nucl Med*. 2020;61:488-495.

doi: 10.2967/jnumed.118.222893

60. Kashyap A, Rapsomaniki MA, Barros V, *et al*. Quantification of tumor heterogeneity: From data acquisition to metric generation. *Trends Biotechnol*. 2022;40:647-676.

doi: 10.1016/j.tibtech.2021.11.006

61. Kocak B, Durmaz ES, Ates E, Kılıckesmez O. Radiomics with artificial intelligence: A practical guide for beginners. *Diagn Interv Radiol*. 2019;25:485-495.

doi: 10.5152/dir.2019.19321

62. Mirshahvalad SA, Eisazadeh R, Shahbazi-Akbari M, Pirich C, Beheshti M. Application of artificial intelligence in oncologic molecular PET-imaging: A narrative review on beyond [^{18}F] F-FDG tracers - Part I. PSMA, choline, and DOTA radiotracers. *Semin Nucl Med*. 2024;54:171-180.

doi: 10.1053/j.semnuclmed.2023.08.004

63. Gillies RJ, Kinahan PE, Hricak H. Radiomics: Images are more than pictures, they are data. *Radiology*. 2016;278:563-77.

doi: 10.1148/radiol.2015151169

ACCSCIENCE PUBLISHING

Advances in Radiotherapy & Nuclear Medicine

REVIEW ARTICLE

Bidirectional regulatory mechanisms of lipids and radiotherapy: Metabolic disorders, therapeutic interventions, and pan-cancer clinical insights

Jinxia Wu[1†] and Jiahua Lyu[2†*]

[1]School of Medicine, University of Electronic Science and Technology of China, Chengdu, Sichuan, China

[2]Department of Radiotherapy, Sichuan Cancer Hospital and Institute, Sichuan Cancer Center, Affiliated Cancer Hospital of University of Electronic Science and Technology of China, Chengdu, Sichuan, China

Abstract

Malignant tumors continue to pose a significant threat to global health. Emerging evidence suggests that abnormal blood lipid levels may influence tumor incidence, and cancer patients frequently exhibit dysregulated lipid profiles. Radiotherapy, a cornerstone in cancer treatment, has been demonstrated to modulate blood lipid levels in patients. Conversely, blood lipid concentrations can significantly impact the efficacy of radiotherapy and the incidence of associated complications. This comprehensive review delves into cutting-edge research illuminating the intricate bidirectional interplay between blood lipid profiles and radiotherapy efficacy in malignant tumor patients. At the same time, it investigates the promising potential of tailored dietary modulation strategies and novel lipid-lowering therapeutics to enhance treatment efficacy and patient prognosis.

Keywords: Radiotherapy; Blood lipids; Cancer; Lipid metabolism; Therapeutic efficacy

1. Introduction

Malignant tumors remain the leading cause of mortality worldwide.[1] According to the Global Cancer Statistics 2022 report, there were approximately 19.97 million new cancer cases and 9.74 million cancer-related deaths globally in 2022.[2]

Blood lipids, encompassing triglycerides (TG), cholesterol, cholesterol esters, phospholipids, and free fatty acids, play a crucial role in cellular metabolism. Emerging evidence suggests that tumorigenesis in specific cancer types may be accompanied by dysregulated blood lipid metabolism. For instance, a lipid analysis of serum samples from 100 breast cancer patients and 100 healthy controls revealed elevated levels of low-density lipoprotein (LDL), TG, and total cholesterol (TC) in cancer patients compared to healthy individuals, underscoring the prevalence of dyslipidemia in cancer populations.[3]

Radiotherapy, a primary modality in cancer treatment, exerts its therapeutic effects through the induction of DNA damage in malignant cells.[4] A growing body of evidence indicates that radiotherapy can significantly alter patients' blood lipid profiles.

[†]*These authors equally contributed to this work.*

***Corresponding author:**
Jiahua Lyu
(winlttljh@163.com)

Citation: Wu J, Lyu J. Bidirectional regulatory mechanisms of lipids and radiotherapy: Metabolic disorders, therapeutic interventions, and pan-cancer clinical insights. *Adv Radiother Nucl Med.* 2025;3(2):16-23. doi: 10.36922/ARNM025070006

Received: February 10, 2025

1st revised: March 13, 2025

2nd revised: March 28, 2025

Accepted: April 2, 2025

Conversely, blood lipid levels can influence radiotherapy's efficacy and safety profile.

This review aims to provide a comprehensive analysis of current clinical studies, focusing on the effects of radiotherapy on blood lipid levels and the impact of blood lipids on radiotherapy outcomes. The ultimate goal is to offer evidence-based insights for optimizing lipid management in radiotherapy patients.

2. The impact of radiotherapy on blood lipids in cancer patients

A systematic literature search was conducted across PubMed, EMBASE, Cochrane Library, and Web of Science, yielding 10 relevant studies (Table 1). Despite methodological and population differences, all studies consistently demonstrated that radiotherapy significantly alters blood lipid profiles in cancer patients.

2.1. Head-and-neck tumors

Squamous cell carcinoma is the predominant histological type of head-and-neck cancer, accounting for over 90% of all cases. In 2022, there were approximately 660,740 newly diagnosed cases worldwide.[5] Smoking, heavy alcohol consumption, and human papillomavirus infection are the most significant risk factors for head-and-neck cancer.[6] Jelonek *et al.*[7] conducted a study on head-and-neck squamous cell carcinoma patients, dividing them into three treatment groups: radiotherapy alone (*n* = 18), concurrent chemoradiotherapy with cisplatin (*n* = 16), and chemotherapy alone (*n* = 13).[7] Mass spectrometry analysis of pre- and post-treatment serum samples revealed significant decreases in phosphatidylcholine (PC) levels in both radiotherapy groups, with more pronounced reductions in the concurrent chemoradiotherapy group. Subsequent analysis demonstrated a negative correlation between serum PC levels and radiation dose/absorbed

Table 1. Radiotherapy effects on blood lipid levels in cancer patients

Author (s)	Year	Diagnosis	Tumor staging	Sample size	Method	Types of lipids	Effect	Baseline
Jelonek *et al.*[7]	2020	HNSCC	TxNxM0	47	LC-MS	PCs	Low	-
Jelonek *et al.*[8]	2021	HNSCC	TxNxM0	45	LC-MS	PCs	Low	-
Tang *et al.*[10]	2020	Lung cancer	NA	256	LC-MS	S1P	Low	Receiving radiotherapy compared to non-radiotherapy patients (222.13±48.63 vs. 315.16±51.06)
Lv *et al.*[11]	2024	NSCLC	Histology grade III–IV	31	LC-MS	PS, PI, and TC	Low	-
Zemanova *et al.*[13]	2016	ESCC	Histology grade II–III	42	LC-MS	PC	High	Healthy compared to patients (5.53±1.23 vs. 5.17±1.11)
Xu *et al.*[15]	2024	Cervical cancer	Histology grade I–IV	114	LC-MS	FFA	Most high	-
Ng *et al.*[17]	2020	HCC	NA	47	LC-MS	FFA and GPL	High	-
Wolny-Rokicka *et al.*[18]	2019	Prostate cancer	NA	91	Roche/Hitachi Cobas C Systems	HDL	Low	-
Shaikh *et al.*[19]	2017	Breast cancer	NA	130	Gas chromatography	TC and LDL-C	Low	-
Giskeødegård *et al.*[20]	2022	Breast cancer	I–III	250	NMR spectroscopy	HDL, LDL-C, and TG	HDL low, LDL-C high, and TG high	-

Note: NA refers to not available.

Abbreviations: ESCC: Esophageal squamous cell carcinoma; FFA: Free fatty acids; GPL: Glycerophospholipids; HCC: Hepatocellular carcinoma; HDL: High-density lipoprotein; HNSCC: Head-and-neck squamous cell carcinoma; LC-MS: Liquid chromatography-mass spectrometry; LDL-C: Low-density lipoprotein cholesterol; NMR spectroscopy: Nuclear magnetic resonance spectroscopy; NSCLC: Non-small cell lung cancer; PC: Phosphatidylcholine; PI: Phosphatidylinositol; PS: Phosphatidylserine; S1P: Sphingosine-1-phosphate; TC: Total cholesterol; TG: Triglycerides.

energy, highlighting the significant impact of radiotherapy on lipid metabolism in head-and-neck squamous cell carcinoma patients.[8]

2.2. Thoracic tumors

Lung cancer is the most commonly diagnosed cancer, with approximately 1.8 million new cases each year. It is also the leading cause of cancer-related deaths, accounting for approximately 1.59 million deaths annually.[9] Sphingosine-1-phosphate (S1P), a bioactive lipid, has been implicated in lung cancer progression and treatment resistance. Tang *et al.*[10] analyzed serum S1P levels in 256 lung cancer patients, revealing significantly lower levels in the 124 patients receiving radiotherapy than in non-radiotherapy patients (222.13 s 48.63 vs. 315.16 ± 51.06). This inverse correlation (Spearman's rho = –0.653, $p<0.001$) suggests radiotherapy-induced modulation of S1P signaling.[10] Lv *et al.*[11] conducted a prospective study using mass spectrometry to analyze plasma lipid profiles in 31 advanced non-small cell lung cancer patients before and after radiotherapy. Significant reductions in phosphatidylserine, TC, and phosphatidylinositol (PI) levels were observed post-radiotherapy, indicating substantial alterations in lipid metabolism.[11]

In the 2022 global cancer statistics, esophageal cancer ranked seventh in incidence among all cancer types and sixth in mortality.[12] Zemanova *et al.*[13] investigated plasma PC fatty acid composition in 42 patients before and after neoadjuvant chemoradiotherapy in esophageal squamous cell carcinoma. The study revealed increased levels of docosahexaenoic acid and total n-3 polyunsaturated fatty acids post-treatment, suggesting radiotherapy-induced modifications in fatty acid metabolism.[13]

2.3. Abdominal tumors

Cervical cancer ranks fourth in incidence among malignancies in women, with China and India accounting for more than one-third of global cases. Among women aged 20 – 39, cervical cancer is the second leading cause of cancer-related mortality.[14] Xu *et al.*[15] employed metabolomics-based liquid chromatography-tandem mass spectrometry to analyze plasma-free fatty acid profiles in 114 cervical cancer patients, including 40 undergoing concurrent chemoradiotherapy. While palmitic and stearic acid levels decreased post-treatment, most fatty acids, including oleic acid, arachidonic acid, and total n-3 polyunsaturated fatty acids, showed significant increases, indicating complex lipid metabolic changes associated with radiotherapy.[15]

Hepatocellular carcinoma (HCC) ranks fourth in global cancer mortality and is the leading cause of death in cirrhosis. HCC has an extremely poor prognosis, with a mortality rate nearly equal to its incidence rate.[16] Ng *et al.*[17] conducted a prospective study on 47 HCC patients treated with stereotactic body radiation therapy. Liquid chromatography-tandem mass spectrometry-based metabolomics revealed increased serum fatty acids and glycerophospholipid post-stereotactic body radiation therapy, suggesting radiation-induced lipid metabolic alterations.[17]

In prostate cancer, an analysis of 91 patients demonstrated significant reductions in high-density lipoprotein (HDL) levels post-radiotherapy ($p=0.0159$).[18] Similarly, Shaikh *et al.*[19] reported decreased TC (224.4 – 150.2 mg/dL) and LDL cholesterol (142.9 – 89.8 mg/dL) levels in 130 breast cancer patients following radiotherapy.[19]

Giskeødegård *et al.*[20] conducted a comprehensive study on 250 breast cancer patients receiving postoperative radiotherapy, utilizing nuclear magnetic resonance spectroscopy to quantify serum metabolites and lipoprotein subfractions. The study revealed reduced esterified cholesterol levels across HDL subfractions, increased free cholesterol levels, and elevated LDL particle numbers, resulting in increased LDL cholesterol and TG levels post-radiotherapy.[20] These findings collectively indicate that radiotherapy induces significant alterations in serum lipid concentrations in cancer patients.

3. The impact of blood lipids on radiotherapy

In summary, radiotherapy is associated with fluctuations in blood lipid levels in cancer patients. Next, we will explore how blood lipids influence the efficacy and complications of radiotherapy (Table 2). This exploration will further guide clinicians in managing patients' baseline lipid levels before radiotherapy, reducing radiotherapy-related adverse reactions, and enhancing radiotherapy's therapeutic effect.

3.1. The impact of blood lipids on the efficacy of radiotherapy

Dyslipidemia is a common comorbidity in cancer patients and, to some extent, reflects underlying lipid metabolism disorders. Some studies have explored the correlation between blood lipid levels and radiotherapy outcomes in cancer patients, providing a lipid-based perspective for optimizing individualized radiotherapy strategies. In addition, these findings contribute to the development of clinical guidelines for blood lipid management in patients undergoing radiotherapy.

Huang *et al.*[21] conducted a retrospective study on 140 high-grade glioma patients undergoing intensity-modulated radiotherapy. Patients were grouped based on the average levels of TC, LDL, and HDL in peripheral blood serum (pre-treatment and 6-month post-treatment) to explore whether pre-treatment and post-treatment changes in these blood lipid levels affected prognosis. Patients with

Table 2. The impact of blood lipids on radiotherapy

Author (s)	Year	Diagnosis	Tumor staging	Sample size	Types of lipids	Effect
Huang *et al.*[21]	2023	High-grade glioma	Histology grade III–IV	140	TC, LDL, and HDL	Higher pre-treatment serum cholesterol and elevated post-IMRT serum LDL levels are associated with poorer prognosis.
Wang *et al.*[22]	2019	NPC	Histology grade III–IV	342	HDL-C	Higher pre-treatment HDL-C levels can predict 5-year failure-free survival in NPC patients.
Zhang *et al.*[23]	2023	NSCLC	Histology grade III–IV	134	TG, TC, and LDL	Low TG, TC, and LDL levels are associated with poorer prognosis in NSCLC patients receiving iRT.
Harima *et al.*[24]	2021	Cervical cancer	T×N × M0	145	ApoC-II	Patients with pre-treatment ApoC-II levels ≤25.8 μg/mL have a shorter pelvic progression-free survival.
Guo *et al.*[25]	2021	Rectal cancer	Histology grade II–III	751	ApoA-I	Patients with pre-treatment serum apolipoprotein A-I (≤1.20 g/L) have a higher incidence of adverse reactions to neoadjuvant chemoradiotherapy.
Goldberg *et al.*[27]	2022	Pediatric cancer	NA	4115	Non-HDL-C	Abnormal non-HDL cholesterol increases the risk of stroke and peripheral vascular disease in patients undergoing radiotherapy.
Cheng *et al.*[28]	2023	Head-and-neck cancer	NA	694	TC	Hypercholesterolemia is associated with post-radiotherapy carotid artery stenosis.
Wang *et al.*[29]	2022	ESCC	I-III	355	Serum lipids	Hyperlipidemia increases the incidence of major coronary events after radiotherapy.

Abbreviations: ApoA-I: apolipoprotein A-I; ApoC-II: Apolipoprotein C-II; ESCC: Esophageal squamous cell carcinoma; HDL: High-density lipoprotein; HDL-C: High-density lipoprotein cholesterol; IMRT: Intensity-modulated radiation therapy; LDL: Low-density lipoprotein; NPC: Nasopharyngeal carcinoma; NSCLC: Non-small cell lung cancer; TC: Total cholesterol; TG: Triglycerides.

high pre-treatment TC levels showed significantly worse 5-year survival rates (4.9% vs. 19.6%) and median survival times (23.6 vs. 24.5 months) than those with lower TC levels. Similarly, patients with higher post-treatment LDL had a 5-year survival rate and median survival time of 11.8% and 20.4 months, respectively, while those with lower LDL had a 5-year survival rate and median survival time of 16.7% and 28.4 months, respectively.[21] These findings suggest that high pre-treatment serum cholesterol and high post-treatment LDL concentrations are associated with poorer prognosis. Wang *et al.*'s[22] retrospective randomized clinical study on 400 nasopharyngeal carcinoma patients revealed that high pre-treatment HDL cholesterol levels improved 5-year failure-free survival (p=0.017).[22]

In a single-center retrospective study by Zhang *et al.*,[23] 134 patients with stage III–IV non-small cell lung cancer undergoing immune therapy combined with radiotherapy were included, and correlations between pre-treatment blood lipid levels and both overall survival and progression-free survival were analyzed. The results indicated that low levels of TG (p=0.0017), TC (p=0.0028), and LDL (p=0.0330) were adverse prognostic factors for progression-free survival.[23]

In a multicenter prospective cohort study by Harima *et al.*,[24] 145 cervical cancer patients were analyzed for changes in serum biomarkers before and after radiotherapy. Multivariable analysis revealed that patients with pre-treatment apolipoprotein C-II (ApoC-II) levels ≤25.8 μg/mL had a shorter pelvic progression-free survival compared to those with ApoC-II levels >25.8 μg/mL (p=0.023).[24] The study demonstrated that pre-treatment ApoC-II levels can effectively predict the radiotherapy prognosis of patients with locally advanced cervical cancer. However, the conclusions need further validation due to the small sample size and the fact that the study was limited to a Japanese population.

A retrospective study by Guo *et al.*[25] analyzed serum lipids in 751 patients with rectal cancer (clinical stage II–III) who received neoadjuvant chemoradiotherapy followed by surgery. The study considered tumor regression grading (5 – 3) as an indicator of adverse reactions to neoadjuvant chemoradiotherapy. The results found that patients with pre-treatment serum apolipoprotein A-I levels ≤1.20 g/L had a higher proportion of neoadjuvant chemoradiotherapy adverse reactions (p=0.003).[25] This indicates that blood lipid levels are associated with the adverse reactions of radiotherapy in rectal cancer patients.

3.2. The impact of blood lipids on radiotherapy complications

Abnormal blood lipid levels can lead to a range of diseases, and studies have shown that higher serum TC and LDL cholesterol levels are associated with an increased mortality rate from cardiovascular diseases, while HDL cholesterol levels are negatively correlated with cardiovascular disease mortality.[26] However, limited studies investigate whether lipid abnormalities affect cardiovascular diseases following radiotherapy.

A cohort study by Goldberg *et al.*[27] assessed lipid levels in 4,115 pediatric cancer survivors who had survived at least 5-year post-treatment to evaluate the prevalence of specific lipid abnormalities and related cardiovascular risks. The results indicated that abnormal non-HDL cholesterol levels increased the risk of stroke and peripheral vascular disease in patients who received radiotherapy (p=0.02).[27] A retrospective study by Cheng *et al.*[28] included 694 head-and-neck cancer patients and analyzed the incidence of carotid artery stenosis after radiotherapy, with a follow-up period of 1 – 3 years. Multivariate analysis showed that hypercholesterolemia (odds ratio: 1.82, 95% confidence interval, 0.97 – 3.41, p=0.06) was associated with carotid artery stenosis after radiotherapy.[28]

A cohort study by Wang *et al.*[29] analyzed 355 esophageal squamous cell carcinoma patients who received radiotherapy, selecting them from clinical databases. The results showed that the probability of major coronary events in patients without a history of hyperlipidemia was 7.1%. In contrast, in patients with a history of hyperlipidemia, the likelihood of major coronary events was 92.9% (p=0.005). This suggests that hyperlipidemia, as a known risk factor for atherosclerosis, increases the incidence of major coronary events after radiotherapy.[29]

4. Mechanisms of lipid metabolism disorders on the effects of radiotherapy

In the preceding sections, we have synthesized evidence demonstrating radiotherapy-induced alterations in blood lipid profiles among cancer patients and the consequential effects of dyslipidemia on therapeutic outcomes. However, mechanistic insights into lipid-mediated modulation of radiotherapy efficacy remain conspicuously absent. We posit that blood lipid homeostasis exerts a regulatory influence on radiotherapeutic responses through tumor microenvironment remodeling. Emerging evidence corroborates tripartite interactions between tumor microenvironment dynamics, lipid metabolism dysregulation, and radiation responsiveness. This review systematically collates contemporary discoveries across these interconnected domains, aiming to illuminate strategic pathways for investigating lipid-driven mechanisms in radiotherapy optimization.

4.1. Abnormal lipid synthesis

Abnormal lipid synthesis encompasses excessive fatty acid production and disrupted cholesterol synthesis. Sterol regulatory element-binding protein 1 (SREBP1) serves as a master regulator, critically governing cholesterol synthesis, fatty acid metabolism, and the delicate balance of lipid homeostasis.[30] The phosphatidylinositol 3-kinase (PI3K)/protein kinase B (AKT)/mammalian target of rapamycin (mTOR) signaling pathway is critical in promoting the expression and activity of SREBP1 and fatty acid synthase (FASN), fostering heightened lipid synthesis that drives tumor cell resistance to radiotherapy. A comprehensive review by Mousavikia *et al.*,[31] analyzing 27 preclinical studies and five clinical trials on colorectal cancer, underscored the potential of PI3K/AKT/mTOR pathway inhibition to significantly amplify radiotherapy efficacy through mechanistic interference with lipid metabolism pathways.[31] In a groundbreaking study, Li *et al.*[32] performed comprehensive western blot analyses on prostate cancer cells subjected to radiotherapy, quantifying the protein expression levels of PI3K, phosphorylated PI3K, AKT, phosphorylated AKT, mTOR, and phosphorylated mTOR – key signaling molecules in oncogenic pathways. Their findings revealed that targeted inhibition of the PI3K/AKT/mTOR cascade significantly suppressed prostate cancer cell proliferation, triggered apoptosis, and markedly enhanced radiosensitivity.[32] In a pivotal discovery, Jin *et al.*[33] demonstrated through colorectal cancer cell experiments that exogenous cholesterol-induced pronounced radioresistance in malignant cells, underscoring the critical need for minimizing dietary cholesterol intake in patients undergoing radiotherapy. Their groundbreaking research further unveiled that silencing the SREBP1/FASN signaling pathway significantly inhibited colorectal cancer cell proliferation and triggered accelerated apoptosis following radiation exposure.[33]

4.2. Ferroptosis and lipid oxidation

Ferroptosis, a distinct form of regulated cell death, orchestrates its lethal cascade through iron-driven lipid peroxidation. When iron overload converges with rampant reactive oxygen species, polyunsaturated fatty acid-containing phospholipids in cellular membranes become vulnerable to relentless peroxidation. This insidious accumulation of lipid peroxides breaches membrane structural integrity, culminating in the catastrophic collapse characteristic of ferroptosis.

Lei *et al.*[34] presented compelling genetic and biochemical evidence to establish a definitive link between radiotherapy and ferroptosis. Their findings revealed that radiotherapy stimulates lipid peroxidation and upregulates *PTGS2* expression, a pivotal biomarker of ferroptosis. Tumor cells exposed to radiotherapy displayed hallmark ferroptotic morphological features, including mitochondrial condensation and heightened membrane density. Crucially, the administration of ferroptosis inhibitors significantly rescues cell viability post-radiotherapy, demonstrating a markedly superior effect to other regulated cell death inhibitors. Notably, the ferroptotic response was shown to correlate directly with both radiation dosage and fractionation schemes, underscoring its dynamic nature in therapeutic contexts.[34]

5. Conclusion and prospect

Blood lipids represent a modifiable factor in cancer treatment, potentially enhancing radiotherapy efficacy through dietary and pharmacological interventions. Studies have shown that oral omega-3 polyunsaturated fatty acids can improve the nutritional status and regulate inflammation markers in lung cancer patients undergoing radiotherapy.[35] Emerging evidence suggests that omega-3 polyunsaturated fatty acids may improve nutritional status and modulate inflammation in lung cancer patients undergoing radiotherapy.[36] Furthermore, some cohort studies have demonstrated that statins can be used in radiotherapy for nasopharyngeal carcinoma, head-and-neck tumors, and chest tumors, reducing the risk of vascular complications, such as stroke and transient ischemic attacks in patients.[37-39] However, the exact mechanisms of how diet and medication regulate blood lipids concerning radiotherapy remain unclear. More extensive, multicenter, randomized controlled trials are needed in the future. Based on the current research, we may attempt to optimize dietary plans by combining patients' blood lipid levels with tumor types to better control lipid levels.

In this review, we discussed the mutual influence between tumor radiotherapy and blood lipid levels and how regulating blood lipids through diet and medication can enhance the efficacy of radiotherapy. Although controlling blood lipids has shown specific synergistic effects in radiotherapy, more extensive clinical studies are still needed to provide evidence for clinical guidelines and expert consensus. The growth characteristics of different tumor types vary, and their lipid demands also differ. Therefore, controlling blood lipids in tumor patients should involve personalized management based on the patient's baseline conditions and tumor type.

Acknowledgments

None.

Funding

This work was supported by the Natural Science Foundation of Sichuan Province (Grant No. 2023NSFSC0712).

Conflict of interest

Jiahua Lyu is an Editorial Board Member of this journal but was not in any way involved in the editorial and peer-review process conducted for this paper, directly or indirectly. Separately, the other author declares no known competing financial interests or personal relationships that could have influenced the work reported in this paper.

Author contributions

Conceptualization: Jiahua Lyu
Writing – original draft: Jinxia Wu
Writing – review & editing: Jiahua Lyu

Ethics approval and consent to participate

Not applicable.

Consent for publication

Not applicable.

Availability of data

Not applicable.

References

1. De Martel C, Georges D, Bray F, Ferlay J, Clifford GM. Global burden of cancer attributable to infections in 2018: A worldwide incidence analysis. *Lancet Glob Health*. 2020;8(2):e180-e190.

   doi: 10.1016/S2214-109X(19)30488-7

2. Zhang X, Yang L, Liu S, *et al*. Interpretation on the report of global cancer statistics 2022. *Zhonghua Zhong Liu Za Zhi*. 2024;46(7):710-721.

   doi: 10.3760/cma.j.cn112152-20240416-00152

3. Kumar V, Singh A, Sidhu DS, Panag KM. A comparitive study to evaluate the role of serum lipid levels in aetiology of carcinoma breast. *J Clin Diagn Res*. 2015;9:PC01-PC03.

   doi: 10.7860/JCDR/2015/12273.5563

4. Yilin Yu, Yu J, Ge S, Su Y, Fan X. Novel insight into metabolic reprogrammming in cancer radioresistance: A promising therapeutic target in radiotherapy. *Int J Biol Sci*. 2023;19(3):811-828.

   doi: 10.7150/ijbs.79928

5. Arboleda LP, De Carvalho GB, Santos-Silva AR, *et al*. Squamous cell carcinoma of the oral cavity, oropharynx, and larynx: A scoping review of treatment guidelines worldwide. *Cancers (Basel)*. 2023;15(17):4405.

   doi: 10.3390/cancers15174405

6. Matos LL, Kowalski LP, Chaves ALF, *et al*. Latin American consensus on the treatment of head and neck cancer. *JCO Glob Oncol*. 2024;10:e2300343.

   doi: 10.1200/GO.23.00343

7. Jelonek K, Krzywon A, Jablonska P, *et al*. Systemic effects of

radiotherapy and concurrent chemo-radiotherapy in head and neck cancer patients-comparison of serum metabolome profiles. *Metabolites*. 2020;10(2):60.

doi: 10.3390/metabo10020060

8. Jelonek K, Krzywon A, Papaj K, *et al.* Dose-dependence of radiotherapy-induced changes in serum levels of choline-containing phospholipids; The importance of lower doses delivered to large volumes of normal tissues. *Strahlenther Onkol*. 2021;197(10):926-934.

   doi: 10.1007/s00066-021-01802-4

9. LePechoux C, Faivre-Finn C, Ramella S, *et al*. ESTRO ACROP guidelines for target volume definition in the thoracic radiation treatment of small cell lung cancer. *Radiother Oncol*. 2020;152:89-95.

   doi: 10.1016/j.radonc.2020.07.012

10. Tang X, Chen H, Chen G, *et al.* Validated LC-MS/MS method of sphingosine 1-phosphate quantification in human serum for evaluation of response to radiotherapy in lung cancer. *Thorac Cancer*. 2020;11(6):1443-1452.

    doi: 10.1111/1759-7714.13409

11. Minghe LV, Shao S, Du Y, Zhuang X, Wang X, Qiao T. Plasma lipidomics profiling to identify the biomarkers of diagnosis and radiotherapy response for advanced non-small-cell lung cancer patients. *J Lipids*. 2024;2024:6730504.

    doi: 10.1155/2024/6730504

12. Han D, Dong J, Wang Q, *et al*. Neoadjuvant radiation target volume definition in esophageal squamous cell cancer: A multicenter recommendations from Chinese experts. *BMC Cancer*. 2024;24(1):1086.

    doi: 10.1186/s12885-024-12825-2

13. Zemanova M, Vecka M, Petruželka L, Staňková B, Žák A, Zeman M. Plasma phosphatidylcholines fatty acids in men with squamous cell esophageal cancer: Chemoradiotherapy improves abnormal profile. *Med Sci Monit*. 2016;22:4092-4099.

    doi: 10.12659/MSM.896799

14. Buskwofie A, David-West G, Clare CA. A review of cervical cancer: Incidence and disparities. *J Natl Med Assoc*. 2020;112:229-32.

    doi: 10.1016/j.jnma.2020.03.002

15. Xu X, Ping P, Zhang Z, Zou L. Plasma free fatty acid levels in cervical cancer: Concurrent chemoradiotherapy improves abnormal profile. *Front Pharmacol*. 2024;15:1352101.

    doi: 10.3389/fphar.2024.1352101

16. Ganesan P, Kulik LM. Hepatocellular carcinoma: New developments. *Clin Liver Dis*. 2023;27(1):85-102.

    doi: 10.1016/j.cld.2022.08.004

17. Sylvia SW, Jang GH, Kurland IJ, Qiu Y, Guha C, Dawson LA. Plasma metabolomic profiles in liver cancer patients following stereotactic body radiotherapy. *EBioMedicine*. 2020;59:102973.

    doi: 10.1016/j.ebiom.2020.102973

18. Wolny-Rokicka E, Tukiendorf A, Wydmański J, Brzezniakiewicz-Janus K, Zembroń-Łacny A. The effect of radiotherapy on the concentration of plasma lipids in elderly prostate cancer patients. *Am J Mens Health*. 2019;13(2):1557988319846328.

    doi: 10.1177/1557988319846328

19. Shaikh S, Channa NA, Talpur FN, Younis M, Tabassum N. Radiotherapy improves serum fatty acids and lipid profile in breast cancer. *Lipids Health Dis*. 2017;16(1):92.

    doi: 10.1186/s12944-017-0481-y

20. Giskeødegård GF, Madssen TS, Sangermani M, *et al*. Longitudinal changes in circulating metabolites and lipoproteins after breast cancer treatment. *Front Oncol*. 2022;12:919522.

    doi: 10.3389/fonc.2022.919522

21. Huang F, Li S, Wang X, *et al*. Serum lipids concentration on prognosis of high-grade glioma. *Cancer Causes Control*. 2023;34(9):801-811.

    doi: 10.1007/s10552-023-01710-1

22. Wang, CT, Chen MY, Guo X, *et al*. Association between pretreatment serum high-density lipoprotein cholesterol and treatment outcomes in patients with locoregionally advanced nasopharyngeal carcinoma treated with chemoradiotherapy: Findings from a randomised trial. *J Cancer*. 2019;10(16):3618-3623.

    doi: 10.7150/jca.32621

23. Zhang J, Shang S, Wang F, *et al*. The baseline serum lipid levels and outcomes of NSCLC patients receiving immunotherapy combined or non-combined with radiotherapy: A single center retrospective study. *Int J Radiat Oncol Biol Phys*. 2023;117(2 Suppl):e11.

    doi: 10.1016/j.ijrobp.2023.06.670

24. Harima Y, Ariga T, Kaneyasu Y, *et al*. Clinical value of serum biomarkers, squamous cell carcinoma antigen and apolipoprotein C-II in follow-up of patients with locally advanced cervical squamous cell carcinoma treated with radiation: A multicenter prospective cohort study. *PLoS One*. 2021;16(11):e0259235.

    doi: 10.1371/journal.pone.0259235

25. Guo SP, Chen C, Zeng ZF, *et al*. Serum apolipoprotein a-I predicts response of rectal cancer to neoadjuvant chemoradiotherapy. *Cancer Manag Res*. 2021;13:2623-2631.

    doi: 10.2147/CMAR.S302677

26. Jung E, Kong SY, Ro YS, Ryu HH, Shin SD. Serum cholesterol levels and risk of cardiovascular death: A systematic review and a dose-response meta-analysis of prospective cohort

studies. *Int J Environ Res Public Health*. 2022;19(14):8272.

doi: 10.3390/ijerph19148272

27. Goldberg JF, Hyun G, Ness KK, *et al*. Dyslipidemia and cardiovascular disease among childhood cancer survivors: A St. Jude lifetime cohort report. *J Natl Cancer Inst*. 2024;116(3):408-420.

    doi: 10.1093/jnci/djad222

28. Cheng YW, Chen CH, Yeh SJ, *et al*. Association between modifiable vascular risk factors and rapid progression of postradiation carotid artery stenosis. *J Chin Med Assoc*. 2023;86(7):627-632.

    doi: 10.1097/JCMA.0000000000000936

29. Wang X, Palaskas NL, Hobbs BP, *et al*. The impact of radiation dose to heart substructures on major coronary events and patient survival after chemoradiation therapy for esophageal cancer. *Cancers (Basel)*. 2022;14(5):1304.

    doi: 10.3390/cancers14051304

30. He Y, Qi S, Chen L, *et al*. The roles and mechanisms of SREBP1 in cancer development and drug response. *Genes Dis*. 2024;11(4):100987.

    doi: 10.1016/j.gendis.2023.04.022

31. Mousavikia SN, Darvish L, Firouzjaei AA, Toossi MTB, Azimian H. PI3K/AKT/mTOR targeting in colorectal cancer radiotherapy: A systematic review. *J Gastrointest Cancer*. 2025;56(1):52.

    doi: 10.1007/s12029-024-01160-1

32. Li P, Cui Y, Hu K, Wang X, Yu Y. Silencing APLNR enhances the radiosensitivity of prostate cancer by modulating the PI3K/AKT/mTOR signaling pathway. *Clin Transl Oncol*. 2024.

    doi: 10.1007/s12094-024-03692-1

33. Jin Y, Chen Z, Dong J, *et al*. SREBP1/FASN/cholesterol axis facilitates radioresistance in colorectal cancer. *FEBS Open Bio*. 2021;11(5):1343-1352.

    doi: 10.1002/2211-5463.13137

34. Lei G, Mao C, Yan Y, Zhuang L, Gan B. Ferroptosis, radiotherapy, and combination therapeutic strategies. *Protein Cell*. 2021;12(11):836-857.

    doi: 10.1007/s13238-021-00841-y

35. Tao X, Zhou Q, Rao Z. Efficacy of ω-3 polyunsaturated fatty acids in patients with lung cancer undergoing radiotherapy and chemotherapy: A meta-analysis. *Int J Clin Pract*. 2022;2022:6564466.

    doi: 10.1155/2022/6564466

36. Polański J, Świątoniowska-Lonc N, Kołaczyńska S, Chabowski M. Diet as a factor supporting lung cancer treatment-a systematic review. *Nutrients*. 2023;15(6):1477.

    doi: 10.3390/nu15061477

37. Lin CY, Chang CL, Lin KC, *et al*. Statin use reduces radiation-induced stroke risk in advanced nasopharyngeal carcinoma patients. *Radiother Oncol*. 2024;191:110067.

    doi: 10.1016/j.radonc.2023.110067

38. Addison D, Lawler PR, Emami H, *et al*. Incidental statin use and the risk of stroke or transient ischemic attack after radiotherapy for head and neck cancer. *J Stroke*. 2018;20(1):71-79.

    doi: 10.5853/jos.2017.01802

39. Boulet J, Peña J, Hulten EA, *et al*. Statin use and risk of vascular events among cancer patients after radiotherapy to the thorax, head, and neck. *J Am Heart Assoc*. 2019;8(13):e005996.

    doi: 10.1161/JAHA.117.005996

ACCSCIENCE PUBLISHING

Advances in Radiotherapy & Nuclear Medicine

REVIEW ARTICLE

Current status and future potential of radiomics in the management of patients with gastric cancer

Qiao Zheng[1†], Haoze Zheng[1†], Ziyang Liu[1], Wenhao Guo[2], Sunjun Li[3], Junhao Ma[1], Yuxin Lou[1], Lijing Liu[4], Congying Xie[1*], and Xiance Jin[1,2*]

[1]Department of Radiation and Medical Oncology, 1st Affiliated Hospital of Wenzhou Medical University, Wenzhou, Zhejiang, China

[2]Department of Education, School of Basic Medical Science, Wenzhou Medical University, Wenzhou, Zhejiang, China

[3]Department of Education, Alberta Institute, Wenzhou Medical University, Wenzhou, Zhejiang, China

[4]Department of Radiation and Medical Oncology, Changxing County People's Hospital, Zhejiang University School of Medicine Second Affiliated Hospital, Hangzhou, Zhejiang, China

Abstract

Gastric cancer (GC) is one of the most common malignant tumors in the world and has attracted much attention due to its high incidence and mortality. Early detection and accurate diagnosis of GC is very important to improve the survival rate of patients. Traditional imaging techniques, such as computed tomography (CT), have played an important role in the diagnosis and staging of GC, but their accuracy and predictive power are still limited. Radiomics, as an emerging multidisciplinary field, combines medical imaging, computer technology, and bioinformatics to reveal potential biological information in image data through quantitative extraction of image features. To review the current status and future potential of radiomics in the diagnosis, prognosis, and outcome prediction for patients with GC, related studies with keywords such as "radiomics," "gastric cancer," and "predict" were retrieved from PubMed (until October 2022). The clinical value of radiomics in GC research, which encompasses diagnosis, clinical staging, and prognostic prediction, was analyzed and summarized. A total of 52 original articles in radiomics were selected for the prediction of diagnostic classification ($n = 9$), tumor-node-metastasis stages ($n = 19$), prognosis and response prediction to treatment ($n = 20$), and the use of deep learning algorithm ($n = 4$). Among these, 39 (75%) were single-center studies and 13 (25%) were multicenter studies, with sample sizes ranging from 47 to 1,778. In terms of imaging modalities, 44 studies utilized CT-based radiomics, six used positron emission tomography-CT, and a few employed magnetic resonance imaging. With the continuous improvement and development in radiomics, it has great potential in the diagnosis, post-treatment follow-up, and treatment decision for patients with GC.

Keywords: Gastric cancer; Radiomics; Assessment; Predict; Prognosis

1. Introduction

Gastric cancer (GC) is the fifth most common cancer worldwide and the third leading cause of cancer-related deaths, with more than 1,000,000 new cases and nearly 800,000 deaths

---

[†]*These authors contributed equally to this work.*

***Corresponding authors:**
Congying Xie
(wzxiecongying@163.com)
Xiance Jin
(jinxc1979@hotmail.com)

Citation: Zheng Q, Zheng H, Liu Z, *et al*. Current status and future potential of radiomics in the management of patients with gastric cancer. *Adv Radiother Nucl Med.* 2025;3(2):24-38.
doi: 10.36922/arnm.8350

Received: December 31, 2024

Revised: March 4, 2025

Accepted: March 19, 2025

each year.[1,2] Gastrectomy with adequate lymphadenectomy is still the main treatment for GC.[3] However, even with radical resection, the overall survival (OS) and disease-free survival (DFS) remain unsatisfactory, with half of GC patients relapsing after surgery.[4,5] In locally advanced cases, the 5-year survival rate is <30%.[6] Therefore, early detection using biomarkers plays a key role in the optimal management of GC.

As early as 1994, the World Health Organization classified *Helicobacter pylori* as a Class I carcinogen, which is closely related to the dysplasia of cancer.[7] In addition, biomarkers such as a carcinoembryonic antigen, carbohydrate antigen (CA) 19-9, CA72-4, CA12-5, and alpha-fetoprotein were investigated intensively in the early diagnosis and staging of gastric tumors in the clinic. However, most of the identified biomarkers failed in the validation studies, and the accuracy of a single biomarker remains to be verified.[8,9] The American Joint Committee on Cancer (8th Edition) suggested that the classification of the tumor-node-metastasis (TNM) stage for GC is based on computed tomography (CT) and endoscopic ultrasound, while the evaluation of metastasis is based on the magnetic resonance imaging (MRI) and positron emission tomography-CT (PET-CT).[10] Despite the application of various imaging techniques, the diagnostic accuracy based on captured image features and visible abnormalities identified through manual interpretation remains limited.[11] Therefore, more effective early diagnosis and prognosis evaluation methods are urgently needed.

In the last decade, along with the development of artificial intelligence, radiomics has been investigated intensively for the diagnosis and prognostic prediction of various cancers.[12] By extracting a great number of two-dimensional and high-dimensional features from images of ultrasound, CT, and MRI using data-characterization algorithms, radiomics is able to analyze tumor heterogeneity and other characteristics non-invasively.[13,14] Radiomic features have been investigated alone or in combination with other parameters such as pathological, physiological, and genomic data for the classification, diagnosis, clinical staging, pathological evaluation, and therapeutic response of patients with GC.[15-17] The purpose of this study is to systematically review the current evidence, clinical value, and future potential of radiomics in the diagnosis, clinical staging, and prognostic prediction for patients with GC.

2. Methodology

2.1. Data sources

PubMed was used to conduct a search for articles related to radiomics for GC using keywords such as "radiomics," "machine learning," "gastric cancer," "gastric carcinoma," "predict," and "prognosis." The articles were selected according to the following recorded information of each qualified article: title, publication year, sample size, sample condition, research purpose, imaging modality, research results, and more. This selection process was carried out by two reviewers (ZH and ZQ), and the selected articles underwent a second screening by a third reviewer (JX).

A total of 52 papers were selected from PubMed (until October 2022), as shown in Figure 1. The papers were divided into four categories according to the research direction: diagnostic classification of GC ($n = 9$), prediction of TNM stages ($n = 19$), prognosis and response prediction to treatment ($n = 20$), and studies with deep learning

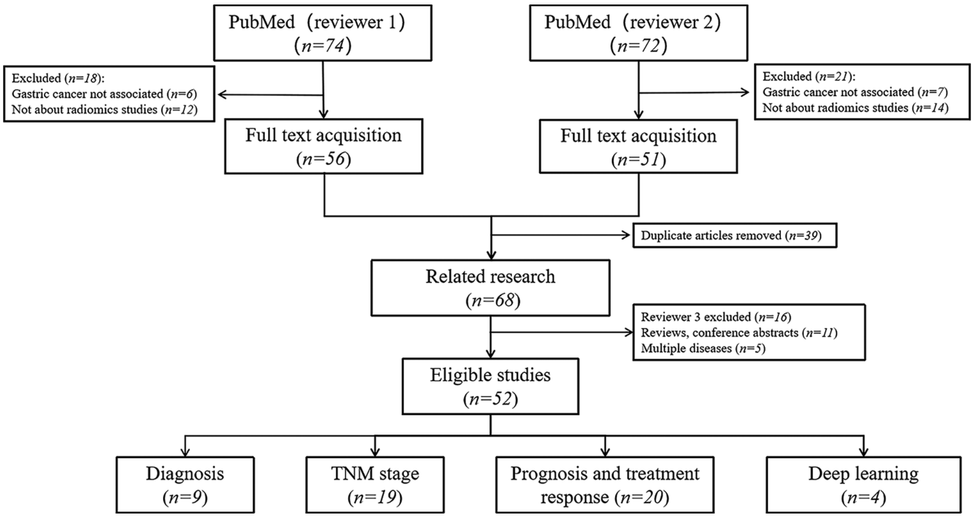

Figure 1. Flow chart of data selection
Abbreviation: TNM: Tumor-node-metastasis.

algorithm (n = 4). These retrospective studies consist of 39 (75%) single-center studies and 13 (25%) multicenter studies with sample sizes ranging from 47 to 1,778. There were 44 studies of CT radiomics, six studies of PET-CT, and a few studies of MRI.

3. Research directions of radiomics

3.1. Radiomic workflow

In radiomics, the initial steps involve acquiring high-quality medical images from modalities such as ultrasound, CT, or MRI by following standardized protocols for consistency. After obtaining the images, the region of interest is identified and delineated manually or using segmentation algorithms. Once defined, quantitative features such as mean, variance, volume, surface area, and texture, such as gray-level co-occurrence matrix (GLCM) and gray-level run-length matrix are extracted using tools like PyRadiomics. Feature selection methods, such as least absolute shrinkage, selection operator, and principal component analysis, are applied to reduce dimensionality and retain the most relevant features. Finally, predictive models are developed using machine learning algorithms such as support vector machines or random forests, and the performance is evaluated using metrics such as accuracy and sensitivity.

3.2. Diagnosis of GC

The diagnosis and identification of GC are the first step in treatment decision-making. Histological diagnosis with endoscopic biopsy is usually applied and considered the gold standard for GC in the pre-operative diagnosis stage as it is hard to differentiate GC from other gastric tumors in the imaging, such as gastric stromal tumors and lymphoma.[18,19] However, radiomics based on CT and MRI images provide a non-invasive method for the differentiation of GC, as shown in Table 1. Ma *et al.*[20] evaluated the value of portal venous CT-based radiomic signature in differentiating

Table 1. Summary of studies on radiomics to identify gastric cancer

Authors	Year	Image	Purpose	Sample	Features	Results
Ma *et al.*[20]	2017	CT	Differentiation of Borrmann type IV GC from primary gastric lymphoma	40 (Single center)	Radiomics + clinical	The combined model showed a diagnostic accuracy of 87.14% (AUC=0.903)
Sun *et al.*[21]	2020	PET-CT	Distinguish between GC and gastric lymphoma	79 (Single center)	Radiomics	The model had an AUC of 0.770 in distinguishing between the gastric low-grade lymphoma and GC
Sun *et al.*[22]	2019	CT	Distinguish between GC and gastric stromal tumor	100 (Single center)	Radiomics + clinical	The combined model yielded the highest AUC value (0.903), specificity (93.33%), and accuracy (86.00%) among the three models
Wang *et al.*[23]	2021	CT	Differentiating gastric neuroendocrine carcinoma from gastric ADC	63 (Single center)	Radiomics + clinical	The nomogram incorporated with the radiomic signature, tumor margin, and LNM showed an AUC of 0.821 in the primary cohort and 0.809 in the validation cohort
Zhang *et al.*[26]	2017	MRI	Predicting histological grade of GC	78 (Single center)	Radiomics	The AUC value of the maximum frequency parameter in distinguishing the differentiation degree of GC was the largest, which was 0.675
Li *et al.*[27]	2019	CT	To predict the adverse histopathological status of GC	554 (Single center)	Radiomics + clinical	The developed calculation method showed good performance in predicting GC AHS and clinical disease
Wang *et al.*[30]	2020	CT	Lauren diffuse type and intestinal type of GC were distinguished before surgery	539 (Single center)	Radiomics + clinical	The radiomic nomogram incorporating the combined radiomic signature, age, T stage, and N stage outperformed the other models with a training AUC of 0.745 and a validation AUC of 0.758
Wang *et al.*[31]	2020	CT	To investigate the role of CT radiomics for the pre-operative distinction of intestinal-type gastric ADCs	187 (Single center)	Radiomics	The nomogram yielded excellent performance for distinguishing intestinal-type ADCs in training and test sets, with AUCs of 0.928 and 0.904, respectively
Chen *et al.*[32]	2022	CT	To distinguish between diffuse type and signet ring cell carcinoma GC before surgery	693 (Multi-center)	Radiomics + clinical	The radiomic nomogram showed good discrimination, with AUC of 0.905, 0.845, and 0.918 in the training, internal, and external validation cohorts, respectively

Abbreviations: ADC: Adenocarcinoma; AHS: Adverse histopathological status; AUC: Area under the curve; CT: Computed tomography; GC: Gastric cancer; MRI: Magnetic resonance imaging; PET-CT: Positron emission tomography-computed tomography.

Borrmann type IV GC (40 cases) from primary gastric lymphoma (30 cases) with 485 radiomic features, achieving a diagnosis accuracy of 81.43%, 84.29%, and 87.14% for the subjective findings model, radiomic signature, and combined model (radiomic signature, subjective CT findings, age, and gender), respectively. Sun *et al.*[21] assessed the texture analysis of PET in the differentiation of GC (45 cases) and gastric lymphoma (34 cases). The result demonstrated that inertia GLCM and entropy GLCM were the most discriminating features with an area under the curve (AUC) of 0.714 and 0.770, respectively, for differentiating gastric lymphoma from GC and low-grade gastric lymphoma from GC. Sun *et al.*[22] investigated the contrast-enhanced CT (CECT)-based radiomics in differentiating GC (60 cases) from gastric stromal tumors (40 cases), and the result indicated that the model integrating subjective CT signs and radiomic signature achieved the highest AUC (0.903), specificity (93.33%), and accuracy (86.00%). In a study conducted by Wang *et al.*,[23] a CT-based radiomic nomogram was developed to differentiate gastric neuroendocrine carcinomas (63 cases) from gastric adenocarcinomas (ADCs) (63 cases). The nomogram achieved an AUC of 0.821 (95% confidence interval [CI] = 0.725 – 0.895) in the primary cohort and 0.809 (95% CI = 0.649 – 0.918) in the validation cohort by integrating the radiomic signature, tumor margin, and lymph node metastasis (LNM) into the model.

The histological grade of GCs plays an important role in selecting the treatment methods and predicting the prognosis.[24,25] Zhang *et al.* and Li *et al.*[26,27] applied apparent diffusion coefficient maps of MRI and CECT images to predict the histopathological grades of 87 patients and 554 patients with GCs, respectively. Both studies demonstrated good performance in successfully differentiating between the histological grades of GC. The Lauren classification is one of the mainstream histological classification methods for GC, which plays a very important role in treatment decision-making and prognosis evaluation.[28,29] Wang *et al.*[30] developed a nomogram based on CT radiomics to differentiate the Lauren diffuse type from the intestinal type preoperatively in 539 GC patients and achieved a validation AUC of 0.758. A study by Wang *et al.*[31] demonstrated that multiphase CT radiomic-based nomogram was promising for a pre-operative distinction of intestinal-type gastric ADCs. In a multicenter study with 693 GC patients, Chen *et al.*[32] discovered that a CT radiomic-based nomogram was able to distinguish the diffuse type and signet ring cell carcinoma preoperatively.

3.3. Prediction of TNM stage

The TNM stage classification is the global standard to classify the stage of solid tumors, which is important in aiding treatment decision-making, providing an indication of prognosis, and assisting the evaluation of treatment outcomes.[33] Clinically, accurate TNM staging before surgery is difficult and usually performed using invasive methods.[34] The emergence of radiomics provided a non-invasive way for TNM classification preoperatively for patients with GC, as shown in Table 2.

Chen *et al.*[35] developed a diffusion-weighted imaging-based radiomic nomogram for LNM prediction in 146 advanced GC patients and achieved an AUC of 0.850, 0.857, and 0.878 in the training, internal validation, and external validation, respectively. CT-based radiomic studies were mainly focused on the pre-operative prediction of LNM.[36-46] Wang *et al.*[38] investigated the value of CT-based radiomics in the differentiation between T2 and T3/4 stage lesions of 244 patients with GC and achieved an AUC of 0.843 (95% CI = 0.746 – 0.914) and 0.818 (95% CI = 0.711 – 0.899) in the training and test cohort, respectively. Yardımcı *et al.*[42] evaluated the feasibility and accuracy of CT texture analysis in the differentiation between T stages (T1 and T2 vs. T3 and T4), N stages (N+ vs. N−), and grades (low-intermediate vs. high) in 114 GC patients, achieving discriminatory capacities of 90.4%, 81.6% and 64.5% for T stage, N stage, and tumor grade, respectively. PET-CT-based radiomics was also reported for the prediction of N2-3b metastasis, LNM, and N stage with promising accuracy.[47,48]

Lymphatic vascular invasion (LVI) and perineural invasion (PNI) are two important prognostic factors for the treatment outcome of patients with GC.[49] Chen *et al.*[50] applied CECT-based radiomics to predict LVI and clinical outcome preoperatively in 160 GC patients and demonstrated that radiomic features may serve as potential markers for the prediction of LVI and progression-free survival for GC patients. Yardımcı *et al.*[51] indicated that CT texture analysis has the potential to predict LVI and PNI in tubular gastric ADC using machine learning. Zheng *et al.*[52] demonstrated that CECT-based radiomics is feasible for the non-invasive pre-operative prediction of PNI in GC. PET-CT-based radiomics was investigated in two studies for LVI prediction, with 101 and 148 enrolled GC cases, achieving the highest AUC of 0.944 and 0.914, respectively, in the validation cohorts for the combined models.[53,54]

3.4. Prediction of tumor prognosis and treatment response

Although the TNM staging system is clinically the main prognostic prediction for patients with GC, it is inadequate for prognosis determination due to the inherent heterogeneity of GC.[55] Biomarkers from advanced molecular biology are promising in prognostic

Table 2. Summary of studies on radiomics for distinguishing tumor-node-metastasis stage in gastric cancer

Authors	Year	Image	Purpose	Sample	Features	Result
Chen *et al.*[35]	2019	MRI	Prediction of LNM in patients with advanced GC	146 (Multi-center)	Radiomics+clinical	The specificity, sensitivity, and accuracy were 0.846, 0.853, and 0.851, respectively, in the internal validation cohort, and 0.714, 0.952, and 0.893, respectively, in the external validation cohort
Jiang *et al.*[36]	2019	CT	Radiomic feature-based CT to predict LNM in GC	1,689 (Multi-center)	Radiomics+clinical	The radiomic models exhibited good discriminability for LN staging in the training, internal, and external validation cohorts
Feng *et al.*[37]	2019	CT	Prediction of LNM in patients with GC based on CT radiomics	490 (Single center)	Radiomics+clinical	In the training data, the predicted AUC of LN+was 0.824 and the predicted AUC of the test data was 0.764
Wang *et al.*[38]	2020	CT	To investigate the value of CT-based radiomics in differentiating stage T2 and stage T3/4 GC	244 (Single center)	Radiomics	Arterial phase-based radiomic model exhibited an AUC of 0.899 in the training cohort and 0.825 in the test cohort
Gao *et al.*[39]	2020	CT	Prediction of LNM in early GC	463 (Single center)	Radiomics+clinical	A radiomic model that incorporated radiomic signature and CT-reported LN status exhibited a good discrimination in the training cohort (AUC=0.91) and testing cohort (AUC=0.89)
Gao *et al.*[40]	2020	CT	Prediction of LNM in GC	768 (Multi-center)	Radiomics+clinical	A radiomic model that incorporated radiomic signature, serum CA72-4, and CT-reported LN status exhibited a good discrimination in the training cohort (AUC=0.92) and validation cohort (AUC=0.86)
Wang *et al.*[41]	2020	CT	Prediction of LNM in GC	274 (Single center)	Radiomics+clinical	The nomogram consisted of radiomic scores and the CT-reported LN status exhibited excellent discrimination in the training and test cohorts with AUCs of 0.886 and 0.881, respectively
Yardımcı *et al.*[42]	2020	CT	To predict the clinical T and N stages and tumor grade of patients with GC before pre-operative NAC	114 (Single center)	Radiomics	Based on the texture features, the differential ability of T stage, N stage, and tumor grade was 90.4%, 81.6%, and 64.5%, respectively
Yang *et al.*[43]	2020	CT	Prediction of LNM in GC	170 (Single center)	Radiomics	The radiomic-clinicopathologic model (training cohort=0.9432±0.0129, validation cohort=0.8764±0.0322) showed a good discrimination capability
Wang *et al.*[44]	2021	CT	Identification of no. 10 LNs status in advanced proximal GC	515 (Single center)	Radiomics+clinical	CT-based radiomic nomogram yielded classification accuracy, with AUCs of 0.896 and 0.814 in the training and validation cohort, respectively.
Sun *et al.*[45]	2021	CT	Prediction of LNM status based on pre-operative CT images	1,618 (Multi-center)	Radiomics+clinical	The radiomic nomograms revealed good prediction performances, with AUCs of 0.716 – 0.871 in the training cohort and 0.678 – 0.768 in the external validation cohort

(Cont'd...)

Table 2. ***(Continued)***

Authors	Year	Image	Purpose	Sample	Features	Result
Wang *et al.*[46]	2021	CT	Prediction of pre-operative LNM in patients with T1–2 GC	159 (Single center)	Radiomics+clinical	A nomogram showed a good discrimination of LNM in both the training cohort (AUC=0.915) and testing cohort (AUC=0.908)
Liu *et al.*[47]	2021	PET-CT	To investigate the pre-operative 18F-FDG PET/CT radiomic features to predict LNMs and the N stage.	185 (Single center)	Radiomics	One CT feature and one PET feature were selected to predict LNMs and achieved the best performance (AUC=82.2%, accuracy=85.2%)
Xue *et al.*[48]	2022	PET-CT	To investigate pre-operative 18F-FDG PET radiomic features to predict N2–3b LNM.	127 (Single center)	Radiomics+clinical	The prediction model exhibited a good calibration and discrimination ability (AUC=0.81)
Chen *et al.*[50]	2020	CT	To predict LVI and clinical outcome in patients with GC before surgery	160 (Single center)	Radiomics+clinical	The Clinical-Rad score model that used all factors showed a good performance (AUC=0.856) in the training cohort
Yardımcı *et al.*[51]	2020	CT	Prediction of LVI and PNI in patients with tubular gastric ADC	68 (Single center)	Radiomics	The mean AUC and accuracy ranges for predicting LVI were 0.777 – 0.894 and 76 – 81.5%, respectively. For predicting PNI, the mean AUC and accuracy ranges were 0.482 – 0.754 and 54 – 68.2%, respectively
Zheng *et al.*[52]	2022	CT	Prediction of PNI	154 (Single center)	Radiomics+clinical	Support vector machine achieved the best AUC of 0.82 in the test cohorts with a sensitivity, specificity, and accuracy of 0.63, 0.91, and 0.77, respectively
Fan *et al.*[53]	2022	PET-CT	To predict LVI status of GC	101 (Single center)	Radiomics+clinical	The combined models showed improved performance than the image models and the clinical models, with the AUC values of AdaBoost and logistic regression classifier yielding 0.944 and 0.921, respectively
Yang *et al.*[54]	2022	PET-CT	Pre-operative prediction of the LVI status of GC	148 (Single center)	Radiomics+clinical	The ROC analysis demonstrated clinical usefulness of PET/CT-RS plus clinical data (AUCs of 0.936 and 0.914 for the training and validation cohort, respectively)

Abbreviations: ADC: Adenocarcinoma; AUC: Area under the curve; CA72-4: Carbohydrate antigen 72-4; CT: Computed tomography; FGD: Fluorodeoxyglucose; GC: Gastric cancer; LN: Lymph node; LNM: Lymph node metastasis; LVI: Lymphatic vascular invasion; MRI: Magnetic resonance imaging; NAC: Neoadjuvant chemotherapy; PET-CT: Positron emission tomography-computed tomography; PNI: Perineural invasion; ROC: Receiver operating characteristic; RS: Radiomic signature.

analysis, but they are not yet available for routine clinical application.[56] With the advancements in medical imaging, radiomic features have shown their potential as prognostic biomarkers to aid in advanced clinical decision-making.[57]

CT is the primary imaging modality applied in these radiomic studies for prognostic prediction in patients with GC, as shown in Table 3. Four studies investigated the risk stratification power of CT-based radiomic features and demonstrated their potential as prognostic biomarkers for patients with GC.[58-61] Five studies demonstrated the feasibility of pre-treatment CT-based radiomic models in the prediction of the pathological response of patients with advanced GC to pre-operative neoadjuvant chemotherapy (NAC) and their potential to assist in surgical decision-making.[62-66] Chen *et al.*[67] predicted the DFS and OS directly for advanced GC patients based on CT radiomics after NAC and achieved C-indices of 0.810 and 0.710 for DFS and OS for the combined model, respectively. Shin *et al.*[68] presented an AUC of 0.714 for a pre-operative CT-based radiomic model in the prediction of recurrence-free

Table 3. Summary of studies on radiomics for predicting tumor prognosis and treatment response

Authors	Year	Image	Purpose	Sample	Features	Result
Giganti *et al.*[58]	2017	CT	To explore the relationship between pre-operative CT texture analysis and OS in patients with GC	56 (Single center)	Radiomics	A number of parameters were significantly associated with the negative outcomes depending on the threshold
Wang *et al.*[59]	2020	CT	To evaluate the splenic tissue characteristics to predict the prognosis of patients with GC	243 (Single center)	Radiomics+clinical	Splenic features extracted from imaging technology can accurately predict the long-term survival of patients with GC
Wang *et al.*[60]	2020	CT	To establish a prognosis model guided by multi-detector CT	353 (Multi-center)	Radiomics+clinical	The radiomic nomogram incorporated with radiomic signature, extramural vessel invasion, clinical T stage, and clinical N stage outperformed all the other models (concordance index=0.720 and 0.727)
Li *et al.*[61]	2019	CT	To investigate the prognostic significance of radiomic features in patients with GC after radical resection	181 (Single center)	Radiomics+clinical	The Harrell concordance index of a nomogram combining radiomic signature and significant clinicopathological risk factors was 0.82
Li *et al.*[62]	2018	CT	To predict the pathological reaction of pre-operative chemotherapy for locally advanced GC	47 (Single center)	Radiomics	The feature selection method adopted by a filter based on linear discriminant analysis+classifier of random forest achieved a significantly prognostic performance in the PP (AUC=0.722±0.108, accuracy=0.793, sensitivity=0.636, and specificity=0.889)
Sun *et al.*[63]	2020	CT	To predict the therapeutic response to NAC and to investigate its efficacy in survival stratification	106 (Single center)	Radiomics+clinical	In the validation cohort, the rad-score demonstrated a good predicting performance in treatment response to the NAC (AUC=0.82)
Mazzei *et al.*[64]	2021	CT	To predict the response to NAC of GC	70 (Single center)	Radiomics	The AUC of all patients by logistic regression was 0.763
Xu *et al.*[65]	2021	CT	To predict and early detect the pathological downstaging with NAC in advanced GC	292 (Single center)	Radiomics	The improved DR model with averaging outcome scores of PR and DR models showed boosted results in two testing cohorts (AUC=0.961 and AUC=0.921, respectively)
Chen *et al.*[66]	2021	CT	To predict the main pathological reactions of advanced GC to NAC	221 (Single center)	Radiomics+clinical	The final established model incorporates ADC differentiation and rad-scores. The model showed satisfactory predictive accuracy with a C-index of 0.763
Chen *et al.*[67]	2021	CT	To predict the DFS and OS of patients with advanced GC after NAC	159 (Single center)	Radiomics+clinical	The combined Rad-clinical models showed improved performance in the testing cohort, with C-indices of 0.810 and 0.710 for DFS and OS, respectively
Shin *et al.*[68]	2021	CT	To predict the recurrence-free survival of locally advanced GC	410 (Single center)	Radiomics+clinical	In internal and external validation, the AUC of the combined model was 0.719 and 0.651, respectively
Klaassen *et al.*[70]	2018	CT	To predict the chemotherapy response of patients with esophageal GC to single hepatic metastases	69 (Single center)	Radiomics	The random forest model for CT scan lesions had an average training AUC of 0.87 and 0.79 for the validation set

(Cont'd...)

Table 3. *(Continued)*

Authors	Year	Image	Purpose	Sample	Features	Result
Li *et al.*[71]	2020	CT	Prediction of DFS and chemotherapy response in stage II/III GC	208 (Single center)	Radiomics+clinical	The C-index of the nomogram was significantly higher than that of TNM stage (0.768 vs. 0.639) in the validation cohort
Wang *et al.*[72]	2020	CT	To predict the HER2 expression before radical gastrectomy in patients with gastric ADC	460 (Single center)	Radiomics+clinical	The maximum diameter of tumor, differentiation degree, CT attenuate value in non-contrast, arterial, and portal phases, and corrected CT attenuate value in the arterial phase were the predictive factors of HER2 expression status
Wang *et al.*[73]	2020	CT	Prediction of HER2 status in patients with GC	132 (Single center)	Radiomics	The AP radiomic model had an AUC of 0.830 for HER2-negative cases in the test cohort
Binnewies *et al.*[74]	2018	CT	Prediction of GC survival and benefit of chemotherapy	1,591 (Multi-center)	Radiomics+clinical	Incorporating the radiomic signature into the radiomic-based nomograms resulted in better performance for the estimation of DFS and OS than the clinicopathological nomograms and TNM staging system
Jiang *et al.*[75]	2020	CT	To develop a non-invasive radiomic-based predictor of ImmunoScore for GC	1,778 (Multi-center)	Radiomics+clinical	The radiomic signature is a reliable tool for the evaluation of immunoscore and retains the prognostic significance in GC
Lin *et al.*[76]	2022	CT	Evaluation of the non-invasive immunosuppression scoring system and treatment outcomes based on radiological characteristics	642 (Multi-center)	Radiomics	Three independent cohorts showed good differentiation of immunosuppressive states (AUC=0.840, 0.809, and 0.843, respectively)
Gao *et al.*[77]	2020	CT	To develop and validate a radiomic signature for evaluation of tumor infiltrating regulatory T cells and outcome prediction of GC patients	165 (Multi-center)	Radiomics	The radiomic signature showed good ability for estimating tumor infiltrating regulatory T cells in the training, validation, and testing cohort, with AUC of 0.884, 0.869, and 0.847, respectively
Li *et al.*[78]	2022	PET-CT	To assess the tumor immune microenvironment and predict survival and chemotherapy benefits in patients with GC based on imaging omics	230 (Single center)	Radiomics	The radiomic tumor immune microenvironment score signature was significantly associated with DFS and OS both in the training and validation cohort ($p<0.001$)

Abbreviations: ADC: Adenocarcinoma; AP: Arterial phase; AUC: Area under the curve; CT: Computed tomography; DFS: Disease-free survival; DR: Detection radiomics; GC: Gastric cancer; HER2: Human epidermal growth factor 2; NAC: Neoadjuvant chemotherapy; OS: Overall survival; PET-CT: Positron emission tomography-computed tomography; PR: Prediction radiomics; TNM: Tumor-node-metastasis.

survival for locally advanced GC patients who underwent curative resection without neoadjuvant therapy.

Radiotherapy and chemotherapy are common cancer treatment methods, which can inhibit the proliferation of cancer cells, effectively control the development of tumors, and reduce the probability of other complications.[69] Although there are few studies on radiotherapy response, we found four studies that predicted the chemotherapy response, as shown in Table 3.[17,70-73] In a multicenter retrospective study conducted by Jiang *et al.*[17] using portal venous phase-enhanced CT of 1,591 patients, 19 stable radiomic features were extracted and selected to construct radiomic signature, which effectively improved the accuracy of survival classification in the form of nomogram (C-index: DFS = 0.850; OS = 0.860). In studies conducted by Wang *et al.* and Wang *et al.*,[72,73] they used human epidermal growth factor 2, a cell-derived oncogene, as a bridge to predict the gene expression levels of patients through radiomics, thus forecasting the prognosis of the disease and therapeutic effect on cancer.

Studies demonstrated that the progression, metastasis, and therapeutic response of cancer are determined by the tumor immune microenvironment.[74] On the other hand, quantitative radiomic features extracted from images are closely associated with molecular phenotypes.[13] Two studies applied non-invasive CT-based radiomics to evaluate the tumor immune and immunosuppressive microenvironment to predict the treatment responses and outcomes for GC patients.[75,76] Similarly, Gao *et al.*[77] evaluated the abundance of tumor-infiltrating regulatory T cells using CT radiomics to predict the outcome of GC. One study measured the tumor immune microenvironment based on PET-CT radiomics to predict the clinical outcomes and chemotherapy response for patients with GC.[78]

3.5. Deep learning radiomics

Machine and deep learning algorithms can mine vast amounts of available image data to reveal underlying complex biological mechanisms and enable personalized and precise cancer diagnosis and treatment plans.[79] Some studies have found that there are similarities and compatibility between radiomics and deep learning, and the combined application of these two methods further improves the prediction accuracy of GC,[16,80-82] as shown in Table 4.

To predict the survival risk of patients with GC, Zhang *et al.*[80] developed three models based on radiomics, clinical parameters, and deep learning, respectively, and they achieved good risk assessment results. Dong *et al.*[82] recruited 730 locally advanced GC patients from six centers and established a deep learning radiomic nomogram based on multi-phase CT to determine the number of LNM in locally advanced GC patients before surgery. It was found that the results are significantly better than those in the single algorithm models (C-index: 0.821 vs. 0.785).[82] Zhang *et al.*[16] developed a nomogram combining radiomic features, clinical parameters, and deep learning to predict early recurrence in 669 multicenter advanced GC patients. The model achieved an AUC of 0.831, 0.826, and 0.806, respectively, in the training set and the two test sets, with the predicted risk showing good agreement with the observed probability of recurrence.

4. Discussion and prospect

From the collected studies, radiomics has shown great potential in the diagnosis, clinical staging, and prognostic prediction for patients with GC. In the differential diagnosis of GC, the evaluation effect of various radiomic models was relatively stable (AUC = 0.770 – 0.903).[20-23] However, in histopathological classification prediction, a significant difference between the earlier model and the most recent model (AUC: 0.675 vs. 0.918) was observed due to the addition of clinical features to the radiomic features.[26-32] Pre-operative prediction of LNM is one of the most popular research directions. The prediction accuracy of the radiomic models obtained in most studies was more

Table 4. Summary of studies on radiomics combined with deep learning in gastric cancer

Authors	Year	Image	Purpose	Sample	Features	Result
Zhang *et al.*[16]	2019	CT	To predict the early recovery before surgery in patients with advanced GC	669 (Multi-center)	Radiomics+clinical+deep learning	The nomogram, combining all these predictors, showed powerful prognostic ability in the training set and two test sets with AUCs of 0.831 and 0.806, respectively
Zhang *et al.*[80]	2021	CT	To predict the risk of OS	640 (Multi-center)	Radiomics+clinical+deep learning	Deep learning model had the best performance for risk prediction of OS according to the C-index (training=0.82, external validation=0.78)
Tan *et al.*[81]	2021	CT	To design a semi-automatic segmentation method based on deep learning	86 (Single center)	Radiomics+deep learning	The predictive ability of the semi-automatic segmentation was better than the manual segmentation (AUC of 0.828 and 0.749, respectively)
Dong *et al.*[82]	2020	CT	Pre-operative LNM rate can be accurately assessed	730 (Multi-center)	Radiomics+clinical+deep learning	The model showed good discrimination of the number of LNM in all cohorts (C-indexes=0.821 in the primary cohort, 0.797 in the external validation cohorts, and 0.822 in the international validation cohort)

Abbreviations: AUC: Area under the curve; CT: Computed tomography; GC: Gastric cancer; LNM: Lymph node metastasis; OS: Overall survival.

than 80%, with the best AUC of 0.908 in the validation set.[36-48] Since PNI and LVI have been identified as important prognostic factors, the AUCs of their predictive models have improved significantly in recent years (LVI = 0.777 – 0.921, PNI = 0.482 – 0.820).[50-54]

The prediction of prognosis is of great significance for patients' risk management and treatment.[83] Studies have confirmed the value of surgery, chemotherapy, and other therapeutic methods in the management of GC.[84] In addition, the feasibility of radiomics for predicting survival or recurrence has been confirmed and verified, with C-index values ranging from 0.710 to 0.820.[58-73] However, radiotherapy is also one of the main methods for the treatment of malignant tumors, and there are relatively few radiomic studies on GC patients who have undergone radiotherapy.[85] Therefore, predicting the efficacy of radiotherapy or chemoradiotherapy in advance using radiomics holds great clinical significance for GC patients.

Radiomics has shown great potential in predicting personalized NAC responses in patients with advanced GC. Radiomic models have demonstrated a stable performance in predicting NAC response, with accuracies ranging from 0.722 to 0.763.[62,64] The integration of machine learning further improved the prediction accuracy, as demonstrated in a study by Xu *et al.*,[65] where the AUC increased from 0.750 to 0.889 across validation cohorts. The combination of radiomic and clinical features also enhanced survival prediction, with Chen *et al.*[67]'s model achieving C-indices of 0.810 for DFS and 0.710 for OS.

CT is the main detection method for GC; thus, most radiomic studies are based on CT images. Although PET-CT can analyze the functional and metabolic information of the lesion qualitatively and quantitatively with clear anatomy, the number of cases available for radiomic studies is limited.[86] Similarly, due to the limited number of cases detected by MRI, there have been few radiomic studies on GC using MRI in recent years. Therefore, radiomic studies based on PET-CT and MRI for GC patients are of great potential. Another future direction may focus on endoscopic ultrasound, which has advantages in the diagnosis of submucosal tumors and prediction of the depth of tumor invasion.[87]

Radiomic studies in GC have several key limitations. First, there is a lack of standardization in the delineation of regions of interest, with most studies relying on manual or semi-automatic segmentation methods, which are time-consuming and prone to subjective bias. The irregular shape of gastric tumors further complicates accurate boundary detection, affecting model performance. Second, imaging acquisition protocols, reconstruction algorithms, and preprocessing methods vary across institutions, leading to inconsistencies in feature extraction and model reproducibility. One limitation of these studies is that they were conducted at a single center with a single image modality, which limits the stability and practicability of the constructed models.[88] In future studies, the sharing of multicenter data should be conducted to improve the effectiveness and practicability of the radiomic models. Another direction is using multi-modal hybrid images for radiomic studies, which inherit the advantages of each single image and contain more types of information to be developed.[89] In addition, while deep learning has shown its potential in automating image segmentation, its integration with radiomics is still in its early stages, and challenges such as model interpretability and data requirements remain unanswered. Finally, the clinical translation of radiomics is hindered by issues such as data standardization, regulatory approval, and the need for multicenter validation. Integrating nomogram and radiomic features with physiological information, pathological indicators, and gene expression may show promising ability to increase the accuracy and stability of the prediction models in future studies.

5. Conclusion

Radiomics can deeply mine medical images to reveal tumor heterogeneity, quantify tumor information, reflect potential molecular biological changes, and improve individualized treatment choices. With the continuous improvement and development of radiomics, it has great potential in the diagnosis, post-treatment follow-up, and treatment decision-making for patients with GC.

Acknowledgments

None.

Funding

This study is financially supported by the Joint Laboratory of Basic Medicine and Intelligent Medicine.

Conflict of interest

Congying Xie is an Editorial Board Member of this journal but was not in any way involved in the editorial and peer-review process conducted for this paper, directly or indirectly. Separately, other authors declared that they have no known competing financial interests or personal relationships that could have influenced the work reported in this paper.

Author contributions

Conceptualization: Xiance Jin
Investigation: Qiao Zheng, Haoze Zheng

Methodology: Ziyang Liu, Wenhao Guo, Sunjun Li, Junhao Ma, Yuxin Lou, Lijing Liu
Formal analysis: Congying Xie
Writing – original draft: Qiao Zheng, Haoze Zheng
Writing – review & editing: Xiance Jin

Ethics approval and consent to participate

Not applicable.

Consent for publication

Not applicable.

Availability of data

Not applicable.

References

1. Bray F, Ferlay J, Soerjomataram I, Siegel RL, Torre LA, Jemal A. Global cancer statistics 2018: GLOBOCAN estimates of incidence and mortality worldwide for 36 cancers in 185 countries. *CA Cancer J Clin*. 2018;68(6):394-424.

   doi: 10.3322/caac.21492

2. Sung H, Ferlay J, Siegel RL, *et al*. Global cancer statistics 2020: GLOBOCAN estimates of incidence and mortality worldwide for 36 cancers in 185 countries. *CA Cancer J Clin*. 2021;71(3):209-249.

   doi: 10.3322/caac.21660

3. Noh SH, Park SR, Yang HK, *et al*. Adjuvant capecitabine plus oxaliplatin for gastric cancer after D2 gastrectomy (CLASSIC): 5-year follow-up of an open-label, randomised phase 3 trial. *Lancet Oncol*. 2014;15(12):1389-1396.

   doi: 10.1016/S1470-2045(14)70473-5

4. Spolverato G, Ejaz A, Kim Y, *et al*. Rates and patterns of recurrence after curative intent resection for gastric cancer: A United States multi-institutional analysis. *J Am Coll Surg*. 2014;219(4):664-675.

   doi: 10.1016/j.jamcollsurg.2014.03.062

5. Deng J, Liang H, Wang D, Sun D, Pan Y, Liu Y. Investigation of the recurrence patterns of gastric cancer following a curative resection. *Surg Today*. 2011;41(2):210-215.

   doi: 10.1007/s00595-009-4251-y

6. Takahashi T, Saikawa Y, Kitagawa Y. Gastric cancer: Current status of diagnosis and treatment. *Cancers* (*Basel*). 2013;5(1):48-63.

   doi: 10.3390/cancers5010048

7. Pasechnikov V, Chukov S, Fedorov E, Kikuste I, Leja M. Gastric cancer: Prevention, screening and early diagnosis. *World J Gastroenterol*. 2014;20(38):13842-13862.

   doi: 10.3748/wjg.v20.i38.13842

8. Matsuoka T, Yashiro M. Biomarkers of gastric cancer: Current topics and future perspective. *World J Gastroenterol*. 2018;24(26):2818-2832.

   doi: 10.3748/wjg.v24.i26.2818

9. Machlowska J, Baj J, Sitarz M, Maciejewski R, Sitarz R. Gastric cancer: Epidemiology, risk factors, classification, genomic characteristics and treatment strategies. *Int J Mol Sci*. 2020;21(11):4012.

   doi: 10.3390/ijms21114012

10. Seevaratnam R, Cardoso R, McGregor C, *et al*. How useful is preoperative imaging for tumor, node, metastasis (TNM) staging of gastric cancer? A meta-analysis. *Gastric Cancer*. 2012;15(Suppl 1):S3-S18.

    doi: 10.1007/s10120-011-0069-6

11. Johnston FM, Beckman M. Updates on management of gastric cancer. *Curr Oncol Rep*. 2019;21(8):67.

    doi: 10.1007/s11912-019-0820-4

12. Bi WL, Hosny A, Schabath MB, *et al*. Artificial intelligence in cancer imaging: Clinical challenges and applications. *CA Cancer J Clin*. 2019;69(2):127-157.

    doi: 10.3322/caac.21552

13. Gillies RJ, Kinahan PE, Hricak H. Radiomics: Images are more than pictures, they are data. *Radiology*. 2016;278(2):563-577.

    doi: 10.1148/radiol.2015151169

14. Aerts HJ, Velazquez ER, Leijenaar RT, *et al*. Decoding tumour phenotype by noninvasive imaging using a quantitative radiomics approach. *Nat Commun*. 2014;5:4006.

    doi: 10.1038/ncomms5006

15. Wang Y, Jin ZY. Radiomics approaches in gastric cancer: A frontier in clinical decision making. *Chin Med J* (*Engl*). 2019;132(16):1983-1989.

    doi: 10.1097/CM9.0000000000000360

16. Zhang W, Fang M, Dong D, *et al*. Development and validation of a CT-based radiomic nomogram for preoperative prediction of early recurrence in advanced gastric cancer. *Radiother Oncol*. 2020;145:13-20.

    doi: 10.1016/j.radonc.2019.11.023

17. Jiang Y, Chen C, Xie J, *et al*. Radiomics signature of computed tomography imaging for prediction of survival and chemotherapeutic benefits in gastric cancer. *EBioMedicine*. 2018;36:171-182.

    doi: 10.1016/j.ebiom.2018.09.007

18. Smyth EC, Nilsson M, Grabsch HI, van Grieken NC, Lordick F. Gastric cancer. *Lancet*. 2020;396(10251):635-648.

    doi: 10.1016/S0140-6736(20)31288-5

19. Zhang Q, Peng C. Cancer-associated fibroblasts regulate the biological behaviour of cancer cells and stroma in gastric cancer. *Oncol Lett*. 2018;15(1):691-698.

doi: 10.3892/ol.2017.7385

20. Ma Z, Fang M, Huang Y, *et al*. CT-based radiomics signature for differentiating Borrmann type IV gastric cancer from primary gastric lymphoma. *Eur J Radiol*. 2017;91:142-147.

    doi: 10.1016/j.ejrad.2017.04.007

21. Sun YW, Ji CF, Wang H, *et al*. Differentiating gastric cancer and gastric lymphoma using texture analysis (TA) of positron emission tomography (PET). *Chin Med J* (*Engl*). 2020;134(4):439-447.

    doi: 10.1097/CM9.0000000000001206

22. Sun ZQ, Hu SD, Li J, Wang T, Duan SF, Wang J. Radiomics study for differentiating gastric cancer from gastric stromal tumor based on contrast-enhanced CT images. *J Xray Sci Technol*. 2019;27(6):1021-1031.

    doi: 10.3233/XST-190574

23. Wang R, Liu H, Liang P, Zhao H, Li L, Gao J. Radiomics analysis of CT imaging for differentiating gastric neuroendocrine carcinomas from gastric adenocarcinomas. *Eur J Radiol*. 2021;138:109662.

    doi: 10.1016/j.ejrad.2021.109662

24. Kim BS, Oh ST, Yook JH, Kim BS. Signet ring cell type and other histologic types: Differing clinical course and prognosis in T1 gastric cancer. *Surgery*. 2014;155(6):1030-1035.

    doi: 10.1016/j.surg.2013.08.016

25. Van der Post RS, Gullo I, Oliveira C, *et al*. Histopathological, molecular, and genetic profile of hereditary diffuse gastric cancer: Current knowledge and challenges for the future. *Adv Exp Med Biol*. 2016;908:371-391.

    doi: 10.1007/978-3-319-41388-4_18

26. Zhang Y, Chen J, Liu S, *et al*. Assessment of histological differentiation in gastric cancers using whole-volume histogram analysis of apparent diffusion coefficient maps. *J Magn Reson Imaging*. 2017;45(2):440-449.

    doi: 10.1002/jmri.25360

27. Li Q, Qi L, Feng QX, *et al*. Machine learning-based computational models derived from large-scale radiographic-radiomic images can help predict adverse histopathological status of gastric cancer. *Clin Transl Gastroenterol*. 2019;10(10):e00079.

    doi: 10.14309/ctg.0000000000000079

28. Smyth EC, Verheij M, Allum W, *et al*. Gastric cancer: ESMO clinical practice guidelines for diagnosis, treatment and follow-up. *Ann Oncol*. 2016;27(Suppl 5):v38-v49.

    doi: 10.1093/annonc/mdw350

29. Chen YC, Fang WL, Wang RF, *et al*. Clinicopathological variation of lauren classification in gastric cancer. *Pathol Oncol Res*. 2016;22(1):197-202.

    doi: 10.1007/s12253-015-9996-6

30. Wang XX, Ding Y, Wang SW, *et al*. Intratumoral and peritumoral radiomics analysis for preoperative Lauren classification in gastric cancer. *Cancer Imaging*. 2020;20(1):83.

    doi: 10.1186/s40644-020-00358-3

31. Wang Y, Liu W, Yu Y, *et al*. Potential value of CT radiomics in the distinction of intestinal-type gastric adenocarcinomas. *Eur Radiol*. 2020;30(5):2934-2944.

    doi: 10.1007/s00330-019-06629-3

32. Chen T, Wu J, Cui C, *et al*. CT-based radiomics nomograms for preoperative prediction of diffuse-type and signet ring cell gastric cancer: A multicenter development and validation cohort. *J Transl Med*. 2022;20(1):38.

    doi: 10.1186/s12967-022-03232-x

33. Edge SB, Byrd DR, Compton CC, *et al*. *AJCC Cancer Staging Manual*. 7th ed. Berlin: Springer; 2009.

34. Kumagai K, Sano T. Revised points and disputed matters in the eighth edition of the TNM staging system for gastric cancer. *Jpn J Clin Oncol*. 2021;51(7):1024-1027.

    doi: 10.1093/jjco/hyab069

35. Chen W, Wang S, Dong D, *et al*. Evaluation of lymph node metastasis in advanced gastric cancer using magnetic resonance imaging-based radiomics. *Front Oncol*. 2019;9:1265.

    doi: 10.3389/fonc.2019.01265

36. Jiang Y, Wang W, Chen C, *et al*. radiomics signature on computed tomography imaging: Association with lymph node metastasis in patients with gastric cancer. *Front Oncol*. 2019;9:340.

    doi: 10.3389/fonc.2019.00340

37. Feng QX, Liu C, Qi L, *et al*. An intelligent clinical decision support system for preoperative prediction of lymph node metastasis in gastric cancer. *J Am Coll Radiol*. 2019;16(7):952-960.

    doi: 10.1016/j.jacr.2018.12.017

38. Wang Y, Liu W, Yu Y, *et al*. Prediction of the depth of tumor invasion in gastric cancer: Potential role of CT radiomics. *Acad Radiol*. 2020;27(8):1077-1084.

    doi: 10.1016/j.acra.2019.10.020

39. Gao X, Ma T, Cui J, *et al*. A CT-based radiomics model for prediction of lymph node metastasis in early stage gastric cancer. *Acad Radiol*. 2021;28(6):e155-e164.

    doi: 10.1016/j.acra.2020.03.045

40. Gao X, Ma T, Cui J, *et al*. A radiomics-based model for prediction of lymph node metastasis in gastric cancer. *Eur J Radiol*. 2020;129:109069.

    doi: 10.1016/j.ejrad.2020.109069

41. Wang Y, Liu W, Yu Y, *et al*. CT radiomics nomogram for the preoperative prediction of lymph node metastasis in gastric cancer. *Eur Radiol*. 2020;30(2):976-986.

doi: 10.1007/s00330-019-06398-z

42. Yardimci AH, Sel I, Bektas CT, *et al*. Computed tomography texture analysis in patients with gastric cancer: A quantitative imaging biomarker for preoperative evaluation before neoadjuvant chemotherapy treatment. *Jpn J Radiol*. 2020;38(6):553-560.

    doi: 10.1007/s11604-020-00936-2

43. Yang J, Wu Q, Xu L, *et al*. Integrating tumor and nodal radiomics to predict lymph node metastasis in gastric cancer. *Radiother Oncol*. 2020;150:89-96.

    doi: 10.1016/j.radonc.2020.06.004

44. Wang L, Gong J, Huang X, *et al*. CT-based radiomics nomogram for preoperative prediction of No.10 lymph nodes metastasis in advanced proximal gastric cancer. *Eur J Surg Oncol*. 2021;47(6):1458-1465.

    doi: 10.1016/j.ejso.2020.11.132

45. Sun Z, Jiang Y, Chen C, *et al*. Radiomics signature based on computed tomography images for the preoperative prediction of lymph node metastasis at individual stations in gastric cancer: A multicenter study. *Radiother Oncol*. 2021;165:179-190.

    doi: 10.1016/j.radonc.2021.11.003

46. Wang X, Li C, Fang M, *et al*. Integrating No.3 lymph nodes and primary tumor radiomics to predict lymph node metastasis in T1-2 gastric cancer. *BMC Med Imaging*. 2021;21(1):58.

    doi: 10.1186/s12880-021-00587-3

47. Liu Q, Li J, Xin B, *et al*. 18F-FDG PET/CT radiomics for preoperative prediction of lymph node metastases and nodal staging in gastric cancer. *Front Oncol*. 2021;11:723345.

    doi: 10.3389/fonc.2021.723345

48. Xue XQ, Yu WJ, Shao XL, *et al*. Radiomics model based on preoperative 18F-fluorodeoxyglucose PET predicts N2-3b lymph node metastasis in gastric cancer patients. *Nucl Med Commun*. 2022;43(3):340-349.

    doi: 10.1097/MNM.0000000000001523

49. Montagnani F, Crivelli F, Aprile G, *et al*. Long-term survival after liver metastasectomy in gastric cancer: Systematic review and meta-analysis of prognostic factors. *Cancer Treat Rev*. 2018;69:11-20.

    doi: 10.1016/j.ctrv.2018.05.010

50. Chen X, Yang Z, Yang J, *et al*. Radiomics analysis of contrast-enhanced CT predicts lymphovascular invasion and disease outcome in gastric cancer: A preliminary study. *Cancer Imaging*. 2020;20(1):24.

    doi: 10.1186/s40644-020-00302-5

51. Yardımcı AH, Koçak B, Turan Bektaş C, *et al*. Tubular gastric adenocarcinoma: Machine learning-based CT texture analysis for predicting lymphovascular and perineural invasion. *Diagn Interv Radiol*. 2020;26(6):515-522.

    doi: 10.5152/dir.2020.19507

52. Zheng H, Zheng Q, Jiang M, *et al*. Contrast-enhanced CT based radiomics in the preoperative prediction of perineural invasion for patients with gastric cancer. *Eur J Radiol*. 2022;154:110393.

    doi: 10.1016/j.ejrad.2022.110393

53. Fan L, Li J, Zhang H, *et al*. Machine learning analysis for the noninvasive prediction of lymphovascular invasion in gastric cancer using PET/CT and enhanced CT-based radiomics and clinical variables. *Abdom Radiol* (*NY*). 2022;47(4):1209-1222.

    doi: 10.1007/s00261-021-03315-1

54. Yang L, Chu W, Li M, *et al*. Radiomics in gastric cancer: First clinical investigation to predict lymph vascular invasion and survival outcome using ^{18}F-FDG PET/CT images. *Front Oncol*. 2022;12:836098.

    doi: 10.3389/fonc.2022.836098

55. Bando E, Makuuchi R, Tokunaga M, Tanizawa Y, Kawamura T, Terashima M. Impact of clinical tumor-node-metastasis staging on survival in gastric carcinoma patients receiving surgery. *Gastric Cancer*. 2017;20(3):448-456.

    doi: 10.1007/s10120-016-0637-x

56. Sohn BH, Hwang JE, Jang HJ, *et al*. Clinical significance of four molecular subtypes of gastric cancer identified by the cancer genome atlas project. *Clin Cancer Res*. 2017;23(15):4441-4449.

    doi: 10.1158/1078-0432.CCR-16-2211

57. Bortolotto C, Lancia A, Stelitano C, *et al*. Radiomics features as predictive and prognostic biomarkers in NSCLC. *Expert Rev Anticancer Ther*. 2021;21(3):257-266.

    doi: 10.1080/14737140.2021.1852935

58. Giganti F, Antunes S, Salerno A, *et al*. Gastric cancer: Texture analysis from multidetector computed tomography as a potential preoperative prognostic biomarker. *Eur Radiol*. 2017;27(5):1831-1839.

    doi: 10.1007/s00330-016-4540-y

59. Wang X, Sun J, Zhang W, *et al*. Use of radiomics to extract splenic features to predict prognosis of patients with gastric cancer. *Eur J Surg Oncol*. 2020;46(10 Pt A):1932-1940.

    doi: 10.1016/j.ejso.2020.06.021

60. Wang S, Feng C, Dong D, *et al*. Preoperative computed tomography-guided disease-free survival prediction in gastric cancer: A multicenter radiomics study. *Med Phys*. 2020;47(10):4862-4871.

    doi: 10.1002/mp.14350

61. Li W, Zhang L, Tian C, *et al*. Prognostic value of computed

tomography radiomics features in patients with gastric cancer following curative resection. *Eur Radiol*. 2019;29(6):3079-3089.

doi: 10.1007/s00330-018-5861-9

62. Li Z, Zhang D, Dai Y, *et al*. Computed tomography-based radiomics for prediction of neoadjuvant chemotherapy outcomes in locally advanced gastric cancer: A pilot study. *Chin J Cancer Res*. 2018;30(4):406-414.

    doi: 10.21147/j.issn.1000-9604.2018.04.03

63. Sun KY, Hu HT, Chen SL, *et al*. CT-based radiomics scores predict response to neoadjuvant chemotherapy and survival in patients with gastric cancer. *BMC Cancer*. 2020;20(1):468.

    doi: 10.1186/s12885-020-06970-7

64. Mazzei MA, Di Giacomo L, Bagnacci G, *et al*. Delta-radiomics and response to neoadjuvant treatment in locally advanced gastric cancer-a multicenter study of GIRCG (Italian Research Group for Gastric Cancer). *Quant Imaging Med Surg*. 2021;11(6):2376-2387.

    doi: 10.21037/qims-20-683

65. Xu Q, Sun Z, Li X, *et al*. Advanced gastric cancer: CT radiomics prediction and early detection of downstaging with neoadjuvant chemotherapy. *Eur Radiol*. 2021;31(11):8765-8774.

    doi: 10.1007/s00330-021-07962-2

66. Chen Y, Wei K, Liu D, *et al*. A machine learning model for predicting a major response to neoadjuvant chemotherapy in advanced gastric cancer. *Front Oncol*. 2021;11:675458.

    doi: 10.3389/fonc.2021.675458

67. Chen Y, Yuan F, Wang L, *et al*. Evaluation of dual-energy CT derived radiomics signatures in predicting outcomes in patients with advanced gastric cancer after neoadjuvant chemotherapy. *Eur J Surg Oncol*. 2022;48(2):339-347.

    doi: 10.1016/j.ejso.2021.07.014

68. Shin J, Lim JS, Huh YM, *et al*. A radiomics-based model for predicting prognosis of locally advanced gastric cancer in the preoperative setting. *Sci Rep*. 2021;11(1):1879.

    doi: 10.1038/s41598-021-81408-z

69. Tan Z. Recent advances in the surgical treatment of advanced gastric cancer: A review. *Med Sci Monit*. 2019;25:3537-3541.

    doi: 10.12659/MSM.916475

70. Klaassen R, Larue RTH, Mearadji B, *et al*. Feasibility of CT radiomics to predict treatment response of individual liver metastases in esophagogastric cancer patients. *PLoS One*. 2018;13(11):e0207362.

    doi: 10.1371/journal.pone.0207362

71. Li J, Zhang C, Wei J, *et al*. Intratumoral and peritumoral radiomics of contrast-enhanced CT for prediction of disease-free survival and chemotherapy response in stage II/III gastric cancer. *Front Oncol*. 2020;10:552270.

    doi: 10.3389/fonc.2020.552270

72. Wang N, Wang X, Li W, *et al*. Contrast-enhanced CT parameters of gastric adenocarcinoma: Can radiomic features be surrogate biomarkers for HER2 over-expression status? *Cancer Manag Res*. 2020;12:1211-1219.

    doi: 10.2147/CMAR.S230138

73. Wang Y, Yu Y, Han W, *et al*. CT radiomics for distinction of human epidermal growth factor receptor 2 negative gastric cancer. *Acad Radiol*. 2021;28(3):e86-e92.

    doi: 10.1016/j.acra.2020.02.018

74. Binnewies M, Roberts EW, Kersten K, *et al*. Understanding the tumor immune microenvironment (TIME) for effective therapy. *Nat Med*. 2018;24(5):541-550.

    doi: 10.1038/s41591-018-0014-x

75. Jiang Y, Wang H, Wu J, *et al*. Noninvasive imaging evaluation of tumor immune microenvironment to predict outcomes in gastric cancer. *Ann Oncol*. 2020;31(6):760-768.

    doi: 10.1016/j.annonc.2020.03.295

76. Lin JX, Lin JP, Weng Y, *et al*. Radiographical evaluation of tumor immunosuppressive microenvironment and treatment outcomes in gastric cancer: A retrospective, multicohort study. *Ann Surg Oncol*. 2022;29(8):5022-5033.

    doi: 10.1245/s10434-022-11499-z

77. Gao X, Ma T, Bai S, *et al*. A CT-based radiomics signature for evaluating tumor infiltrating Treg cells and outcome prediction of gastric cancer. *Ann Transl Med*. 2020;8(7):469.

    doi: 10.21037/atm.2020.03.114

78. Li J, Zhang C, Guo H, *et al*. Non-invasive measurement of tumor immune microenvironment and prediction of survival and chemotherapeutic benefits from ^{18}F fluorodeoxyglucose PET/CT images in gastric cancer. *Front Immunol*. 2022;13:1019386.

    doi: 10.3389/fimmu.2022.1019386

79. Avanzo M, Wei L, Stancanello J, *et al*. Machine and deep learning methods for radiomics. *Med Phys*. 2020;47(5):e185-e202.

    doi: 10.1002/mp.13678

80. Zhang L, Dong D, Zhang W, *et al*. A deep learning risk prediction model for overall survival in patients with gastric cancer: A multicenter study. *Radiother Oncol*. 2020;150:73-80.

    doi: 10.1016/j.radonc.2020.06.010

81. Tan JW, Wang L, Chen Y, *et al*. Predicting chemotherapeutic response for far-advanced gastric cancer by radiomics with deep learning semi-automatic segmentation. *J Cancer*. 2020;11(24):7224-7236.

    doi: 10.7150/jca.46704

82. Dong D, Fang MJ, Tang L, *et al*. Deep learning radiomic nomogram can predict the number of lymph node metastasis in locally advanced gastric cancer: An international multicenter study. *Ann Oncol*. 2020;31(7):912-920.

doi: 10.1016/j.annonc.2020.04.003

83. Berlth F, Bollschweiler E, Drebber U, Hoelscher AH, Moenig S. Pathohistological classification systems in gastric cancer: Diagnostic relevance and prognostic value. *World J Gastroenterol*. 2014;20(19):5679-5684.

doi: 10.3748/wjg.v20.i19.5679

84. Cann C, Ciombor KK. Systemic therapy for gastric cancer: Perioperative strategies and beyond. *J Surg Oncol*. 2022;125(7):1151-1160.

doi: 10.1002/jso.26834

85. Zhang N, Fei Q, Gu J, Yin L, He X. Progress of preoperative and postoperative radiotherapy in gastric cancer. *World J Surg Oncol*. 2018;16(1):187.

doi: 10.1186/s12957-018-1490-7

86. Marcus C, Subramaniam RM. PET/computed tomography and precision medicine: Gastric cancer. *PET Clin*. 2017;12(4):437-447.

doi: 10.1016/j.cpet.2017.05.004

87. Kim GH. Systematic endoscopic approach to early gastric cancer in clinical practice. *Gut Liver*. 2021;15(6):811-817.

doi: 10.5009/gnl20318

88. Berenguer R, Pastor-Juan MDR, Canales-Vázquez J, *et al*. Radiomics of CT features may be nonreproducible and redundant: Influence of CT acquisition parameters. *Radiology*. 2018;288(2):407-415.

doi: 10.1148/radiol.2018172361

89. Wei L, Osman S, Hatt M, El Naqa I. Machine learning for radiomics-based multimodality and multiparametric modeling. *Q J Nucl Med Mol Imaging*. 2019;63(4):323-338.

doi: 10.23736/S1824-4785.19.03213-8

ACCSCIENCE PUBLISHING

Advances in Radiotherapy & Nuclear Medicine

ORIGINAL RESEARCH ARTICLE

Shielding design calculations for a radiotherapy vault of a 6 and 10-megavoltage medical linear accelerator operating with or without a flattening filter

Mostafa M. Elashmawy*

Department of Radiation Protection, Radiation Control Division, Nuclear and Radiological Research Center, Egyptian Atomic Energy Authority, Cairo, Egypt

Abstract

This study focuses on upgrading the shielding design of a Co-60 radiotherapy unit to accommodate a linear accelerator operating at 6 and 10 megavoltage, which can function in both flattening filter (FF) and flattening filter-free (FFF) modes. Shielding calculations were performed using analytical methods from the National Council on Radiation Protection and Measurements Report No. 151 and International Atomic Energy Agency Safety Reports Series No. 47, considering standard (40 patients/day) and heavy (60 patients/day) workloads. Barrier thicknesses were determined to ensure the instantaneous dose rate (IDR) behind primary barriers is ≤7.5 µSv/h in FF mode and ≤20 µSv/h in FFF mode, as recommended in the Institute of Physics and Engineering in Medicine Report No. 75. Results showed that workload had no significant effect on the primary barrier thickness. Moreover, strict adherence to the IDR criteria increased shielding demands ranging from 11% to 46% while reducing the personal equivalent dose to 1.2 – 13.4% of the dose constraints. This highlights a potential overdesign that could substantially increase raise construction costs. Therefore, applying the IDR criteria violates the radiation protection principles, namely, "optimization." An alternative approach has been proposed to optimally use the IDR criteria by including the patient's transmission factor in the current IDR criteria or by adopting higher values of IDR strictly to verify the shielding efficiency. Higher IDR adoption would result in lower linear accelerator vault costs and more realistic shielding calculations consistent with operating conditions.

Keywords: Medical linear accelerator; Radiotherapy; Flattening filter; Shielding calculations; Instantaneous dose rate; Optimization

***Corresponding author:**
Mostafa M. Elashmawy
(mostafa_ashmawy2002@yahoo.com)

Citation: Elashmawy MM. Shielding design calculations for a radiotherapy vault of a 6 and 10-megavoltage medical linear accelerator operating with or without a flattening filter. *Adv Radiother Nucl Med.* 2025;3(2):39-51. doi: 10.36922/ARNM025070007

Received: February 14, 2025

Revised: March 27, 2025

Accepted: April 11, 2025

Published online: April 25, 2025

1. Introduction

Megavoltage (MV) photon beams produced by linear accelerators at various energies are the most commonly used radiation sources in modern radiation oncology and radiotherapy. The primary goal in treatment planning is to deliver an appropriate dose to the tumor while minimizing exposure to surrounding tissues and organs at risk. This objective has been progressively enhanced using different radiotherapy techniques, such as three-dimensional conformal radiotherapy, intensity-modulated radiotherapy

(IMRT), and volumetric-modulated arc therapy (VMAT). In recent years, IMRT and VMAT have increasingly replaced three-dimensional conformal radiotherapy.

Conventionally, it was believed that an ideal photon beam used in treatment planning should be uniform across the treatment field. This uniformity is obtained using a flattening filter (FF) positioned in the linear accelerator (linac) head. However, the widespread adoption of non-uniform beam distribution has challenged this assumption. Removing the FF results in flattening filter-free (FFF) beams, now widely used for stereotactic and non-stereotactic radiotherapy treatments. As a result, advanced treatment techniques prefer FFF beams over FF beams.[1-6]

Numerous studies[3,4,7-12] have thoroughly examined the main dosimetric properties of FFF beams, the precision of dose calculations, and the quality of treatment plans for IMRT with unflattened beams. The FFF beams exhibit distinct characteristics compared to standard FF beams, specifically in terms of high dose rate and a profile shape that is peaked along the beam's central axis. Moreover, removing the FF significantly lowers the leakage radiation from the treatment head and softens the photons' energy spectrum.[13-16] Furthermore, since the FF is a source of photoneutrons, its removal reduces neutron production from the linac's head.

The main objective of the radiation protection program in medical linear accelerator facilities is to protect workers, the general public, and the environment from the harmful effects of ionizing radiation (gamma rays and photo-neutrons) transmitted outside the linac's vault. Thus, shielding requirements are defined by the dosimetric characteristics of the clinically applied MV photon beams – more precisely, by the beam modality used during treatment (FF or FFF). In all cases, shielding design should avoid unnecessary overestimation. A balanced approach must be taken, considering both the actual shielding needs under normal operating working conditions and the associated construction cost.

This study aims to present a case analysis evaluating the shielding requirements for an existing Co-60 radiotherapy bunker intended to adequately accommodate an Elekta Versa HD medical linear accelerator operating at 6 and 10 MV, with and without an FF. The shielding evaluation considers both a standard operating workload (40 patients/day) and an overload (60 patients/day) of 50% for each accelerator energy. The final thicknesses of the primary barriers were determined such that the expected instantaneous dose rate (IDR) behind the barriers does not exceed 7.5 μSv/h for FF mode and 20 μSv/h for FFF mode, in accordance with the recommendations of the Institute of Physics in Medicine and Engineering Report No. 75 (IPEM 75).[17] The shielding evaluation and determination were performed for the existing vault using the analytical equations listed in the International Atomic Energy Agency Safety Reports Series No. 47 (IAEA SRS-47)[18] and the National Council on Radiation Protection and Measurements Report No. 151 (NCRP 151).[19] Both primary and secondary barriers were assessed, with a particular focus on primary barriers that are directly exposed to the beam. The impact of applying the IDR criteria on shielding design has not been extensively studied. In this work, the thicknesses of the primary barriers obtained with and without adhering to the above-mentioned IDR criteria were analyzed in detail and evaluated in the context of fundamental radiation protection principles, with particular emphasis on the "optimization" principle. The necessary recommendations were proposed regarding using the IDR criteria in its current form or modifying its use to suit the working conditions in radiation therapy units without overestimating the barriers' thicknesses. This study represents a step-by-step, comprehensive, practical guide for determining shielding requirements for a real linac bunker, with detailed explanations for each step.

2. Methods

2.1. Bunker description and shielding upgrade approach

Figure 1 represents the linac's bunker before and after the shielding upgrade. The existing primary barrier thickness (1.35 m) is inadequate for 6 or 10 MV linacs. One of the primary barriers is adjacent to the public waiting area, that is, fully occupied, and fortunately, there is enough space to extend it using ordinary concrete (density = 2.35 g/cm^3). The same situation applied to the primary ceiling, and it is also possible to extend the ceiling's shielding since the bunker's roof is dedicated to the linac's chillers and the hospital's heating, ventilation, and air conditioning system. The other primary barrier is adjacent to the maze of another bunker, that is, partially occupied, and the space is very limited for implementing any concrete shielding beyond this barrier. Therefore, the necessary shielding extension will be partially implemented using ordinary concrete inside the bunker; the largest thickness available for this internal extension is 0.5 m × 3.12 m. This internal shielding extension is very advantageous to support the ceiling's shielding extension from a structural engineering point of view. The remaining shielding extension will be implemented using high-density material, such as iron, outside the bunker.

The left secondary barrier of the bunker's maze is comparatively short and thin (0.95 m). This results in a

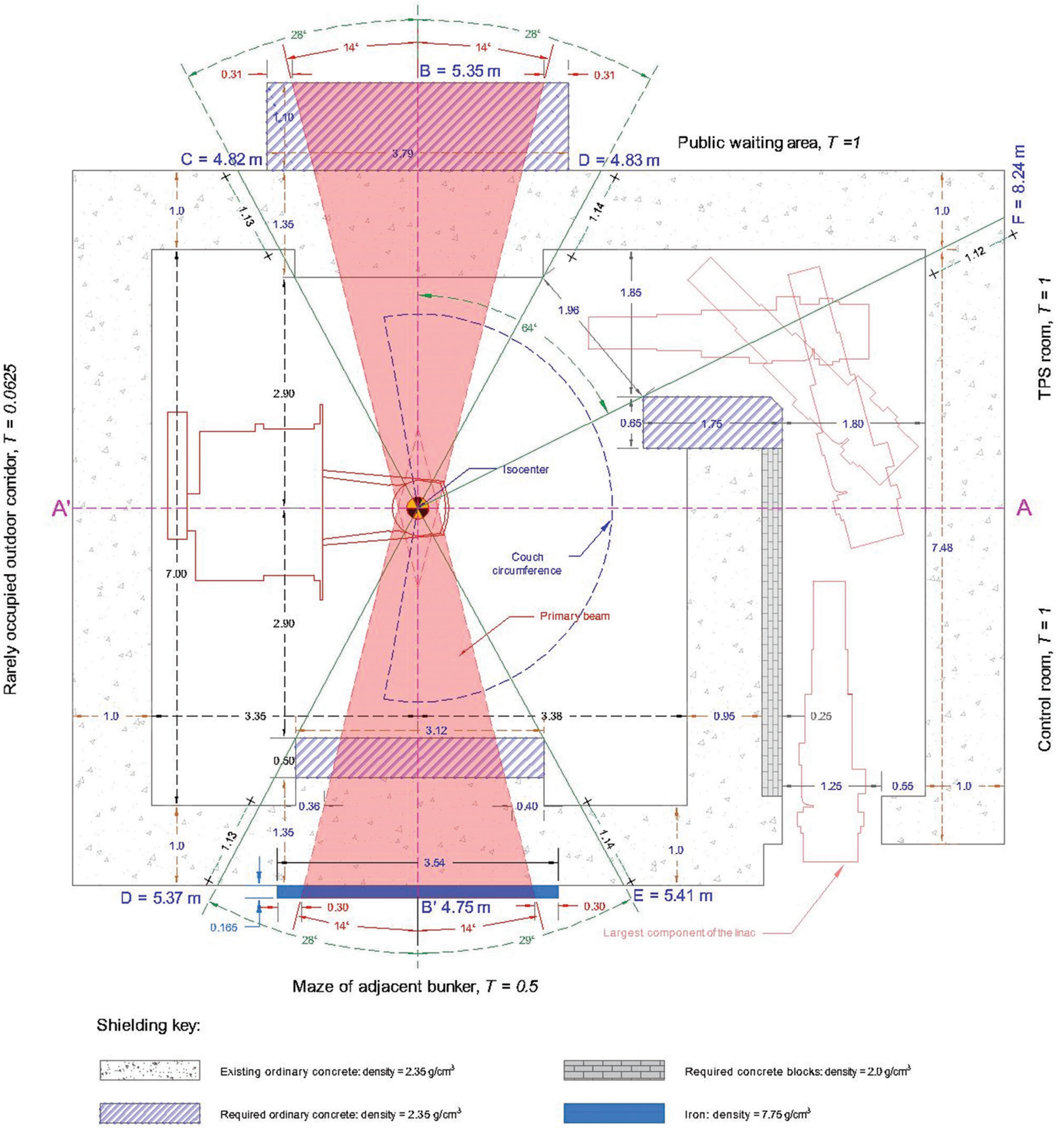

Figure 1. Vault design for a 6 and 10 MV linear accelerator with one primary barrier made from ordinary concrete while the other comprises ordinary concrete and iron. Image created by the author.
Abbreviation: TPS: Treatment Planning System room.

wide cross-section of the inner maze entrance, raising the radiation levels (neutrons and gamma) at the bunker's door. To increase this barrier's thickness, 25 cm of concrete blocks with a density of at least 2.0 g/cm^3 – equivalent to 21 cm of concrete – will be added, making the barrier's total effective thickness approximately 116 cm of ordinary concrete. Concrete blocks were utilized since concrete cannot be easily poured at a thin thickness (25 cm).

In addition, the inner maze entrance was modified by adding a shielding extension of ordinary concrete, with dimensions of 1.75 m × 0.65 m. This alteration effectively converted the original single-leg maze into a two-leg configuration, significantly reducing the radiation (gamma and neutrons) within the maze. As a result, radiation dose behind the right-side barrier of the maze where two rooms are fully occupied, namely, the treatment planning system and control rooms, are also expected to decrease.

The internal shielding extensions were designed based on two criteria, as illustrated in Figure 1: first, to allow free movement of the linac treatment couch without any obstacles while maintaining sufficient space for the linac operator to position patients comfortably, and second, to allow for the safe and free maneuvering of the largest component of the Elekta Versa HD linac through the inner maze entrance.

Given that the minimum slant path through the shielding is approximately 114 cm, the thicknesses of the other secondary barriers (1.0 m) were left unaltered. This design assumption will be validated through calculations and radiation measurements.

2.2. The national council on radiation protection and measurements report no. 151 and safety reports series no. 47 shielding calculation approach

The weekly dose constraint (P_w) received by a person behind a primary barrier is determined by Equation I.

$$P_w = \frac{B_0 \times W \times U \times T}{d + SAD} \left(\mu Sv / week \right) \tag{I}$$

The dose constraint (P_w) received by a person behind a secondary barrier is determined by the sum of the doses received due to secondary radiation, namely, head leakage [P_L] and patient scatter [P_p], as in Equations II and III,

$$P_w = P_L + P_P \ (\mu Sv/week) \tag{II}$$

$$P_w = \frac{B_L \times W^* \times T}{1000 \times d} + \frac{B_P \times a \times W \times T \times (F/400)}{d_{sca} \times d_{sec}} \left(\mu Sv / week \right) \tag{III}$$

Where W is the weekly workload (Gy/week) at the isocenter, W^* is the weekly workload (Gy/week) produced by the linac, T is the occupancy factor, a is the scatter fraction from the patient, U is the wall use factor, F is field size incident on the patient, and SAD is the source to isocenter distance. B_0 is the barrier transmission against primary radiation, d is the distance from the isocenter to the calculation point, B_L is the barrier transmission against leakage radiation, d_{sca} is the distance from the source to the patient, B_P is the barrier transmission against patient scatter radiation, and d_{sec} is the distance from the patient to the calculation point.

The designed dose constraint (P_w) behind a particular primary barrier is achieved at a specific value of the transmission factor B_0 of that barrier. This transmission factor is achieved using a particular thickness of the barrier of specific density that can attenuate the radiation dose to the designed dose constraint. The required transmission factor B_0 could be determined using Equation IV,

$$TVLs = log_{10} \left(\frac{1}{B_0} \right) \tag{IV}$$

Where $TVLs$ are the number of the tenth value layers (TVLs) required to achieve the designed B_0. The transmission factor B_0 of that barrier is then given in Equation V,

$$B_0 = \left(\frac{P_0 \times (SAD + d)^2}{D_0} \right) \tag{V}$$

Where D_0 is the dose rate at the isocenter, and P_0 is the equivalent dose rate constraint behind the barrier. IPEM 75[17] proposed $P_0 = 7.5$ µSv/h when testing the transmission factor at the FF modality and 20 µSv/h in the case of the FFF beam modality. In this study, all parameters, as mentioned earlier, were retrieved from the NCRP 151 except the TVLs, which were extracted from the IAEA SRS-47 because the TVL values reported therein are more consistent with the experimental data results in recent studies.[20,21]

Exposure to the radiation from the linac vault represents planned exposure controlled within the framework of dose constraints to ensure that the radiation exposure is as low as reasonably achievable.[22] Accordingly, the shielding design calculations are carried out using the following assumptions: (i) annual dose limit [P_o] = 20 (1) mSv/year for occupational (public) and (ii) annual dose constraints [P] = 6 (1) mSv/year for occupational (public). This means the weekly dose constraints [P_w] = 120 (20) µSv/week.

The thicknesses of the primary and secondary barriers are determined so that the weekly dose constraints are not exceeded.

2.3. Workload considerations

Two workload cases have been considered in this study; the first one is 40 patients/day, representing the standard workload in all literature. The number 40 patients/day means five patients are treated in 1 h along an 8-h working day. Another case represents an overloaded facility with 60 patients/day, which means that seven to eight patients are treated in an hour or the working day is longer than 8 h.

Many of the radiotherapy facilities in Egypt are operating at an overload, with an average of 60 patients per day. Table 1 summarizes the two cases of workload distribution during the working week.

3. Results

3.1. Primary barrier at point B (public waiting area)

This barrier is made entirely of ordinary concrete. The unshielded weekly dose behind this primary barrier is determined as in Equation VI,

$$W \times T \times U/((d+0.3)+SAD)^2 \qquad \text{(VI)}$$

Where, the occupancy factor $T = 1$, the use factor $U = 0.25$, dose constraint = 20 μSv/week, $d = 5.35$, and $SAD = 1$ m.

3.1.1. Case 1: Working load of 40 patients/day

The weekly unshielded dose at 10 MV (20 patients) is presented in Equation VII.

$$360 \times 1 \times 0.25/6.65^2 = 2.04\ Sv/week \qquad \text{(VII)}$$

To reduce this value to the weekly dose constraints for the public (20 μSv/week), the transmission factor becomes $B = 9.83 \times 10^{-6}$. Accordingly, the number of TVLs needed to achieve this value is 5.0; considering that the TVL at 10 MV is 38.9 cm, the primary barrier should be 1.95 m thick.

The weekly unshielded dose at 6 MV (20 patients) is presented in Equation VIII.

$$360 \times 1 \times 0.25/6.65^2 = 2.04\ Sv/week \qquad \text{(VIII)}$$

To reduce this value to the weekly dose constraints for the public (20 μSv/week), the transmission factor becomes $B = 9.83 \times 10^{-6}$. Accordingly, the number of TVLs needed to achieve this value is 5.0; considering that the TVL at 6 MV is 34.3 cm, the primary barrier should be 1.72 m thick.

The difference between the two thicknesses is 23 cm. This difference reduces the weekly dose at 6 MV to 4.26 μSv/week, making the total weekly dose 24.6 μSv. Therefore, one half-value layer (HVL) of 10 MV will be added to the total thickness to ensure that the weekly dose rate is <20 μSv/week; the final thickness of the primary barrier will be 2.07 m. The total weekly dose from the two energies at this final thickness is 11.94 μSv/week.

However, in the case of 10 MV FF beam modality, to fulfill the IDR of ≤7.5 μSv/h at a dose rate of 600 MU/min at the linac's isocenter, the primary barrier thickness should be 2.35 m. In addition, in the case of 10 MV FFF beam modality, to fulfill the IDR criteria of ≤20 μSv/h at a dose rate of 2,400 MU/min at the linac's isocenter, the primary barrier thickness should be 2.42 m. Accordingly, the highest value will be considered. Consequently, using IDR criteria necessitates that the primary barrier thickness for the workload of 40 patients/week should be increased by 17.0%.

The expected equivalent dose behind the primary barrier at the final thickness, 2.42 m, equals 1.434 μSv/week or 71.7 μSv/year, which means that the use of IDR criteria reduces the equivalent dose to just 7.17% of the annual dose constrain, that is, 1 mSv/year.

3.1.2. Case 2: Working load of 60 patients/day

The weekly unshielded dose at 10 MV (40 patients) is presented in Equation IX.

Table 1. Details of weekly workload distribution for a 6 and 10-MV linear accelerator

Planned weekly workload using 6 and 10 MV linear accelerator	Energy (treatment modality)	Patients per day	Dose fraction (Gy/patient)	Weekly workload (Gy/week)	Total dose at isocenter Gy/week	IMRT ratio	Total dose produced by linear accelerator (Gy/week)
Case 1: 40 patients/day	10 (3D)	10	3	180	360	1	855
	10 (IMRT)	5	3	90		5	
	10 (VMAT)	5	3	90		2.5	
	6 (3D)	10	3	180	360	1	855
	6 (IMRT)	5	3	90		5	
	6 (VMAT)	5	3	90		2.5	
Case 2: 60 patients/day	10 (3D)	20	3	360	720	1	1,710
	10 (IMRT)	10	3	180		5	
	10 (VMAT)	10	3	180		2.5	
	6 (3D)	10	3	180	360	1	855
	6 (IMRT)	5	3	90		5	
	6 (VMAT)	5	3	90		2.5	

Abbreviations: 3D: Three-dimensional; IMRT: Intensity-modulated radiotherapy; VMAT: Volumetric-modulated arc therapy.

$$720 \times 1 \times 0.25/6.65^2 = 4.07\ Sv/week \tag{IX}$$

To reduce this value to the weekly dose constraints for the public (20 μSv/week), the transmission factor becomes $B = 4.91 \times 10^{-6}$. Accordingly, the number of TVLs needed to achieve this value is 5.31; considering that the TVL at 10 MV is 38.9 cm, the primary barrier should be 2.07 m thick.

The weekly unshielded dose at 6 MV (20 patients) is presented in Equation X.

$$360 \times 1 \times 0.25/6.65^2 = 2.5\ Sv/week \tag{X}$$

To reduce this value to the weekly dose constraints for the public (20 μSv/week), the transmission factor becomes $B = 9.83 \times 10^{-6}$. Accordingly, the number of TVLs needed to achieve this value is 5.0; considering that the TVL at 6 MV is 34.3 cm, the primary barrier should be 1.72 m thick.

The difference between the two thicknesses is 34.7 cm; this difference reduces the weekly dose at 6MV to 1.94 μSv/week, which makes the total weekly dose 21.94 μSv/week. Therefore, one HVL of 10 MV will be added to the total thickness to ensure that the weekly dose rate is <20 μSv/week and the final thickness of the primary barrier will be 2.18 m. The total weekly dose from the two energies at this final thickness is 10.88 μSv/week.

Since the primary barrier thickness is 2.42 m based on the IDR criteria mentioned above, the primary barrier thickness for the workload of 60 patients/week must be increased by 10.73%.

The expected equivalent dose behind the primary barrier at the final thickness, 2.42 m, equals 2.684 μSv/week or 134.2 μSv/year, which means that the use of IDR criteria reduces the equivalent dose to just 13.4% of the annual dose constrain, that is, 1 mSv/year. For this primary barrier (*B*), it is worth noting that the IDR in the FF case decreases from 7.5 μSv/h at 2.35 m to 5 μSv/h at 2.42 m, the thickness required in the FFF case.

3.2. Primary barrier at point B′

This barrier is made partially of ordinary concrete, and any additional thickness is made of iron. At this point, the occupancy factor $T = 0.5$, the use factor $U = 0.25$, and the dose constraint = 120 μSv/week.

3.2.1. Case 1: Working load of 40 patients/day

The weekly unshielded dose at 10 MV (20 patients) is presented in Equation XI.

$$360 \times 0.25 \times 0.5/6.05^2 = 1.23\ Sv/week \tag{XI}$$

To reduce this value to the weekly dose constraints for the workers (120 μSv/week), the transmission factor becomes $B = 9.76 \times 10^5$. Accordingly, the number of TVLs needed to achieve this value is 4.0; considering that the TVL at 10 MV is 38.9 cm, the primary barrier should be 1.56 m thick.

The weekly unshielded dose at 6 MV (20 patients) is presented in Equation XII.

$$360 \times 0.25 \times 0.5/6.05^2 = 1.23\ Sv/week \tag{XII}$$

To reduce this value to the weekly dose constraints for the workers (120 μSv/week), the transmission factor becomes $B = 9.76 \times 10^5$. Accordingly, the number of TVLs needed to achieve this value is 4.0; considering that the TVL at 6 MV is 34.3 cm, the primary barrier should be 1.38 m thick.

The difference between the two thicknesses is 18.4 cm; this difference reduces the weekly dose at 6 MV to 34.78 μSv/week, which made the total weekly dose 154.78 μSv/week. Therefore, one HVL of 10 MV will be added to the total thickness to ensure the weekly dose rate is < 120 μSv/week. Hence, the final thickness of the primary barrier will be 1.68 m. The total weekly dose from the two energies at this final thickness is 75.85 μSv/week.

In the case of 10 MV FF beam modality, to fulfill the IDR criteria of ≤7.5 μSv/h at a dose rate of 600 MU/min at the linac's isocenter, the primary barrier thickness should be 2.38 m. In the case of 10 MV FFF beam modality, to fulfill the IDR criteria to be ≤20 μSv/h at a dose rate of 2,400 MU/min at the linac's isocenter, the primary barrier thickness should be 2.45 m. Accordingly, the highest value will be considered. Consequently, using IDR criteria necessitates that the primary barrier thickness for the workload of 40 patients/week must be increased by 46%.

The expected equivalent dose behind the primary barrier at the final thickness, 2.45 m, equals 1.429 μSv/week or 71.45 μSv/year, which means that the use of IDR criteria reduces the equivalent dose to just 1.91% of the annual dose constrain, that is, 6 mSv/year.

3.2.2. Case 2: Working load of 60 patients/day

The weekly unshielded dose at 10 MV (40 patients) is presented in Equation XIII.

$$720 \times 0.25 \times 0.5/6.05^2 =2.46\ Sv/week \tag{XIII}$$

To reduce this value to the weekly dose constraints for the workers (120 μSv/week), the transmission factor becomes $B = 4.88 \times 10^{-5}$. Accordingly, the number of TVLs needed to achieve this value is 4.31; considering that the TVL at 10 MV is 38.9 cm, the primary barrier should be 1.68 m thick.

The weekly unshielded dose at 6 MV (20 patients) is presented in Equation XIV.

$$360 \times 0.25 \times 0.5/6.05^2 = 1.23\ Sv/week \qquad \text{(XIV)}$$

To reduce this value to the weekly dose constraints for the workers (120 μSv/week), the transmission factor becomes $B = 9.76 \times 10^5$. Accordingly, the number of TVLs needed to achieve this value is 4.0; considering that the TVL at 6 MV is 34.3 cm, the primary barrier should be 1.38 m thick.

The difference between the two thicknesses is 30 cm; this difference reduces the weekly dose at 6 MV to 15.84 μSv/week, which made the total weekly dose 135.84 μSv/week. Therefore, one HVL of 10 MV must be added to the total thickness to ensure the weekly dose rate is <120 μSv/week. The final thickness of the primary barrier will be 1.8 m. The total weekly dose from the two energies at this final thickness is 67.21 μSv/week.

Since the primary barrier thickness is 2.45 m based on the IDR criteria mentioned above, there is a 36.45% increase in the barrier thickness. Notably, for this primary barrier (B'), the IDR of the FF decreases from 7.5 μSv/h at 2.38 m to 5 μSv/h at 2.45 m, which is the thickness of the FFF case.

The expected equivalent dose behind the primary barrier at the final thickness, 2.45 m, equals 2.679 μSv/week or 134 μSv/year, indicating that the use of IDR criteria reduces the equivalent dose to just 2.23% of the annual dose constrain, that is, 6 mSv/year.

Given that only 185 cm of concrete exists, the remaining required thickness of the primary barrier (60 cm) should be compensated with a high-density material due to the limited space available. This required 60 cm thickness corresponds to 1.54 TVL at 10 MV. Considering that the TVL at 10 MV for iron is 10.5 cm, a 16.2 cm layer of iron should be used. Hence, for practical reasons, 16.5 cm of iron will be implemented.

Figure 2 represents the primary barrier's final design with an additional iron thickness. As shown, there are two options: (i) use one iron layer weighing approximately 16.9 tons or (ii) use multilayers of iron with different thicknesses and dimensions. In this case, calculations were conducted in 40 cm steps in horizontal and vertical directions. This was done because the layers will be arranged and fixed on the wall using 40 cm × 40 cm tiles of iron, which will be well welded together. The thickness of each layer is determined based on its distance from the isocenter and the slant path of radiation inside the concrete, as shown in Figure 2. Using the multi-layers of iron requires only 13 tons, saving about 3.6 tons. Notably, the thickness of the existing (1.35 m) and new concrete (0.5 m) is adequate if the IDR criteria were not applied.

The ceiling shielding calculations at point G were performed similarly to those followed in primary barriers B and B'. Although the occupancy factor of the roof is very small, the final thickness is determined based on 20 μSv/h criteria at 10 MV (FFF).

Table 2 summarizes the shielding calculation results obtained for the two workload cases. Notably, the maximum barrier's thickness is obtained when IDR criteria were applied at 10 MV (FFF), that is, ≤20 μSv/h, regardless of any thickness obtained at 6 MV or 10 MV (FF). Table 3 summarizes the expected equivalent dose received by personnel behind the primary barriers B and B'.

3.3. Secondary barriers at points C, D, E, F, and G

Points C, D, E, and F have the same scattering angle (28° – 29°) and the same slant radiation path inside the concrete (approximately 1.13 cm). Accordingly, the following observations are made:

(i) The distances of points C and D from the isocenter are longer than those of E and F
(ii) The occupancy factor at C and E is greater than that at points E and F
(iii) The dose constraint at points C and E is less than at points E and F.

Thus, the shielding requirements at points C and D are greater than those needed for E and F. Similarly, the shielding requirements at point G are less than those required at points C and D since its distance from the isocenter is much longer (8.24 m) and its scattering angle is greater (65°). Therefore, if the existing thickness (1.0 m) of all secondary barriers is adequate at points C or D, it will also be sufficient at E, F, and G. The shielding requirement at point C is presented by evaluating the leakage and patient scatter at this barrier.

The use factor for leakage radiation is 1, given that it hits all barriers regardless of the linac's head angle. Secondary barriers adjacent to the primary barriers receive significant patient scatter radiation only when the primary beam is directed at the primary barriers. Thus, assuming that the use factor at points C, D, E, and F equals 0.25, that is, the same use factor as primary barriers will be reasonable. Using a use factor of 1 for an adjacent secondary barrier exaggerates conservatism. This study uses this assumption and verifies its validity through an experimental radiation survey at a later stage. Notably, the use factor for secondary barriers adjacent to the primary barriers in NCRP 151, SRS 47, and IPEM 75 equals unity.

Although the average field size used in treating patients daily is $20 \times 20\ cm^2$, the same approach mentioned in NCRP

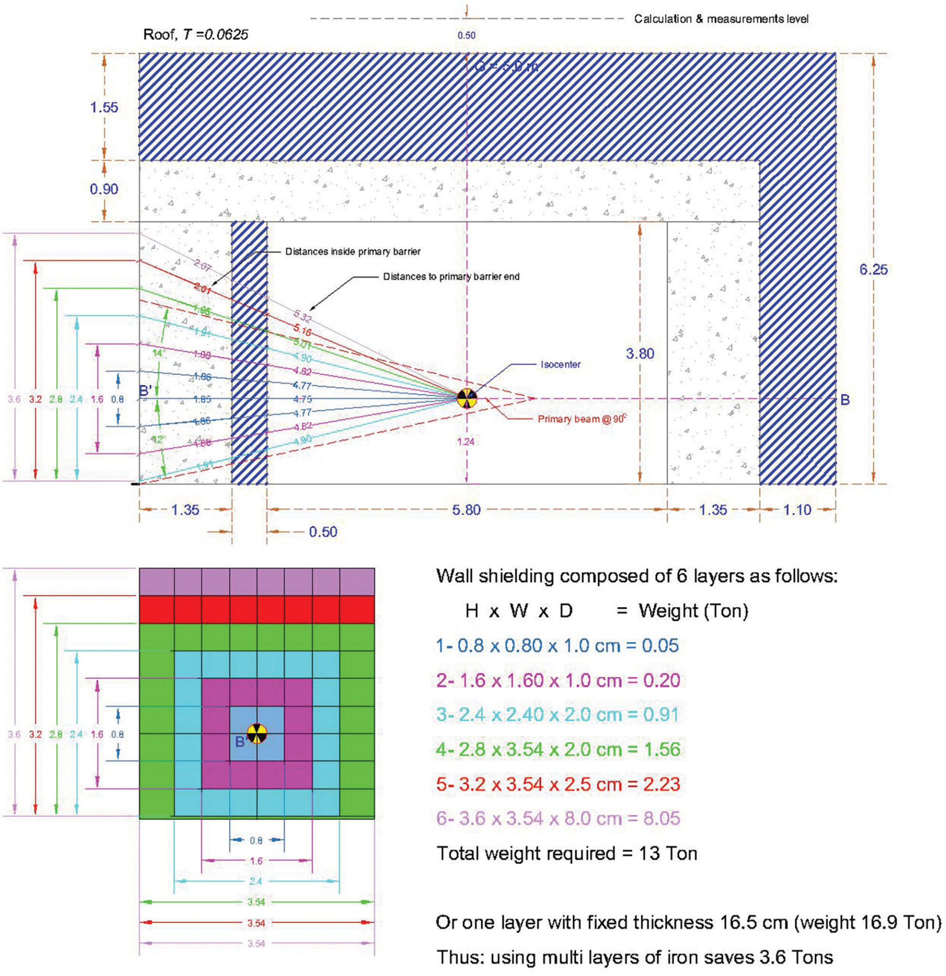

Wall shielding composed of 6 layers as follows:

H x W x D = Weight (Ton)

1- 0.8 x 0.80 x 1.0 cm = 0.05

2- 1.6 x 1.60 x 1.0 cm = 0.20

3- 2.4 x 2.40 x 2.0 cm = 0.91

4- 2.8 x 3.54 x 2.0 cm = 1.56

5- 3.2 x 3.54 x 2.5 cm = 2.23

6- 3.6 x 3.54 x 8.0 cm = 8.05

Total weight required = 13 Ton

Or one layer with fixed thickness 16.5 cm (weight 16.9 Ton)

Thus: using multi layers of iron saves 3.6 Tons

Figure 2. Primary barrier detail design composed of ordinary concrete and multi-layers of iron with different dimensions. Image created by the author.

Table 2. Summary of the shielding calculation results for primary barriers

Barrier thickness demands (in m)	Workload (No. patient/day)	Criteria, concrete thickness (m), and no. TVL			% Increment in shielding thickness due to using IDR criteria, $\frac{b-a}{a}$
		[a]Weekly dose constraints	IDR=7.5 μSv/h (10 MV FF)	[b]IDR=20 μSv/h (10 MV FFF)	
Point B	40 patients/day	2.07 m no. TVL=5.3	2.35 m no. TVL=6.04	2.42 m no. TVL=6.21	17.01
	60 patients/day	2.18 m no. TVL=5.61	2.35 m no. TVL=6.04	2.42 m no. TVL=6.21	10.73
Point B' (maze of the adjacent bunker)	40 patients/day	1.68 m no. TVL=4.31	2.38 m no. TVL=6.11	2.45 m no. TVL=6.29	45.96
	60 patients/day	1.75 m no. TVL=4.61	2.38 m no. TVL=6.11	2.45 m no. TVL=6.29	36.45

Abbreviations: FF: Flattening filter; FFF: Flattening-free filter; IDR: Instantaneous dose rate; MV: Megavoltage; TVL: Tenth-value layer.

151, SRS 47, and IPEM 75 will be followed, i.e., a field size of 40 × 40 cm^2 will be used as a conservative measure, despite it being overly conservative.

In summary, it was deemed unjustified to apply two overly conservative assumptions simultaneously when calculating shielding requirements for secondary barriers:

Table 3. The expected equivalent dose received by personnel behind the primary barriers B and B'

Barrier	Dose limit	Dose constraint	Expected annual dose	% of annual dose constraint
B	1 mSv/year	1 mSv/year	40 patient/day: 71.7 μSv 60 patients/day: 134.2 μSv	100×71.1/1,000=7.17 100×134.2/1,000=13.42
B'	20 mSv/year	6 mSv/year	40 patient/day: 71.45 μSv 60 patients/day: 134 μSv	100×71.1/6,000=1.191 100×134.2/6,000=2.23

(i) using a 40 × 40 cm field size instead of the average 20 × 20 cm and (ii) assigning a use factor of 1 for secondary barriers adjacent to primary barriers. Therefore, the first assumption was retained, while the second was revised to reflect practical clinical conditions better, as previously indicated.

3.3.1. Case 1: Working load of 40 patients/day

The weekly unshielded leakage dose at 10 MV (20 patients) is presented in Equation XV.

$$855 \times 0.001/5.12^2 = 32.6\ mSv/week \qquad \text{(XV)}$$

The transmission factor was deemed as $B = 6.13 \times 10^{-4}$ to reduce this value to the weekly dose constraints for the public (20 μSv/week). Accordingly, the number of TVLs needed to achieve this value is 3.21; considering that the TVL leakage for 10 MV is 30.5 cm, the secondary barrier should be 0.98 m thick.

The weekly unshielded leakage dose at 6 MV (20 patients) is presented in Equation XVI.

$$855 \times 0.001/5.12^2 = 32.6\ mSv/week \qquad \text{(XVI)}$$

Similarly, the transmission factor becomes $B = 6.13 \times 10^{-4}$ to reduce the obtained value. The number of TVLs needed to achieve this value is 3.21; considering that the TVL leakage for 6 MV is 27.9 cm, the secondary barrier should be 0.90 m thick. A simple calculation shows that the total leakage radiation from 6 and 10 MV at the existing slant thickness (1.14 m) equals 5.95 μSv/week.

The weekly unshielded patient scatter dose at 10 MV (20 patients) is presented in Equation XVII.

$$W \times T \times U \times a \times F^2/400 \times d^2 = 360 \times 1 \times 0.25 \times 3.18 \times 10^{-3} \times 1{,}600/400 \times 5.12^2 = 43.7\ mSv/week \qquad \text{(XVII)}$$

To reduce this value to the weekly dose constraints for the public, the transmission factor becomes $B = 4.57 \times 10^{-4}$. Accordingly, the number of TVLs needed to achieve this value is 3.34; taking into consideration that the TVL leakage for 10 MV is 27.5 cm, the secondary barrier should be 0.92 m thick.

The weekly unshielded patient scatter dose at 6 MV (20 patients) is presented in Equation XVIII.

$$W \times T \times U \times a \times F^2/400 \times d^2 = 360 \times 1 \times 0.25 \times 2.77 \times 10^{-3} \times 1{,}600/400 \times 5.12^2 = 38\ mSv/week \qquad \text{(XVIII)}$$

To reduce this value to the weekly dose constraints for the public, the transmission factor becomes $B = 4.28 \times 10^{-4}$. Accordingly, the number of TVLs needed to achieve this value is 3.28; considering that the TVL leakage for 6 MV is 26.1 cm, the secondary barrier should be 0.86 m thick. A simple calculation shows that the total patient scatter radiation from 6 and 10 MV at the existing slant thickness (1.14 m) equals 4.75 μSv/week.

Accordingly, the total weekly dose from leakage and scatter radiation at point C equals 10.7 μSv, less than the weekly dose constraints, 20 μSv/week. Hence, the existing thickness is adequate for the workload of 40 patients/day.

3.3.2. Case 2: Working load of 60 patients/day

The weekly unshielded leakage dose at 10 MV (40 patients) is presented in Equation XIX.

$$1{,}710 \times 0.001/5.12^2 = 65.2\ mSv/week \qquad \text{(XIX)}$$

To reduce this value to the weekly dose constraints for the public, the transmission factor becomes $B = 3.06 \times 10^{-4}$. Accordingly, the number of TVLs needed to achieve this value is 3.51; considering that the TVL leakage for 10 MV is 30.5 cm, the secondary barrier should be 1.07 m thick.

The weekly unshielded dose at 6 MV (20 patients) is presented in Equation XX.

$$855 \times 0.001/5.12^2 = 32.6\ mSv/week \qquad \text{(XX)}$$

The transmission factor becomes $B = 6.14 \times 10^{-4}$ to reduce this value to the weekly dose constraints for the public. Hence, the number of TVLs needed to achieve this value is 3.21. Given that the TVL leakage for 6 MV is 27.9 cm, the secondary barrier should be 0.90 m thick. A simple calculation shows that the total leakage radiation from 6 and 10 MV at the existing slant thickness is 14.57 μSv/week.

The weekly unshielded patient scatter dose at 10 MV (40 patients) is presented in Equation XXI.

$$720 \times 1 \times 0.25 \times 3.18 \times 10^{-3} \times 1{,}600/400 \times 5.12^2 = 87.3\ mSv/week \qquad \text{(XXI)}$$

To reduce this value to the weekly dose constraints for the public, the transmission factor becomes $B = 2.3 \times 10^{-4}$. Accordingly, the number of TVLs needed to achieve this value is 3.64; considering that the TVL leakage for 10 MV is 27.5 cm, the secondary barrier should be 1 m thick.

The weekly unshielded patient scatter dose at 6 MV (20 patients) is presented in Equation XXII.

$$360 \times 1 \times 0.25 \times 2.77 \times 10^{-3} \times 1{,}600/400 \times 5.12^{2} = 38\ mSv/week \quad \text{(XXII)}$$

The transmission factor becomes $B = 4.28 \times 10^{-4}$ to reduce this value to the weekly dose constraints. Hence, the number of TVLs needed to achieve this value is 3.28; considering that the TVL leakage for 6 MV is 26.1 cm, the secondary barrier should be 0.86 m thick. A simple calculation shows that the total scatter radiation from 6 and 10 MV at the existing slant thickness equals 7.87 μSv/week.

Accordingly, the total weekly dose from leakage and scatter radiation at point C is 22.44 μSv. Given that the total dose of 22.44 μSv is only slightly greater than the weekly dose constraint, 20 μSv, the existing thickness is left unaltered. Since the existing secondary barrier at point C, with a thickness of 1 m, is considered adequate, the secondary barriers at points D, E, F, and G are also regarded as adequate.

4. Discussion

The shielding calculations performed, particularly for primary barriers B and B', showed that the final thickness of the barriers is determined solely by the IDR criteria at 10 MV in FFF mode. Specifically, the barrier thickness must ensure that the IDR does not exceed 20 μSv/week at the maximum dose rate at the isocenter. In practical terms, neither the standard workload (40 patients/day) nor the heavy workload (60 patients/day) influences the determination of barrier thickness. Furthermore, the IDR criteria for 6 MV, whether in FF or FFF mode, are irrelevant in this context, as their IDRs are inherently lower than those for 10 MV. This leads to several important questions:

(i) If the thickness of the primary barrier can be determined in a single calculation step, what is the practical value of performing extensive and time-consuming calculations shown above?
(ii) Although applying the IDR criterion significantly reduces the personal equivalent doses behind the barrier, does it truly satisfy the core radiation protection principles, namely optimization; in other words, is the thickness justified and well optimized?
(iii) Do the IDR criteria reflect the same parameters and conditions used in evaluating the barrier thickness by the equations mentioned in NCRP 151 or SRS 47?

Certainly, applying the IDR criteria does not comply with the optimization principle. Applying the dose constraint principle provides a significant safety factor to protect personnel in radiotherapy facilities. In addition, the analytical equations listed in NCRP 151 and SRS 47 for primary barriers, in particular, are highly conservative as they are formulated without accounting for the presence of patients or phantoms in the path of the radiation. Moreover, the IDR criteria do not consider use or occupancy factors, which are fundamental in traditional shielding design. This omission leads to overly conservative estimates, resulting in exaggerated barrier thicknesses. Therefore, the current application of the IDR criteria in determining the final barrier thickness should be reconsidered, or its intended role should be more clearly defined.

In this context, it is important to present the expected IDR behind the primary barriers based on the barrier thicknesses determined using the analytical equations provided in NCRP 151 and SRS 47. Table 4 shows the expected dose rate for both FF and FFF modes at the actual barrier thicknesses obtained at the workloads of 40 and 60 patients per day. The expected weekly equivalent dose and its percentage to the weekly dose constraint are also included. Based on the table, all the IDRs for FF listed significantly exceed 7.5 μSv/h, and all the IDR values of FFF exceed 20 μSv/h. Despite these exceedances, the expected equivalent doses behind the barrier remain well below the weekly dose constraint. Therefore, the current approach to applying IDR (FF/FFF) criteria should be reconsidered. The following recommendations are proposed to optimize their usage:

Table 4. IDR of FF and FFF behind the primary barriers B and B' at the thicknesses obtained using NCRP 151 analytical equations

Barrier ID (patients/day)	Thickness (m)	IDR (FF) 600 MU/min	IDR (FFF) 2,400 MU/min	P_w, weekly dose constraint	P_{cw}, weekly equivalent dose	P_{cw}/P_w (%)
B (60)	2.12	20 μSv/h	80 μSv/h	20 μSv	10.88 μSv	54.4
B (40)	2.07	40 μSv/h	160 μSv/h	20 μSv	11.94 μSv	59.7
B' (60)	1.95	240 μSv/h	960 μSv/h	120 μSv	67.22 μSv	56.02
B' (40)	1.68	480 μSv/h	1,920 μSv/h	120 μSv	75.85 μSv	63.21

Abbreviations: FF: Flattening filter; FFF: Flattening-free filter; IDR: Instantaneous dose rate; NCRP 151: National Council on Radiation Protection and Measurements Report No. 151.

(i) The IDR (FF/FFF) criteria could only be used after incorporating the patient transmission factor and verified experimentally using appropriate phantoms
(ii) Since no patient or phantoms are used while applying the IDR (FF/FFF) criteria, these criteria should be used exclusively for shielding effectiveness verification and validation
(iii) The IDR (FF/FFF) values should not be used to determine the equivalent dose behind the barriers; instead, they should verify the barriers' transmission factor and refine the expected equivalent dose only when barrier densities differ from that used in calculations
(iv) During shielding verification, it is sufficient to use IDR only in FF mode, as these dose rates are lower than those in FFF mode
(v) High dose rate measurements using IDR (FF/FFF) should be acknowledged only in the context of shielding effectiveness.

Therefore, it is necessary to enhance the safety culture and professional awareness among workers in radiotherapy units and regulatory bodies. There must be a clear understanding that the operational context of medical linacs in radiotherapy fundamentally differs from that of nuclear medicine. Radiation measurements using the IDR (FF/FFF) reflect testing conditions, not working conditions. High radiation levels observed during these tests are not indicative of typical staff exposure but rather a tool to validate the adequacy of structural shielding.

Certainly, regulatory authorities can set a reasonable maximum level for IDR (FF/FFF) during shielding efficiency tests based on the occupancy factor and the personnel behind the primary barriers. However, the higher it is, the lower the degree of overestimation in the required wall thickness. In any case, shielding efficiency tests and the expected high radiation readings can be performed safely under a strict radiation protection program and the supervision of a qualified radiation protection expert.

5. Conclusion

This study represents a case study for upgrading the shielding of an existing Co-60 radiotherapy bunker to accommodate a medical linac operating at 6 MV and 10 MV in FF and FFF modes. Shielding calculations were performed systematically using analytical equations listed in NCRP 151, SRS 47, and IPEM 75.

The shielding evaluation took into account a standard operating workload (40 patients/day) and an overload (60 patients/day) of 50% for each accelerator energy, with the final wall thickness restricted so that the expected IDR behind the primary barriers in FF and FFF modes do not exceed 7.5 μSv/h and 20 μSv/h, respectively.

Results showed that adhering to the IDR criteria yields an increment in shielding demands ranging from 11% to 46% depending on the dose constraints (public or occupational) as well as on the occupancy factor of the adjacent areas. This will be significantly reflected in the cost of the linac vault. Moreover, complying with IDR criteria reduces the expected equivalent dose behind barriers ranging from 1.2% to 13.4% of the dose constraints. The results proved that applying the IDR criteria yields a violation of the radiation protection principles, in particular, optimization. On the other hand, non-complying with the IDR criteria, the expected weekly equivalent dose behind barriers still shows conservative values ranging from 54% to 63% of the weekly dose constraints.

Thus, this study presents an alternative approach to use the IDR criteria optimally. This study concludes that the current values of IDR, that is, ≤7.5 μSv/h at FF and ≤20 μSv/h at FFF, can be used provided that the patient's transmission factor is included, or higher values of IDR are used only when testing the shielding efficiency; the higher the IDR adopted, the lower the cost of the linac vault.

Some workers may not accept the newly adopted high IDR due to their lack of understanding of how shielding requirements of a linac bunker are obtained. The workers, staff, and regulatory bodies should recognize that such high IDRs are expected only at extreme conditions used to verify the shielding effectiveness measurements. Such measurements are made occasionally, just after shielding implementations, and never be experienced during daily working normal conditions. Such high dose rates could be measured safely remotely under the supervision of a professional radiation protection expert, considering all protective measures.

Therefore, the safety culture and professional awareness regarding the working, inspecting or authorizing linac's bunker should be raised and flourished among working staff and regulatory bodies, particularly in developing countries.

Further studies should focus on evaluating the actual personal equivalent doses received by individuals behind shielding barriers in different radiotherapy units and comparing them with the thickness of those barriers. These studies should focus on linac-based radiotherapy units that use the FFF technology with different workloads that cover different treatment protocols and modalities. Relevant international institutions, especially the International Commission on Radiological Protection, could launch a task group to reconsider the concept of IDR in radiotherapy units – how to use it, and the purpose of its use – followed by necessary recommendations to ensure achieving an actual balance between the cost of shielding barriers and the expected equivalent personal doses behind these barriers. The experimental validation of the shielding calculations presented in this study will be reported in a separate article.

Acknowledgments

None.

Funding

None.

Conflict of interest

The author declares he has no competing interests.

Author contributions

This is a single-authored article.

Ethics approval and consent to participate

Not applicable.

Consent for publication

Not applicable.

Availability of data

All data are presented within the manuscript.

References

1. Jeraj R, Mackie TR, Balog J, *et al*. Radiation characteristics of helical tomotherapy. *Med Phys*. 2004;31(2):396-404.

   doi: 10.1118/1.1639148

2. Vassiliev ON, Titt U, Pönisch F, Kry SF, Mohan R, Gillin MT. Dosimetric properties of photon beams from a flattening filter free clinical accelerator. *Phys Med Biol*. 2006;51(7):1907-17.

   doi: 10.1088/0031-9155/51/7/019

3. Cashmore J. The characterization of unflattened photon beams from a 6 MV linear accelerator. *Phys Med Biol*. 2008;53(7):1933-1946.

   doi: 10.1088/0031-9155/53/7/009

4. Kragl G, Af Wetterstedt S, Knäusl B, *et al*. Dosimetric characteristics of 6 and 10MV unflattened photon beams. *Radiother Oncol*. 2009;93(1):141-146.

   doi: 10.1016/j.radonc.2009.06.008

5. Georg D, Knöös T, McClean B. Current status and future perspective of flattening filter free photon beams. *Med Phys*. 2011;38(3):1280-1293.

   doi: 10.1118/1.3554643

6. Dzierma Y, Licht N, Nuesken F, Ruebe C. Beam properties and stability of a flattening-filter free 7 MV beam-an overview. *Med Phys*. 2012;39(5):2595-2602.

   doi: 10.1118/1.3703835

7. Hrbacek J, Lang S, Klöck S. Commissioning of photon beams of a flattening filter-free linear accelerator and the accuracy of beam modeling using an anisotropic analytical algorithm. *Int J Radiat Oncol Biol Phys*. 2011;80(4):1228-1237.

   doi: 10.1016/j.ijrobp.2010.09.050

8. Kragl G, Albrich D, Georg D. Radiation therapy with unflattened photon beams: Dosimetric accuracy of advanced dose calculation algorithms. *Radiother Oncol*. 2011;100(3):417-423.

   doi: 10.1016/j.radonc.2011.09.001

9. Lang S, Reggiori G, Puxeu Vaquee J, *et al*. Pretreatment quality assurance of flattening filter free beams on 224 patients for intensity modulated plans: A multicentric study. *Med Phys*. 2012;39(3):1351-1356.

   doi: 10.1118/1.3685461

10. Paynter D, Weston SJ, Cosgrove VP, Evans JA, Thwaites DI. Beam characteristics of energy-matched flattening filter free beams. *Med Phys*. 2014;41(5):052103.

    doi: 10.1118/1.4871615

11. Xiao Y, Kry SF, Popple R, *et al*. Flattening filter-free accelerators: A report from the AAPM Therapy Emerging Technology Assessment Work Group. *J Appl Clin Med Phys*. 2015;16(3):5219.

    doi: 10.1120/jacmp.v16i3.5219

12. Budgell G, Brown K, Cashmore J, *et al*. IPEM topical report 1: guidance on implementing flattening filter free (FFF) radiotherapy. *Phys Med Biol*. 2016;61(23):8360-8394.

    doi: 10.1088/0031-9155/61/23/8360

13. Dalaryd M, Kragl G, Ceberg C, *et al*. A Monte Carlo study of a flattening filter-free linear accelerator verified with measurements. *Phys Med Biol*. 2010;55(23):7333-7344.

    doi: 10.1088/0031-9155/55/23/010

14. Georg D, Kragl G, Wetterstedt S, McCavana P, McClean B, Knöös T. Photon beam quality variations of a flattening filter free linear accelerator. *Med Phys*. 2010;37(1):49-53.

    doi: 10.1118/1.3264617

15. Kragl G, Baier F, Lutz S, Albrich D, *et al*. Flattening filter free beams in SBRT and IMRT: Dosimetric assessment of peripheral doses. *Z Med Phys*. 2011;21(2):91-101.

    doi: 10.1016/j.zemedi.2010.07.003

16. Almberg SS, Frengen J, Lindmo T. Monte Carlo study of in-field and out-of-field dose distributions from a linear

accelerator operating with and without a flattening-filter. *Med Phys*. 2012;39(8):5194-5203.

doi: 10.1118/1.4738963

17. IPEM Report 75. In: Horton P, Eaton D, editors. *Design and Shielding of Radiotherapy Treatment Facilities*. 2nd ed. United Kingdom: IOP Publishing; 2017.
18. International Atomic Energy Agency Safety Reports Series, No.47. *Radiation Protection in the Design of Radiotherapy Facilities*. Austria: IAEA; 2006.
19. NCRP Report No. 151. *Structural Shielding Design and Evaluation for Megavoltage x- and Gamma-Ray Radiotherapy Facilities. National Council on Radiation Protection and Measurements (NCRP)*; 2005.
20. Rijken J, Bhat M, Crowe S, Trapp J. Conservatism in linear accelerator bunker shielding. *Australas Phys Eng Sci Med.* 2019;42(3):781-787.

    doi: 10.1007/s13246-019-00782-1
21. Rijken J, Towns S, Healy B. The need to update NCRP 151 data for 10 MV linear accelerator bunker shielding based on new measurements and Monte Carlo simulations. *J Radiol Prot*. 2021;41(4):842-852.

    doi: 10.1088/1361-6498/ac2e0b
22. The 2007 recommendations of the international commission on radiological protection. ICRP Publication 103. *Ann ICRP.* 2007;37(2-4):1-332.

    doi: 10.1016/j.icrp.2007.10.003

ACCSCIENCE PUBLISHING

Advances in Radiotherapy & Nuclear Medicine

ORIGINAL RESEARCH ARTICLE

^{18}F-FDG uptake in patients with hypercholesterolemia using a standard compartmental modeling approach

Mamdouh S. Al-enezi*

Department of Diagnostic Radiology, College of Applied Medical Science, University of Hail, Hail, Saudi Arabia

Abstract

Hypercholesterolemia is a major risk factor of atherosclerotic cardiovascular disease. However, current risk stratification models lack consideration of calcium burden. This study aimed to examine the association between calcium burden and *inflammatory response in hypercholesterolemia patients*. Eighteen participants were prospectively scheduled for 18F-fluorodeoxyglucose (^{18}F-FDG) PET/CT examination. They were classified into a control group (CL, n=4), a hypercholesteremia group (HC, n=8), and a stable angina group (SA, n=6). Arterial calcium was defined at attenuation ≥130 Hounsfield units in arterial regions of interest (ROIs), and calcium density was divided into four groups based on the Agatston strategy. Calcium area was defined by at least two adjoining pixels and normalized to artery area, forming two groups based on the mean area. The metabolic rate of glucose (MRGlu) was estimated using a two-tissue compartment model. For all ROIs, MRGlu was significantly higher in both HC and SA groups compared to CL (p<0.05). Among no-calcium groups (CL, HC, and SA), no statistical significance was observed (p>0.05). In with-calcium groups, MRGlu in HC was significantly higher than in CL and SA (p<0.05). At the highest calcium density cluster, the difference between CL and HC was also significant (p<0.05). CL and SA showed a similar pattern of decreasing MRGlu with increasing calcium area (p<0.05 when compared with no-calcium), while the HC group showed a marked increase in MRGlu with higher calcium area (p<0.05) compared to CL and AS. Hypercholesterolemia is associated with increased glucose metabolism. Higher calcium area and density in hypercholesterolemia patients appear metabolically active. The results suggest that incorporating calcium burden in hypercholesterolemia risk stratification models may enhance risk assessment.

Keywords: Hypercholesterolemia; Atherosclerosis; Calcium; Inflammation; Computed tomography; Positron emission tomography; Fluorodeoxyglucose; Compartmental modeling

***Corresponding author:**
Mamdouh S. Al-enezi
(ms.alenezi@uoh.edu.sa)

Citation: Al-enezi, MS. ^{18}F-FDG uptake in patients with hypercholesterolemia using a standard compartmental modeling approach. *Adv Radiother Nucl Med.* 2025;3(2):52-60. doi: 10.36922/arnm.8540

Received: January 15, 2025

1st revised: February 25, 2025

2nd revised: April 20, 2025

Accepted: April 23, 2025

1. Introduction

Cardiovascular disease (CVD) refers to all pathologies that affect the blood circulatory system. It encompasses a set of heterogeneous diseases, with the most common being atherosclerotic cardiovascular disease (ASCVD).[1,2] ASCVD is the main CVD subtype responsible for both mortality and morbidity.[3] Older adults are at high risk of ASCVD and its complications.[4-6]

ASCVD begins with histologic changes within the arterial wall, driven by inflammation and other factors. Consequently, the permeability of endothelial cells layer increases, resulting in lipid accumulation and infiltration of inflammatory cells within the arterial wall, leading to the formation of atherosclerotic plaque.[7]

These lesions are progressive and may advance to cause a significant limitation or obstruction of blood flow, in addition to artery-to-artery thromboembolism.[8] ASCVD presents in varying degrees of complexity, ranging from stable to acute clinical events,[9] and about 50% of ASCVD patients who die suddenly have no prior warning signs.[3]

Several known factors contribute to atherosclerosis and its downstream sequelae leading to acute clinical events. Among these, hypercholesterolemia is a key factor.[10] Hypercholesterolemia has been found to induce atherosclerosis in both human and experimental animals through several atherogenic processes,[10,11] and is considered a major cause of the initiation and progression of ASCVD, increasing the risk of ASCVD up to five-fold.[12]

Common risk stratification models for ASCVD in patients with hypercholesterolemia include the cholesterol-year score,[13] the Spanish Familial Hypercholesterolemia Cohort Study,[14] and the French Familial Hypercholesterolemia Registry.[15] However, these models lack consideration of calcium burden in hypercholesterolemic patients. Atherosclerosis imaging techniques allow for a more accurate analysis of the pathological processes and plaque characteristics, which may refine ASCVD risk assessment.

Computed tomography (CT) is a very frequently used imaging modality to assess calcium burden in ASCVD.[16] Although the role of calcium burden is debated – considered a marker of vulnerable plaque in some studies,[17,18] while others associate plaque calcification with plaque stability and an inverse relationship with ASCVD risk[19,20] – it remains an important parameter.

^{18}F-Fluorodeoxyglucose (^{18}F-FDG) positron emission tomography/CT (PET/CT) has proven to be a powerful molecular imaging modality for analyzing inflammatory activity in atherosclerotic plaques, providing accurate information on vascular metabolic activity.[16,18,21,22]

The extent and density of aortic calcification have been shown to correlate with increased atherosclerotic inflammatory activity, as measured by ^{18}F-FDG uptake.[22,23] In addition, calcium burden on CT and ^{18}F-FDG uptake on PET have been correlated in the abdominal aorta and iliac arteries.[16,24]

Thus, the aim of this study is to explore the association between calcium burden in the arterial walls of the aorta and iliac arteries (as assessed by CT imaging) and inflammatory activities (quantified by 18F-FDG uptake using a standard compartmental modeling approach) in hypercholesterolemic patients. This aim extends to examining the relationship between calcium burden, cholesterol burden, and inflammatory response – as defined by the metabolic rate of glucose (MRGlu) – and whether the calcium burden in hypercholesterolemic patients differs from that in individuals with normal lipid levels or stable angina (SA), based on MRGlu values.

2. Materials and methods

Eighteen participants scheduled for ^{18}F-FDG CT/PET examination were prospectively enrolled in this study. The inclusion criteria comprised individuals with hypercholesterolemia, SA, and healthy controls who consented to participate. Classification was based on clinical examination, including the absence of clinical signs and symptoms, and normal blood pressure, glucose, and lipid profile.

Exclusion criteria included oncology patients and glucose levels >7 mmol/L.[25] Measurements of glucose, total cholesterol (TC), high-density lipoprotein cholesterol (HDL-C), low-density lipoprotein cholesterol (LDL-C), triglyceride (TG), and C-reactive protein (CRP) were obtained from all participants after overnight fasting.

Low-dose unenhanced CT images were acquired immediately before the PET acquisition using a PET/CT scanner (Philips Medical Systems, Netherlands) and were used for attenuation and scatter correction, anatomic localization, and calcium burden. Dynamic PET images were acquired over 30 min immediately following a bolus intravenous injection of ^{18}F-FDG radiopharmaceutical agent (Sherbrooke Molecular Imaging Center [CIMS], CIUSSS de l'Estrie - Centre Hospitalier Universitaire de Sherbrooke, Canada). PET and CT images were reconstructed using a Philips Gemini TF 16 PET/CT scanner (Philips Medical Systems, Netherlands), equipped with time-of-flight capability. The injected activity of ^{18}F-FDG ranged from 220 to 350 MBq, normalized to the participant's weight. PET data were reconstructed using the iterative 3D row action maximum likelihood algorithm into 26 frames (12 × 2 min, 8 frames × 4 min, and 6 frames × 24 min). CT and PET voxel dimensions were $1 \times 1 \times 4$ mm^3 and $4 \times 4 \times 4$ mm^3, respectively.

Regions of interest (ROIs) for arteries were segmented semi-automatically from CT images using an edge-based active contour model to delineate the optimal object boundary.[26] Each ROI was validated using the colocalized ROI on the corresponding PET slice – identified using Digital Imaging and Communications in Medicine header information at the first 2 min, segmented similarly to the CT images. The arterial wall calcification on CT was defined visually by attenuation values ≥130 Hounsfield units. Calcium density was divided into four groups (K1 – K4) from the lowest to the highest density, following the Agatston *et al.* scoring strategy.[27] Calcium area was defined as at least two adjoining pixels within the CT arterial ROI with attenuation ≥130 Hounsfield units, and was normalized to the artery area to yield the calcium area ratio. This ratio was then divided into two groups based on whether the value was below or above the mean calcium area ratio (20%).[28]

Arterial and tissue ^{18}F-FDG activity curves as a function of time were extracted using factor analysis of dynamic sequence (FADS) in dynamic PET data. Partial volume correction was performed using the modified Müller-Gartner method.[29] The transport rate constants K_1, K_2, and K_3 were calculated using a two-tissue-compartment model implemented in MATLAB R2024b (The MathWorks, USA). Detailed descriptions of this model can be found elsewhere.[30]

The net influx rate (K_n) of ^{18}F-FDG was calculated using Equation I.

$$K_n = \frac{K_1 \times K_3}{K_2 + K_3} \tag{I}$$

where K_1, K_2, and K_3 are transport rate constants; K_n is expressed in mL/g/min assuming a tissue density of 1 g/mL.[31]

The MRGlu per ROI was then calculated using Equation II.

$$\mathrm{MRGlu} = K_n \times \frac{\text{Glucose}}{\text{Lumped constant}} \times 100 \tag{II}$$

where K_n is the net influx rate; MRGlu is expressed in μmol/100 g/min, with the lumped constant set at 0.89.[32] MRGlu values were assessed in the aorta and iliac arteries to estimate inflammatory activities.

Continuous data were tested for normality using the D'Agostino-Pearson omnibus test. The goodness of fit was evaluated using Pearson's correlation coefficient. Parametric variables were expressed as mean ± standard deviations (SD) and compared using the Mann–Whitney U test. A non-significant threshold was set at $p>5\%$. All statistical analyses were conducted in MATLAB R2024b.

3. Results

Participants were classified into three groups based on clinical characteristics: Control subjects (CL, $n=4$; mean age=70.00±3.91 years), hypercholesteremia subjects (HC, $n=8$; mean age=69.25±3.96 years), and SA patients (SA, $n=6$; mean age=70.00±1.50 years).

The clinical variables and the estimated MRGlu values for all three groups are presented in Table 1, expressed as mean ± SD. These measurements were collected before the ^{18}F-FDG-PET examinations.

The average glucose levels for all participants were within the recommended range, as detailed in Table 1 (expressed in mmol/L).[25]

The standard irreversible two-tissue compartment model for ^{18}F-FDG consists of two compartments and four rate constants that describe the transport and metabolism of ^{18}F-FDG (Figure 1A). After cellular uptake, ^{18}F-FDG is phosphorylated by hexokinase into ^{18}F-FDG-6-phosphate, which is metabolically trapped, as it cannot be further degraded or easily dephosphorylated; the metabolized tracer (^{18}F-FDG) compartment (MTC) is assumed to be irreversible with $K_4=0$. The goodness of fit between the raw data and model-fitted curves is represented by the squared Pearson's correlation coefficient (r^2), shown in Figure 1B, ranging from 0.8 to 0.997, with a mean value of 0.94 ± 0.04. Figure 1C displays decay-corrected time-activity curves for the arterial input function (arterial input function, extracted from FADS, solid line), tissue signal (star markers), and model-fitted curves for free and metabolized compartments (FTC and MTC, respectively).

Table 1. The clinical variables for CL, HC, and SA groups

Parameters	CL	HC	SA	*p*
Age (years)	70.00±3.91	69.25±3.96	70.00±1.50	>0.05
Weight (kg)	63.50±5.52	76.92±10.02	80.06±25.60	<0.05
Total cholesterol (mmol/L)	3.43±0.60	5.47±1.29	3.74±0.96	<0.05
High-density lipoprotein cholesterol (mmol/L)	1.36±0.37	1.32±0.21	1.27±0.30	>0.05
Low-density lipoprotein cholesterol (mmol/L)	1.44±0.69	3.46±1.26	1.85±0.53	<0.05
Triglyceride (mmol/L)	1.40±0.59	1.50±0.63	1.36±0.63	>0.05
Glucose (mmol/L)	5.23±0.61	4.58±0.86	5.16±0.33	>0.05
C-reactive protein (mg/L)	2.75±0.12	6.82±7.85	3.93±0.04	<0.05
MRGlu (μmol/100 g/min)	12.50±8.45	15.14±9.89	14.70±8.93	<0.05

Notes: All data expressed as mean±standard deviations; *p* was derived from a statistical comparison among groups using the Mann–Whitney *U* test.
Abbreviations: CL: Control; HC: Hypercholesteremia; SA: Stable angina; MRGlu: Metabolic rate of glucose.

The statistical comparison of total MRGlu values of all ROIs for the CL, HC, and SA groups is illustrated in Figure 2A. Both HC and SA groups had significantly higher MRGlu values compared to the CL group ($p<0.05$). However, there was no significant difference between the HC and SA group ($p>0.05$).

Each group (CL, HC, SA) was further subdivided based on the presence or absence of arterial wall calcium (as determined by CT attenuation values above or below 130 HU) into 6 subgroups: Control group, no calcium (CLN), control group, with calcium (CLC), hypercholesterolemia, no calcium (HCN), hypercholesterolemia, with calcium (HCC), stable angina, no calcium (SAN) and stable angina, with calcium (SAC). The MRGlu values of these groups, compared using the Mann–Whitney U test, are presented in Figure 2B. No significant differences were found among the no-calcium groups (CLN, HCN, and SAN; $p<0.05$). However, among the with-calcium groups, MRGlu values were significantly higher in HCC compared to both CLC and SAC ($p<0.05$). The CLC group had the lowest MRGlu values, significantly different from the SAC group as well ($p<0.05$).

Further, with-calcium segments in each group (CL, HC, SA) were stratified by calcium density using Agatston-based clustering (K1 – K4). Figure 3 shows the mean MRGlu values across calcium density clusters. No stWWWatistical differences were found among groups for clusters K1 – K3 ($p>0.05$). However, in the densest cluster (K4), the HC group had significantly higher MRGlu values compared to the CL group ($p<0.05$), though differences between HC and SA groups were not significant ($p<0.05$).

Figure 4 shows the distribution of MRGlu values for no-calcium ROIs (A0), with-calcium ROIs that possess an area ratio <20% (A1), and with-calcium ROIs that possess an area ratio >20% (A2). In CL and SA groups, MRGlu values decreased with increasing calcium area ratio, with significant changes observed between A0 and A1/A2

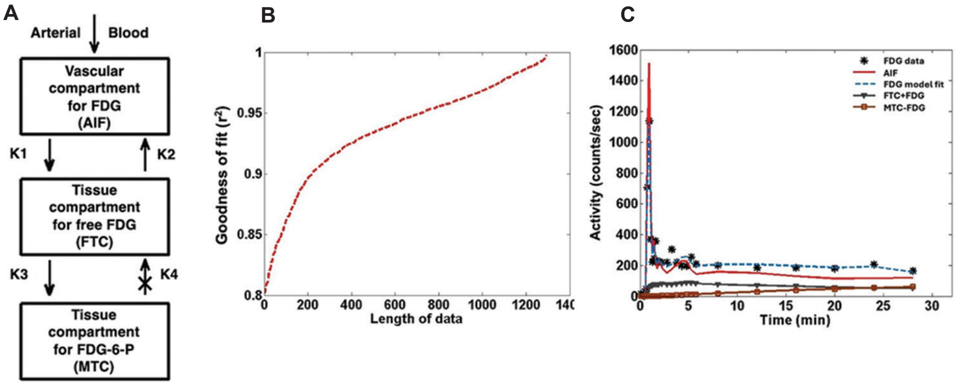

Figure 1. The illustration of 2-tissue compartment model. (A) The standard irreversible (K4=0) two-tissue compartment model for ^{18}F-FDG. (B) The goodness of fit, represented by Pearson's correlation coefficient squared (r^2), for different length of data. (C) Time course of measured ^{18}F-FDG activity in a sample ROI, arterial ^{18}F-FDG activity curve (AIF), and total model-estimated concentrations, such as model fit ($r^2=0.94\pm0.04$), FTC and MTC for ^{18}F-FDG. Abbreviations: MTC: Metabolized tracer compartment; FTC: Free tissue compartment.

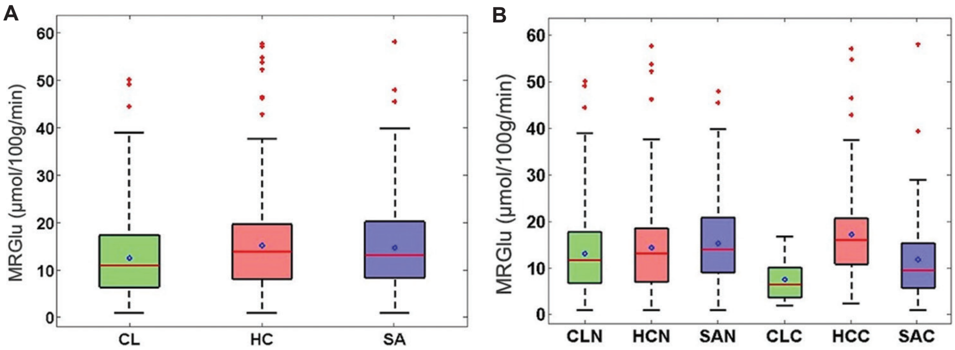

Figure 2. Box-and-whisker-plot analysis for the MRGlu values. (A) Total MRGlu measurements of all ROIs for CL, HC, and SA groups. (B) MRGlu measurements of no-calcium ROIs for the CLN, HCN, and SAN, as well as for with-calcium ROIs for the same groups (CLC, HCC, and SAC).

Note: *Indicates outliers and they were not significant.

Abbreviations: MRGlu: Metabolic rate of glucose; CL: Control; HC: Hypercholesteremia; SA: Stable angina; CLC: Control group, with calcium; HCC: Hypercholesterolemia, with calcium; SAC: Stable angina, with calcium.

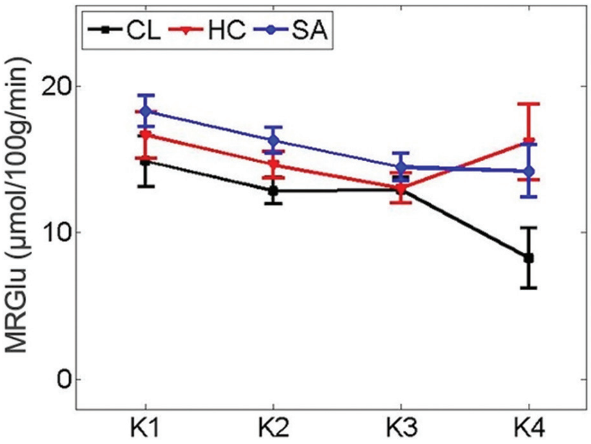

Figure 3. Connected line plot of corresponding MRGlu values for four calcium density clusters (from lower density cluster "K1" to higher density cluster "K4", in ascending order) for CL, HC, and SA groups. A statistically significant difference was observed between CL and both SA and HC ($p<0.05$) at the highest density cluster (K4).

Abbreviations: MRGlu: Metabolic rate of glucose; CL: Control; HC: Hypercholesterolemia; SA: Stable angina.

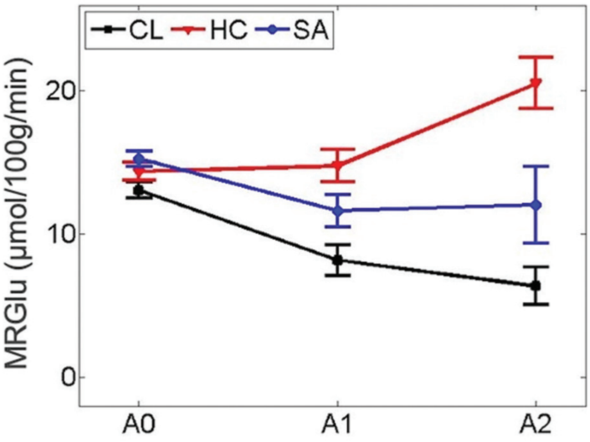

Figure 4. Connected line plot of MRGlu values for no calcium cluster (A0) and two calcium area clusters: ROIs with calcium area ratio <20% (A1) and ROIs with calcium area ratio >20% (A2), for CL, HC, and SA groups. A statistically significant difference ($p<0.05$) was observed in the A2 cluster between CL and both SA and HC groups.

Abbreviations: MRGlu: Metabolic rate of glucose; CL: Control; HC: Hypercholesterolemia; SA: Stable angina.

($p<0.05$). In contrast, the HC group showed a significant increase in MRGlu, particularly at A2, compared to both CL and SA groups ($p<0.05$).

4. Discussion

^{18}F-FDG PET/CT is a highly sensitive molecular imaging modality that enables the assessment of inflammatory activities within atherosclerotic plaques and provides insights into metabolic activity in the vascular wall.[16,18,21] However, the precision and accuracy of quantification methods can vary significantly.

Absolute quantification of ^{18}F-FDG uptake, as used in this study, is more accurate and reproducible than semi-quantitative approaches.[33] A major challenge with the standard compartment model is its reliance on a 60-min acquisition time, which may limit its clinical utility. However, previous studies have demonstrated that a 30-min acquisition is adequate for accurate modeling using a two-tissue compartment model, including for multi-bed acquisitions.[33-37]

Yet, it is not predominantly utilized in clinical practice. Most metrics used in quantifying ^{18}F-FDG uptake in published studies were based on standardized uptake value (SUV) or tissue-to-background ratio (TBR). Although SUV is often utilized and preferred, in atherosclerosis settings, SUV values may be biased due to noticeable variation in arterial region with high background signal.[38] Other sources of variation may include body weight fluctuations over time, injection protocols, and fasting duration, as SUV is sensitive to these factors.[39,40] TBR, as another popular metric, is another view of SUV – it is the result of dividing the two SUV values. In addition, TBR is also subjected to circulation time, which has a major impact on TBR in atherosclerosis settings, making TBR less reproducible.[41]

Moreover, hypercholesterolemia is an important cause of increasing the risk of ASCVD five-fold.[12] Nonetheless, all common risk stratification models[13-15] disregard the calcium burden consideration in risk assessment for hypercholesterolemia patients.

Thus, the aim of this work was to study the association of high attenuation arterial walls in CT imaging and inflammatory activities identified by absolute quantification of 18F-FDG uptake using a standard compartmental modeling approach for hypercholesterolemic patients. The aim is extended to study the calcium burden and its association with cholesterol *burden and inflammatory response* (as defined by MRGlu) *in* hypercholesterolemic patients and whether such calcium burden is differentiated from that seen in normal and SA participants.

Age and HC are tightly correlated to the metabolic activity of glucose (^{18}F-FDG uptake) in the aorta and iliac arteries.[42-44] Such findings are in agreement with the observation herein with regard to the aorta and iliac arteries (Figure 2A); the HC group was shown to have statistically higher MRGlu values compared to the CL group ($p<0.05$).

Calcium intensity and HC have been demonstrated to be positively correlated and also positively associated with acute ASCVD events.[45,46] This aligns with the degree of inflammation and largest calcium density in this present study (Figure 3), where MRGlu values for the HC group at the K4 cluster of calcium density were statistically higher than those for the CL group at the same cluster ($p<0.05$).

Calcium area was shown to be statistically higher in terms of MRGlu values for the HC group at the A2 cluster (area ratio >20%, according to the mean value of calcium area ratio), as illustrated in Figure 4, with reference to both CL and SA groups ($p<0.05$).

Calcium area has been reported to be a positive predictor of CVD.[47,48] In addition, calcium volume was associated with HC in other studies.[47,49] The incidence of vascular calcium burden increases with age, and its presence usually represents advanced atherosclerosis.[50] Calcium burden progression has been linked to metabolic disorders, among which is hypercholesterolemia.[51,52] Moreover, hypercholesterolemia and age are among several factors known to contribute effectively to ASCVD.[11,53-55] Hypercholesterolemia has been also shown to be involved in the subclinical progression of atherosclerosis.[56]

This positive correlation of MRGlu values and calcium burden in hypercholesterolemia patients demonstrated in this study highlights the need for calcium burden consideration in risk stratification models for hypercholesterolemia patients.

In this study, there were some limitations. One limitation is the relatively small number of participants. The second limitation is the cross-sectional design; therefore, a longitudinal study design is necessary to confirm the findings of this study. The third limitation is that the study did not consider sex in the analysis, particularly for calcium density, where a recent study suggested that lower calcium density in women is tightly associated with ASCVD mortality risk, while the situation in men is the reverse (higher calcium density); however, for calcium area, both sexes show a strong association between higher calcium area and ASCVD mortality risk.[57]

5. Conclusion

Hypercholesterolemia is associated with regional glucose metabolism, as identified by the MRGlu on ^{18}F-FDG PET/CT, and it reflects inflammatory activities at the arterial walls in hypercholesterolemia patients. Calcium burden at arterial wall regions – identified by area and density – in these patients is coupled with inflammatory activities. The results suggest that vascular calcium burden may be accelerated by hypercholesterolemia and could be a target of cholesterol-lowering medications. Therefore, incorporating calcium burden consideration into risk stratification models may improve risk assessment in patients with hypercholesterolemia.

Acknowledgments

The author wishes to thank Dr. M. Bentourkia, Dr. Éric Turcotte, Éric Lavallee, and the clinical team at the Sherbrooke Molecular Imaging Centre, Université de Sherbrooke, for their technical assistance.

Funding

None.

Conflict of interest

The author declares no conflicts of interest.

Author contributions

This is a single-authored article.

Ethics approval and consent to participate

The current prospective study was approved by the Research Ethics Committee of the Faculty of Medicine and Health Sciences, University of Sherbrooke, Canada (2019-3145). All participants provided written informed consent for scanning with ^{18}F-Fluorodeoxyglucose positron emission tomography/CT.

Consent for publication

Patients consented on the publication of their data.

Availability of data

The data supporting the findings of this study are available within the article.

References

1. Wong ND, Budoff MJ, Ferdinand K, *et al.* Atherosclerotic cardiovascular disease risk assessment: An American Society for Preventive Cardiology clinical practice statement. *Am J Prev Cardiol.* 2022;10:100335.

   doi: 10.1016/j.ajpc.2022.100335

2. Frąk W, Wojtasińska A, Lisińska W, Młynarska E, Franczyk B, Rysz J. Pathophysiology of cardiovascular diseases: New insights into molecular mechanisms of atherosclerosis, arterial hypertension, and coronary artery disease. *Biomedicines.* 2022;10(8):1938.

   doi: 10.3390/biomedicines10081938

3. Benjamin EJ, Blaha MJ, Chiuve SE, *et al.* Heart disease and stroke statistics-2017 update: A report from the American Heart Association. *Circulation.* 2017;135(10):e146-e603.

   doi: 10.1161/CIR.0000000000000485

4. Yan L, Ye X, Fu L, Hou W, Lin S, Su H. Construction of vulnerable plaque prediction model based on multimodal vascular ultrasound parameters and clinical risk factors. *Sci*

Rep. 2024;14(1):24255.

doi: 10.1038/s41598-024-75375-4

5. Moran AE, Forouzanfar MH, Roth GA, *et al*. Temporal trends in ischemic heart disease mortality in 21 world regions, 1980 to 2010: The Global Burden of Disease 2010 study. *Circulation*. 2014;129(14):1483-1492.

   doi: 10.1161/CIRCULATIONAHA.113.004042

6. Fleg JL, Forman DE, Berra K, *et al*. Secondary prevention of atherosclerotic cardiovascular disease in older adults: A scientific statement from the American Heart Association. *Circulation*. 2013;128(22):2422-2446.

   doi: 10.1161/01.cir.0000436752.99896.22

7. Rafieian-Kopaei M, Setorki M, Doudi M, Baradaran A, Nasri H. Atherosclerosis: Process, indicators, risk factors and new hopes. *Int J Prev Med*. 2014;5(8):927-946.

8. Viedma-Guiard E., Guidoux C, Amarenco P, Meseguer E. Aortic Sources of Embolism. *Front Neurol*. 2021;11:606663.

   doi: 10.3389/fneur.2020.606663

9. Bentzon JF, Otsuka F, Virmani R, Falk E. Mechanisms of plaque formation and rupture. *Circ Res*. 2014;114(12):1852-1866.

   doi: 10.1161/CIRCRESAHA.114.302721

10. Fan J, Watanabe T. Atherosclerosis: Known and unknown. *Pathol Int*. 2022;72(3):151-160.

    doi: 10.1111/pin.13202

11. Prasad K, Mishra M. Mechanism of hypercholesterolemia-induced atherosclerosis. *Rev Cardiovasc Med*. 2022;23(6):212.

    doi: 10.31083/j.rcm2306212

12. Jansen ACM, van Aalst-Cohen ES, Tanck MW, *et al*. The contribution of classical risk factors to cardiovascular disease in familial hypercholesterolaemia: Data in 2400 patients. *J Intern Med*. 2004;256(6):482-490.

    doi: 10.1111/j.1365-2796.2004.01405.x

13. Schmidt HH, Hill S, Makariou EV, Feuerstein IM, Dugi KA, Hoeg JM. Relation of cholesterol-year score to severity of calcific atherosclerosis and tissue deposition in homozygous familial hypercholesterolemia. *Am J Cardiol*. 1996;77(8):575-580.

    doi: 10.1016/s0002-9149(97)89309-5

14. Pérez de Isla L, Alonso R, Mata N, *et al*. Predicting cardiovascular events in familial hypercholesterolemia: The SAFEHEART registry (Spanish familial hypercholesterolemia cohort study). *Circulation*. 2017;135:2133-2144.

    doi: 10.1161/CIRCULATIONAHA.116.024541

15. Béliard S, Boccara F, Cariou B, *et al*. High burden of recurrent cardiovascular events in heterozygous familial hypercholesterolemia: The French familial hypercholesterolemia registry. *Atherosclerosis*. 2018;277:334-340.

    doi: 10.1016/j.atherosclerosis.2018.08.010

16. Al-Enezi MS. Assessment of the correlation between arterial lumen density and its metabolic activity in atherosclerotic patients using ^{18}F-FDG positron emission tomography/computed tomography. *Am J Nucl Med Mol Imaging*. 2023;13(1):18-25.

17. Blomberg BA, de Jong PA, Thomassen A, *et al*. Thoracic aorta calcification but not inflammation is associated with increased cardiovascular disease risk: Results of the CAMONA study. *Eur J Nucl Med Mol Imaging*. 2017;44(2):249-258.

    doi: 10.1007/s00259-016-3552-9

18. Al-Enezi MS, Bentourkia M. PET-18F-FDG Pharmacokinetic Modeling Without Blood Sampling in Arteries with Atherosclerosis. In: *2020 IEEE Nuclear Science Symposium and Medical Imaging Conference* (*NSS/MIC*). Boston, MA, USA: IEEE, 2020. p1-3.

    doi: 10.1109/NSS/MIC42677.2020.9507855

19. Criqui MH, Denenberg JO, Ix JH, *et al*. Calcium density of coronary artery plaque and risk of incident cardiovascular events. *JAMA*. 2014;311(3):271-278.

    doi: 10.1001/jama.2013.282535

20. Razavi AC, Whelton SP, Blumenthal RS, Blaha MJ, Dzaye O. Beyond the Agatston calcium score: Role of calcium density and other calcified plaque markers for cardiovascular disease prediction. *Curr Opin Cardiol*. 2025;40(1):56-62.

    doi: 10.1097/HCO.0000000000001185

21. Lairez O, Hyafil F. A clinical role of PET in atherosclerosis and vulnerable plaques? *Semin Nucl Med*. 2020;50(4):311-318.

    doi: 10.1053/j.semnuclmed.2020.02.017

22. Al-Enezi MS. Arterial tissue-to-psoas muscle ratio: A novel metric for quantifying fluorodeoxyglucose uptake in predicting the association between atherosclerotic inflammation and arterial calcification. *Eurasian J Med Oncol*. 2025;9(1):214-222.

    doi: 10.36922/ejmo.7727

23. Okamura Y, Nakanishi R, Hashimoto H, Mizumura S, Homma S, Ikeda T. Relationship Between ^{18}F-fluorodeoxyglucose uptake on positron emission tomography and aortic calcification. *Ann Nucl Cardiol*. 2022;8(1):57-66.

    doi: 10.17996/anc.22-00160

24. Høilund-Carlsen PF, Piri R, Madsen PL, *et al*. Atherosclerosis burdens in diabetes mellitus: Assessment by PET imaging. *Int J Mol Sci*. 2022;23(18):10268.

    doi: 10.3390/ijms231810268

25. Bucerius J, Hyafil F, Verberne HJ, *et al*. Position paper of the cardiovascular committee of the European Association of Nuclear Medicine (EANM) on PET imaging of atherosclerosis.

Eur J Nucl Med Mol Imaging. 2016;43(4):780-792.

doi: 10.1007/s00259-015-3259-3

26. Caselles V, Kimmel R, Sapiro G. Geodesic active contours. *Int J Comput Vision*. 1997;22:61-79.

    doi: 10.1109/ICCV.1995.466871

27. Agatston AS, Janowitz WR, Hildner FJ, Zusmer NR, Viamonte M Jr., Detrano R. Quantification of coronary artery calcium using ultrafast computed tomography. *J Am Coll Cardiol*. 1990;15(4):827-832.

    doi: 10.1016/0735-1097(90)90282-t

28. Ohya M, Otani H, Kimura K, *et al*. Vascular calcification estimated by aortic calcification area index is a significant predictive parameter of cardiovascular mortality in hemodialysis patients. *Clin Exp Nephrol*. 2011;15(6):877-883.

    doi: 10.1007/s10157-011-0517-y

29. Rousset OG, Ma Y, Evans AC. Correction for partial volume effects in PET: Principle and validation. *J Nucl Med*. 1998;39(5):904-911.

30. Burger C, Buck A. Requirements and implementation of a flexible kinetic modeling tool. *J Nucl Med*. 1997;38(11):1818-1823.

31. Guo N, Lang L, Gao H, *et al*. Quantitative analysis and parametric imaging of ^{18}F-labeled monomeric and dimeric RGD peptides using compartment model. *Mol Imaging Biol*. 2012;14(6):743-752.

    doi: 10.1007/s11307-012-0541-7

32. Graham MM, Muzi M, Spence AM, *et al*. The FDG lumped constant in normal human brain. *J Nucl Med*. 2002;43(9):1157-1166.

33. Al-Enezi MS, Bentourkia M. Kinetic modeling of dynamic PET-^{18}F-FDG atherosclerosis without blood sampling. *IEEE Trans Radiat Plasma Med Sci*. 2020;4(6):729-734.

    doi: 10.1109/TRPMS.2020.3005364

34. Galli G, Indovina L, Calcagni ML, Mansi L, Giordano A. The quantification with FDG as seen by a physician. *Nucl Med Biol*. 2013;40(6):720-730.

    doi: 10.1016/j.nucmedbio.2013.06.009

35. Torizuka T, Nobezawa S, Momiki S, *et al*. Short dynamic FDG-PET imaging protocol for patients with lung cancer. *Eur J Nucl Med*. 2000;27(10):1538-1542.

    doi: 10.1007/s002590000312

36. Strauss LG, Dimitrakopoulou-Strauss A, Haberkorn U. Shortened PET data acquisition protocol for the quantification of 18F-FDG kinetics. *J Nucl Med*. 2003;44(12):1933-1939.

37. Dimitrakopoulou-Strauss A, Pan L, Strauss LG. Quantitative approaches of dynamic FDG-PET and PET/CT studies (dPET/CT) for the evaluation of oncological patients. *Cancer Imaging*. 2012;12(1):283-289.

    doi: 10.1102/1470-7330.2012.0033

38. Cai D, He Y, Yu H, Zhang Y, Shi H. Comparative benefits of Ki and SUV images in lesion detection during PET/CT imaging. *EJNMMI Res*. 2024;14(1):98.

    doi: 10.1186/s13550-024-01162-x

39. Bertoglio D, Deleye S, Miranda A, Stroobants S, Staelens S, Verhaeghe J. Estimation of the net influx rate K_i and the cerebral metabolic rate of glucose MR_{glc} using a single static [^{18}F]FDG PET scan in rats. *Neuroimage*. 2021;233:117961.

    doi: 10.1016/j.neuroimage.2021.117961

40. Wang R, Chen H, Fan C. Impacts of time interval on 18F-FDG uptake for PET/CT in normal organs: A systematic review. *Medicine* (*Baltimore*). 2018;97(45):e13122.

    doi: 10.1097/MD.0000000000013122

41. Chen W, Dilsizian V. PET assessment of vascular inflammation and atherosclerotic plaques: SUV or TBR? *J Nucl Med*. 2015;56(4):503-504.

    doi: 10.2967/jnumed.115.154385

42. Yun M, Jang S, Cucchiara A, Newberg AB, Alavi A. 18F FDG uptake in the large arteries: A correlation study with the atherogenic risk factors. *Semin Nucl Med*. 2002;32(1):70-76.

    doi: 10.1053/snuc.2002.29279

43. Tatsumi M, Cohade C, Nakamoto Y, Wahl RL. Fluorodeoxyglucose uptake in the aortic wall at PET/CT: Possible finding for active atherosclerosis. *Radiology*. 2003;229(3):831-837.

    doi: 10.1148/radiol.2293021168

44. Ben-Haim S, Kupzov E, Tamir A, Israel O. Evaluation of 18F-FDG uptake and arterial wall calcifications using 18F-FDG PET/CT. *J Nucl Med*. 2004;45(11):1816-1821.

45. Santos RD. Calcified and noncalcified coronary plaques and atherosclerotic cardiovascular events in patients with severe hypercholesterolemia-moving forward with risk stratification and therapy. *JAMA Netw Open*. 2022;5(2):e2148147.

    doi: 10.1001/jamanetworkopen.2021.48147

46. Cahalane R, Akyildiz A, Kavousi M, *et al*. Cross-sectional validation of a novel computed tomography-based carotid mean calcium density measurement. *J Am Heart Assoc*. 2023;12(13):e027866.

    doi: 10.1161/JAHA.122.027866

47. Criqui MH, Knox JB, Denenberg JO, *et al*. Coronary artery calcium volume and density: Potential interactions and overall predictive value: The multi-ethnic study of atherosclerosis. *JACC Cardiovasc Imaging*. 2017;10(8):845-854.

    doi: 10.1016/j.jcmg.2017.04.018

48. Razavi AC, van Assen M, De Cecco CN, *et al*. Discordance

between coronary artery calcium area and density predicts long-term atherosclerotic cardiovascular disease risk. *JACC Cardiovasc Imaging*. 2022;15(11):1929-1940.

doi: 10.1016/j.jcmg.2022.06.007

49. Rozie S, de Weert TT, de Monyé C, *et al*. Atherosclerotic plaque volume and composition in symptomatic carotid arteries assessed with multidetector CT angiography; relationship with severity of stenosis and cardiovascular risk factors. *Eur Radiol*. 2009;19(9):2294-2301.

    doi: 10.1007/s00330-009-1394-6

50. Allison MA, Criqui MH, Wright CM. Patterns and risk factors for systemic calcified atherosclerosis. *Arterioscler Thromb Vasc Biol*. 2004;24(2):331-336.

    doi: 10.1161/01.ATV.0000110786.02097.0c

51. Kronmal RA, McClelland RL, Detrano R, *et al*. Risk factors for the progression of coronary artery calcification in asymptomatic subjects: Results from the Multi-Ethnic Study of Atherosclerosis (MESA). *Circulation*. 2007;115(21):2722-2730.

    doi: 10.1161/CIRCULATIONAHA.106.674143

52. Al Helali S, Hanif MA, Alshugair N, *et al*. Associations between hypothyroidism and subclinical atherosclerosis among male and female patients without clinical disease referred to computed tomography. *Endocr Pract*. 2023;29(12):935-941.

    doi: 10.1016/j.eprac.2023.08.012

53. Chen W, Bural GG, Torigian DA, Rader DJ, Alavi A. Emerging role of FDG-PET/CT in assessing atherosclerosis in large arteries. *Eur J Nucl Med Mol Imaging*. 2009;36(1):144-151.

    doi: 10.1007/s00259-008-0947-2

54. Ahlman MA, Grayson PC. Advanced molecular imaging in large-vessel vasculitis: Adopting FDG-PET into a clinical workflow. *Best Pract Res Clin Rheumatol*. 2023;37(1):101856.

    doi: 10.1016/j.berh.2023.101856

55. Srivastava RAK. A Review of progress on targeting LDL receptor-dependent and -independent pathways for the treatment of hypercholesterolemia, a major risk factor of ASCVD. *Cells*. 2023;12(12):1648.

    doi: 10.3390/cells12121648

56. Padro T, Escate R, Perez De Isla L, *et al*. miRNA signature related to atherosclerotic lesion induced shear stress modifications in familial hypercholesterolemia patients with subclinical atherosclerosis: A bioinformatics systems biology study. *Cardiovasc Res*, 2024;120(Supplement_1):cvae088.170.

    doi: 10.1093/cvr/cvae088.170

57. Razavi AC, Kim C, van Assen M, *et al*. Thoracic aortic calcium density and area in long-term atherosclerotic cardiovascular disease risk among men versus women. *Circ Cardiovasc Imaging*. 2023;16(12):e015690.

    doi: 10.1161/CIRCIMAGING.123.015690

ACCSCIENCE PUBLISHING

Advances in Radiotherapy & Nuclear Medicine

ORIGINAL RESEARCH ARTICLE

Renal function reconstruction and modeling in dynamic scintigraphy

Faycal Kharfi[1]*, Haithem Aloui[2], and Rabie Benlabga[2]

[1]Laboratory of Dosing, Analysis, and Characterization with High Resolution, Department of Physics, Faculty of Sciences, Ferhat Abbas University Setif 1, Setif, Setif, Algeria

[2]Service of Nuclear Medicine, Babors Medical Clinic, Setif, Setif, Algeria

Abstract

Dynamic renal scintigraphy is a key imaging technique for assessing renal function using time-activity curves (TACs), which represent radiotracer uptake and clearance. TAC accuracy depends on the region of interest (ROI) selection and the modeling approach used. This study aims to: (i) Reconstruct TACs manually using gray-level values in scintigraphic images and compare them to machine-generated TACs using key kinetic parameters (T_{max}, $T_{1/2}$, and the 30-min min/max ratio); and (ii) evaluate the effectiveness of a one-compartment empirical mathematical model for TAC fitting and its physiological relevance. Twelve clinical cases were analyzed, with TACs reconstructed manually using a rectangular ROI selection method and compared to those automatically generated by the scintigraphy machine. An empirical mathematical fitting function was developed to improve TAC fitting. Manually reconstructed TACs showed better dynamic behavior and physiological accuracy over machine-generated TACs, particularly due to differences in ROI selection and signal processing. Using gray-level values instead of raw radioactive counts enhanced the depiction of kidney dynamics. The proposed mathematical model demonstrated a strong correlation (R^2 close to 1) and low error metrics, confirming its suitability for renal function assessment. While a free-hand ROI selection may improve accuracy, the rectangular method gives valuable results for the considered cases. This study highlights the importance of ROI selection in TAC reconstruction and demonstrates how manual methods and mathematical modeling can enhance renal functional assessment in clinical practice. Future work should validate these findings in larger datasets and assess the reproducibility of the proposed approach across different patient populations and imaging systems.

Keywords: Dynamic renal scintigraphy; Time-activity curve; Kinetic parameters; Mathematical modeling; Renal function assessment

1. Introduction

Dynamic renal scintigraphy is a diagnostic imaging technique used to assess the function and blood flow of the kidneys. It involves injecting a small amount of radioactive tracer, usually technetium-99m diethylene triamine penta-acetic acid or technetium-99m mercaptoacetyltriglycine (MAG3), into the bloodstream. As the radioactive tracer circulates through the bloodstream, it is filtered by the kidneys and excreted into the

***Corresponding author:**
Faycal Kharfi
(kharfifaycal@univ-setif.dz)

Citation: Kharfi F, Aloui H, Benlabga R. Renal function reconstruction and modeling in dynamic scintigraphy. *Adv Radiother Nucl Med.* 2025;3(2):61-72. doi: 10.36922/ARNM025070008

Received: February 15, 2025

Revised: March 14, 2025

Accepted: April 21, 2025

urine. A gamma camera is used to detect the radiation emitted by the tracer, allowing the visualization of the kidneys and the urinary system in real time. Dynamic renal scintigraphy provides valuable information about renal function, including glomerular filtration rate (GFR), renal blood flow, and tubular function. It is commonly used in renal function evaluation, renal transplant assessment, and various kidney disorder diagnoses, such as hydronephrosis, renal obstruction, and renal artery stenosis. The "dynamic" aspect of the procedure refers to the continuous imaging of the kidneys over a period of time, typically several minutes, allowing clinicians to observe the tracer's movement through the renal system and assess kidney function dynamically. This dynamic imaging is often accompanied by static images taken at specific time points to provide additional information.

Renal function modeling in dynamic scintigraphy uses mathematical algorithms to analyze imaging data and assess renal function. This allows a more comprehensive assessment of renal function beyond simple visual observation. The typical steps for renal function reconstruction and modeling are:

(i) Data acquisition: Dynamic renal scintigraphy involves acquiring a series of images over time as the radioactive tracer circulates through the kidneys. These images are typically obtained using a gamma camera.
(ii) Image processing: The acquired images are processed to correct for factors such as background noise, scatter, and attenuation. This ensures the accuracy of the data used for analysis.
(iii) Region of interest (ROI) selection: ROIs are delineated on the images to isolate the kidneys and other relevant structures, such as the bladder and blood vessels.
(iv) Time-activity curve (TAC) generation: The intensity of the radioactive tracer within the kidneys is measured over time to create TACs. These curves represent the uptake, distribution, and clearance of the tracer within the kidneys.[1]
(v) Renal function parameters: Various parameters can be derived from the TACs to assess renal function, including:
    - GFR: GFR is a key indicator of renal function and can be estimated from the rate of tracer clearance from the blood.
    - Renal blood flow: The perfusion of blood through the kidneys can be estimated from the initial uptake and distribution of the tracer.
    - Tubular function: Parameters such as tubular extraction rate and tubular secretion rate can be derived from the TACs to assess tubular function.
(vi) Modeling techniques: Mathematical models, such as compartmental models and deconvolution techniques, can be applied to the TACs to reconstruct the underlying physiological processes involved in renal function. These models help to quantify and analyze the data in a more detailed manner.
(vii) Clinical interpretation: The derived parameters and modeling results are interpreted in the context of the patient's clinical condition to aid in diagnosis and treatment planning. Abnormalities in renal function parameters can indicate various renal disorders, such as renal artery stenosis, obstruction, or impaired renal function.

Renal function reconstruction and modeling in dynamic scintigraphy play a valuable role in the assessment of renal function and can provide valuable insights for clinicians in the diagnosis and management of renal diseases.

TACs play a critical role in dynamic renal scintigraphy by quantitatively assessing renal function based on tracer kinetics. Traditional TACs are generated automatically by scintigraphy machines using predefined algorithms and standard ROI selection techniques, typically based on radioactive counting. However, these machine-generated TACs may not fully capture the physiological dynamics of renal function due to their dependence on fixed ROI placement and automated signal processing methods.[2] In addition, standard one-compartment models used in renal function modeling assume homogeneous tracer distribution, which may not accurately represent complex renal clearance mechanisms. While alternative models, such as multi-compartment or physiologically based models, offer more detailed representations, they are computationally intensive and not widely implemented in clinical practice. Moreover, manual TAC reconstruction, which can provide a more physiologically relevant representation by incorporating gray-level value measurements, remains underexplored. There is also a lack of studies comparing different ROI selection techniques, such as rectangular versus free-hand approaches, and their impact on TAC accuracy. To address these gaps, this study aims to assess the accuracy of manually reconstructed TACs, validate an empirical mathematical model for renal function evaluation, and explore the influence of ROI selection methods on TAC accuracy.

The main objective of this work is to experimentally reconstruct TACs from clinical dynamic scintigraphy data and compare them with those automatically generated by the scintigraphy machine based on the main kinetic parameters that can be extracted from clinical TACs.[3-5] The second objective is to compare rectangular and free-hand ROI selection methods using six additional cases. The third objective is to evaluate empirical mathematical fitting functions and a one-compartment model used for the construction of TACs by modeling the physiological processes in the kidneys.

2. Materials and methods

2.1. Dynamic renal scintigraphy

In this work, the GE Discovery NM630 Gamma camera (GE Hualun Medical Systems Co, China was used for imaging data collection and clinical TAC construction. This camera is used in nuclear medicine for many purposes, including dynamic renal scintigraphy. It is a specialized gamma camera designed for high-resolution imaging with enhanced sensitivity and speed. The camera detects the gamma rays emitted by the radiopharmaceutical and creates images that show the distribution and function of the kidneys over time. During dynamic renal scintigraphy with the GE Discovery NM630 Gamma camera, multiple images are taken at different time points after the injection of the radiopharmaceutical. This allows for the assessment of renal blood flow, GFR, renal function, and the detection of any abnormalities such as obstruction or reflux. The dynamic images produced by this technique provide information to healthcare professionals for the diagnosis and management of various kidney disorders, including renal artery stenosis, renal transplant evaluation, and renovascular hypertension. In addition, it can help in the evaluation of renal function before and after interventions such as surgery or renal artery angioplasty.

The data used in this study were collected from patients who underwent dynamic renal scintigraphy over the past 2 years at the Babor Medical Clinic. In compliance with local regulations, data were anonymized by enabling the anonymization option in the DICOM files before extraction. Dynamic renal scintigraphy began immediately after the intravenous injection of TC-99m diethylene triamine penta-acetic acid (DTPA), with the dose based on the patient's weight and other factors, and by considering 12 healthy and pathogenic cases from the Setif region (Algeria) with different sexes and ages. The detectors were positioned in an H-shaped configuration over the abdomen, and the patient was placed in the supine position. Dynamic renal scintigraphy was performed according to standard protocols.[6] In the imaging protocols used in this work, 30 frames were captured during the 1st min, and then 90 frames were captured at a sequence of three frames per minute. The image acquisition process continued for a total duration of 30 min to monitor the tracer uptake, distribution, and clearance in the kidneys. "*Xeleris* GE health care (USA)," was used to automatically generate the clinical TAC, allowing clinicians to select the ROI corresponding to the two kidneys and background on the image sum of all captured frames. It is necessary to ensure that the entire kidney (for functional determination) and the renal pelvis (for pyelocaliceal drainage) are included in the ROI. A larger ROI is preferred over a narrowly surrounding region around the kidney.

From the established TAC, the parameters characterizing the kinetics of renal function that can be assessed are the following:

(i) Split function: It is particularly useful in identifying unilateral changes or differences in renal function and is calculated by generating a TAC that plots the amount of radioactive material in the kidney over time. The split function value is obtained by dividing the counts collected during the uptake phase for each kidney by the sum of the counts from both kidneys. Normal range values of this index are between 42% and 58%.[7-12]

(ii) Relative uptake: The measurement of the radiopharmaceutical's relative uptake is crucial in assessing the specific renal function, which varies depending on the radiopharmaceutical used. When using 99mTc-MAG3 and DTPA, a common approach involves placing an ROI over each kidney and calculating the integrated counts within the renal ROI during specific time intervals (e.g., 1 – 2 min, 1 – 2.5 min, or 2 – 3 mins) after injection. Another method that can be used is the Rutland-Patlak plot.[7-12]

(iii) Time to peak (TTP or T_{max}): It refers to the time it takes for the tracer concentration to reach its highest point or the peak value (maximum concentration in the kidney) when the accumulation trend of the radiopharmaceutical is reversed. In general, for a healthy kidney, TTP values are about 5 min, and the maximum activity at the peak decreases to half the value after 15 min from the injection.[13]

(iv) Clearance time ($T_{1/2}$): It is a quantitative parameter commonly used to describe the rate at which the radiopharmaceutical is cleared from the kidney. It represents the time taken for the radiopharmaceutical activity to decrease by half in the ROI after reaching its peak uptake. This parameter is important in diuretic renography for detecting urinary tract obstruction.[13]

(v) The 30-min min/max ratio: It reflects the time it takes for the radiopharmaceutical to pass through the kidneys. It indicates the amount of residual activity in the cortex. It is calculated by comparing the radioactivity level in the kidneys at 30 min to the peak concentration. This ratio is helpful in diagnosing urinary tract blockages and renovascular hypertension.[13]

(vi) Upslope ratio: It refers to the ratio of the maximum slope of the TAC during the ascending limb to the average slope of the entire curve. This parameter indicates the rate at which the radiopharmaceutical is taken up by the kidney tissue.

(vii) Downslope ratio: The ratio between the slope of the descending limb of the TAC (representing radiotracer excretion) and the peak activity or uptake slope is used to assess the rate of tracer clearance from the renal parenchyma.

2.2. Manual reconstruction of the TAC using the region of interest selection method

In this work, we proposed a manual method for establishing TACs based on the analysis of scintigraphic images obtained according to clinical protocols and the measurement of gray-level values within specific ROIs corresponding to the kidneys and background. These images were derived from the physical signal (radioactive counting) after undergoing several processing and conversion steps (e.g., amplification, gain, filtering, and analog-to-digital conversion). The procedure, applied to 12 cases, was performed according to the following main steps:

(i) Extraction of patient files, including scintigraphic images, in DICOM format.
(ii) Analyzing of images by micro-DICOM software (v.3.1.1, MicroDicom Ltd, Bulgaria).
(iii) Delineation of the necessary ROIs was performed according to analytic recommendations, ensuring consistent kidney dimensions and coverage across all scintigraphic images (frames). The selection of ROI corresponding to the right and left kidney areas, along with the background on the scintigraphy frames, can be performed using two methods: The free-hand method or the regular shape method. In this work, the regular method was employed using rectangular ROIs (Figure 1).
(iv) Manual construction of TAC from the extracted gray-level values measured on ROIs.

The proposed method for manual TAC reconstruction in dynamic renal scintigraphy relies on analyzing scintigraphic images obtained according to clinical protocols. These images were generated through a sequence of physical and digital processing steps applied to radioactive signals detected by the gamma camera. Below is a detailed breakdown of the steps involved in image formation, processing, and the subsequent TAC reconstruction:

Step#1: The acquisition of physical signal (radioactive counting): The dynamic renal scintigraphy begins with the intravenous injection of a TC-99m DTPA radiopharmaceutical. Once injected into the bloodstream, the tracer is filtered by the kidneys, allowing for an evaluation of renal function through its uptake and clearance. The emitted gamma radiation from the tracer is detected using a gamma camera (GE Discovery NM630), which captures images of the kidneys over time. The imaging protocol employed in this study reportedly included:

(i) 30 frames during the 1st min, allowing an analysis of early tracer uptake.

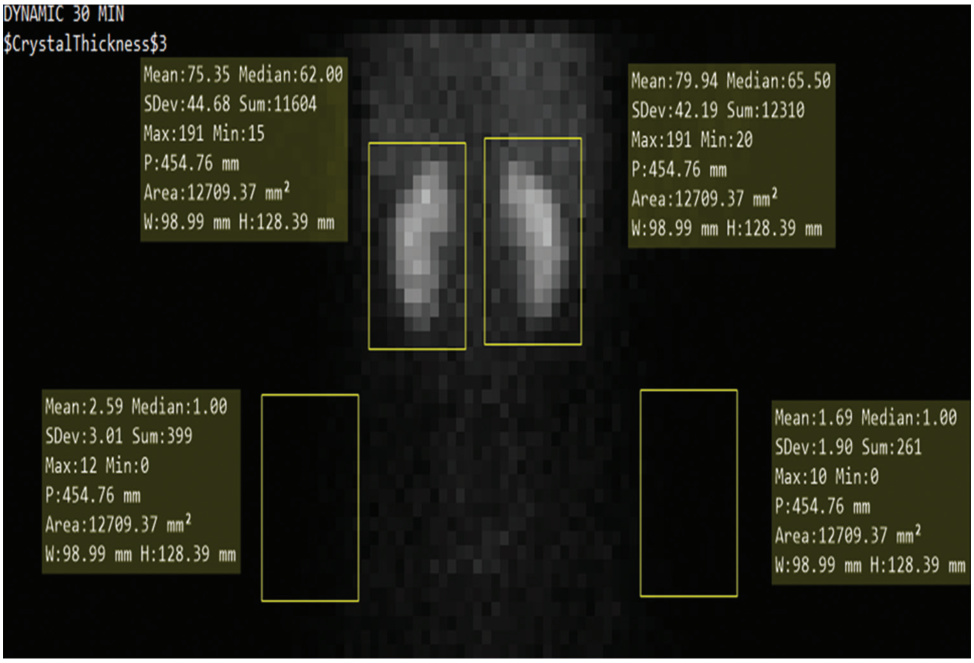

Figure 1. Regular rectangular region of interest selection method used in this study for delineating kidney regions and background areas in scintigraphic images. This method ensures consistency in kidney dimensions and coverage across all scintigraphic frames.

(ii) 90 additional frames at one frame per minute, ensuring a complete observation of renal function over 30 min.

Step#2: The processing and conversion of signals: Since the manually reconstructed TACs are based on gray-level values, these images must undergo several transformation steps before they can be analyzed. The radioactive signals detected by the gamma camera are subjected to various physical and digital processing operations aimed at enhancing accuracy:

(i) Gamma-ray detection: The radiation emitted by the radiopharmaceutical is detected by the gamma camera. It has been noted that this detected signal consists of electrical pulses, which correspond to the intensity of gamma radiation.
(ii) Amplification: To enhance sensitivity, the weak gamma signal is amplified through a photomultiplier tube. This component converts the low-energy gamma photons into stronger electrical signals.
(iii) Gain adjustment: The amplified signal is then subjected to gain correction, a step which is intended to optimize signal detection while reducing unwanted variations. This adjustment ensures that the system maintains an appropriate balance between sensitivity and noise reduction.
(iv) Filtering: Various filtering techniques are applied to refine the detected signal. Energy windowing and scatter correction are commonly utilized to remove background noise and irrelevant signals, thereby improving the reliability of the extracted data.
(v) Analog-to-digital conversion: To allow for further digital analysis, the processed signals are converted into numerical pixel values. This conversion assigns intensity values to pixels in the generated images, enabling subsequent image processing and data extraction.

Step#3: The manual reconstruction of TACs: Once the images are processed, manual TAC reconstruction is performed. The method follows a structured approach:

(i) Extraction of scintigraphic images: The scintigraphic images, stored in DICOM format, are retrieved from the gamma camera system for further analysis.
(ii) Image visualization and ROI selection: The micro-DICOM software (v3.1.1) is employed to display and analyze the extracted images. The ROIs for both kidneys and background areas are then delineated, ensuring that renal function is assessed in a controlled and reproducible manner.
(iii) Methods of ROI selection: Two main approaches for defining the ROIs:
    - Regular shape method (rectangular ROI): This approach, which was implemented in this study, ensures consistency by using a rectangular selection over the kidneys. It is believed to offer improved reproducibility by maintaining standardized ROI dimensions across different frames.
    - Freehand method: Although not applied in this study, this alternative method allows for a more precise delineation of the kidneys' actual shape. While offering greater flexibility, it has been suggested that it may introduce variability depending on operator expertise.
(iv) Extraction of gray-level data: Following ROI selection, gray-level values are extracted from the scintigraphic images. These values reflect the distribution of the radioactive tracer within the kidneys over time.
(v) Construction of TACs: The extracted gray-level data is used to manually reconstruct TACs, which describe the uptake and clearance of the radiopharmaceutical over the 30-min imaging period. The manually generated TACs are then compared with the machine-generated TACs, allowing an evaluation of their accuracy in representing renal function.

2.3. Region of interest selection methods

To study the impact of ROI selection methods in dynamic renal scintigraphy, two selection methods were compared:

(i) Rectangular ROI selection: A fixed, standardized rectangular shape applied to selected data.
(ii) Free-hand ROI selection: A manually drawn contour following the anatomical shape of the kidneys.

The comparison was applied for six additional cases (P1 – P6). The comparison of ROI selection methods was performed to determine whether free-hand ROI selection improves the accuracy of renal function assessment of the considered cases in terms of kinetic parameters.

2.4. TAC modeling using a one-compartment model and fitting function

Most kinetic analyses in dynamic renal scintigraphy rely on mathematical models, typically compartmental models, to study the behavior of a tracer from injection to clearance. These models incorporate an input function that represents the amount of radioactivity injected into the patient. The proposed models take integro-differential forms and are time-dependent. Such modeling can provide information and data on the dynamics of the tracer within the patient and the target organ (the kidney) without the need for experiments or clinical trials. The estimation of the kinetic parameters within the compartmental model is a non-linear regression that uses iterative algorithms, based on the following assumptions:[13]

(i) The measurements are conducted under the condition that physiological processes remain in a steady state throughout the experiment;
(ii) The radioligand used does not significantly affect the physiological or biochemical processes being studied; and
(iii) The homogeneity of the tracer concentration is within each compartment.

Commonly, a compartmental model is defined by a system of differential equations where each equation corresponds to the sum of all transfer rates to and from a specific compartment:

$$\frac{dC_i(t)}{dt} = \sum_{i=1}^{N} \left[k_{ij} C_j(t) - k_{ij} C_i(t) \right]_{i \neq j} \tag{I}$$

Where $C_i(t)$ is the tracer concentration in compartment i, k_{ij} is the transfer rate constant to compartment i from compartment j, and N is the number of compartments in the model.

In this work, a one-compartment model was used. This model assumes that the system used in this study comprises only one homogenous compartment (Figure 2). After the administration via an extravascular route, the radioactive tracer transfer through the kidney proceeds as follows:[14]

$$\frac{dC_{CE}(t)}{dt} = k_1 C_P(t) - k_2 C_{CE}(t) \tag{II}$$

Where k_1 is related to the glomerular filtration and equal to the ratio of GFR to the extravascular functional renal cortical volume (GFR/V_{EC}),[15-17] k_2 is related to the urination, C_P is the plasma activity concentration, and C_{EC} is the extravascular functional renal cortical activity concentration.

The solution to the differential equation (Equation II), which describes the variation of activity ($A(t)$) as a function of time (t), is given by the following equation:[14]

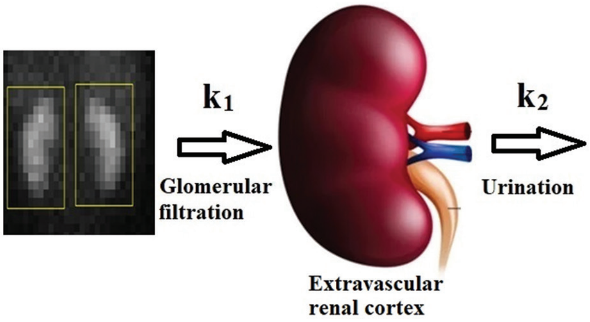

Figure 2. Example of segmentation of the functional renal cortex (left) and schematic representation of the one-compartment tracer kinetic model (right). The one-compartment model describes the uptake and clearance of the radiopharmaceutical tracer in the kidney, with rate constants k_1 (glomerular filtration) and k_2 (urination) representing tracer kinetics.

$$A(t) = A_0 (1 - e^{-k_1 . t}) \times e^{-k_2 . t} \tag{III}$$

In this work, instead of using the analytical solution given by Equation III, an empirical solution was adopted based on imaging data and the manual reconstruction of the TAC. Following multiple trials and with consideration of renal physiology and function, the manually reconstructed TAC was fitted using a suitable mathematical function. This fitting function describes the variation of gray level over time and is presented in Equation IV:

$$GL = \frac{A_0}{(1 + \frac{C_e}{t})^{\alpha_e} + (1 + \frac{t}{C_s})^{\alpha_s}} \tag{IV}$$

Where GL is the gray level of a separated frame, A_0 is the activity concentration of the tracer that is injected and metabolized by the kidney, C_e is the perfusion time constant, α_e is a weighting factor of the perfusion phase, C_s is a time constant in the secretion-drainage phase (urination), α_s is a weighting factor related to the secretion-drainage phase, and t is the time variable.

3. Results

Figure 3 demonstrates an example of clinical (machine) and manually reconstructed TACs of Case 1.

Figure 4 shows the TAC modeling for Case 1 using the mathematical fitting function (Equation IV) based on the one-compartment model.

Table 1 compares the kinetic parameters of the renal function automatically generated by the scintigraphy machine's algorithm with those manually extracted using the proposed model.

Manually reconstructed renal TACs were found to be dependent on the ROI selection methods. While the results obtained using the manual method were accurate and of good quality, the free-hand selection method is believed to offer better results, particularly for mathematical modeling and data fitting. This approach may enhance the accuracy of the main kinetic parameters extracted from the data. Moreover, the renal function curves established manually using gray-level values from individual scintigraphic images exhibited better dynamic behavior than those from the machine (automatic), which are based on radioactive counting. This difference is due to the gain adjustment between radioactive counts and gray level during the analog-to-digital conversion phase. In addition, the processing of the physical signals (radioactive counting) also plays a critical role in influencing the final TAC output.

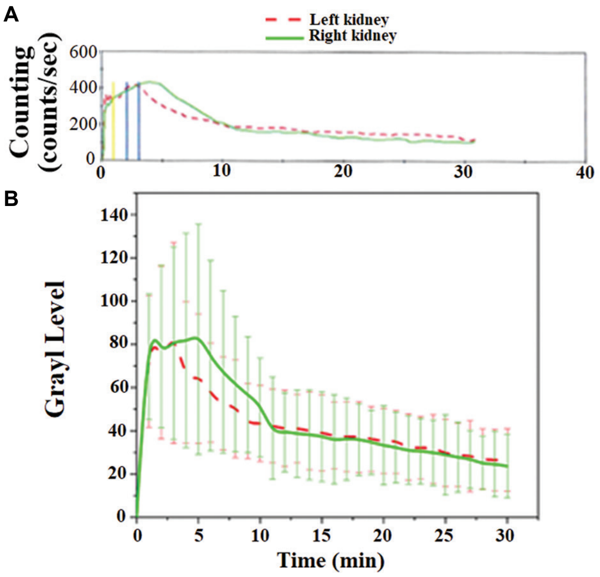

Figure 3. Comparison of TACs for Case 1. (A) TAC was generated automatically by the scintigraphy machine. (B) TAC was reconstructed manually from processed dynamic renal scintigraphic images using the proposed regular rectangular region of interest selection method. The manually reconstructed TAC exhibits a more detailed dynamic behavior than the machine-generated TAC.
Abbreviation: TACs: Time-activity curves.

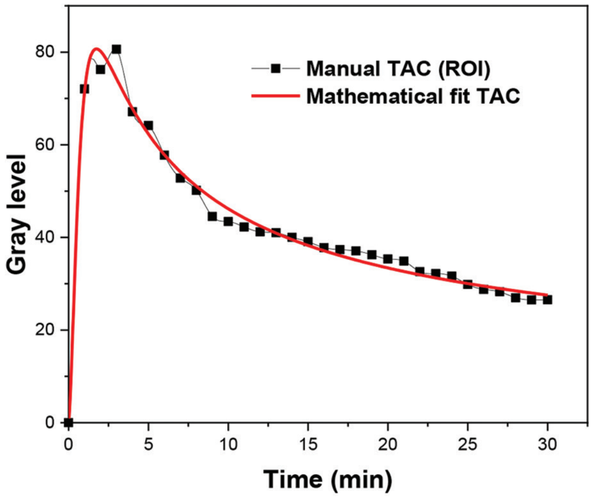

Figure 4. Mathematical modeling of the manually reconstructed TAC for the healthy kidney in Case 1. The experimental data points extracted from scintigraphic images (black circles) were fitted using the proposed empirical fitting function based on a one-compartment model with additional adjusting parameters. The fitted curve (solid red line) closely follows the manual TAC, demonstrating the accuracy of the proposed model.
Abbreviation: TAC: Time-activity curve.

Table 2 presents a numerical comparison of the kinetic parameters extracted using both ROI selection methods (rectangular and free-hand).

The statistical analysis of the results in Table 2 is summarized in Table 3.

The results and statistical analyses demonstrate that the free-hand ROI selection method yields significantly lower T_{max} values, indicating a more precise capture of peak tracer uptake. This method also exhibits a significantly shorter tracer elimination time, likely due to better exclusion of background noise. Regarding the 30-min min/max ratio, the free-hand ROI selection method shows a significantly lower residual activity, allowing for more accurate isolation of renal function. Overall, the free-hand ROI selection method provides physiologically more accurate TACs by closely contouring kidney anatomy and minimizing background activity. In contrast, the rectangular ROI selection method provides consistency across cases but may include non-kidney regions, which can lead to slightly overestimated retention values.

To evaluate the effectiveness and accuracy of the proposed fitting function and empirical model, standard goodness-of-fit metrics were used, including the correlation factor (R^2), adjusted R^2, and reduced χ^2. For Case 1, Table 4 indicates a high-quality fit, with R^2 and adjusted-R^2 values close to 1, and a low reduced χ^2, confirming the model's robustness. The fitting parameters, particularly C_s and α_s, reflect the pathological status of the left and right kidneys. Similar results were observed across all other cases.

The proposed clinical data fitting function proved suitable for the extraction of key kinetic parameters of renal function. It can be applied in any simulation aimed at evaluating new radiopharmaceuticals (radiotracers) for use in dynamic renal scintigraphy, as well as for other tasks of interest.

4. Discussion

The findings of this study underscore the significant advantages of manual reconstruction and mathematical modeling of TACs in dynamic renal scintigraphy over the automatic algorithms of standard imaging systems. By integrating manual ROI selection with an empirical mathematical fitting function, this study successfully reconstructed TACs with greater accuracy and physiological relevance.[18]

The manually reconstructed TACs demonstrated improved dynamic behavior compared to the machine-generated TACs. This superiority can be attributed to the differences in data processing techniques. While machine-generated TACs rely on raw radioactive counts, the manual method incorporates gray-level values that undergo additional processing steps, such as analog-to-digital conversion and filtering. This approach likely enhances

Table 1. Comparison between the main kinetic parameters obtained automatically (clinical) and those manually extracted through mathematical modeling of the 12 time-activity curves

Kinetic parameters	Right kidney		Left kidney	
	Automatic data	Manual data	Automatic data	Manual data
Case 1				
T_{max} (min)	4.05	4.26	2.71	2.88
$T_{1/2}$ (min)	5.67	6.18	7.00	6.70
30-min min/max ratio	0.26	0.28	0.31	0.32
Case 2				
T_{max} (min)	1.01	1.43	3.34	3.35
$T_{1/2}$ (min)	10.67	12.79	15.00	15.65
30-min min/max ratio	0.47	0.39	0.42	0.37
Case 3				
T_{max} (min)	4.00	4.20	4.10	4.18
$T_{1/2}$ (min)	9.50	8.70	9.20	8.60
30-min min/max ratio	0.30	0.28	0.29	0.30
Case 4				
T_{max} (min)	3.50	3.76	3.60	3.88
$T_{1/2}$ (min)	10.00	10.18	10.20	9.80
30-min min/max ratio	0.28	0.30	0.30	0.31
Case 5				
T_{max} (min)	4.50	4.66	4.40	4.32
$T_{1/2}$ (min)	8.50	8.25	7.50	7.70
30-min min/max ratio	0.25	0.26	0.26	0.28
Case 6				
T_{max} (min)	3.50	3.83	1.75	1.85
$T_{1/2}$ (min)	11.00	10.54	12.00	12.78
30-min min/max ratio	0.32	0.31	0.34	0.33
Case 7				
T_{max} (min)	4.20	4.28	4.10	4.07
$T_{1/2}$ (min)	9.00	8.95	8.80	8.70
30-min min/max ratio	0.27	0.28	0.28	0.27
Case 8				
T_{max} (min)	7.50	7.76	6.75	6.90
$T_{1/2}$ (min)	25.05	26.30	24.30	26.65
30-min min/max ratio	0.70	0.78	0.65	0.68
Case 9				
T_{max} (min)	4.70	4.90	8.05	8.26
$T_{1/2}$ (min)	8.25	9.70	30.00	29.12
30-min min/max ratio	0.35	0.37	0.75	0.78
Case 10				
T_{max} (min)	4.50	4.25	4.71	4.08
$T_{1/2}$ (min)	8.00	7.81	7.50	7.70
30-min min/max ratio	0.25	0.26	0.26	0.27

(*Cont'd...*)

Table 1. (*Continued*)

Kinetic parameters	Right kidney		Left kidney	
	Automatic data	**Manual data**	**Automatic data**	**Manual data**
Case 11				
T_{max} (min)	4.15	4.05	4.71	4.32
$T_{1/2}$ (min)	5.75	6.60	7.00	7.14
30-min min/max ratio	0.22	0.28	0.30	0.31
Case 12				
T_{max} (min)	4.15	4.35	9.00	9.22
$T_{1/2}$ (min)	6.20	6.45	35.00	36.20
30-min min/max ratio	0.26	0.27	0.45	0.48

Table 2. Comparison of the kinetic parameters between the two region-of-interest selection methods

Case	Kidney	ROI selection method	T_{max} (min)	$T_{1/2}$ (min)	30-min min/max ratio
P1	Left	Rectangular	4.2	8.5	0.32
		Free-hand	4.0	7.9	0.28
P2	Right	Rectangular	3.8	9.2	0.35
		Free-hand	3.5	8.7	0.30
P3	Left	Rectangular	4.5	7.8	0.29
		Free-hand	4.3	7.4	0.26
P4	Right	Rectangular	5.1	10.1	0.38
		Free-hand	4.8	9.6	0.33
P5	Left	Rectangular	4.0	8.9	0.31
		Free-hand	3.8	8.2	0.27
P6	Right	Rectangular	3.7	9.5	0.34
		Free-hand	3.4	9.1	0.29

Table 3. Statistical analysis of the comparison between the two ROI selection methods

Statistical parameters	ROI selection method	
	Rectangular	**Free-hand**
Mean and standard deviation		
T_{max} (min)	4.22±0.52	4.00±0.49
$T_{1/2}$ (min)	8.99±0.83	8.32±0.74
30-min min/max ratio	0.33±0.03	0.29±0.02
Paired t-test results (rectangular vs. free-hand)		
T_{max}	p=0.035*	
$T_{1/2}$	p=0.041*	
30-min min/max ratio	p=0.029*	
Correlation analysis (R^2 values between the TACs of both methods)	R^2=0.94	

Note: *p<0.05.
Abbreviations: TAC: Time-activity curve; ROI: Region-of-interest.

Table 4. Fitting function and mathematical model parameters of Case 1

Fitting function parameters	Left kidney	Right kidney
A_0	5,687	200,181
C_e	0.98	3.35
α_e	1.90	1.45
C_s	4.91	0.0011
α_s	0.48	0.88
Reduced χ^2	4.77	13.95
R^2	0.98	0.97
R^2 adjusted	0.98	0.96

Notes: A_0 indicates the activity concentration of the tracer that is injected and metabolized by the kidney; C_e indicates the perfusion time constant; α_e indicates a weighting factor of the perfusion phase; C_s indicates a time constant in the secretion-drainage phase (urination); α_s indicates a weighting factor related to the secretion-drainage phase, and t is the time variable.

sensitivity to subtle physiological variations, reflected in the closer alignment of manually derived kinetic parameters (e.g., T_{max} and $T_{1/2}$) with expected renal physiology.[19]

The comparative analysis of the kinetic parameters, including T_{max}, $T_{1/2}$, and the 30-min min/max ratio, revealed small yet significant differences between manual and automatic methods. For example, in all analyzed cases, manual reconstruction resulted in slightly higher T_{max} values, reflecting a potentially more accurate depiction of tracer dynamics. Similarly, the improved correlation factors (R^2 and reduced χ^2 values) for the mathematical fitting function indicate the robustness of the proposed model in capturing physiological processes.

The proposed empirical mathematical model demonstrated excellent accuracy in modeling TACs, as evidenced by high R^2 and adjusted R^2 values. Parameters such as Cs and αs, derived from the fitting function, provided insights into the pathological status of the kidneys. This adaptability of the model highlights its potential utility in clinical and research settings, including the evaluation of new radiopharmaceuticals and the investigation of renal pathophysiology.

One notable limitation of this study is the dependency of manual TAC reconstruction on the ROI selection method. While the rectangular ROI selection method used here ensured consistency, a free-hand approach may offer even greater accuracy by better conforming to kidney shapes. Future studies should explore the impact of different ROI selection methods on the accuracy of TACs and kinetic parameters. In addition, extending this methodology to a larger cohort with diverse renal pathologies could validate its generalizability and clinical applicability. If accuracy is prioritized, the free-hand ROI selection method is preferable. However, if standardization and reproducibility are the main concerns, the rectangular ROI selection method may still be useful. The presented comparison demonstrates how the choice of ROI selection method can influence kinetic parameters in renal scintigraphy.

The proposed manual method offers an alternative approach to TAC reconstruction by leveraging gray-level values rather than direct radioactive counting. It involves several crucial steps, including image acquisition, processing, ROI selection, data extraction, and TAC reconstruction. While this method enhances dynamic accuracy, future studies could focus on minimizing inter-operator variability and evaluating its applicability across diverse renal conditions and imaging systems to improve generalizability to complex cases and pathologies.

The findings of this study suggest that manual reconstruction and modeling of TACs could enhance the diagnostic accuracy of dynamic renal scintigraphy, particularly in complex or borderline cases. The ability to extract more physiologically relevant parameters could improve the detection of subtle renal dysfunctions and provide a more detailed assessment for treatment planning. In clinical practice, this can be particularly advantageous in detecting early-stage renal dysfunction, assessing post-transplant renal function, or identifying subtle abnormalities that might be overlooked by machine-generated TACs.

5. Conclusion

This study demonstrates the effectiveness of manual reconstruction and empirical modeling of TACs in dynamic renal scintigraphy. The manually established TACs provide more physiologically relevant insights compared to those automatically generated by scintigraphy machines. By leveraging gray-level data and a one-compartment model, the proposed approach achieved superior dynamic behavior and higher accuracy in extracting key kinetic parameters, such as T_{max} and $T_{1/2}$. The fitting function developed in this work proved robust, with excellent correlation coefficients and goodness-of-fit metrics. These results highlight the potential of manual TAC modeling in improving diagnostic accuracy and exploring renal pathophysiology. Moreover, the method offers a valuable framework for evaluating new radiopharmaceuticals and advancing clinical applications. However, future work should address the limitations of ROI selection methods and validate the findings across larger patient cohorts. Overall, this study advances the understanding of renal function reconstruction and modeling, paving the path for enhanced clinical and research applications in nuclear medicine.

Acknowledgments

None.

Funding

None.

Conflict of interest

The authors declare no conflicts of interest.

Author contributions

Conceptualization: Faycal Kharfi
Investigation: All authors
Methodology: Faycal Kharfi
Writing – original draft: Faycal Kharfi
Writing – review & editing: Faycal Kharfi

Ethics approval and consent to participate

Patient data were used anonymously in accordance with local ethical guidelines. The study does not involve clinical trials and does not require informed consent.

Consent for publication

Patient data were used anonymously and do not require consent for publication.

Availability of data

The data are not publicly available.

References

1. Alsabea H. Type of renal scintigraphy. *J Nucl Med Radiat Ther*. 2017;8(6):347.

   doi: 10.4172/2155-9619.1000347

2. Esser JP. *Dynamic Renal Scintigraphy (Part I)*. Amersfoort: Meander Medical Centre; 2014.

3. Tyagi N, Pandey A, Parihar A, *et al*. Analysis of the efficacy of elastography in comparison with dynamic renal nuclear scintigraphy in the evaluation of unilateral pelvie-ureteric junction obstruction. *J Pediatr Surg*. 2024;59:605-609.

   doi: 10.1016/j.jpedsurg.2023.11.017

4. Volkan-Salanci B, Erbas B. Diuretic renal scintigraphy in adults: Practical aspects and reporting. *Semin Nucl Med*. 2021;52:445-452.

   doi: 10.1053/j.semnuclmed.2021.12.006

5. Nilsson JN, Elovsson R, Thor D, Calissendorff J, Ardenfors O. Radioiodine treatment outcome by dosimetric parameters and renal function in hyperthyroidism. *Thyroid Res*. 2022;15:8.

   doi: 10.1186/s13044-022-00126-4

6. François H, Richardson A, Boubaker A, *et al. Dynamic Renal Imaging in Obstructive Renal Pathology a Technologist's Guide*. Austria: European Association Nuclear Medicine; 2009. p. 1-23.

   doi: 10.52717/NAYK4703

7. Grzegorz Filipczak K, Cichocki P, Kusmierek J, Plachcinska A. Kidney efficiency index - quantitative parameter of a dynamic renal scintigraphy. I. Theory and preliminary verification. *Nucl Med Rev*. 2020;23(2):78-83.

   doi: 10.5603/NMR.2020.0025

8. Wu R, Huang D, Wang Z, *et al*. The Application of Renal Dynamic Imaging in Measuring Renal Function of En-Bloc Pediatric Kidneys Transplanted into Recipients. In: Liu C, editors. *Proceedings of the 23rd Pacific Basin Nuclear Conference. Springer Proceedings in Physics*. Vol. 3. Singapore: Springer; 2023. 233-245.

   doi: 10.1007/978-981-19-8899-8-24

9. Grilo N, Schurch B. Renal Function Evaluation. In: Liao L, Madersbacher H, editors. *Handbook of Neurourology*. Singapore: Springer; 2023.

   doi: 10.1007/978-981-99-1659-7-21

10. Civan C, Simsek DH, Kiran MY, *et al*. Comparison of 2D planar and 3D volumetric methods for estimation of split renal function by 99mTc-DMSA scintigraphy. *Phys Med*. 2022;95:83-88.

    doi: 10.1016/j.ejmp.2022.01.010

11. Reichkendler MH, Berg RMG, De Nijs R, Nørgaard H, Schmidt IM, Borgwardt L. Planar scan vs. SPECT/low-dose CT for estimating split renal function by ^{99m}Tc-DMSA scintigraphy in children. *Eur J Nucl Med Mol Imaging*. 2020;47(3):729-733.

    doi: 10.1007/s00259-019-04575-2

12. Orrico M, Cosma L, Ricci M, *et al*. Early renal function alterations in renal branches vs. Renal fenestrations - a dynamic scintigraphy based prospective study. *Eur J Vasc Endovasc Surg*. 2020;60(3):395-401.

    doi: 10.1016/j.ejvs.2020.05.023

13. Taylor AT. Radionuclides in nephrourology, part 1: Radiopharmaceuticals, quality control, and quantitative indices. *J Nucl Med*. 2014;55(4):608-615.

    doi: 10.2967/jnumed.113.133447

14. Kersting D, Sraieb M, Seifert R, *et al.* First experiences with dynamic renal [$^{68]}$Ga]Ga-DOTA PET/CT: A comparison to renal scintigraphy and compartmental modelling to non-invasively estimate the glomerular filtration rate. *Eur J Nucl Med Mol Imaging*. 2022;49:3373-3386.

    doi: 10.1007/s00259-022-05781-1

15. Murray AW, Barnfield MC, Waller ML, Telford T, Peters AM. Assessment of glomerular filtration rate measurement with plasma sampling: A technical review. *J Nucl Med Technol*. 2013;41(2):67-75.

    doi: 10.2967/jnmt.113.121004

16. Rahimi A, Hosntalab M, Babapour Mofrad F, Amoui M, Bagci U. An automatic segmentation framework for computer-assisted renal scintigraphy procedure. *Med Biol Eng Comput*. 2023;61:285-295.

    doi: 10.1007/s11517-022-02717-7

17. Aggarwal P, Gunasekaran V, Gowtham M, *et al*. Assessment of post-pyeloplasty renal drainage in antenatally detected hydronephrosis by $^{99]m}$Tc-L, L-Ethylenedicysteine renal scintigraphy: The importance of delayed imaging. *Ann Nucl Med*. 2024;39:266-272.

    doi: 10.1007/s12149-024-01994-6

18. Zheng X, Wei W, Huang Q, Song S, Huang G. Automated

region of interest detection method in scintigraphic glomerular filtration rate estimation. *IEEE J Biomed Health Informatics*. 2019;23(2):787-794.

doi: 10.1109/JBHI.2018.2845879

19. Pi Y, Zhao Z, Yang P, *et al*. Deep regression using $^{99]m}$Tc-DTPA dynamic renal imaging for automatic calculation of the glomerular filtration rate. *Eur Radiol*. 2023;33:34-42.

    doi: 10.1007/s00330-022-08970-6

ACCSCIENCE PUBLISHING

Advances in Radiotherapy & Nuclear Medicine

ORIGINAL RESEARCH ARTICLE

Radical radiotherapy using volumetric-modulated arc therapy for treating bladder and pelvic lymph nodes in locally advanced bladder cancer: A retrospective single-center study

Nilesh Tambe, Stephen Kendall, Vikram Bansal, Faheem Bashir, Theingi Aung, Sanjay Dixit, Pattu Pughazenthi, and Mohan Hingorani*

Department of Clinical Oncology, Queen's Centre for Oncology and Haematology, Hull University Teaching Hospitals NHS Trust, Castle Hill Hospital, Cottingham, Yorkshire, United Kingdom

***Corresponding author:**
Mohan Hingorani
(mohan.hingorani3@nhs.net)

Citation: Tambe N, Kendall S, Bansal V, *et al*. Radical radiotherapy using volumetric-modulated arc therapy for treating bladder and pelvic lymph nodes in locally advanced bladder cancer: A retrospective single-center study. *Adv Radiother Nucl Med*. 2025;3(2):73-85.
doi: 10.36922/ARNM025090009

Received: February 25, 2025

Revised: March 17, 2025

Accepted: April 7, 2025

Abstract

The prognosis of patients with muscle-invasive bladder cancer (MIBC) and pelvic nodes remains poor. We developed a novel radiotherapy (RT) protocol using volumetric-modulated arc therapy (VMAT) to treat bladder and locoregional nodes in MIBC. This study explores the safety, efficacy, and development of the VMAT protocol. Between June 2020 and August 2024, a total of 17 patients were treated using the novel VMAT protocol. The treatment regimen consisted of 57.5 Gy in 23 fractions to the bladder and 46 Gy in 23 fractions to the pelvic nodes. The present study reports on various parameters, including patient-related, disease-related, and treatment-related characteristics, along with toxicity profiles and long-term outcomes (response rates, nature of progression, and survival). The RT protocol was well tolerated, with 15 patients (88%) completing treatment as planned. Most acute toxicities were grade 1 or 2. One patient (6%) experienced a grade 3 acute toxicity (pain and local discomfort), while two patients (12%) experienced grade 3 late toxicity (colovesical fistula and severe radiation-induced cystitis). Following treatment, 12 patients (71%) had a response or a stable disease. Two patients (12%) developed local recurrence, six (35%) developed metastatic relapse, and nine patients (53%) showed no progression. The median progression-free survival was 15.8 months (95% confidence interval [CI]: 12.4 – 64.6), while the median overall survival was 23.1 months (95% CI: 13.6 – 64.6). This study has several limitations, primarily due to its retrospective design and small patient cohort. Furthermore, there was considerable variability in histology, fitness scores, and concomitant chemotherapy treatment. Nonetheless, the findings demonstrate the safety and feasibility of the VMAT protocol for treating the bladder and pelvic nodes in locally advanced MIBC, and they provide a rationale for future prospective studies to further evaluate the role of pelvic RT in this population.

Keywords: Bladder cancer; Radiation therapy; Chemotherapy

1. Introduction

Bladder cancer is the seventh most common cancer in the United Kingdom (UK), accounting for 3% of all cancers, with over 10,000 new cases diagnosed each year.[1,2]

Radical cystectomy (with or without neoadjuvant chemotherapy [NAC]) is the standard of care for patients with localized muscle-invasive bladder cancer (MIBC).[3,4] Trimodality therapy (TMT) is a bladder preservation strategy that combines radiotherapy (RT) with concurrent radiosensitizers after maximal transurethral resection of the bladder tumor (TURBT). The historical view of radical cystectomy being the gold standard of care in MIBC has been challenged by more recent data that have shown TMT to be equivalent, if not superior, in terms of disease control.[5]

Radical RT protocols in the UK usually employ a conventionally fractionated dose of 64 Gy in 32 fractions or a hypofractionated dose of 55 Gy in 20 fractions delivered to the entire bladder using a three-dimensional conformal technique or intensity-modulated RT (IMRT).[1] Supporters of conventional fractionation argue that a lower dose per fraction should result in a superior therapeutic index – characterized by a higher probability of tumor control and reduced rates of late toxicity – due to the presumed high α/β ratio of bladder cancer. However, a recent meta-analysis of individual patient data from the BCON and BC2001 trials, which allowed both dosing regimens, demonstrated similar toxicity rates and better locoregional control with hypofractionation.[6]

The survival outcomes of localized MIBC have significantly improved over the years. In a propensity-matched score analysis of MIBC treated with cystectomy or TMT, the 5-year disease-specific survival rate was 73.2% and 76.6% in the cystectomy and TMT groups, respectively.[7] However, there is limited data regarding the optimal management of patients with pelvic node-positive, non-metastatic bladder cancer, and the prognosis of these patients remains uncertain and poorly defined. A growing body of evidence indicates that this is a unique clinical entity with an intermediate prognosis that falls between advanced metastatic bladder cancer and bladder-confined MIBC.

The clinical management of bladder cancer, whether clinically or pathologically node-positive, has seen significant variation as practice patterns have continued to change. A palliative approach that involves systemic therapy alone, with local therapy saved for symptom control, is preferred by certain multidisciplinary teams. Others advocate for a curative-intent strategy that includes NAC with either cystectomy or TMT.[8,9]

Although several studies have shown that neoadjuvant and adjuvant chemotherapy reduces the rate of distant metastases, individuals with node-positive illness are also at a considerable risk of locoregional recurrence.[3,4,10]

There is a lack of good-quality evidence on the role of TMT in treating patients with node-positive disease. Delivering the prescribed dose to the target volume without raising the risk of acute and long-term toxicity is one of the primary challenges when using RT to treat patients with node-positive bladder cancer. However, the complex and dynamic manipulation of radiation beams has been made possible by advances in RT planning conformal approaches such as IMRT, enabling proper target coverage while sparing nearby organs at risk (OAR). In a study conducted by Sondergaard *et al.*,[11] 16 patients were treated with IMRT, delivering 60 Gy to the bladder and 48 Gy to the pelvic lymph nodes. The dose-volume histogram parameters for relevant normal tissues (e.g., bowel, bowel cavity, rectum, and femoral heads) for the IMRT plans were compared with the corresponding dose-volume histogram from the conformal sequential boost technique. IMRT demonstrated statistically significant sparing of normal tissue. For the bowel, a significant reduction was observed at all dose levels between 20 and 50 Gy ($p<0.05$), such as from 180 to 121 cm^3 at 50 Gy. Similar patterns were observed for the bowel cavity, rectum, and femoral head. The acute gastrointestinal (GI) toxicity was 38%. IMRT to the urinary bladder and elective lymph nodes resulted in considerable sparing of normal tissue compared to the conformal sequential boost technique.

To explore the use of TMT for treating patients with node-positive bladder cancer post-surgery, we developed a unique RT protocol utilizing volumetric modulated arc therapy (VMAT). The purpose of this study is to examine the evolution of the VMAT protocol and to assess the efficacy of RT in managing patients with primary bladder cancer and potentially involved locoregional pelvic lymph nodes.

2. Materials and methods

2.1. Study population

The novel VMAT-RT protocol was implemented in 2020, involving the delivery of 57.5 Gy in 23 fractions to the bladder and 46 Gy in 23 fractions to the nodes. We reviewed the RT planning systems (Varian Eclipse, US) to identify patients who received treatment with this protocol between June 2020 and August 2024. A total of 17 patients who were treated with this protocol were identified. All patients were discussed at the urology multi-disciplinary team meeting, had a histological confirmation of malignancy, and underwent computed tomography (CT) scans for staging of their disease. Based on the CT scan, all patients had disease limited to the pelvis, with no lymphadenopathy observed above the aortic bifurcation. As none of the patients were deemed appropriate for surgery, radical RT (with or without concurrent chemotherapy) was recommended. Due to the retrospective nature of the study, obtaining consent for participation from the study subjects was not feasible.

The following parameters were identified and assessed through a review of the patients' clinical records:

i. Patient characteristics, including age, sex, comorbidities, and the reason for not proceeding with surgery
ii. Features of the disease – histology, stage (tumor [T] and node [N]), and date of diagnosis
iii. Treatment characteristics and toxicity – information about concomitant chemotherapy, early toxicity (less than 3 months), late toxicity (more than 3 months), and RT (number of completed fractions)
iv. Treatment response following chemoradiotherapy (CRT) completion – complete response was defined as complete tumor response on both CT scan and cystoscopy performed 3 months after treatment completion; stable disease was characterized by persistent tumor at cystoscopy, but no progression evident on staging CT scan; progressive disease was defined as unequivocal evidence of progression on cystoscopy or CT scan
v. Survival outcomes – overall survival (OS) and progression-free survival (PFS) estimated from the date of diagnosis, as well as the type (local vs. metastatic) and site of progression.

2.2. Development of VMAT clinical protocol

The standard RT dose is 55 Gy in 20 fractions for localized bladder cancer and 46 Gy in 23 fractions for pelvic nodes. The dose to the nodes was predefined at 46 Gy in 23 fractions. Radiobiological modeling was employed to estimate the biologically effective dose (BED) – equivalent to 55 Gy in 20 fractions delivered over 23 fractions as a synchronous integrated boost to the bladder. The BED was calculated using an α/β value of 10 for the tumor, and the aim was to keep BED for the primary tumor similar to the bladder-only clinical protocol (i.e., equivalent to 55 Gy in 20 fractions), without increasing the dose or the dose per fraction to the pelvic nodes, which was maintained at 46 Gy in 23 fractions.

The BED calculations were performed to calculate the dose per fraction to the primary tumor (i.e., bladder planning target volume [PTV]) for 23 fractions using Equation 1.

$$BED = nd[1 + \frac{d}{\left(\alpha/\beta\right)}] \quad (1)$$

Note: d is the dose per fraction, and n is the number of fractions.

The above dose modeling generated a dose fractionation of 57.5 Gy in 23 fractions with BED_{10} of 71.88 Gy, which was similar to BED_{10} of 70.13 Gy observed with 55 Gy in 20 fractions.

2.3. Treatment simulation

All patients were scanned supine with an empty bladder and rectum. Ankle and knee support were used to immobilize and achieve set-up reproducibility. A 100 mL Omnipaque intravenous contrast was administered with a 70 sec delay. No oral contrast was used for these patients.

2.4. Target delineation

The primary clinical target volume (CTVp) included the bladder and any extravesical extension, with a 5 mm margin applied mainly at the tumor site. The inclusion of prostatic urethra in the volume was at a clinician's discretion, and the whole prostate was included in patients with tumors located at the base or invading the prostate. In addition, the clinical target volume for the elective nodes (CTVn) started at the lower border of L5, using a 7 mm margin around the vessels, including common iliac, internal and external iliac, pre-sacral (from S1 to S3), and pelvic lymph nodes down to the level of obturators (top of pubic symphysis). The bowel, bladder, bone, and muscle were excluded from the CTVn. The primary PTV (PTVp) was produced using a 15 – 20 mm superiorly and 15 mm posteriorly, anteriorly, inferiorly, and laterally from the CTVp. The node PTV was produced using 10 mm in all directions from the CTVn.

2.5. Treatment planning

All patients were treated with VMAT using either Halcyon (Varian, United States) or TrueBeam (Varian, US) linear accelerators. The doses were calculated using the Acuros (dose to medium) algorithm (version 16, Varian, US). The treatment plans were optimized to achieve PTV coverage of V95% ≥99% (i.e., the volume of PTV receiving 95% of the prescription dose should be ≥99%) and V105% ≤2%. In addition to the target and OAR volumes, optimization structures were produced around the PTVp and node PTVs using an inner margin of 0.5 cm and outer margin of 1.5 cm to enhance target conformity. Upper objectives were used on these structures during optimization (Figure 1).

2.6. Treatment delivery

Before treatment delivery, all patients underwent daily cone beam CT imaging, and the setup differences were corrected for all fractions.

2.7. Statistical analysis

Descriptive statistics, such as the frequency (percentage) for categorical variables, were used to summarize the

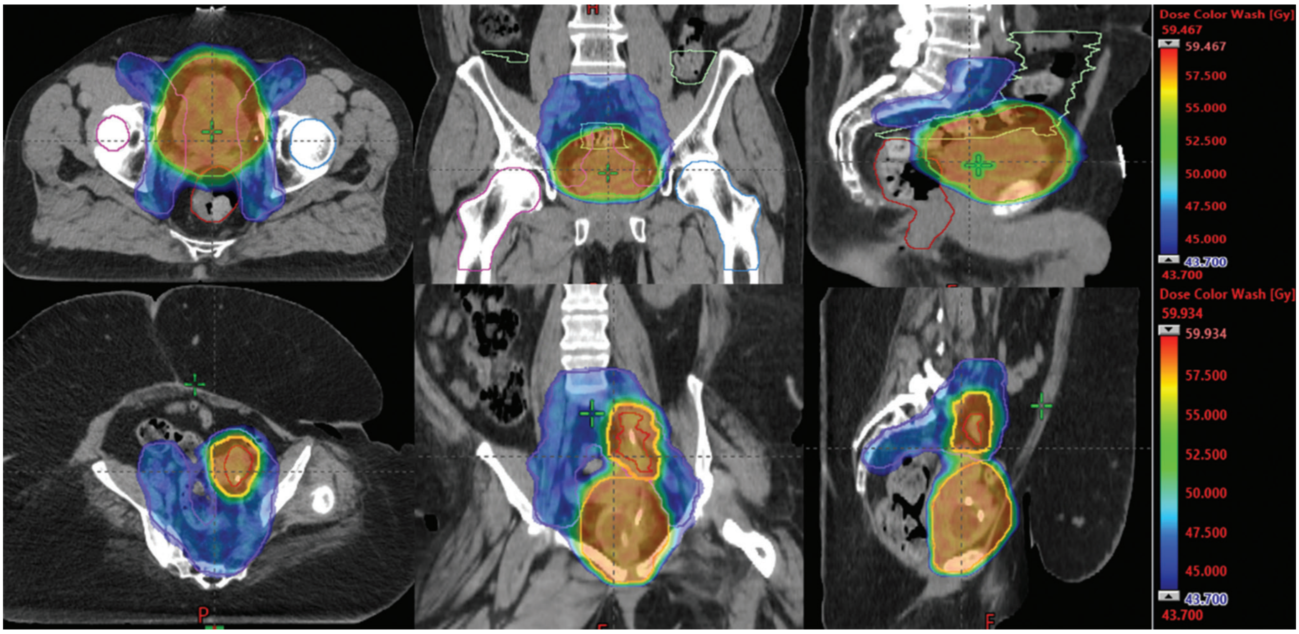

Figure 1. Dose distribution achieved with volumetric-modulated arc therapy (the dose color wash scale between 43.7 Gy [95% of the 46 Gy, node planning target volume prescription] and the max dose). The images at the top show the primary and prophylactic node volumes, as well as organs-at-risk structures, with dose distribution. The bottom images show the dose distribution for a node-positive patient, where the positive nodes received the same dose as the primary (i.e., 57.5 Gy), and the elective nodes received 46 Gy in 23 fractions.

distribution of various patient-, tumor-, and treatment-related variables. For the analysis of OS, disease-specific death was considered the sole event, while patients who were alive or had died from unrelated causes were censored at the time of their last visit. For PFS analysis, an event was defined as disease progression or recurrence, as indicated by radiological imaging and/or clinical deterioration. The durations of PFS and OS were calculated from the date of diagnosis. Survival probabilities were estimated using the Kaplan–Meier method. All statistical analyses were performed using the StatsDirect software system (StatsDirect Ltd, Version 4, UK).

3. Results

3.1. Patient characteristics and disease features

A total of 17 patients received RT to the bladder and pelvic nodes using VMAT protocol, with a male predominance (male, $n = 12$; female, $n = 5$). The median age was 66 years (range: 30 – 83 years). The reasons for not proceeding to surgery included locally advanced disease ($n = 8$), concomitant comorbidities ($n = 6$), unfavorable histology such as neuroendocrine transformation ($n = 2$), and patient choice ($n = 1$). The comorbidities, according to the American Society of Anesthesiologist status (ASA), were ASA1 ($n = 6$), ASA2 ($n = 4$), ASA3 ($n = 5$), and ASA4 ($n = 2$). The following comorbidities were frequently noted: pulmonary hypertension with Eisenmenger syndrome ($n = 1$), cerebrovascular disease ($n = 1$), peripheral vascular disease ($n = 1$), sleep apnea ($n = 1$), chromic paraplegia ($n = 1$), ischemic heart disease ($n = 3$), hypertension ($n = 4$), and type II diabetes ($n = 3$). The majority of patients ($n = 10$) had transitional cell carcinoma (TCC), followed by TCC with divergent squamous ($n = 4$), TCC with neuroendocrine differentiation ($n = 2$), and pure poorly differentiated neuroendocrine (small cell phenotype) carcinoma ($n = 1$). The distribution of T stages was T2 ($n = 5$), T3 ($n = 10$), and T4 ($n = 2$). Two patients had N0 stage disease, and 15 patients had N1 stage disease, with positive pelvic nodes on cross-sectional imaging (Table 1).

3.2. Treatment characteristics and toxicity (Tables 2 and 3)

3.2.1. Upfront (induction) chemotherapy

Ten patients (59%) received an upfront (induction) systemic anti-cancer therapy (SACT) before proceeding to RT. The commonly employed regimens included gemcitabine/cisplatin ($n = 5$), carboplatin/gemcitabine ($n = 1$), atezolizumab ($n = 1$), cisplatin/etoposide ($n = 1$), carboplatin and etoposide ($n = 1$), and cisplatin/gemcitabine followed by pembrolizumab ($n = 1$). Seven patients (41%) proceeded to RT without any induction chemotherapy.

The median number of cycles was three; however, at least two patients (12%) received a prolonged duration of

Table 1. Patient demographics and disease-related characteristics

Parameter	Value
Sex (number of patients, *n*=17)	
Male	12
Female	5
Age (years)	
Median (range)	66 (30 – 83)
Comorbid status	
ASA1	6
ASA2	4
ASA3	5
ASA4	2
Histology	
Transitional cell cancer	10
TCC with squamous differentiation	4
Neuroendocrine differentiation	3
Reason for not proceeding to surgery	
Locally advanced disease	8
Comorbidities	6
Histology	2
Patient's choice	1
Staging (T stage)	
T2	5
T3	10
T4	2
Staging (N stage)	
N0	2
N1	15

Abbreviations: ASA: American Society of Anesthesiologists; N: Node; T: Tumor; TCC: Transitional cell carcinoma.

Table 2. Treatment characteristics and toxicity

Parameter	Value
Induction systemic therapy	
Gemcitabine/cisplatin	5
Carboplatin/gemcitabine	1
Cisplatin/etoposide	1
Carboplatin and etoposide	1
Atezolizumab	1
Gemcitabine and cisplatin followed by pembrolizumab	1
No induction treatment	7
Radiotherapy (57.5 Gy in 23 fractions)	
Completed	15
Stopped early	2
Concurrent chemotherapy	
Gemcitabine	9
Cisplatin	4
Cisplatin/etoposide	1
Mitomycin/fluorouracil	1
No concurrent chemotherapy	2
Toxicity	
Early (<3 months)	
Fatigue	14
Nausea	4
Diarrhea	9
Pain/local discomfort	9
Increased frequency micturition	8
Dysuria	6
Hematuria	2
Constipation	2
Skin erythema	1
≥Grade 3 toxicity	1
Late (>3 months)	
Gastrointestinal toxicity	3
Genitourinary toxicity	2
≥Grade 3 toxicity	2

systemic therapy before proceeding to CRT. One patient (6%) was treated with three cycles of gemcitabine/cisplatin followed by ten 3 weekly cycles of pembrolizumab. A second patient received atezolizumab for 2 years before proceeding to CRT (Table 2).

3.2.2. RT (with or without concurrent chemotherapy)

A total of 15 patients (88%) received concurrent chemotherapy (gemcitabine, $n = 9$; cisplatin, $n = 4$; cisplatin/etoposide, $n = 1$; and mitomycin/fluorouracil, $n = 1$), and two patients (12%) received only RT.

All treatments were planned using VMAT and delivered through either Halcyon or TrueBeam linear accelerators. Treatment plans were optimized to achieve the clinical goals (Table 3). Two full arcs were used for patients treated on TrueBeam, and three arcs were used for patients treated on Halcyon. The desired PTV coverage – specifically, 99% of the PTV covered by at least 95% of the prescription dose – was achieved in all patients. OAR doses were also achieved for most patients; however, the bowel bag constraint (V45 Gy < 195 cc) could only be achieved for two out of 17 patients. The rectum constraints (V40 Gy < 60%, V50 Gy < 50%, and V57.5 Gy < 5%) were exceeded in three, one, and four patients, respectively. No correlation was observed between OAR doses and the linear accelerator used for the treatment. Two out of

Table 3. Clinical constraints and achieved doses for the planning target volume and organs at risk

Structure	Clinical constraints	Achieved clinical goals	Standard deviation
PTVnDVH[a]	V76% > 99%	99.74	0.17
PTVp	V95% > 99%	99.79	0.32
	V105% < 2.0%	0.02	0.03
Left femoral head	V50 Gy <25%	0.00	0.00
Right femoral head	V50% < 25%	0.01	0.04
Rectum	V40 Gy <60%	46.49	16.08
	V50 Gy <50%	23.00	13.98
	V57.5 Gy <5%	6.47	8.80
Small bowel[b]	V45 Gy <195 cc	378.01	118.16

Notes: [a]PTVnDVH refers to the PTVn excluding PTVp; [b]Small bowel refers to the bowel bag.
Abbreviations: PTVn: Node planning target volume; PTVnDVH: Planning target volume normalized dose volume histogram; PTVp: Primary planning target volume.

17 patients had a nodal boost and were treated to 57.5 Gy in 23 factions (same as the PTVp) due to node-positive disease (Table 3).

All patients underwent cone-beam CT imaging before treatment delivery. Patient setup, bladder volume, and OAR volumes were reviewed, and setup corrections were applied before treatment delivery. None of the patients had any issues with the setup.

3.2.3. Toxicity

All patients were interviewed by the staff before the treatment, with toxicities recorded in the encounter workspace within the Aria radiation oncology radiation software system (Varian, US) The data indicate that all patients generally tolerated the treatment well, with acute toxicities predominantly rated as grade 1 or lower. There were 58 adverse events observed within 3 months of RT (early toxicity), with most graded as grade 1 or 2, and only one event was graded as clinically significant grade 3 toxicity. The most common toxicity observed was fatigue ($n = 14$), followed by diarrhea ($n = 9$), pain or local discomfort ($n = 9$), increased frequency of micturition ($n = 8$), dysuria ($n = 6$), nausea ($n = 4$), hematuria ($n = 2$), constipation ($n = 3$), proctitis ($n = 2$), and skin erythema ($n = 1$).

There were five adverse events observed after 3 months of treatment completion, with three events observed for GI, and two events observed for genitourinary. Two of these events were rated as grade 3, with one patient developing a colovesical fistula, and another patient experiencing significant morbidity due to poor bladder filling caused by radiation-inducing fibrosis, warranting surgical intervention.

3.3. Outcomes and survival analysis

3.3.1. Initial assessment of response (3 months after completion of CRT)

Three patients (18%) had no available assessment records. During treatment, two patients (12%) developed progression, with one (6%) developing liver metastases while the other patient (6%) developing liver and lung metastases. A total of 12 patients (71%) had post-treatment staging CT scans after 3 months of treatment completion, and eight (47%) of them had a cystoscopy performed at that time. Seven patients (41%) achieved a complete response, with no evidence of tumor progression on staging CT and no visible/residual tumor on cystoscopy. Five patients (29%) had a stable disease, with no progression on staging CT scans. However, four (23%) of these patients did not undergo a cystoscopy to confirm the completeness of the response, and one (6%) had a residual tumor visible on the cystoscopy (Figure 2A).

3.3.2. Long-term outcomes (progression-free and OS)

Following CRT, eight patients (47%) developed progression, with two patients (12%) experiencing local progression, and six patients (35%) experiencing metastatic progression. The isolated metastatic relapses most frequently occurred in the liver (n = 3), liver and lungs (n = 1), bone (n = 1), as well as the brain and nodes (n = 1). Following treatment, nine patients (53%) showed no signs of progression or relapse. Ten patients (59%) had passed away at the last follow-up (FU) visit (median FU: 15 months), with three patients (18%) dying due to unrelated causes and seven patients (41%) dying due to progressive disease (Figure 2B). Seven (41%) patients were alive and well, with no signs of recurrence. The median PFS was 15.8 months (95% confidence interval [CI]: 12.4 – 64.6). The median OS was 23.1 months (95% CI: 13.6 – 64.6), and the mean OS was 32.04 months (95% CI: 16.6 – 47.4) (Figure 3).

We investigated the effects of induction SACT, histology, and comorbidity status on OS. Patients who received induction SACT had a significantly improved OS compared to those who did not receive induction SACT (median OS: 40.1 vs. 13.6 months; hazard ratio [HR]: 0.16; 95% CI: 0.02 – 1.12; p=0.002). Patients with pure TCC had a non-significant trend toward improved OS (median OS not reached) compared to those with divergent squamous or neuroendocrine differentiation (median OS: 17.93 months; HR: 0.60; 95% CI: 0.13 – 2.68; p=0.49). Patients with ASA1 or ASA2 had a non-significant trend toward improved OS (median OS: 40.1 months) compared to those with ASA3 or ASA4 (median OS: 23.1 months; HR: 0.50; 95% CI: 0.09 – 2.64, p=0.32) (Figure 4).

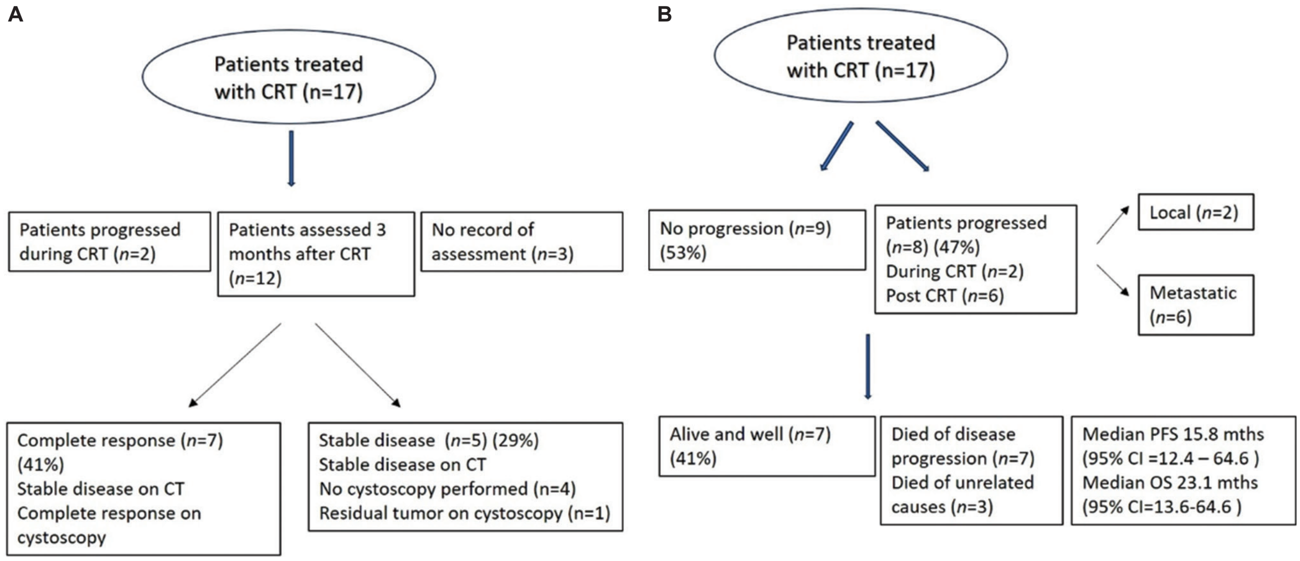

Figure 2. Schematic illustration of assessment of response post-radiotherapy and long-term outcomes. (A) Two patients showed disease progression during RT. The initial response was assessed 3 months after RT in 12 patients. Seven (41%) patients had a complete response, and five (29%) patients had stable disease post-RT; (B) Eight patients progressed post-RT, with six patients developing metastatic relapse and only two patients developing local recurrence. Nine (53%) patients developed no progression.

Abbreviations: CRT: Chemoradiotherapy; CT: Computed tomography; OS: Overall survival; PFS: Progression-free survival; RT: Radiotherapy.

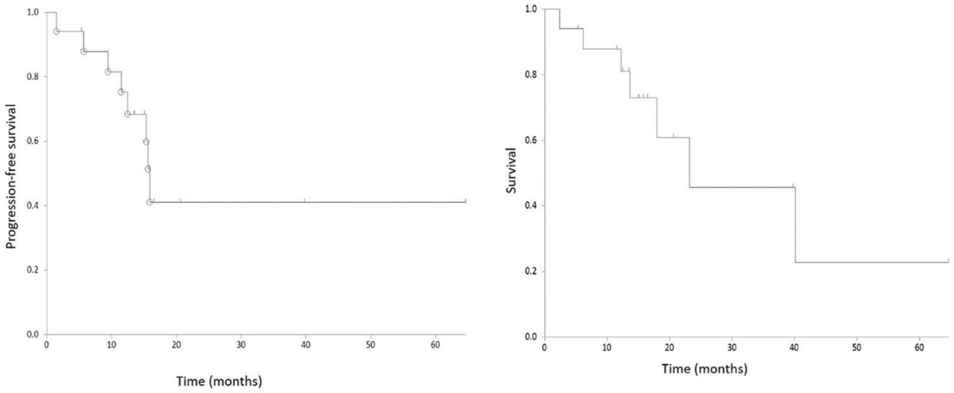

Figure 3. Kaplan–Meier survival analysis. After median follow-up of 15 months, ten patients had died: seven due to progressive disease, and three due to unrelated causes. Seven (41%) patients were alive and well. The median progression-free survival was 15.8 months (95% CI: 12.4 – 64.6). The median overall survival (OS) was 23.1 months (95% CI: 13.6 – 64.6) and the mean OS was 32.04 months (95% CI: 16.6 – 47.4).

Abbreviation: CI: Confidence interval.

4. Discussion

This study provides a retrospective analysis of bladder cancer patients who underwent RT (with or without concurrent chemotherapy) using a novel VMAT protocol. The protocol delivered 57.5 Gy in 23 fractions to the bladder and primary tumor, as well as 46 Gy in 23 fractions to the pelvic lymph nodes. Due to the comorbidities, low fitness scores (ASA3 or ASA4, *n* = 7), adverse histology, or personal choice, radical cystectomy was not considered appropriate. Thus, these patients were treated with TMT, which involved TURBT followed by RT, and most patients also received concurrent chemotherapy.

Technological developments in RT delivery, from the four-field box approach to three-dimensional conformal RT (3D-CRT), IMRT, and VMAT, have made it possible to modulate the radiation dose, concentrating the high-dose regions around the tumor while minimizing the dose to adjacent OARs. When it comes to the definitive treatment of bladder cancer, IMRT using the VMAT technique may provide dosimetric and therapeutic advantages over 3D-CRT. A study by Sherry *et al.*[12] reported the dosimetric advantages of VMAT, observing over 50% reduction in the rectum and bowel (V40, V45, V50, V55, and V60) doses in the VMAT group compared to 3D-CRT. Daily

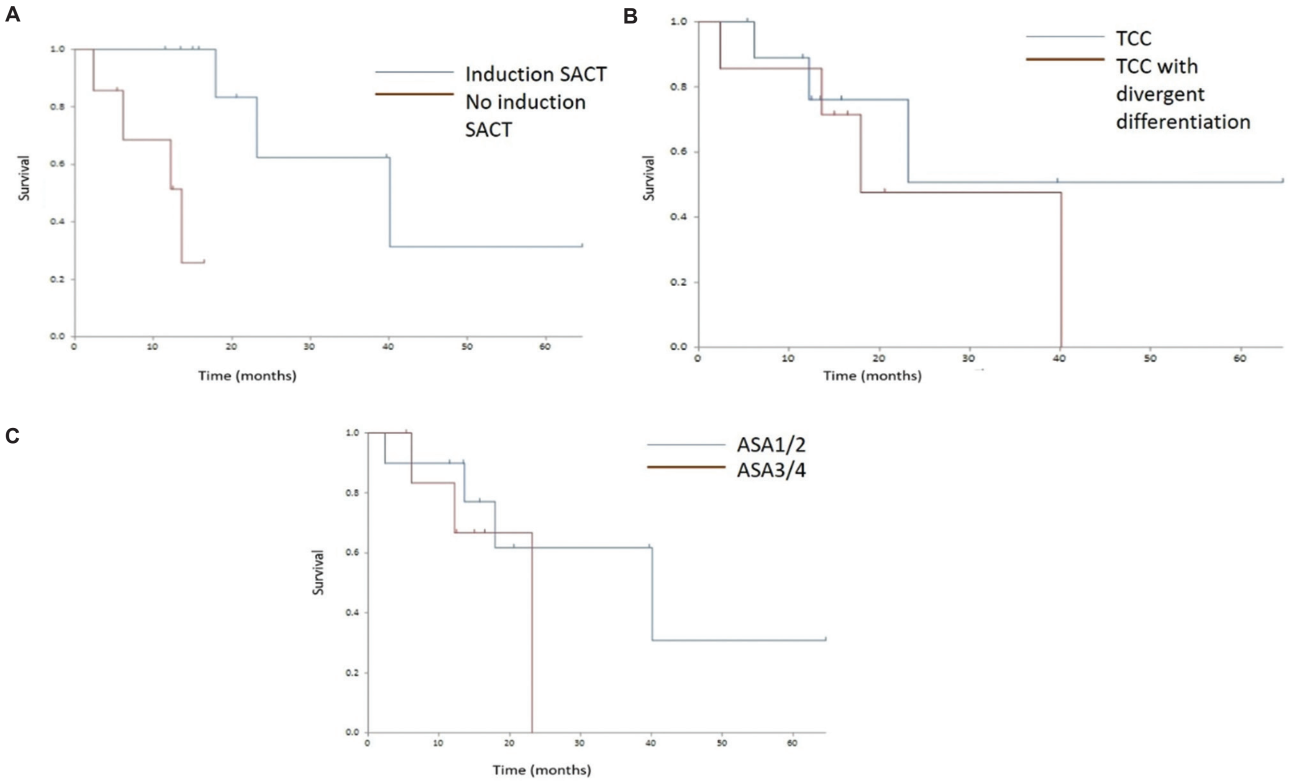

Figure 4. Effects of different variables on survival. (A) Effect of induction SACT: Patients who received induction SACT had a significantly improved OS compared to those who did not (median OS: 40.1 months vs. 13.6 months; HR: 0.16; 95% CI: 0.02 – 1.12; p=0.002); (B) Effect of histology: Patients with pure TCCs had a non-significant trend toward improved OS (median OS not reached), compared to those with divergent squamous or neuroendocrine differentiation (median OS: 17.93 months; HR: 0.60; 95% CI: 13 – 2.68; p=0.49); (C) Effect of co-morbidity: Patients with ASA1 or ASA2 had a non-significant trend toward improved OS (median OS: 40.1 months), compared to those with ASA3 or ASA4 (median OS: 23.1 months; HR: 0.50; 95% CI: 0.09 – 2.64; p=0.32).

Abbreviations: ASA: American Society of Anesthesiologists; HR: Hazard ratio; OS: Overall survival; SACT: Systemic anti-cancer therapy; TCC: Transitional cell carcinoma.

imaging with imaging-guided RT detects variations in the size, shape, and location of organs between fractions. Smaller radiation volumes can be used with image-guided RT without running the risk of geographical miss as it can detect differences in organ movements and bladder filling across fractions.[13]

The key prospective studies that investigated the role of radical RT in localized MIBC using conformal techniques are summarized in Table 4.[14-17] In a multicenter phase 3 trial reported by James *et al.*,[12] 360 patients with MIBC were randomized to receive RT, with or without concurrent chemotherapy. The chemotherapeutic protocol included mitomycin C (12 mg/m^2) on day 1 and fluorouracil (500 mg/m^2 of body-surface area per day), during fractions 1 – 5 and 16 – 20 of RT. The locoregional disease-free survival (DFS) rates after 2 years were 54% (95% CI: 46 – 62) in the radiation group and 67% (95% CI: 59 – 74) in the CRT group. The HR for the CRT group was 0.68 (95% CI: 0.48 – 0.96, p=0.03), with a median FU of 69.9 months. During treatment, the CRT group experienced slightly more grade 3 or 4 adverse events than the RT group (36.0% vs. 27.5%, p=0.07), but not during FU (8.3% vs. 15.7%, p=0.07).

In a study by Hoskin *et al.*,[16] 333 patients with MIBC were randomly assigned to either RT alone or RT with concurrent hypoxia adjustment using carbogen and nicotinamide (CON) in a phase 3 randomized trial. The patients were treated with either 64 Gy in 32 fractions over 6.5 weeks or 55 Gy in 20 fractions over 4 weeks. After 6 months, the complete cystoscopy response rate was 76% for RT alone and 81% for RT+CON (p=0.3). The 3-year OS were 46% and 59% (p=0.04) for RT alone and RT+CON arms, respectively. RT+CON significantly decreased the probability of death (p=0.03) and relapse (p=0.05) in the multivariate comparison. The therapy groups did not differ significantly in terms of GI or late urinary morbidity.

In a prospective phase 2 study, 50 MIBC patients received concurrent gemcitabine at 100 mg/m^2 on days 1,

Table 4. Prospective studies of conformal radiotherapy with concurrent chemotherapy in muscle-invasive bladder cancer using conformal techniques

Study, patient number (*n*), and study type	RT dose	Chemotherapy/radiosensitizing regime	Toxicity	Survival
James *et al.*,[12] *n*=360, phase 3 RCT of RT compared to CRT	64 Gy in 32 fractions for 6.5 weeks or 52.5 Gy in 20 fractions for 4 weeks	Mitomycin/fluorouracil	Grade 3 – 4 adverse events for RT (27.5%) and CRT (36.0%)	2-year survival rate of 67% for CRT, compared to 54% for RT HR: 0.68; 95% CI: 0.48 – 0.96; *P*=0.03
Hoskin *et al.*[16] *n*=333, phase 3 RCT of RT compared to RT+CON	64 Gy in 32 fractions for 6.5 weeks or 52.5 Gy in 20 fractions for 4 weeks	Carbogen/nicotinamide	No difference in grade 3 – 4 of GI or GU toxicity	3-year survival rate of 59% for RT+CON, compared to 46% for RT (*p*=0.04)
Choudhury *et al.*,[17] *n*=50, phase 2 prospective single-arm study	55 Gy in 20 fractions for 4 weeks	Gemcitabine	Four patients could not complete chemotherapy due to bowel toxicity	3-year survival rate of 75%
Sabaa *et al.*,[15] *n*=104, phase 2 prospective single-arm study	Conventional fractionation 64 Gy in 32 fractions	Gemcitabine/cisplatin	No significant grade 3 – 4 toxicity was observed and all patients completed treatment as planned	5-year survival rate of 59.4%

Abbreviations: CI: Confidence interval; CON: Carbogen and nicotinamide; CRT: Chemoradiotherapy; GI: Gastrointestinal; GU: Genitourinary; HR: Hazard ratio; RCT: Randomized controlled trial; RT: Radiotherapy.

8, 15, and 22, along with a 28-day RT regimen consisting of 55 Gy in 20 fractions. All patients completed RT, and 46 (92%) of them were able to complete all four gemcitabine cycles. Two patients (4%) stopped their treatment after two cycles, while two (4%) stopped after three cycles. Out of 47 patients who had a post-treatment cystoscopy, 44 (88%) of them had a full endoscopic response. Out of 36 patients who were still alive at the median FU of 36 months (range: 15 – 62 months), 32 (64%) of them had a functional and intact bladder. Two (4%) patients died as a result of treatment-associated complications, five patients (10%) died due to intercurrent disease, and seven patients (14%) died due to metastatic MIBC. Cystectomy was performed on three patients (6%) due to recurrent illness and one (2%) due to toxicity. The OS was 75%, and cancer-specific survival was 82% after 3 years.[15]

Multiple single-arm prospective studies in RT oncology have evaluated the role of radical RT in conjunction with concurrent cisplatin-based chemotherapy and reported a 3-year survival rate ranging from 60% to 80%. Based on this evidence, concurrent CRT is currently considered the gold standard of care for patients undergoing TMT as part of a bladder preservation strategy.

Few studies have investigated the role of RT for patients with advanced bladder cancer and node-positive disease. A multicenter retrospective study looking at survival outcomes in patients with node-positive MIBC was reported by Swinton *et al.*[18] Participating UK oncology centers that offered both TMT and radical cystectomy provided data on patients (*n* = 287) with clinically node-positive, non-metastatic MIBC. All patients had a median OS of 1.55 years (95% CI: 1.35 – 1.82 years). When compared to palliative care, undergoing radical treatments was associated with an enhanced OS rate (HR: 0.32; 95% CI: 0.23 – 0.44; *p*<0.001). Patients who had radical treatment (*n* = 163) either underwent radical cystectomy (*n* = 76) or received a radical dose of RT (*n* = 87). The multivariate analysis revealed no correlation between the choice of radical treatment and OS (HR: 0.94; 95% CI: 0.63 – 1.41; *p*=0.76) or PFS (HR: 0.74; 95% CI: 0.50 – 1.08*;* *p*=0.12). Swinton *et al.* recommended that all patients with node-positive MIBC should have access to bladder-sparing TMT treatment due to limited prognosis and the recognized morbidities associated with radical cystectomy. Tan *et al.*[9] reported on a phase 2 prospective study of intensity-modulated pelvic node and bladder RT, conducted to assess the feasibility of delivering IMRT to treat the bladder and pelvic nodes in patients with node-positive or high-risk node-negative bladder cancer. In this study, they delivered 64 Gy in 32 fractions to the tumor bed, 60 Gy in 32 fractions to the positive nodes, and 52 Gy in 32 fractions to the bladder, excluding the tumor bed and elective nodes. The trial reported acute grade 1 and 2 GI and genitourinary toxicities in 81.1% and 70.6% of patients, respectively, and grade 3 toxicities of 5.4% and 20.6%, respectively. Grade 3 late toxicities were 5%, with one patient reporting grade 3 cystitis and hematuria. No grade 3 or 4 toxicities were reported in year 2. The median 1-, 2-, and 5-year pelvic relapse-free survival rates were 55%, 37%, and 26%, respectively. The median OS was 1.9 years (95% CI: 1.1 – 3.8), with 1-, 2-, and 5-year OS rates of 68%, 50%, and 34%, respectively. Sondergaard *et al.*[11] treated 16 patients with 60 Gy to the bladder and

48 Gy to nodes and reported that six (38%) of the patients had grade 1 and 2 lower toxicities after IMRT, while no grade 3 and 4 toxicities were reported in this study.

The role of pelvic RT in MIBC has also been evaluated in the adjuvant (post-operative) setting. In a multicenter phase 2 trial by Fonteyne *et al.*,[19] 17 patients received IMRT, delivering 50 Gy in 25 fractions to the tumor bed and pelvic nodes. Acute grade 2 GI toxicity was observed in 62% of patients, while 4% developed acute grade 3 GI toxicity. One patient had grade 5 diarrhea and vomiting due to obstruction after 1 month. In a trial by Murthy *et al.*,[20] 18 patients were treated to the tumor bed and pelvic node to 50.4 Gy in 28 fractions, and they reported that RT to the lymph nodes increased DFS from 70% to 85%.

The present study describes a novel hypofractionated RT dose-fractionation schedule (57.5 Gy to the primary tumor and 46 Gy in 23 fractions to the nodes) using VMAT for treating bladder and pelvic nodes in patients with MIBC. To our knowledge, this protocol has not been reported previously. The development of the protocol was based on sound radiobiological modeling with a BED equivalent to a hypofractionated schedule of 55 Gy in 20 fractions (α/β value of 10), with similar probabilities of tumor control. The BED_{2Gy} for late toxicity in the new protocol (with an α/β value of 2 for late-responding tissues) was 64.68 Gy, compared to 65.3 Gy for the hypofractionated schedule of 55 Gy in 20 fractions. Therefore, it was hypothesized that the use of the new protocol of 57.5 Gy in 23 fractions would be associated with similar levels of tumor control and toxicity as the hypofractionated schedule of 55 Gy in 20 fractions. In MIBC, pelvic RT is often administered using conventional fractionation, which uses 46 – 48 Gy to target the nodes and 60 – 64 Gy to target the primary tumor. A recent meta-analysis of patients with localized MIBC found that hypofractionated RT was linked to improved locoregional control as compared to conventional fractionation. Therefore, a hypofractionated pelvic RT technique may offer benefits in terms of promoting effective local control.

Six patients (35%) in the study cohort had major comorbidities, and two patients (12%) had adverse histology with neuroendocrine transformation, making them a prognostically unfavorable group of patients. A total of 15 patients (88%) had evidence of clinically node-positive disease, and two patients (12%) received elective nodal irradiation in the presence of high-risk MIBC. Ten patients (59%) received SACT with platinum-based doublet combination chemotherapy – the most commonly employed regime (n = 8). One patient (6%) received cisplatin/gemcitabine chemotherapy followed by maintenance pembrolizumab, and another (3%) patient received upfront atezolizumab. The median number of cycles administered was three, and patients were reviewed after the completion of chemotherapy to ensure they had no significant residual toxicity before commencing RT. NAC targets micrometastatic disease and may reduce primary tumor volume after incomplete TURBT, while also improving the OS and DFS rates. In the BA06 study, NAC with cisplatin, methotrexate, and vinblastine was administered, followed by either cystectomy or RT. The trial reported a 16% reduction in the risk of death, with the 3-year survival rate increasing from 50% to 56% in favor of NAC.[10] Before cystectomy or RT, platinum-based neoadjuvant combination chemotherapy has demonstrated the potential to deliver a 5% absolute OS benefit and a 9% DFS benefit at 5 years.[21]

The use of induction SACT was associated with a significant prolongation of OS rate in patients (median OS: 40.1 vs. 13.6 months; HR: 0.16; 95% CI: 0.02 – 1.12; p=0.002). The survival benefit was much higher than those reported in previous studies. However, the results may be skewed in favor of SACT due to two patients (6%) who had a prolonged duration of immunotherapy before proceeding with RT.

Most patients in our study cohort also received concurrent chemotherapy with a single agent, either gemcitabine or cisplatin – the most commonly employed regimens. Most of the acute toxicities reported were grade 1 or 2, including fatigue, diarrhea, pain or local discomfort, increased frequency of micturition, and dysuria. One patient (6%) had a grade 3 acute toxicity event (pain and local discomfort), and two patients (17%) experienced grade 3 late toxicity events (colovesical fistula and severe radiation-induced cystitis). The retrospective nature of the study limits the accurate assessment of toxicities. Nonetheless, the toxicity rates reported in our study are consistent with those reported by other studies. In our study, 70% of patients (n = 12) had a complete response or stable disease after CRT completion. More than 50% of patients (n = 9) remained disease-free at the last FU, with 47% (n = 8) developing disease progression (local progression, n = 2; metastatic progression, n = 6). The median PFS was 15.8 months. Seven patients (41%) were alive and well, with no signs of recurrence, and the median OS was 23.1 months (95% CI: 13.6 – 64.6).[9]

Our results indicate that the VMAT protocol of 57.5 Gy in 23 fractions prescribed to the bladder and primary tumor, as well as 46 Gy in 23 fractions to the pelvic lymph nodes, can be safely delivered along with concurrent chemotherapy. This protocol resulted in minimal clinically significant grade 3 toxicity and an approximately 70% response rate, including a 41% complete clinical response rate. Moreover, the treatment was extremely effective in achieving good local control, with only two patients developing local progression. Approximately 75% ($n = 6$) of relapses were metastatic in nature. The above results contradict those reported by Tan *et al*.,[9] in which 70% of patients relapsed, and 52.6% developed locoregional recurrence. In comparison, 52.9% of our patients remained disease-free, and most of the relapses (35%) were metastatic in nature. The lower rates of overall relapse and local recurrence observed in our study could be explained by the shorter FU period or the potentially higher therapeutic effectiveness of hypofractionated RT compared to conventional RT. These results are encouraging, especially as they come from a subgroup of patients with a poor prognosis.

The current study has a number of limitations, most of which are associated with its retrospective design and small patient population. Furthermore, there was a notable variation within the research cohort in terms of histology, fitness ratings, and concomitant chemotherapy treatment. Moreover, in the absence of a direct comparison, the study cannot evaluate the dosimetric advantages of VMAT over standard conformal RT techniques. Thus, these results should be interpreted with caution. However, the findings contribute significant information to the expanding body of evidence, supporting the probable role of RT in treating patients with MIBC and node-positive disease. The report emphasizes the need for further research and the planning of larger prospective studies to explore the potential role of RT in patients with MIBC and locoregional pelvic lymph nodes.

Future research should explore the intriguing effects of combining immunotherapy with RT. By targeting the programmed cell death 1 receptor, its ligand, or the cytotoxic T lymphocyte antigen 4, immune checkpoint inhibitors (ICIs) alter the immune response to cancer cells.[22] Current phase 2 and phase 3 clinical trials are investigating the addition of ICIs as the “fourth modality” to trimodality treatment for localized MIBC.[23] Preclinical data suggest that ICIs and RT may synergize, with radiation stimulating an immune response by releasing antigens from the tumor, which has been hypothesized to account for the sporadic “abscopal” effects of radiation.[24] The potential for dose-limiting GI toxicity (e.g., colitis) is one of the primary concerns when combining immunotherapy and RT, and this becomes particularly relevant once the pelvic lymph nodes are included in the irradiated volumes.[25] The presence of cancer cells induces a systemic response, leading to metabolic and immunological changes, which can be assessed using biomarkers. These changes may help identify patients with high-risk diseases who could benefit from more aggressive (multimodality) therapies. The inclusion of biomarkers in future research is imperative to evaluate the treatment effects and outcomes.[26]

5. Conclusion

The prognosis for patients with bladder cancer and pelvic nodes remains poor, and in the absence of surgery, most of these patients are treated with the best supportive care or palliative systemic therapy options. We successfully implemented a novel pelvic RT protocol for MIBC treatment, which was well tolerated with low levels of clinically significant acute or late toxicities. The OAR constraints were met using both TrueBeam and Halcyon VMAT, with plans consisting of two arcs or three arcs. The present study demonstrates the safety and feasibility of using this VMAT protocol in a fragile and prognostically unfavorable group of patients, with approximately 70% response rate and more than 90% local control rate. Most relapses were metastatic in nature, with a median OS of 23.1 months. The results from the study support the design of larger prospective studies to further evaluate the role of RT in patients with MIBC and pelvic nodes.

Acknowledgments

None.

Funding

None.

Conflict of interest

The authors declare that they have no competing interests.

Author contributions

Conceptualization: Nilesh Tambe, Stephen Kendall, Mohan Hingorani
Formal analysis: Mohan Hingorani
Investigation: Nilesh Tambe, Stephen Kendall, Mohan Hingorani
Methodology: Nilesh Tambe, Stephen Kendall, Mohan Hingorani
Writing – original draft: Nilesh Tambe, Stephen Kendall, Mohan Hingorani
Writing – review & editing: All authors

Ethics approval and consent to participate

The study was reported to the Trust clinical governance team and the Audit Management and Tracking (AMaT) online portal. Due to the retrospective nature of the study, obtaining consent for participation from the study subjects was not feasible.

Consent for publication

This is a retrospective analysis of patients who provided informed consent for the treatment. No patient-identifiable information has been used in the manuscript.

Availability of data

The data for this study can be obtained by submitting a request to the lead or corresponding author.

References

1. National Institute for Health and Care Excellence. *2019 Surveillance of Bladder Cancer: Diagnosis and Management* (*NICE guideline NG2*). London: National Institute for Health and Care Excellence (NICE); 2019.
2. Cancer Research UK. *Bladder Cancer Statistics*. Cancer Research UK; 2024. Available from: https://www.cancerresearchuk.org/health-professional/cancer-statistics/statistics-by-cancer-type/bladder-cancer#heading-one [Last accessed on 2025 May 01].
3. Abrahamsson J, Kollberg P, Almquist H, *et al.* Complete metabolic response with [18 F]fluorodeoxyglucose-positron emission tomography/computed tomography predicts survival following induction chemotherapy and radical cystectomy in clinically lymph node positive bladder cancer. *BJU Int.* 2022;129(2):174-181.

   doi: 10.1111/bju.15374
4. Afferi L, Zamboni S, Karnes RJ, *et al.* The impact of treatment modality on survival in patients with clinical node-positive bladder cancer: Results from a multicenter collaboration. *World J Urol.* 2021;39(2):443-451.

   doi: 10.1007/s00345-020-03205-z
5. Zlotta AR, Ballas LK, Niemierko A, *et al.* Radical cystectomy versus trimodality therapy for muscle-invasive bladder cancer: A multi-institutional propensity score matched and weighted analysis. *Lancet Oncol.* 2023;24(6):669-681.

   doi: 10.1016/S1470-2045(23)00170-5
6. Choudhury A, Porta N, Hall E, *et al.* Hypofractionated radiotherapy in locally advanced bladder cancer: An individual patient data meta-analysis of the BC2001 and BCON trials. *Lancet Oncol.* 2021;22(2):246-255.

   doi: 10.1016/S1470-2045(20)30607-0
7. Kulkarni GS, Hermanns T, Wei Y, *et al.* Propensity score analysis of radical cystectomy versus bladder-sparing trimodal therapy in the setting of a multidisciplinary bladder cancer clinic. *J Clin Oncol.* 2017;35(20):2299-2305.

   doi: 10.1200/JCO.2016.69.2327
8. Venkatesulu B, Liauw SL, Joshi M, *et al.* Multidisciplinary management and radiotherapy recommendations for clinically and pathologically node-positive bladder cancer. *Semin Radiat Oncol.* 2023;33(1):35-50.

   doi: 10.1016/j.semradonc.2022.10.005
9. Tan MP, Harris V, Warren-Oseni K, *et al.* The intensity-modulated pelvic node and bladder radiotherapy (IMPART) trial: A phase II single-centre prospective study. *Clin Oncol* (*R Coll Radiol*). 2020;32(2):93-100.

   doi: 10.1016/j.clon.2019.07.017
10. Griffiths G, Hall R, Sylvester R, *et al.* International phase III trial assessing neoadjuvant cisplatin, methotrexate, and vinblastine chemotherapy for muscle-invasive bladder cancer: Long-term results of the BA06 30894 trial. *J Clin Oncol.* 2011;29(16):2171-2177.

    doi: 10.1200/JCO.2010.32.3139
11. Søndergaard J, Høyer M, Petersen JB, Wright P, Grau C, Muren LP. The normal tissue sparing obtained with simultaneous treatment of pelvic lymph nodes and bladder using intensity-modulated radiotherapy. *Acta Oncol.* 2009;48(2):238-244.

    doi: 10.1080/02841860802251575
12. Sherry AD, Stewart A, Luo G, Kirschner AN. Intensity-modulated radiotherapy is superior to three-dimensional conformal radiotherapy in the trimodality management of muscle-invasive bladder cancer with daily cone beam computed tomography optimization. *J Radiat Oncol.* 2019;8(4):395-403.

    doi: 10.1007/s13566-019-00411-0
13. Kong V, Hansen VN, Hafeez S. Image-guided adaptive radiotherapy for bladder cancer. *Clin Oncol* (*R Coll Radiol*). 2021;33(6):350-368.

    doi: 10.1016/j.clon.2021.03.023
14. Sabaa MA, El-Gamal OM, Abo-Elenen M, Khanam A. Combined modality treatment with bladder preservation for muscle invasive bladder cancer. *Urol Oncol.* 2010;28(1):14-20.

    doi: 10.1016/j.urolonc.2008.07.005
15. Choudhury A, Swindell R, Logue JP, *et al.* Phase II study of conformal hypofractionated radiotherapy with concurrent gemcitabine in muscle-invasive bladder cancer. *J Clin Oncol* 2011;29(6):733-738.

    doi: 10.1200/JCO.2010.31.5721
16. Hoskin PJ, Rojas AM, Bentzen SM, Saunders MI. Radiotherapy with concurrent carbogen and nicotinamide in bladder carcinoma. *J Clin Oncol.* 2010;28(33):4912-4918.

    doi: 10.1200/JCO.2010.28.4950
17. James ND, Hussain SA, Hall E, *et al.* Radiotherapy with or without chemotherapy in muscle-invasive bladder cancer. *N Engl J Med.* 2012;366(16):1477-1488.

    doi: 10.1056/NEJMoa1106106
18. Swinton M, Mariam NBG, Tan JL, *et al.* Bladder-sparing treatment with radical dose radiotherapy is an effective

alternative to radical cystectomy in patients with clinically node-positive nonmetastatic bladder cancer. *J Clin Oncol.* 2023;41(27):4406-4415.

doi: 10.1200/JCO.23.00725

19. Fonteyne V, Dirix P, Van Praet C, *et al*. Adjuvant radiotherapy after radical cystectomy for patients with high-risk muscle-invasive bladder cancer: Results of a multicentric phase II trial. *Eur Urol Focus.* 2022;8(5):1238-1245.

    doi: 10.1016/j.euf.2021.11.004

20. Murthy V, Maitre P, Singh M, *et al*. Study protocol of the bladder adjuvant radiotherapy (BART) trial: A randomised phase III trial of adjuvant radiotherapy following cystectomy in bladder cancer. *Clin Oncol* (*R Coll Radiol*). 2023;35(9):e506-e515.

    doi: 10.1016/j.clon.2023.04.010

21. Vale CL. Neoadjuvant chemotherapy in invasive bladder cancer: Update of a systematic review and meta-analysis of individual patient data: Advanced bladder cancer (ABC) meta-analysis collaboration. *Eur Urol.* 2005;48(2):202-206.

    doi: 10.1016/j.eururo.2005.04.006

22. Van Hattum JW, De Ruiter BM, Oddens JR, Hulshof MCC, De Reijke TM, Bins AD. Bladder-sparing chemoradiotherapy combined with immune checkpoint inhibition for locally advanced urothelial bladder cancer-a review. *Cancers* (*Basel*). 2022;14(1):38.

    doi: 10.3390/cancers14010038

23. Ghatalia P, Plimack ER. Adding a fourth modality to trimodal therapy for muscle-invasive bladder cancer. *Eur Urol.* 2022;82(5):527-528.

    doi: 10.1016/j.eururo.2022.08.017

24. Wilkins A, Ost P, Sundahl N. Is there a benefit of combining immunotherapy and radiotherapy in bladder cancer? *Clin Oncol* (*R Coll Radiol*). 2021;33(6):407-414.

    doi: 10.1016/j.clon.2021.02.014

25. Swinton M, Devi A, Song YP, Hoskin P, Choudhury A. Beyond surgery: Bladder preservation and the role of systemic treatment in localised muscle-invasive bladder cancer. *World J Urol.* 2024;42(1):210.

    doi: 10.1007/s00345-024-04892-8

26. Matuszczak M, Kiljańczyk A, Salagierski M. A liquid biopsy in bladder cancer-the current landscape in urinary biomarkers. *Int J Mol Sci.* 2022;23(15):8597.

    doi: 10.3390/ijms23158597

ACCSCIENCE
PUBLISHING

Advances in Radiotherapy & Nuclear Medicine

SHORT COMMUNICATION

Influence of variations in photon beam quality index on tissue inhomogeneity correction factors in radiation therapy treatment planning

Md Akhtaruzzaman[1]* and Pawel Kukolowicz[2]

[1]Department of Radiation Oncology, Evercare Hospital Chattogram, Chattogram, Bangladesh

[2]Department of Medical Physics, Maria Sklodowska-Curie National Research Institute of Oncology, Warsaw, Poland

Abstract

This study was carried out to investigate how variations in the beam quality index (QI)-so-called tissue phantom ratio ($TPR_{20,10}$) affect tissue inhomogeneity correction factors (ICFs) in external beam radiotherapy treatment plans. A total of 90 three-dimensional conformal radiotherapy (3DCRT) treatment plans for lung, gynecological, and prostate cancers and 15 stereotactic body radiation therapy (SBRT) plans for lung cancer were analyzed. For the 3DCRT plans, ICFs were evaluated across a range of beam QI values. For 6 MV photon beams, the $TPR_{20,10}$ values were set at 0.670 ± 3%, while for 15 MV photon beams, the range was 0.760 ± 3%. SBRT plans were generated using two 6 MV photon beam configurations from a Varian TrueBeam accelerator – one employing a flattening filter (6 MV, $TPR_{20,10} = 0.688$) and the other operating in flattening filter-free (FFF) mode (6 MV FFF, $TPR_{20,10} = 0.632$). All dose calculations were performed using the Eclipse treatment planning system with the anisotropic analytical algorithm. For the calculations for 3DCRT plans, a 6.0% variation in the beam QI resulted in maximum differences in ICFs of 16.3% for lung cases with 6 MV beams and 12.5% for 15 MV beams. In gynecological and prostate cases, the ICF differences remained below 2.0% and 1.0%, respectively. In addition, for lung SBRT plans, a 5.6% discrepancy in $TPR_{20,10}$ between 6 MV and 6 MV FFF beams led to ICF variations of <3.0%. These findings suggest that while variations in the beam QI significantly influence ICFs in lung cancer 3DCRT plans, their impact is less pronounced in gynecological and prostate treatments. This underscores the necessity of carefully accounting for beam quality variations during radiotherapy treatment planning to ensure accurate dose delivery and optimal patient outcomes.

Keywords: Treatment plans; Photon beams; Inhomogeneity correction factors; Beam quality

***Corresponding author:**
Md Akhtaruzzaman
(akhtaruzzaman@evercarebd.com)

Citation: Akhtaruzzaman M, Kukolowicz P. Influence of variations in photon beam quality index on tissue inhomogeneity correction factors in radiation therapy treatment planning. *Adv Radiother Nucl Med.* 2025;3(2):86-91. doi: 10.36922/arnm.6851

Received: December 2, 2024

Revised: February 20, 2025

Accepted: March 14, 2025

1. Introduction

Radiation therapy has been used for decades to manage a broad spectrum of cancers.7[1,2] Its efficacy depends on accurately delivering the prescribed dose to the target whereas minimizing the dose absorbed by nearby organs at risk. Achieving this objective necessitates precise delineation of all pertinent anatomical structures and meticulous dose calculation.[3] According to the International Commission on Radiation Units and Measurements Reports 50 and 62, the total error in radiotherapy, encompassing activities such as target delineation, treatment planning, dose calculation, patient positioning, and treatment delivery, should remain under 5%.[4,5] To maintain this degree of accuracy, systematic quality assurance procedures for computerized treatment planning systems (TPSs) have been established by several task groups over the past decades. These recommendations cover areas such as anatomical and beam descriptions, dose calculations, as well as data output and transfer. Nowadays, 3D TPSs that utilize a range of dose calculation algorithms are widely employed in radiotherapy planning.[6-9]

For inhomogeneous geometries, comparing measured and calculated dose distributions in the presence of tissue inhomogeneities is essential, typically using inhomogeneity correction factors (ICFs). However, acquiring these measurements is challenging due to the time and resources required. Some studies have reported findings on these measurements,[10-13] yet questions on whether ICFs determined by one institution can be applied universally and how variations in a user's beam quality index (QI) might influence the results remain unanswered.

This research aims to investigate the effects of changes in the beam QI, particularly the tissue phantom ratio ($TPR_{20,10}$) on ICFs in external beam radiation therapy treatment plans.

2. Materials and methods

Photon energies of 6 MV and 15 MV were utilized to evaluate the correlation between ICFs and the beam QI ($TPR_{20,10}$). The $TPR_{20,10}$ values varied within the following range:

$(TPR_{10}^{20} = 0.67 \pm k * 0.01)$ for 6 MV, $k = -3, -2, -1, 0, 1, 2, 3$

$(TPR_{10}^{20} = 0.76 \pm k * 0.01)$ for 15 MV, $k = -3, -2, -1, 0, 1, 2, 3$

For each energy level, $TPR_{20,10}$ values were collected from the Secondary Standard Dosimetry Laboratory at the Maria Sklodowska-Curie National Research Institute of Oncology in Warsaw, Poland.[14] Subsequently, ICFs were determined using the Eclipse version 13.6 TPS by Varian Medical Systems (Palo Alto, CA) with the anisotropic analytical algorithm.

For every $TPR_{20,10}$ value, a separate set of percent depth dose (PDD) curves was generated for field sizes ranging from 5×5 to 30×30 cm^2 using Gerbi's formula.[15] The same beam profiles and output factors measured for 6 MV and 15 MV beams, corresponding to $TPR_{20,10}$ values of 0.670 and 0.760, respectively, were applied. As Gerbi's formula provides PDDs at a source-to-surface distance (SSD) of 100 cm, these values were converted to an SSD of 90 cm using Mayneord's factor (F) before being input into the TPS.

A total of 90 patients – comprising 30 cases each of lung, gynecological, and prostate tumors – were selected to study the impact of tissue inhomogeneities on dose calculation in treatment planning. Each patient received treatment using the three-dimensional conformal radiotherapy (3DCRT) technique, facilitated by a Varian Clinac 2300CD linear accelerator equipped with 120 multileaf collimators (MLCs) (Varian Medical System, Palo Alto, USA), at the Maria Sklodowska-Curie National Research Institute of Oncology in Warsaw, Poland. The treatment plans for lung, gynecology, and prostate cases, represented in Figure 1A-C, respectively, were recalculated without incorporating beam modifiers, and ICFs were determined for each beam angle by comparing dose distributions computed with and without inhomogeneity corrections. All calculations were carried out at the isocenter.

In addition, the ICFs for fifteen lung tumor patients treated using stereotactic body radiation therapy (SBRT) were determined. For these cases, treatment plans were created using 6 MV photons with a QI of 0.668 from a Varian TrueBeam linear accelerator (equipped with a 120-leaf MLC) (Varian Medical System, Palo Alto, USA) and were generated using multiple arcs (clockwise and anticlockwise, with angles defined according to the Varian/IEC scale) (manufacturer, country). An example of SBRT plan is shown in Figure 1D. These SBRT plans were then recalculated with a 6 MV flattening filter-free (FFF) photon beams employing beam quality of 0.632, and ICFs were computed for both beam qualities. Along with the 3DCRT cases, the ICFs for the SBRT plans were calculated at the isocenter.

To compare ICFs calculated among various beam qualities, we conducted a statistical analysis using Origin

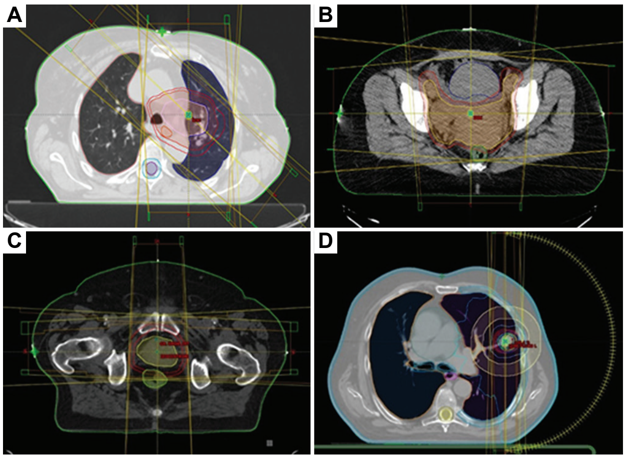

Figure 1. The three-dimensional conformal radiotherapy and stereotactic body radiation therapy (SBRT) treatment plans generated using Eclipse treatment planning system: (A) Lung; (B) Gynecology; (C) Prostate; and (D) Lung SBRT plan

(version 9.1, OriginLab Corporation, USA). A paired t-test was performed to compare the means of ICFs. This test is appropriate to evaluate whether the mean difference between paired observations is statistically significant. In our analysis, a $p<0.05$ indicates a significant difference.

3. Results and discussion

This study thoroughly evaluated how variations in the beam QI ($TPR_{20,10}$) influence ICFs in 3DCRT treatment plans by employing 6 MV and 15 MV photon beams, which are widely used for clinical purposes.[16] A substantial number of treatment plans were analyzed, ensuring a robust dataset for interpretation. The ICF values for lung, gynecological, and prostate tumors are illustrated in Figure 2A and B (at a specific gantry angle, with the baseline beam qualities established at 0.670 for 6 MV and 0.760 for 15 MV. In lung cases, ICFs were observed to increase with higher beam quality indices, while gynecology cases exhibited only minimal changes, and prostate cases showed a decrease. These trends confirm a consistent relationship between beam quality and ICFs across different treatment sites, in line with previous studies.[17,18] Specifically, for 6 MV beams, ICFs variations were 5.6% for lung, <1.0% for gynecology, and 1.7% for prostate tumors. For 15 MV beams, the corresponding variations were 4.9%, 0.5%, and 1.0%, respectively.

Figure 3A-F presents the mean ICFs as a function of the beam QI for lung, gynecological, and prostate tumors treated with 3DCRT with both photon energies. In lung cases, the ICFs behavior is non-linear for both 6 MV and 15 MV beams (Figure 3A and B). Initially, ICFs decline as the beam QI increases, suggesting a reduced impact of tissue inhomogeneities at certain quality levels. However, beyond the reference beam quality, ICFs begin to rise again – a behavior likely driven by complex alterations in scatter and attenuation within lung tissue. Relative to the reference, ICFs varied by 16.3% for 6 MV and 12.5% for 15 MV beams, emphasizing the sensitivity of dose corrections to beam quality fluctuations. These observations highlight the critical importance of precise ICFs determination during treatment planning, particularly for lung tumors, to maintain accurate dose delivery.[19,20]

In contrast, the mean ICFs for gynecology cases show only minor variation – remaining below 2.0% for 6 MV and below 1.0% for 15 MV beams (Figure 3C and D) – indicating that beam quality exerts a minimal influence on dose distribution in these tissues. Prostate treatments also display a non-linear relationship between ICFs and beam quality, with maximum variations of 8.5% for 6 MV and 6.3% for 15 MV beams (Figure 3E and F), suggesting that ICFs in prostate cases are somewhat more sensitive to changes in beam quality. In addition, in intensity-modulated radiation therapy using 6 MV beams, incorporating inhomogeneity corrections resulted in an average decrease of 5.0% in the prescription point dose.[21]

For lung SBRT treatment plans, a 5.6% difference in the beam QI – from 0.632 to 0.688 – between 6 MV and 6 MV FFF beams resulted in an ICFs variation of <3.0% (Figure 4). This relatively small change indicates that, within the SBRT setting, beam quality variations have only a limited effect on dose distribution in lung tissue, regardless of the use of a flattening filter. However, it is important to note that Ding *et al*. reported that differences

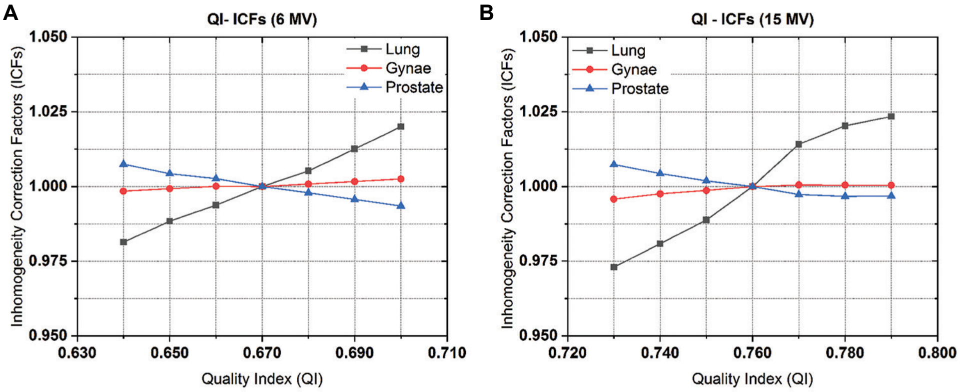

Figure 2. The relationship between inhomogeneity correction factors (ICFs) and the beam quality index as a function of beam quality index ($TPR_{20,10}$) for lung, gynecology, and prostate tumors treated with the three-dimensional conformal radiotherapy technique using 6 MV (A) and 15 MV (B) photon energies. At a $TPR_{20,10}$ of 0.670, the absolute ICFs values were 1.233 for lung, 1.051 for gynecology, and 0.916 for prostate tumors. At a $TPR_{20,10}$ of 0.760, the corresponding ICFs were 1.117 for lung, 1.032 for gynecology, and 0.940 for prostate tumors.

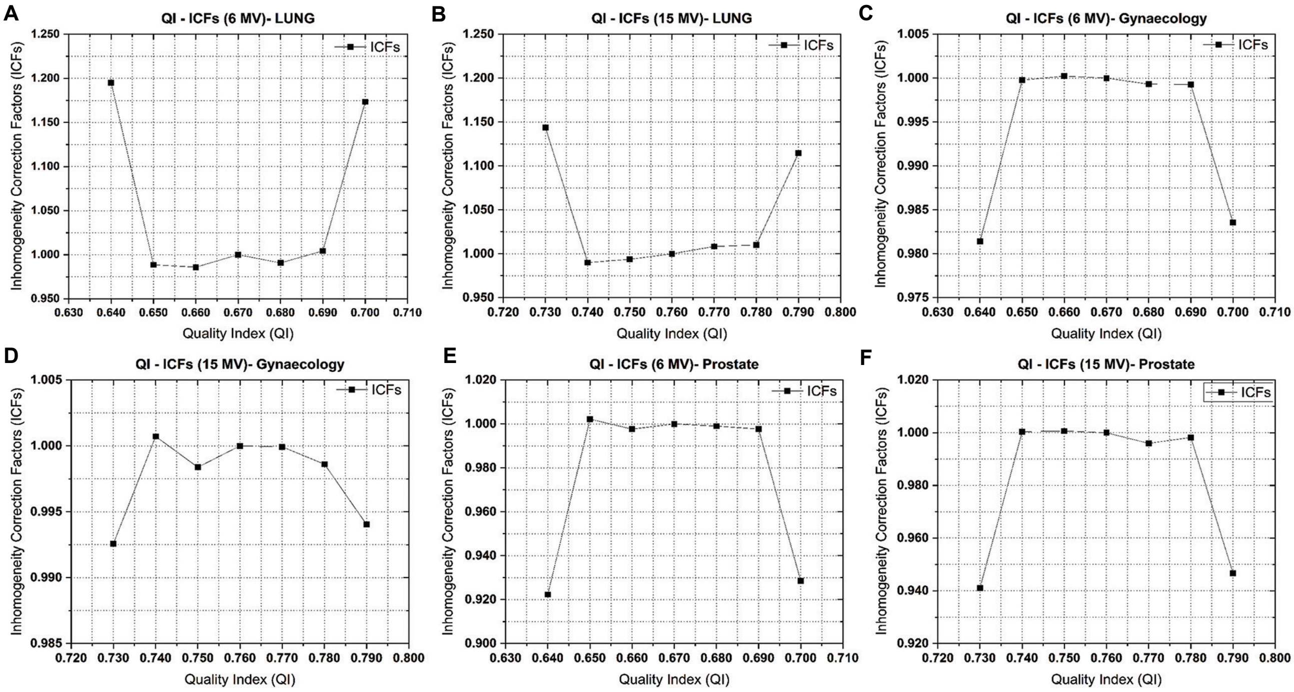

Figure 3. The mean inhomogeneity correction factors (ICFs) plotted against the beam quality index for three-dimensional conformal radiotherapy treatment plans: (A and B) represent lung cases, (C and D) represent gynecology, and (E and F) represent prostate cases. The absolute ICF values have been normalized using the reference beam qualities of 0.670 for 6 MV and 0.760 for 15 MV.

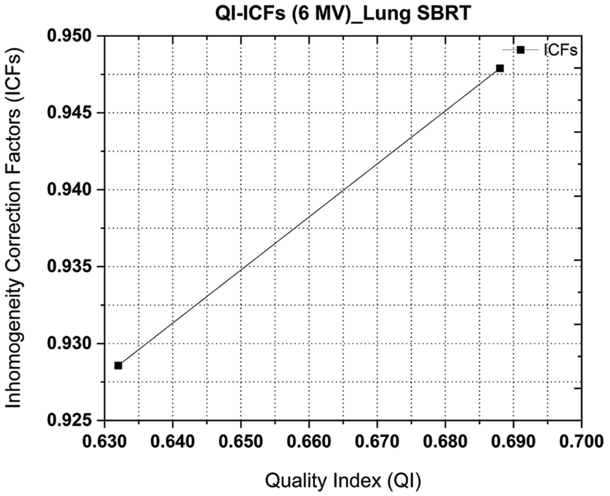

Figure 4. The mean inhomogeneity correction factors as a function of the beam quality index for lung stereotactic body radiation therapy treatment plans using 6 MV and 6 MV flattening filter-free photon beams

between dose calculation algorithms could lead to dose distribution variations of up to 10.0%.[22]

4. Conclusion

The effect of energy variations ($TPR_{20,10}$) on ICFs was found to be more significant in lung 3DCRT treatment plans compared to other treatment sites. Nevertheless, this variation is not deemed clinically significant. This study underscores the importance of accurately determining ICFs during treatment planning, particularly for lung tumors, given the complex interplay between beam quality and ICFs. This study highlights the necessity for precise beam quality measurements to ensure consistent and effective dose delivery across different types of tumor and treatment sites.

Acknowledgments

We extend our acknowledgments to the colleagues of Medical Physics Department of the Maria Sklodowska-Curie National Research Institute of Oncology, Warsaw, Poland. Their exceptional supports with resources, technical expertise, and spirit of cooperation have been pivotal to the successful completion of the study.

Funding

None.

Conflict of interest

The authors declare that they have no competing interests.

Author contributions

Conceptualization: All authors

Formal analysis: Md Akhtaruzzaman
Investigation: Md Akhtaruzzaman
Methodology: Md Akhtaruzzaman
Writing–original draft: Md Akhtaruzzaman
Writing–review & editing: Pawel Kukolowicz

Ethics approval and consent to participate

This study was exempt from ethical approval from an Institutional Review Board (IRB) or Ethics Committee of National Institute of Oncology in Warsaw, Poland.

Consent for publication

Not applicable.

Availability of data

The data used in this study can be obtained by contacting the corresponding author, Md Akhtaruzzaman, at akhzam@gmail.com and/or akhtaruzzaman@evercarebd.com

References

1. Li J, Zhang T. Implementation of convolution/superposition model of photon dose calculation. In: *7th Asian-Pacific Conference on Medical and Biological Engineering*. 2008. p. 442-446.

   doi: 10.1007/978-3-540-79039-6_110

2. Wieslander E. *Verification of Dose Calculation Algorithms in Treatment Planning Systems for External Radiation Therapy: A Monte Carlo Approach* [doctoral thesis]. Sweden: Lund University; 2006.

3. Robinson D. Inhomogeneity correction and the analytic anisotropic algorithm. *J Appl Clin Med Phys*. 2008;9(2): 112-122.

   doi: 10.1120/jacmp.v9i2.2801.

4. International Commission on Radiation Units and Measurements (ICRU). *Prescribing, Recording, and Reporting Photon Beam Therapy*. ICRU Report No 50; 1993.

5. International Commission on Radiation Units and Measurements (ICRU). *Prescribing, Recording, and Reporting Photon Beam Therapy (Supplement to ICRU Report 50)*. ICRU Report No 62; 1999.

6. Cheng CW, Das IJ, Tang W, *et al*. Dosimetric comparison of treatment planning systems in irradiation of breast with tangential fields. Int J Radiat Oncol Biol Phys. 1997;38(4):835-842.

   doi: 10.1016/S0360-3016(97)00048-8

7. Paelinck L, Reynaert N, Thierens H, *et al*. Experimental verification of lung dose with radiochromic film: Comparison with Monte Carlo simulations and commercially available treatment planning systems. *Phys Med Biol*. 2005;50(9): 2055-2059.

   doi: 10.1088/0031-9155/50/9/009.

8. Mesbahi A, Zergoug I. Dose calculations for lung inhomogeneity in high-energy photon beams and small beamlets: A comparison between XiO and TiGRT treatment planning systems and MCNPX Monte Carlo code. *Iran J Med Phys*. 2015;12(3):167-177.

   doi: 10.22038/ijmp.2015.6218

9. International Atomic Energy Agency (IAEA). *Commissioning and Quality Assurance of Computerized Planning Systems for Radiation Treatment of Cancer*. Technical Report Series No. 430; 2004.

10. Papanikolaou N, Battista JJ, Boyer AL, *et al. Tissue Inhomogeneity Corrections for Megavoltage Photon Beams*. Report of the AAPM Task Group No. 85. Madison, WI: Medical Physics Publishing; 2004.

11. Hunt MA, Desobry GE, Fowble B, Coia LR. Effect of low-density lateral interfaces on soft-tissue doses. *Int J Radiat Oncol Biol Phys*. 1997;37(2):475-482.

    doi: 10.1016/S0360-3016(96)00477-5

12. Stathakis S, Kappas C, Theodorou K, *et al*. An inhomogeneity correction algorithm for irregular fields of high-energy photon beams based on Clarkson integration and the 3D beam subtraction method. *J Appl Clin Med Phys*. 2006;7(1):1-13.

    doi: 10.1120/jacmp.v7i1.2188

13. Ono K, Endo S, Tanaka K, *et al*. Dosimetric verification of the anisotropic analytical algorithm in lung equivalent heterogeneities with and without bone equivalent heterogeneities. *Med Phys*. 2010;37(8):4456-4463.

    doi: 10.1118/1.3455709

14. Akhtaruzzaman M, Kukolowicz P. Dependence of tissue inhomogeneity correction factors on nominal photon beam energy. *Nukleonika*. 2018;63(1):3-7.

    doi: 10.1515/nuka-2018-0001

15. Gerbi BJ. A mathematical expression for percentage depth dose accurate from Co-60 to 24 MV. *Med Phys*. 1991;18(4):724-726.

    doi: 10.1118/1.596695

16. Podgorsak EB. *Radiation Oncology Physics: A Handbook for Teachers and Students*. Vienna: International Atomic Energy Agency (IAEA); 2005.

17. Akhtaruzzaman M, Kukolowicz P. The dependence of inhomogeneity correction factors on photon beam quality index performed with the anisotropic analytical algorithm. *Pol J Med Phys Eng*. 2020;26(3):127-134.

    doi: 10.2478/pjmpe-2020-0016

18. Wong JW, Purdy JA, Harms WB, *et al*. Role of inhomogeneity corrections in three-dimensional photon treatment planning. *Int J Radiat Oncol Biol Phys*. 1991;21(1):59-69.

doi: 10.1016/0360-3016(91)90132-6.

19. Murphy R, Hill T, Rapley P, *et al*. The influence of the inhomogeneity correction factor on dose distributions in lung cancer radiation therapy treatment plans: A retrospective study. *Int J Radiat Oncol Biol Phys*. 2012;84(3):S600.

    doi: 10.1016/j.ijrobp.2012.07.1498.

20. Mah K, Van Dyk J. On the impact of tissue inhomogeneity corrections in clinical thoracic radiation therapy. *Int J Radiat Oncol Biol Phys*. 1991;21(5):1257-1267.

    doi: 10.1016/0360-3016(91)90232-7.

21. Han Y, Park W, Huh SJ. The impact of tissue inhomogeneity corrections in the treatment of prostate cancer with intensity-modulated radiation therapy. *Korean J Med Phys*. 2004;15(3):149-155.

22. Ding GX, Duggan DM, Lu B, *et al*. Impact of inhomogeneity corrections on dose coverage in the treatment of lung cancer using stereotactic body radiation therapy. *Med Phys*. 2007;34(7):2985-2994.

    doi: 10.1118/1.2745923

ACCSCIENCE PUBLISHING

Advances in Radiotherapy & Nuclear Medicine

SHORT COMMUNICATION

Study on the impact of treatment planning system target volume delineation on the efficacy of iodine-125 seed therapy for non-small cell lung cancer

Ke Xu, Xiaoli Liu, Jinxin Zhao, Zezhou Liu, Guohui Cao, Juan Wang, and Hongtao Zhang*

Department of Oncology, Hebei Provincial Radioactive Seeds Brachytherapy Institute Hebei Provincial Tumor, Radioactive Seeds Implantation Diagnosis and Treatment Center, Hebei General Hospital, Shijiazhuang, China

Abstract

This study evaluates the impact of target delineation on the dosimetric outcomes and therapeutic efficacy of iodine-125 seed implantation in the treatment of non-small cell lung cancer. A retrospective analysis was conducted on 31 patients who underwent iodine-125 seed implantation at our center. Post-operative dosimetric parameters, including target volume (Vol), minimum peripheral dose received by 90% of the target Vol (D_{90}), as well as the percentage of target Vol covered by 100% (V_{100}), 150% (V_{150}), and 200% (V_{200}) of the prescription dose, were recorded. Patients were divided into two groups based on treatment response: Group A (complete remission [CR]) and Group B (non-CR group). In addition, the gross target Vol (GTV) of both groups was expanded by 5 mm (clinical target volume $[CTV]_{5mm}$) and 1 cm (CTV_{1mm}), and the corresponding dosimetric parameters were obtained. The independent sample *t*-tests were used to assess differences between the two groups. All patients successfully completed surgery; among them, 15 achieved CR, 12 had partial response, three had stable disease, and one experienced disease progression. Intraoperative complications included pneumothorax (32%), with three cases (10%) requiring pleural drainage, and intrapulmonary hemorrhage (42%), including hemoptysis (13%), all of which recovered after hemostatic treatment. No other adverse reactions occurred. Statistical analysis revealed no significant difference in dosimetric parameters between the two groups immediately after surgery. However, for CTV_{5mm}, D_{90} was significantly lower than its immediate post-operative value (p=0.03, <0.05), whereas the other parameters were not significantly different. Expanding the GTV by 5 mm to define the CTV improves treatment outcomes and may enhance local tumor control.

Keywords: Target delineation; Brachytherapy; Treatment efficacy; Dosimetric outcomes

***Corresponding author:**
Hongtao Zhang
(90030109@hebmu.edu.cn)

Citation: Xu K, Liu X, Zhao J, *et al*. Study on the impact of treatment planning system target volume delineation on the efficacy of iodine-125 seed therapy for non-small cell lung cancer. *Adv Radiother Nucl Med*. 2025;3(2):92-97.
doi: 10.36922/arnm.8512

Received: January 13, 2025

Revised: February 14, 2025

Accepted: March 19, 2025

1. Introduction

Lung cancer is a malignant tumor with a high incidence and mortality rate worldwide. Non-small cell lung cancer (NSCLC) comprises approximately 80% of all lung cancer cases.[1] The use of iodine-125 seeds has demonstrated effective therapeutic outcomes in the treatment of early NSCLC, particularly in resection margin supplementary radiotherapy, radical treatment, advanced NSCLC management, and palliative care for extrapulmonary metastases.[2-5] Accurate target delineation is essential for ensuring the efficacy of radiotherapy[6,7] and plays a critical role in iodine-125 seed implantation. Traditionally, target delineation for seed implantation involves clinicians manually outlining the tumor as the clinical target. However, this approach is susceptible to subjective biases from the operator and variations in scanning time and image quality, which can lead to inaccurate target delineation. Such inaccuracies may adversely affect the effectiveness of seed implantation and contribute to tumor recurrence. Stereotactic body radiotherapy (SBRT) demonstrates favorable outcomes with a comparatively lower recurrence rate in the treatment of early-stage NSCLC.[8-10] This study compares the dosimetric impact of target delineation standards between transitional particle implantation using SBRT and traditional clinical target volume (CTV) methods, aiming to explore how target delineation influences the efficacy of iodine-125 seed treatment for NSCLC.

2. Materials and methods

2.1. Patient data

Thirty-one patients with NSCLC who received iodine-125 seed implantation at Radioactive Seeds Implantation Diagnosis and Treatment Center, Shijiazhuang, China, between January 2018 and January 2023, were retrospectively analyzed. All patients met the following criteria before the operation: (1) No major organ dysfunction and a general condition score (PS) ≤3; (2) pathological confirmation of NSCLC via biopsy. Following multidisciplinary discussion, the patients were deemed ineligible for surgical resection or multiple-line treatment and consented to seed implantation; (3) routine blood tests, biochemical analysis, coagulation function assessments, and evaluations of heart, lung, liver, and kidney functions can indicate tolerance to the procedure; (4) An estimated survival time of more than 3 months. The exclusion criteria were: (1) Severe organ dysfunction, such as severe heart failure or significant lung, liver, or kidney dysfunction; (2) severe coagulation dysfunction; (3) an estimated survival time of <3 months. This study was approved by the Medical Ethics Committee of Hebei General Hospital.

2.2. Main reagents and instruments

The computerized three-dimensional treatment planning system (TPS) from Prowess Panther Brachy V5.0 (United States) was used. The 18G implant needle (J820-C) and Mick200-TPV applicator gun were purchased from Mick Radio Nuclear (USA). (Positron Emission Tomography–Computed Tomography [PET-CT]; DiscoveryCT750HD, GE Healthcare, USA) was used for imaging. The radioactive iodine-125 particles (Model 6711-99, Beijing Zhibo Company, China) possessed a length of 4.8 mm, a diameter of 0.6 – 0.8 mCi, an energy of 27 – 35 keV, and a half-life of 59.4 days. For the activity meter, the RM-905a well-type ionization chamber (China Institute of Metrology) was employed. The negative pressure vacuum pad (Zibo Tianchen Medical Instrument Factory, China), dimension of size is 120 cm × 80 cm × 4 cm.

2.3. Seed implantation

One week before surgery, a routine enhanced CT scan with a slice thickness of 5 mm, was performed for localization. The CT images were imported into the TPS planning system. The CTV and organs at risk (OARs) were delineated according to the International Commission on Radiation Units and Measurement Report No.83.[11] The prescribed dose was 140 Gy, with a particle activity of 0.6 – 0.8 mCi. The number of particles required and the dose to OARs were calculated using the TPS planning system.

Particle implantation was performed using an 18G disposable implantation needle under real-time CT guidance to avoid critical organs. Post-implantation CT scanning was conducted to evaluate particle distribution. If dose cold spots or underdosed regions were identified, additional particles were implanted as needed.

After surgery, the last intraoperative CT scan image was uploaded to the TPS planning system to evaluate parameters including target volume (Vol), minimum peripheral dose received by 90% of the target volume (D_{90}), percentage of target volume covered by 100% of the prescription dose (V_{100}), percentage of target Vol covered by 150% of the prescription dose (V_{150}), and percentage of target Vol covered by 200% of the prescription dose (V_{200}). For target area expansion, the gross target Vol (GTV) was automatically expanded by 5 mm (CTV_{5mm}) and 1 cm (CTV_{1mm}) using the TPS software to assess changes in Vol, D_{90}, V_{100}, V_{150}, and V_{200}. Follow-up assessments were conducted monthly for the first 6 months post-implantation and every 3 months thereafter. Treatment efficacy was compared with previous evaluations, and adverse events were recorded.

2.4. Observation indexes

Efficacy was assessed based on the response evaluation criteria in solid tumors version 1.1.[12] The complete remission (CR) category was assigned when all target lesions disappeared, with the short diameter of any pathological lymph node (whether a target lesion or not) reduced to <10 mm. The partial remission (PR) category was indicated when the total diameter of all target lesions was reduced by at least 30% compared to baseline. Progressive disease (PD) was defined as an increase of at least 20% in the total diameter of target lesions, using the smallest recorded total diameter as a reference (including baseline if it is the smallest). In addition, the absolute increase in sum must be at least 5 mm, or the appearance of one or more new lesions was also classified as PD. The stable disease (SD) category was assigned when there was insufficient reduction to qualify as PR and insufficient increase to qualify as PD.

Adverse reactions after seed implantation were evaluated according to the grading standard for acute radiation injury and the grading scheme for late radiation injury.[13]

2.5. Statistical methods

Statistical Package for the Social Sciences 25.0 statistical software (IBM, United States) was used for data analysis. Independent sample *t*-test was used to compare Vol and related dosimetric parameters between Groups A (CR) and B (non-CR group). There were 14 patients in Group A and 17 patients in Group B. Independent sample *t*-test was used to compare the CTV_{5mm} and CTV_{1cm} and their corresponding dosimetric parameters of Groups A and B, respectively.

3. Results

3.1. Efficacy determination

In Group A, the CR rate was 100% (14/14), with no cases of PR, SD, or PD (0/14). In Group B, the CR rate was 0% (0/17), whereas the PR rate was 71% (12/17), the SD rate was 24% (4/17), and the PD rate was 5% (1/17).

3.2. Adverse reactions

Pneumothorax occurred in 10 patients (32%) during the operation, with three patients exhibiting moderate pneumothorax (10%), all of whom were successfully treated with closed thoracic drainage. Intrapulmonary hemorrhage was observed in 13 cases (42%), whereas hemoptysis occurred in 4 cases (13%), both of which resolved following hemostatic treatment. Notably, no cases of radiation pneumonitis or particle translocation were reported, and no complications of grade 3 or above were observed.

3.3. Independent sample *t*-test results

There was no significant difference in dosimetric parameters between Group A and Group B immediately following the operation. However, when the GTV was expanded by 5 mm (CTV_{5mm}), the D_{90} parameter showed a significant difference compared to immediate post-operative measurements ($p=0.03$, $p<0.05$), whereas other parameters did not demonstrate statistically significant differences (Tables 1-4).

4. Discussion

Surgery is the first choice and the most effective treatment for patients with early-stage NSCLC. The extent of lung resection, bronchial resection, and lymph node dissection is determined by tumor location and stage, with surgical guidelines requiring a bronchial resection margin of at least 2 cm from the tumor. In external radiotherapy, a margin is usually added to the GTV to define the CTV,

Table 1. The dosimetry parameters of Groups A and B

Group	Vol (cc)	D_{90} (Gy)	V_{100} (%)	V_{150} (%)	V_{200} (%)
CTV					
A	41.5±6.3	164.5±8.3	94.5±1.0	75.7±3.3	54.4±4.7
B	49.8±9.2	142.2±1.3	91.6±1.1	62.7±3.7	37.8±3.9
CTV_{5mm}					
A	75.3±10.0	103.8±4.5	74.8±2.7	49.6±3.4	32.7±3.2
B	82.9±14.9	87.9±1.7	66.3±1.9	39.7±2.2	22.2±2.0
CTV_{1cm}					
A	136.3±17.5	60.7±3.8	44.7±3.0	28.8±2.5	18.7±2.0
B	131.0±21.1	55.5±1.2	43.2±1.6	24.9±1.5	14.4±1.4

Notes: Data are expressed as mean±standard deviation; CTV: Clinical target volume; CTV_{5mm}: Clinical target volume5mm; CTV_{1mm}: Clinical target volume$_{1mm}$; Vol: Target volume; D_{90}: Minimum peripheral dose received by 90% of the target volume; V_{100}: Percentage of target volume covered by 100% of the prescription dose; V_{150}: Percentage of target volume covered by 150% of the prescription dose; V_{200}: Percentage of target volume covered by 200% of the prescription dose.

Table 2. Statistics for dosimetry parameter comparison between Groups A and B

Parameter	F	Significance	t	*p*	95% confidence interval	
					Lower limit	Upper limit
Vol	0.912	0.348	−0.747	0.461	−31.221	14.527
D_{90}	8.699	0.006	2.655	0.013	5.094	39.508
V_{100}	0.119	0.733	1.947	0.062	−0.150	5.950
V_{150}	0.192	0.665	2.655	0.013	2.975	23.065
V_{200}	0.363	0.552	2.708	0.011	4.041	29.145

Notes: Vol: Target volume; D_{90}: Minimum peripheral dose received by 90% of the target volume; V_{100}: Percentage of target volume covered by 100% of the prescription dose; V_{150}: Percentage of target volume covered by 150% of the prescription dose; V_{200}: Percentage of target volume covered by 200% of the prescription dose.
Abbreviations: F: F-statistic; t: t-statistic; *p*: *p*-value.

Table 3. Statistics for CTV$_{5mm}$ dosimetry parameter comparison between Groups A and B

Parameter	F	Significance	t	p	95% confidence interval	
					Lower limit	Upper limit
Vol	1.550	0.223	−0.428	0.672	−44.395	29.048
D_{90}	5.307	0.029	3.280	0.003	5.979	25.868
V_{100}	2.131	0.155	2.586	0.015	1.768	15.232
V_{150}	1.121	0.299	2.484	0.019	1.741	18.112
V_{200}	1.078	0.308	2.789	0.009	2.791	18.236

Notes: CTV$_{5mm}$: Clinical target volume$_{5mm}$; Vol: Target volume; D_{90}: Minimum peripheral dose received by 90% of the target volume; V_{100}: Percentage of target volume covered by 100% of the prescription dose; V_{150}: Percentage of target volume covered by 150% of the prescription dose; V_{200}: Percentage of target volume covered by 200% of the prescription dose. Abbreviations: F: F-statistic; t: t-statistic; *p*: *p*-value.

Table 4. Statistics for CTV$_{1mm}$ dosimetry parameter comparison between groups A and B

Parameter	F	Significance	t	p	95% confidence interval	
					Lower limit	Upper limit
Vol	0.563	0.459	0.194	0.848	−50.845	61.458
D_{90}	8.958	0.006	1.314	0.199	−2.935	13.442
V_{100}	3.134	0.088	0.452	0.655	−5.413	8.480
V_{150}	2.389	0.133	1.384	0.177	−1.909	9.855
V_{200}	0.931	0.343	1.770	0.088	−0.671	9.217

Notes: CTV1mm: Clinical target volume$_{1mm}$; Vol: Target volume; D_{90}: Minimum peripheral dose received by 90% of the target volume; V_{100}: Percentage of target volume covered by 100% of the prescription dose; V_{150}: Percentage of target volume covered by 150% of the prescription dose; V_{200}: Percentage of target volume covered by 200% of the prescription dose. Abbreviations: F: F-statistic; t: t-statistic; *p*: *p*-value.

with an expansion of 6 mm for squamous cell carcinoma and 8 mm for adenocarcinoma.[14] Radioactive particle implantation is a kind of precise radiotherapy which requires that the marginal dose of the treatment target area meet the prescribed dose while minimizing damage to surrounding normal tissues. The TPS employs a dose-Vol evaluation model to assess the efficacy of iodine-125, with accurate tumor target delineation being a critical determinant of treatment success. Proper delineation ensures adequate prescription dose coverage of the tumor target and implantation efficacy.

D_{90} is a critical dosimetric parameter that significantly influences the efficacy of particle implantation.[15,16] It is defined as the minimum peripheral dose received by 90% of the target area. Without a well-defined target area, dose delivery is compromised. Thus, accurate delineation of the target area is essential for optimizing the effects of particle therapy. The size and boundaries of the target area directly impact particle and dose distribution. However, accurate delineation presents several challenges: (1) The delineation process must integrate CT imaging to ascertain the size and boundaries of the tumor, yet the imaging boundaries often differ from the actual tumor boundaries; (2) the tumor's location or shape may change due to respiratory movements, which can compromise the accuracy of target delineation; (3) the presence of complex local anatomical structures or tumors adjacent to critical organs complicates the target delineation process; (4) variability in physician expertise can lead to inconsistencies in the target delineation. These factors contribute to suboptimal delineation of the target area definition, ultimately impacting the treatment efficacy.

In this study, 31 NSCLC patients treated by seed implantation were divided into Group A (CR group, n = 15) and Group B (non-CR group, n = 16) based on treatment response. The immediate post-operative D_{90} of both groups was more than 140 Gy, with no statistical difference. To investigate this discrepancy, target Vols were expanded by 5 mm and 1 cm for both groups. Comparative analysis revealed no significant difference in target Vols after expansion, yet a significant difference in post-operative D_{90} was observed between groups: 103.8 ± 4.5 Gy in Group A versus 87.9 ± 1.7 Gy in Group B. This suggests that while both groups initially met dosimetric requirements, Group B had a smaller target Vol. When the target area was expanded by 5 mm, the tumor Vol increased, leading to insufficient dose coverage and diminished implantation efficacy, contributing to tumor recurrence. Recent research has suggested that optimal concentrations of trace elements in the body may play a role in improving treatment response and overall survival in lung cancer patients.

5. Conclusion

The design of an optimal treatment plan is an important step in particle implantation, with accurate target delineation being essential for ensuring therapeutic efficacy. This study suggests that a 5 mm expansion based on CTV yields a better outcome. However, certain limitations must be acknowledged, including a small sample size, short follow-up duration, and the lack of consideration for the potential role of trace elements in tumor treatment. In addition, as this study applies only to medical units equipped with a TPS planning system, its generalizability is limited. Future research will aim to expand the sample size and extend follow-up time to enhance the robustness and applicability of the findings.

Acknowledgments

None.

Funding

This study was funded by the Research Fund Project of Hebei Provincial Health and Family Planning Commission (20242265).

Conflict of interest

Hongtao Zhang is the Editorial Board Member of this journal but was not in any way involved in the editorial and peer-review process conducted for this paper, directly or indirectly. Separately, other authors declared that they have no known competing financial interests or personal relationships that could have influenced the work reported in this paper.

Author contributions

Conceptualization: Hongtao Zhang, Juan Wang
Formal analysis: Ke Xu
Investigation: Jinxin Zhao, Zezhou Liu
Methodology: Guohui Cao, Xiaoli Liu
Writing – original draft: Ke Xu
Writing – review & editing: Xiaoli Liu, Ke Xu

Ethics approval and consent to participate

This study has been approved by the Ethics Committee Application for Approval of Research Protocol, Hebei General Hospital (NO.2025-LW-0078).

Consent for publication

Not applicable.

Availability of data

The original findings presented in this study are included in the article/supplementary material. Further inquiries can be directed to the corresponding author.

References

1. Torre LA, Siegel RL, Jemal A. Lung cancer statistics. *Adv Exp Med Biol*. 2016;893:1-19.

   doi: 10.1007/978-3-319-24223-1-1

2. Yizong W. *Clinical Application of Iodine-125 Seed Implantation to Locally Advanced and Advanced Non-Small Cell Lung Cancer*. Taiwan: Soochow University; 2016.

3. Guo Y, Zhang Z, Huo X, Dong H. Effect of ^{125}I implantation on pulmonary function in impossible non-small cell lung cancer. *Int J Radiat Med Nucl Med*. 2019;43(3):230-234.

   doi: 10.3760/cma.j.issn.1673-4114.2019.03.006

4. Li Bo, De Mei C. Study on the value of 125I radioactive seed implantation in the treatment of recurrent and metastatic lesions of lung cancer. *J Imaging Res Med Appl*. 2024;8(15):176-178.

   doi: 10.3969/j.issn.2096-3807.2024.15.056

5. Guohui C, Juan W, Zeyang W, *et al*. Clinical efficacy and influencing factors of 125I seeds implantation in the treatment of patients with advanced lung cancer after radiotherapy and chemotherapy. *Chin J Nucl Med Mol Imaging*. 2023;43(1):16-19.

   doi: 10.3760/cma.j.cn321828-20210625-00210

6. Yuxuan C. Application of PET/CT image fusion in precise delineation of three-dimensional conformal radiotherapy target area for NSCLC. *J Med Theory Pract*. 2022;35(8):1322-1324.

   doi: 10.19381/j.issn.1001-7585.2022.08.023

7. Jinbo Y, Ye Z, Wencheng Z, *et al*. Chinese expert consensus on radiation therapy doctor's evaluation of radiation therapy plan. *Chin J Cancer Prev Treat*. 2024;31(8):453-470.

   doi: 10.16073/j.cnki.cjcpt.2024.08.01

8. Diamant A, Heng VJ, Chatterjee A, *et al*. Comparing local control and distant metastasis in NSCLC patients between cyberknife and conventional SBRT. *Radiother Oncol*. 2020;144:201-208.

   doi: 10.1016/j.radonc.2020.01.017

9. Min F, Xianghui D, Xiaojing L. Clinical application and prospect of SBRT in treatment of oligo-metastatic NSCLC. *Chin J Radiat Oncol*. 2023;32(7):633-637.

   doi: 10.3760/cma.j.cn113030-20220725-00250

10. Shi Y, Ma X, He D, Dong B, Qiao T. Neoadjuvant SBRT combined with immunotherapy in NSCLC: From mechanisms to therapy. *Front Immunol*. 2023;14:1213222.

    doi: 10.3389/fimmu.2023.1213222

11. International Commission on Radiation Units and Mea-Surements. Prescribing, recording, and reporting photon-beam intensity- modulated radiation therapy (IMRT). *J ICRU*. 2010;10(1):NP.

12. Eisenhauer EA, Therasse P, Bogaerts J, *et al*. New response evaluation criteria in solid tumors: Revised RECIST guideline (version 1.1). *Eur J Cancer*. 2009;45(2):228-247.

    doi: 10.1016/j.ejca.2008.10.026

13. Cox JD, Stetz J, Pajak TF. Toxicity criteria of the radiation therapy oncology group (RTOG) and the European organization for research and treatment of cancer (EORTC). *Int J Radiat Oncol Biol Phys*. 1995;31(5):1341-1346.

    doi: 10.1016/0360-3016(95)00060-C

14. Dongping S. *Establishment and Radiotherapy Application of a Displacement Model for the Solitary Pulmonary Tumor Basedon4DCT*. China: Shandong University; 2019.

15. Ke X, Huimin Y, Enli C, *et al*. Preliminary study on relationship between postoperative dose parameters and curative effect of iodine-125 seed in treatment of lung squamous cell carcinoma. *J Pract Oncol*. 2023;38(3):245-250.

doi: 10.13267/j.cnki.syzlzz.2023.038

16. Shitong W, Yonghuai W, Ruoyu W, *et al*. Short- and long-term efficacy and influencing factors of iodine-125 seed implantation for relapsed primary lung cancer. *J China Med Univ*. 2023;52(12):1087-1091.

doi: 10.12007/j.issn.0258-4646.2023.12.006

ACCSCIENCE
PUBLISHING

Advances in Radiotherapy & Nuclear Medicine

LETTER TO EDITOR

Artificial intelligence in radiation oncology

Melek Yakar*

Department of Radiation Oncology, Faculty of Medicine, Osmangazi University, Eskişehir, Turkey

Dear Editor,

Radiation oncology plays a pivotal role in cancer treatment and the techniques and instruments involved are constantly refined through technological advancements. In recent years, artificial intelligence (AI) applications have garnered attention in this domain due to their potential to enhance treatment processes, improve accuracy, and personalize patient care. Particularly, the use of AI algorithms across a broad spectrum – from radiotherapy (RT) planning stages to predicting oncological outcomes and treatment-related toxicities—offers significant advantages to both clinicians and patients.[1]

AI applications in radiation oncology extend from clinical decision-making algorithms to tumor and organ segmentation, and the evaluation of radiological images.[2] However, challenges such as data privacy, biases in algorithms, and difficulties in clinical implementation highlight the need for further research in this area.

This letter discusses the present applications and future potentials of AI in radiation oncology, emphasizing the technical and ethical challenges encountered during the integration of these technologies.

The steps in radiation oncology include clinical evaluation of the patient, simulation, segmentation, and fusion of imaging techniques, RT planning, quality assurance, treatment delivery, and patient follow-up (oncological outcomes and treatment toxicities), with AI-related studies present at each step.[3] The RT workflow begins with patient evaluation. The clinicians must consider multiple parameters, such as the patient's disease stage, histopathology, surgical reports (if available), medical imaging studies, age, performance status, comorbidities, and hematological and biochemical parameters, to make a treatment decision.

Although disease stage appears to be the most critical parameter when making decisions guided by clinical guidelines, other factors such as radiomics and genetic mutations significantly influence disease prognosis. However, it is challenging for a clinician to simultaneously evaluate and decide upon such a large dataset. Therefore, AI-supported decision systems are expected to play a critical role in personalized treatments.

AI also has the potential to automate, accelerate, and standardize the processes during segmentation and treatment planning. Deep learning (DL) algorithms assist clinicians in segmenting both target volumes and organs at risk (OARs), speeding up the processes while reducing inter-operator variability, resulting in more standardized segmentation.[4]

The processing and analysis of radiological images is another key area where AI is effectively employed. Radiomics, a method used to extract advanced features from images, provides valuable insights into tumor biology, facilitating personalized

***Corresponding author:**
Melek Yakar
(myakar@ogu.edu.tr)

Citation: Yakar M. Artificial intelligence in radiation oncology. *Adv Radiother Nucl Med.* 2025;3(2):98-101. doi: 10.36922/arnm.8429

Received: January 7, 2025

Accepted: March 14, 2025

treatment strategies.[1] AI offers predictive algorithms to predict treatment-related toxicities.[5,6] This approach not only improves patients' quality of life but also prevents unnecessary healthcare expenditures.

Patient follow-up after treatment is another area where the use of AI is expanding. Algorithms monitor treatment responses, enabling clinicians to intervene early. Moreover, AI-based algorithms developed with appropriate baseline data can predict patients' oncological outcomes, allowing for more radical treatments or avoiding unnecessary therapies.[7,8]

Mobile applications are also gaining importance. Remote monitoring systems are effectively used to assess post-treatment symptoms and quality of life. Mobile applications can be leveraged to provide patient education, thereby improving treatment adherence.[9]

In radiation oncology, an increasing amount of heterogeneous data is accumulated, including clinical information, planning computed tomography scans, and dosimetric data. Machine learning plays an increasingly significant role in RT processes due to its ability to analyze large and heterogeneous datasets to make predictions. Specifically, algorithms such as support vector machines, random forests, and k-nearest neighbors are used to analyze patient's data for toxicity prediction and the evaluation of treatment outcomes.[7-10]

DL models have enabled substantial advancements in RT planning and image processing. Convolutional neural networks provide high accuracy, particularly in tumor segmentation and OAR delineation processes in medical imaging.[11,12] Through the radiomics approach, advanced features imperceptible to the human eye can be extracted from radiological images, offering insights into tumor biology. This method facilitates the integration of imaging data with genetic, proteomic, and metabolomic data, playing a critical role in personalized medicine applications.[1] In addition, dosiomics, which uses radiomic tools to characterize RT dose heterogeneity, provides more comprehensive information compared to traditional dose-volume histograms. AI enables the analysis of this high-dimensional data to yield clinically meaningful outcomes. By automating RT planning, AI offers significant time and resource efficiency. Algorithms used in areas, such as automatic segmentation and dose distribution optimization accelerate workflows while ensuring standardization and enhancing treatment quality.[13,14]

Although AI provides innovations and conveniences in radiation oncology, there are challenges and limitations associated with its adoption and integration. Standardization is still lacking in many areas. For instance, questions such as which algorithm should be used in specific scenarios, which techniques should be employed to extract radiomic features, and how many cases are required for algorithm training to achieve accurate results remain unanswered and need to be standardized. Training AI systems, standardizing them, and making them suitable for routine clinical practice require large volumes of patients' data. However, patient's confidentiality and data security are critical concerns. The risk of unauthorized access poses a significant challenge for healthcare providers and researchers. Therefore, anonymization and secure storage of data are essential. Integrating AI-based systems into clinical applications and implementing them in routine practice is a lengthy and complex process.[15] Without sufficient evidence on the effectiveness and reliability of these technologies, pre-mature implementation in clinical settings could lead to incorrect treatments and unexpected toxicities, resulting in a loss of trust among clinicians and patients. In addition, aligning existing clinical workflows with AI systems can be time-consuming and costly.

AI models can also be affected by biases present in the training datasets. For example, algorithms trained on datasets lacking in demographic diversity may produce inaccurate results for certain patient groups. This could lead to disparities and inaccuracies in treatment outcomes. Thus, ensuring data diversity and ethical considerations during model development is crucial.[16]

Ensuring that AI models provide consistent results across diverse patient populations and clinical conditions is essential for their clinical application. However, the generalizability of these models cannot always be guaranteed. Models trained on small or imbalanced datasets may perform poorly in different patient populations, highlighting the need for thorough validation and optimization of these systems. The inclusion of AI in clinical decision-making processes also introduces ethical and legal challenges. For instance, if an AI system makes an error, who should bear the responsibility – the clinician or the technology provider? As AI continues to be increasingly utilized in healthcare, it is imperative to develop unbiased, data-driven algorithms that are frequently monitored and updated.

While AI is unlikely to entirely replace clinical judgment, it can aid clinicians in making better decisions. Unlike human's decision-making processes, AI's decisions and judgments are systematic, operating within defined algorithms. However, in the absence of an effective legal framework, the responsibility for AI-related decisions currently lies with those who design and use these systems.[17]

Despite the ethical and legal dilemmas surrounding AI usage, present advancements suggest that AI will coexist with existing systems or even replace some of them. Furthermore, in the face of such extensive big data, not utilizing AI may be both scientifically and ethically questionable.

The success of AI systems depends on large, accurate, and diverse datasets. Such datasets can help prevent algorithmic biases and enhance generalizability. To achieve this, internationally standardized and secured datasets should be established, accompanied with measures to ensure data privacy.

For AI algorithms to transition into clinical practice, multicenter validation studies must be conducted. It is essential to demonstrate that model performance yields consistent results across diverse patient populations. In addition, to enable the effective and accurate use of AI, training programs should be organized for clinicians and professionals working in healthcare technologies.

Ethical and legal guidelines must be established internationally to define AI's role in clinical decision-making. These guidelines should delineate AI's boundaries as a tool and ensure that these technologies operate under human oversight while prioritizing ethical principles, such as informed patient consent.

Although the use of AI in radiation oncology is still in its early stages, implementing the above recommendations will bring these technologies one step closer to a reliable, effective, and widespread clinical application. This progress has the potential to transform healthcare by improving patient outcomes and increasing the efficiency of medical services.

Conflict of interest

The author declares that she has no conflict of interest and has no competing interests.

References

1. Lambin P, Rios-Velazquez E, Leijenaar R, *et al*. Radiomics: Extracting more information from medical images using advanced feature analysis. *Eur J Cancer*. 2012;48(4):441-446.

   doi: 10.1016/j.ejca.2011.11.036

2. Jiang F, Jiang Y, Zhi H, *et al*. Artificial intelligence in healthcare: Past, present and future. *Stroke Vasc Neurol*. 2017;2(4):230-243.

   doi: 10.1136/svn-2017-000101

3. Yakar M, Etiz D. Artificial intelligence in radiation oncology. *Artif Intell Med Imaging*. 2021;2(2):13-31.

   doi: 10.35711/aimi.v2.i2.13

4. Huynh E, Hosny A, Guthier C, *et al*. Artificial intelligence in radiation oncology. *Nat Rev Clin Oncol*. 2020;17(12):771-781.

   doi: 10.1038/s41571-020-0417-8

5. Yakar M, Etiz D, Metintas M, Ak G, Celik O. Prediction of radiation pneumonitis with machine learning in stage III lung cancer: A pilot study. *Technol Cancer Res Treat*. 2021;20:15330338211016373.

   doi: 10.1177/15330338211016373

6. Akcay M, Etiz D, Celik O, Ozen A. Evaluation of acute hematological toxicity by machine learning in gynecologic cancers using postoperative radiotherapy. *Indian J Cancer*. 2022;59(2):178-186.

   doi: 10.4103/ijc.IJC_666_19

7. Akcay M, Etiz D, Celik O, Ozen A. Evaluation of prognosis in nasopharyngeal cancer using machine learning. *Technol Cancer Res Treat*. 2020;19:1533033820909829.

   doi: 10.1177/1533033820909829

8. Akcay M, Etiz D, Celik O. Prediction of survival and recurrence patterns by machine learning in gastric cancer cases undergoing radiation therapy and chemotherapy. *Adv Radiat Oncol*. 2020;5(6):1179-1187.

   doi: 10.1016/j.adro.2020.07.007

9. Janssen S, El Shafie RA, Ruder AM, *et al*. Mobile applications in radiation oncology-current choices and future potentials. *Strahlenther Onkol*. 2023;199(4):337-349.

   doi: 10.1007/s00066-023-02048-y

10. Bibault JE, Giraud P, Burgun A. Big Data and machine learning in radiation oncology: State of the art and future prospects. *Cancer Lett*. 2016;382(1):110-117.

    doi: 10.1016/j.canlet.2016.05.033

11. Bibault JE, Giraud P. Deep learning for automated segmentation in radiotherapy: A narrative review. *Br J Radiol*. 2024;97(1153):13-20.

    doi: 10.1093/bjr/tqad018

12. Samarasinghe G, Jameson M, Vinod S, *et al*. Deep learning for segmentation in radiation therapy planning: A review. *J Med Imaging Radiat Oncol*. 2021;65(5):578-595.

    doi: 10.1111/1754-9485.13286

13. Liu X, Chen X, Chen D, *et al*. A patient-specific auto-planning method for MRI-guided adaptive radiotherapy in prostate cancer. *Radiother Oncol*. 2024;200:110525.

    doi: 10.1016/j.radonc.2024.110525

14. Zeverino M, Piccolo C, Wuethrich D, *et al*. Clinical implementation of deep learning-based automated left breast simultaneous integrated boost radiotherapy treatment planning. *Phys Imaging Radiat Oncol*. 2023;28:100492.

    doi: 10.1016/j.phro.2023.100492

15. Gichoya JW, Thomas K, Celi LA, *et al*. AI pitfalls and what not to do: Mitigating bias in AI. *Br J Radiol*. 2023;96(1150):20230023.

doi: 10.1259/bjr.20230023

16. Mittermaier M, Raza MM, Kvedar JC. Bias in AI-based models for medical applications: Challenges and mitigation strategies. *NPJ Digit Med*. 2023;6(1):113.

doi: 10.1038/s41746-023-00858-z

17. Naik N, Hameed BM, Shetty DK, *et al*. Legal and ethical consideration in artificial intelligence in healthcare: Who takes responsibility? *Front Surg*. 2022;9:862322.

doi: 10.3389/fsurg.2022.862322

ACCSCIENCE
PUBLISHING

OUR JOURNALS

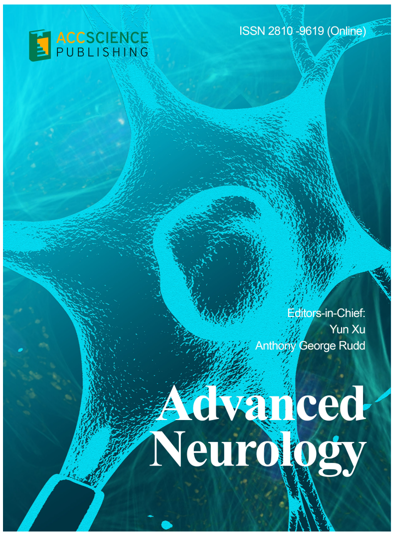

Advanced Neurology is a peer-reviewed and open-access journal that aims to publish and disseminate novel research in the breadth of neurology and neuroscience. The journal aims to advance our understanding in the nervous system and provide a platform to neuroscientists and physicians to showcase their findings in original fundamental and clinical research as well as to present new ideas that highlight the changes in the neurological clinical practice.

Advanced Neurology covers subject areas, including but not limited to the following:

- Neurological disorders
- Neurodegenerative disease
- Cerebrovascular disease
- Epilepsy and movement disorders
- Neuroimmune disease
- Neurological infections
- Muscle disease
- Molecular and cellular neuroscience
- Systems neuroscience
- Cognitive neuroscience
- Computational modeling of nervous system

Global Translational Medicine is a quarterly journal that focuses on medicine, biological sciences, and biomaterials engineering. The goal of *Global Translational Medicine* is to provide a platform to researchers for showcasing their latest research works in translational medicine so as to advance the field towards the betterment of human health. Despite the advancement of omics and new technologies, the process of transforming these technologies and scientific research results into effective therapies and putting them into clinical use still has a long way to go. *Global Translational Medicine* provides a platform to fill the gaps in preclinical and inter-disciplinary research, to promote clinical translation of scientific research results, and to contribute to the conception of new and improved preventive measures as well as diagnostic and therapeutic techniques of diseases.

Global Translational Medicine covers the following themes: cardiovascular disease, metabolism/diabetes/obesity, neuroscience/neurology, cancer, biomaterials and their applications in medicine, proteomics/metabolomics, pharmacogenomics, biomarkers, bioinformatics and data mining, animal and clinical research, and medical methods arising from interdisciplinary crossover.

Start a new journal

Write to us via email if you are interested to start a new journal with AccScience Publishing. Please attach your CV, professional profile page and a brief pitch proposal in your email. We shall inform you of our decision whether we are interested to collaborate in starting a new journal.

Contact: info@accscience.com

https://accscience.com/journal/ARNM

ACCSCIENCE
PUBLISHING

Contact
www.accscience.com
9 Raffles Place, Republic Plaza 1 #06-00 Singapore 048619
Email: editorial@accscience.com
Phone: +65 8182 1586